University of Oxford

Department of Chemistry



Titanium layered double hydroxides for photocatalytic applications

Katarina Cermelj

Balliol College

Trinity Term 2020

This thesis is submitted in partial fulfilment of the requirement for the degree of Doctor of Philosophy at the University of Oxford

Preface

The work described in this thesis was carried out in the Chemistry Research Laboratory at the University of Oxford between October 2016 and September 2020 under the supervision of Professor Dermot O'Hare. All the work was performed by the author unless otherwise stated and no part has been previously submitted for any other degree.

Abstract

Titanium layered double hydroxides for photocatalytic applications

Katarina Cermelj **DPhil Thesis**

Balliol College **Trinity Term 2020**

This thesis discusses the development of novel titanium-containing layered double hydroxides (Ti-LDHs) as semiconductor photocatalysts for the photo-oxidation of simple organic molecules. LDHs are introduced in Chapter 1 as compositionally flexible anionic clays, whose layered structure and tuneable properties make them highly interesting in a wide range of applications, including environmental purification, drug delivery and photocatalysis. In the latter case, LDHs have been used primarily in the photocatalytic degradation of organic pollutants, photo-reduction of CO_2 and photocatalytic water splitting. Only limited research has been done into the controlled organic molecule photo-oxidation, where the oxidation is stopped at an intermediate stage rather than proceeding all the way to degradation products.

Chapter 2 outlines the five different synthetic methods for Ti-LDH preparation and their viability in the synthesis of pure NiTi- and MgAlTi-LDHs with different Ni:Ti and Al:Ti ratios, respectively. The crystallinity, morphology, structure, composition and band gap energies of the Ti-LDHs were analysed, so as to determine the effect of the synthetic conditions and Ti content on their properties. Furthermore, the highly crystalline urea hydrothermal MgAlTi-LDH samples were characterised by high-angle annular dark-field imaging (HAADF) as well as by ^{1}H, ^{27}Al and $^{47/49}Ti$ solid state NMR spectroscopy.

In Chapter 3, the activity of the Ti-LDHs in the photo-oxidation of diphenylmethanol is studied, and compared to that of anatase TiO_2 as a benchmark photocatalyst. The importance of short-wavelength radiation is discussed, especially for control experiments in the absence of a catalyst. The effects of the synthetic method, Ti content, catalyst and reactant loading, and irradiation time were examined for selected Ti-LDHs.

Chapter 4 extends the study of the photocatalytic properties of Ti-LDHs beyond diphenylmethanol photo-oxidation to also include benzyl alcohol, cyclooctanol and benzylamine. This allows the determination of whether Ti-LDHs can be used to photo-oxidise a wider range of functional groups as part of either aromatic or aliphatic systems.

Lastly, Chapter 5 details the synthesis and characterisation of TiO_2@Ti-LDH core-shell hybrid materials, and looks at their application in the photo-oxidation of diphenylmethanol. The conversion using the core-shell photocatalysts was compared to that obtained with a mechanical mixture of TiO_2 and Ti-LDHs, in order to study any synergistic heterojunction effects.

Acknowledgements

The last four years have been an adventure with more twists and turns than anyone could have predicted – from months-long periods filled with failed experiments and unexplainable data (which, thankfully, was explained eventually), to a cookbook deal and a global pandemic. To say that this DPhil was unconventional would be an understatement. This work would have been impossible without the contribution of a number of people, who lent me their time, expertise and support along the way.

Firstly, thank you to Professor Dermot O'Hare for giving me the opportunity to be part of his research group, and for all the guidance and advice throughout my studies. I would also like to thank the Clarendon Fund and Balliol college for the financial support – receiving the Clarendon and Balliol Jowett scholarships has been a privilege and I am incredibly thankful for it.

To Dr JC Buffet: thank you for all your support, help and patience – especially during all those weeks and months where none of the data made sense and I was despairing over this project going anywhere. Although I didn't have an "official" supervisor, the advice and expertise of Dr Dana-Georgiana Crivoi have been indispensable in navigating my way around catalytic setups and analysing the resulting data – thank you also for your unwavering support (in the lab and beyond) and the funny dog video breaks.

To Joyce and Tom: we've made it! It's crazy to think that we've been together on this Chemistry journey for eight years, first as fellow undergraduates and then as (hopefully wiser and more experienced) DPhil students. Special thanks to Joyce for being first an awesome tutorial partner and then later a fun and supportive LDH colleague.

While my weekdays were spent in the lab, my evenings and weekends were devoted to baking and working on my cookbook. Although I am now firmly convinced that only a crazy person would attempt to finish a DPhil and write a book at the same time, this rather exhausting time was made infinitely easier by my colleagues in the O'Hare research group. Thank you especially to Justin for our baking chats and being an excellent taste-tester, to Jess for indulging my baking- and book-related monologues, and to Phil for our discussions and making me laugh even when completely stressed out.

Finally, and most importantly, thank you to my parents – for your love, support and endless patience. Thank you for dealing with my stressing and overthinking, and for always knowing exactly what advice to give. None of this would be possible without you.

Nomenclature

Below is a summary of the terms and abbreviations used in this thesis.

Term/abbreviation	Definition
ºC	Degrees Celsius
Å	Ångström (10^{-10} m)
AMO	Aqueous miscible organic
AMOST	Aqueous miscible organic solvent treatment
ARR	Ammonia releasing reagent
BET	Brunauer-Emmett-Teller
CB	Conduction band
CDL	Crystallite domain length
CP-MAS	Cross polarisation magic angle spinning
cm	Centimeter (10^{-2} m)
DFT	Density functional theory
DI	Deionised
DP-MAS	Direct polarisation magic angle spinning
DRUV-vis	Diffuse reflectance ultraviolet-visible
dTGA	First derivative of thermogravimetric analysis curve
EtOH	Ethanol
eV	Electron volt
FTIR	Fourier transform infrared
FWHM	Full width at half maximum
g	Gram
h	Hour

HAADF	High angle annular dark-field imaging
HMT	Hexamethylenetetramine
Hz	Hertz
ICP-MS	Inductively coupled plasma mass spectrometry
^{i}Pr	Isopropyl (–$CH(CH_3)_2$)
IR	Infrared
K	Kelvin
L	Litre
LDH	Layered double hydroxide
m	Meter
M	mol dm^{-3}
MAS	Magic angle spinning
min	Minute
mg	Milligram (10^{-3} g)
Mg_6AlTi-LDH	$[Mg_{0.75}Al_{0.125}Ti_{0.125}(OH)_2](CO_3)_{0.188} \bullet xH_2O$
$Mg_{12}Al_3Ti$-LDH	$[Mg_{0.756}Al_{0.189}Ti_{0.063}(OH)_2](CO_3)_{0.166} \bullet xH_2O$
$Mg_{12}AlTi_3$-LDH	$[Mg_{0.756}Al_{0.063}Ti_{0.189}(OH)_2](CO_3)_{0.229} \bullet xH_2O$
mL	Millilitre (10^{-3} L)
MHz	Megahertz (10^6 Hz)
mol	Mole
mmol	Millimole (10^{-3} mol)
NaOEt	Sodium ethoxide
Ni_2Ti-LDH	$[Ni_{0.67}Ti_{0.33}(OH)_2](CO_3)_{0.32} \bullet xH_2O$
Ni_3Ti-LDH	$[Ni_{0.75}Ti_{0.25}(OH)_2](CO_3)_{0.25} \bullet xH_2O$
Ni_4Ti-LDH	$[Ni_{0.80}Ti_{0.20}(OH)_2](CO_3)_{0.20} \bullet xH_2O$
Ni_5Ti-LDH	$[Ni_{0.83}Ti_{0.17}(OH)_2](CO_3)_{0.17} \bullet xH_2O$

Ni_6Ti-LDH	$[Ni_{0.86}Ti_{0.14}(OH)_2](CO_3)_{0.14} \bullet xH_2O$
NMR	Nuclear magnetic resonance
O_h	Octahedral
Ph	Phenyl ($–C_6H_5$)
ppm	Parts per million
PXRD	Powder X-ray diffraction
rpm	Revolutions per minute
s	Second
SEM	Scanning electron microscopy
SEM-EDX	Scanning electron microscopy with energy dispersive X-ray analysis
SOD	Superoxide dismutase
ssNMR	Solid state nuclear magnetic resonance
TBA	Tert-butyl alcohol
T_d	Tetrahedral
TEM	Transmission electron microscopy
TEM-EDX	Transmission electron microscopy with energy dispersive X-ray analysis
TEMPO	Tetramethylpiperidine *N*-oxide
TGA	Thermogravimetric analysis
UV	Ultraviolet
UV-vis	Ultraviolet-visible spectroscopy
VB	Valence band
W	Watt
wt%	Weight percentage

Table of contents

Preface ..... **i**
Abstract ..... **ii**
Acknowledgements ..... **iii**
Nomenclature ..... **v**
Table of contents ..... **viii**
Chapter 1 Introduction **1**
1.1 Layered double hydroxides **1**
1.2 Methods of synthesis **6**
1.2.1 Co-precipitation method 6
1.2.2 Homogeneous precipitation method 7
1.2.3 Other methods of synthesis 7
1.3 Semiconductor photocatalysis **9**
1.4 Photo-oxidation of organic reactants **13**
1.4.1 Diphenylmethanol (benzhydrol) photo-oxidation 13
1.4.2 Benzyl alcohol photo-oxidation 14
1.4.3 Aliphatic alcohol photo-oxidation 16
1.4.4 Benzylamine photo-oxidation 17
1.5 Layered double hydroxides in photocatalysis **18**
1.5.1 Photocatalytic degradation of organic pollutants 19
1.5.2 Photocatalytic water splitting 19
1.5.3 Photo-reduction of CO_2 21
1.5.4 Photo-oxidation of organic reactants 21
1.5.5 The role of titanium-LDHs in photocatalysis 30
1.6 Thesis overview **32**
1.7 References **33**
Chapter 2 Synthesis and characterisation of NiTi- and MgAlTi-layered double hydroxides **37**
2.1 Introduction **37**
2.2 Synthetic methods and characterisation techniques **39**
2.3 Variation and optimisation of synthetic methods **42**
2.4 Variation of metal ratios **53**
2.5 Thermogravimetric analysis and chemical formulae **60**
2.6 Band gaps and Ti oxidation states **63**
2.7 Advanced analysis of high crystallinity MgAlTi-LDHs **67**
2.8 Conclusions **74**

2.9 References 75
Chapter 3 Photo-oxidation of diphenylmethanol 77
3.1 Introduction 77
3.2 Photo-reactor setup and reaction conditions 80
3.3 Characterisation techniques and product mixture analysis 83
3.4 The effect of short-wavelength UV radiation 86
3.5 Control reactions and TiO_2 baseline reactions 88
3.6 The effect of Ti-LDH composition and synthetic method 93
3.7 Variation of catalyst loading and reactant concentration 101
3.8 Kinetic studies and catalyst re-cycling 104
3.9 Conclusions 108
3.10 References 109
Chapter 4 Photo-oxidation of benzyl alcohol, cyclooctanol and benzylamine 111
4.1 Introduction 111
4.2 Photo-reactor setup and reaction conditions 114
4.3 Characterisation techniques and product mixture analysis 116
4.4 Photo-oxidation of benzyl alcohol 120
4.5 Photo-oxidation of cyclooctanol 126
4.6 Photo-oxidation of benzylamine 129
4.7 Comparison of the four different reactants 133
4.8 Conclusions 135
4.9 References 136
Chapter 5 Core-shell titanium dioxide@Ti-LDH hybrid materials 137
5.1 Introduction 137
5.2 Synthetic methods and characterisation techniques 141
5.3 TiO_2@Ti-LDH synthesis and characterisation 143
5.3.1 TiO_2 characterisation 143
5.3.2 The effect of the synthetic method on TiO_2@Ni_4Ti-LDHs 143
5.3.3 The effect of the synthetic method on TiO_2@$Mg_{12}Al_3$Ti-LDHs 146
5.3.4 The effect of the TiO_2:LDH ratio on TiO_2@$Mg_{12}Al_3$Ti-LDHs 148
5.3.5 The effect of the ageing time on TiO_2@$Mg_{12}Al_3$Ti-LDHs 149
5.4 Thermogravimetric analysis and composition of TiO_2@$Mg_{12}Al_3$Ti-LDHs 152
5.5 Band gaps of selected TiO_2@MgAlTi-LDHs 155
5.6 TiO_2@MgAlTi-LDHs in diphenylmethanol photo-oxidation 158
5.7 Conclusions 161
5.8 References 163
Chapter 6 Conclusions and outlook 165
Chapter 7 Experimental details 171
7.1 Analytical techniques for LDH characterisation 171

7.1.1 Diffuse reflectance UV-visible spectroscopy (DRUV-vis) 171
7.1.2 Fourier transform infrared (FTIR) spectroscopy 171
7.1.3 High-angle annular dark-field imaging (HAADF) 171
7.1.4 Inductively coupled plasma mass spectrometry (ICP-MS) 172
7.1.5 Powder X-ray diffraction (PXRD) 172
7.1.6 Scanning electron microscopy (SEM) and scanning electron microscopy with energy-dispersive X-ray analysis (SEM-EDX) 172
7.1.7 Solid state nuclear magnetic resonance (ssNMR) spectroscopy 173
7.1.8 Surface area analysis 173
7.1.9 Thermogravimetric analysis (TGA) 173
7.1.10 Transmission electron microscopy (TEM) and transmission electron microscopy with energy-dispersive X-ray analysis (TEM-EDX) 174
7.2 Analytical techniques for photo-oxidation conversion and selectivity calculations 175
7.2.1 Nuclear magnetic resonance (NMR) spectroscopy 175
7.2.2 Ultraviolet-visible (UV-vis) spectroscopy 175
7.3 Experimental details for Chapter 2 176
7.3.1 Materials 176
7.3.2 Synthesis of NiTi-LDHs 176
7.3.3 Synthesis of MgAlTi-LDHs 179
7.3.4 Variation of Ni:Ti and Al:Ti metal ratios 182
7.3.5 Ti-LDH product workup 183
7.4 Experimental details for Chapter 3 188
7.4.1 Materials 188
7.4.2 Photo-reactor setup 188
7.4.3 Actinometry 189
7.4.4 Control reactions 190
7.4.5 Product mixture workup 191
7.4.6 TiO_2 baseline reactions 191
7.4.7 Variation of the Ti-LDH photocatalysts 192
7.4.8 Variation of catalyst loading 192
7.4.9 Variation of reactant concentration 193
7.4.10 Kinetic studies 193
7.4.11 Catalyst re-cycling 193
7.5 Experimental details for Chapter 4 195
7.5.1 Materials 195
7.5.2 Photo-reactor setup 195
7.5.3 No catalyst control reactions 195
7.5.4 Benzyl alcohol photo-oxidation 195
7.5.5 Cyclooctanol photo-oxidation 196

7.5.6 Benzylamine photo-oxidation 197
7.6 Experimental details for Chapter 5 198
7.6.1 Materials 198
7.6.2 Synthesis of TiO_2@NiTi-LDHs 198
7.6.3 Synthesis of TiO_2@MgAlTi-LDHs 201
7.6.4 TiO_2@Ti-LDH product workup 204
7.6.5 Diphenylmethanol photo-oxidation 206
7.7 References 207
Appendix A: Appendix for Chapter 2 ..... A.1
A.1 TEM of constant pH aqueous co-precipitation NiTi-LDH A.1
A.2 PXRD patterns of NiTi- and MgAlTi-LDHs A.1
A.3 FTIR spectra of NiTi- and MgAlTi-LDHs A.3
A.4 BET specific surface areas of NiTi- and MgAlTi-LDHs A.5
A.5 TEM images of NiTi-LDHs with different Ti content A.6
A.6 TEM images of MgAlTi-LDHs with different Ti content A.7
A.7 TGA plots of NiTi-LDHs A.8
A.8 TGA plots of MgAlTi-LDHs A.11
A.9 Chemical formulae of NiTi- and MgAlTi-LDHs A.14
A.10 Detailed compositional analysis of Ti-LDHs A.16
A.11 UV-vis spectra of NiTi- and MgAlTi-LDHs A.18
Appendix B: Appendix for Chapter 3 ..... B.1
B.1 An overview of reactant concentrations and catalyst loadings in diphenylmethanol photo-oxidation reactions B.1
Appendix C: Appendix for Chapter 4 ..... C.1
C.1 An overview of reactant concentrations and catalyst loadings in benzyl alcohol, cyclooctanol and benzylamine photo-oxidation reactions C.1
Appendix D: Appendix for Chapter 5 ..... D.1
D.1 PXRD patterns of TiO_2@MgAlTi-LDHs D.1

Chapter 1 Introduction

1.1 Layered double hydroxides

Layered double hydroxides (LDHs) are a family of anionic clays, with a chemical composition represented by the general formula $[M^{z+}_{1-x}M'^{w+}_{x}(OH)_2]^{a+}$ $(X^{n-}_{a/n}) \bullet bH_2O$, where usually $z = 2$ with $M^{2+} = Ca^{2+}$, Mg^{2+}, Zn^{2+}, Ni^{2+}, Mn^{2+}, Co^{2+}, Fe^{2+}, and $w = 3$ with $M'^{3+} = Al^{3+}$, Cr^{3+}, Mn^{3+}, Fe^{3+}, Ga^{3+}, Co^{3+}, Ni^{3+}, so that $a = x$.[1]

LDHs are also known as "hydrotalcite-like" materials, after the naturally occurring mineral hydrotalcite, a hydroxycarbonate of magnesium and aluminium that was discovered in Sweden around 1842.[2] Simultaneously, the isostructural mineral pyroaurite, a hydroxycarbonate of magnesium and iron, was discovered. The exact formula of hydrotalcite was later determined to be $[Mg_6Al_2(OH)_{16}]CO_3 \bullet 4H_2O$, such that $x = 0.25$ in the general formula above.

The structure of an LDH can be related to that of brucite, $Mg(OH)_2$, which consists of neutral layers of edge-sharing magnesium hydroxide octahedra.[3] Partial isomorphous substitution of M^{2+} cations by M'^{3+} cations in the octahedral sites results in a net positive charge of the hydroxide layers, which is balanced by anions in the interlayer space.[4] The anions thus separate the hydroxide layers, thereby making them accessible to water molecules.[5] In the general formula, the number of water molecules, b, includes both those in the interlayer region and those physically adsorbed onto the LDH surface.[6] The former are hydrogen-bonded to the hydroxyl groups in the layers and to the intercalated anions,[7] while still retaining a significant amount of their translational mobility.[5]

Naturally occurring LDHs exist in two polymorphic forms, a 2-layer hexagonal and a 3-layer rhombohedral form.[6] In the hexagonal form, the lattice parameter, c, is equal to

twice the interlayer separation, while in the rhombohedral form it is equal to three times the interlayer separation.[1]

Figure 1.1 shows a simplified structure of carbonate-intercalated LDHs with different M^{2+}/M'^{3+} molar ratios, as well as the intercalated water molecules and carbonate anions present in the interlayer region.[8]

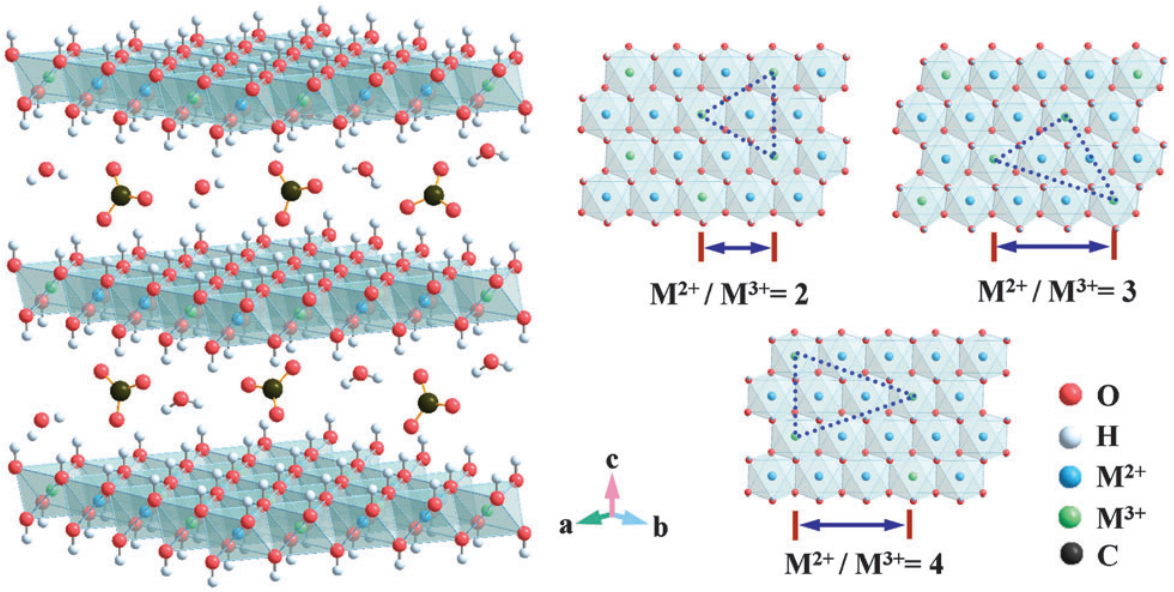


Figure 1.1 The idealised structure of carbonate-intercalated LDHs with different M^{2+}/M^{3+} molar ratios showing the metal hydroxide octahedra stacked along the crystallographic *c*-axis, as well as the water molecules and anions present in the interlayer region.[8] (Reproduced from reference 8.)

The cations in the metal hydroxide layers are arranged so that M'^{3+}–M'^{3+} close contact is minimised due to the repulsion of the higher positive charges. Consequently, it has been found that pure M(II)M'(III)-LDH phases exist only for $0.2 \leq x \leq 0.33$, corresponding to M(II):M'(III) ratios from 4:1 to 2:1.[6,9]

Outside of these parameters, impurity regions of M(II) and/or M'(III) hydroxides and oxides are usually formed, although exceptions to this general rule do exist. For example, a MgFe-LDH with a Mg:Fe ratio of 5:1 has been reported.[10] LDHs with a metal ratio of 1:1 have also been prepared. For instance, Sotiles *et al.* have synthesised a range of

MnAl-LDHs with a Mn:Al ratio close to 1:1.[11] These LDHs include solvated alkali metals and sulfate anions as the intercalated species, such that their molecular formula is $[Mn_3Al_3(OH)_{12}](SO_4)_2A \bullet nH_2O$, where A = Li, Na or K.

Although M(II)M'(III)-LDHs (z = 2, w = 3) are the most widely studied LDH family, LDHs where z = 1 (w = 3) and w = 4 (z = 2) have also been reported. In the former case, LiAl-LDHs are the most extensively studied example.[1,12] In the latter case, Ti^{4+} is the most frequently reported tetravalent cation to be incorporated into the LDH metal hydroxide layers (e.g. in NiTi-, ZnTi- and CoTi-LDHs),[13,14] although tricationic MgAlZr(IV)-, NiAlZr(IV)-, ZnAlZr(IV)- and MgAlSn(IV)-LDHs have also been prepared.[15-18]

The presence of mono- and tetra-valent cations disrupts the typical crystallisation patterns of LDHs. Whereas M(II)M'(III)-LDHs, such as MgAl-LDHs, show little evidence of cation ordering (i.e. Mg^{2+} and Al^{3+} occupy the same crystallographic set of octahedral coordination sites), LiAl-LDHs show cation ordering where lithium cations occupy octahedral vacancies in the $Al(OH)_3$ layers.[1,2,19]

M(II)Ti(IV)-LDHs, on the other hand, frequently show a decreased crystallinity and less well-defined morphology compared to M(II)M'(III)-LDH counterparts. Ternary M(II)M'(III)Ti(IV)-LDHs, such as MgAlTi-LDHs, have also been synthesised and it has been found that varying the Al:Ti ratio affects the degree of LDH crystallinity as observed from the sharpness and intensity of the (00l) powder X-ray diffraction (PXRD) reflections.[20] Specifically, a larger Ti content, quantified by the $Ti^{4+}/(Ti^{4+} + Al^{3+})$ ratio, corresponds to a reduced (00l) peak intensity, indicating a reduced LDH crystallinity.

The decreased crystallinity of M(IV)-containing LDHs has been ascribed to two factors: the larger size and the higher charge of M^{4+} cations. For instance, the ionic radius of the

Ti^{4+} cation in octahedral coordination, is 0.61 Å, which is notably larger than that of Al^{3+} in the same coordination environment (0.54 Å). This size disparity can result in the distortion of the LDH metal hydroxide layers and consequently in a reduced crystallinity and a less well-defined morphology. This difference in ionic radii also results in an increased d_{003}-spacing of Ti-LDHs as compared to Al-LDHs, as determined from a shift of the (003) PXRD basal reflection.[20] The presence of Ti^{4+} cations with the higher charge also increases the cation-cation same charge repulsion within the LDH metal hydroxide layers, while also increasing the net positive charge on the layers, requiring a larger amount of CO_3^{2-} intercalated anions to balance out the charge.[20] The presence of Ti^{4+} cations also changes the values of x accessible to pure M(II)Ti(IV)-LDH phases, with $0.14 \leq x \leq 0.33$ and the corresponding M(II):Ti(IV) ratios ranging from 6:1 to 2:1.[21-24]

In addition to the metal cations in the hydroxide layers, the intercalated molecules also influence the chemical and physical properties of the LDHs, which can be harnessed for application purposes. The dimensions, functional groups and number of the guest molecules determine their orientation within the interlayer space, as well as their mono- or bilayer formation, all of which in turn determine the separation of the metal hydroxide layers.[2] Further important factors are the host-guest (electrostatic[25,26] and hydrogen bonding[27,28]) and guest-guest (hydrogen bonding,[26] hydrophobic,[29] and π-π stacking[26,30]) interactions.

The intercalated anions can be simple inorganic anions (e.g. CO_3^{2-}, SO_4^{2-}, NO_3^-, halides), polyoxometalates (e.g. $Cr_2O_7^{2-}$, WO_4^{2-}), transition metal complexes (e.g. $[Fe(CN)_6]^{3/4-}$), polymers, and organic anions such as (di)carboxylates, alkyl sulfates and sulfonates, as well as biologically active materials such as porphyrins, nucleoside phosphates, drugs, vitamins, amino acids and fatty acids.[1,2]

Due to their layered structure, flexible composition and tuneable properties, LDHs have a wide range of applications, acting as adsorbents in environmental purification,[31-33] catalysts,[2,32,34] flame retardant materials,[2,35-37] corrosion inhibitors,[2,38] ion-exchange materials,[1,2] polymer additives,[35] drug carrier agents,[35,39] and photocatalysts.[14,40-42]

1.2 Methods of synthesis

1.2.1 Co-precipitation method

The first synthetic LDHs were prepared by Feitknecht in 1942 by the co-precipitation method where very dilute solutions of M^{2+} and M'^{3+} salts are reacted with dilute basic solutions.[43,44] In this method, the LDH metal hydroxide layers are nucleated and grown from an aqueous solution containing the suitable metal salts as well as the anions to be intercalated. The anions need to have a high affinity for the metal hydroxide layers, otherwise the counter anions of the metal salts may be preferentially intercalated, thereby contaminating the LDH.[31] Therefore, metal salts such as nitrates or chlorides are often chosen as starting materials, since NO_3^- and Cl^- anions have a low affinity for LDH metal hydroxide layers as compared to the usually preferable CO_3^{2-} or SO_4^{2-} anions.[25]

In order to co-precipitate two or more cations it is necessary for the precipitations to take place under conditions of supersaturation, which are achieved by physical (evaporation) or chemical methods (control of pH), the latter being more frequently utilised in LDH synthesis.[2] Cavani *et al.* described three different co-precipitation methods for LDH synthesis, all of which include some form of addition of NaOH and/or $NaHCO_3$ to the metal salt solution.[2] In all cases, in order to ensure simultaneous precipitation of both cations and thus LDH formation, it is necessary to perform the co-precipitation at a pH at which both the M^{2+} and M'^{3+} hydroxides precipitate.[31] Following the mixing and precipitation, the LDH products are aged at either room[9,45,46] or elevated temperatures.[3,28,31,35]

1.2.2 Homogeneous precipitation method

Costantino *et al*. have applied the so-called homogeneous precipitation method to the LDH synthesis and found that it leads to the formation of LDHs with a good crystallinity degree and a narrow particle size distribution.[47] Specifically, they used the urea method, in which LDH precipitation is enabled by the thermally induced hydrolysis of urea in the presence of a mixture of M^{2+} and M'^{3+} salts.[47] Urea has a number of properties that make its use as an agent for precipitation from homogeneous solution very attractive. It is a weak Brønsted base (pK_b = 13.8), highly soluble in water, and its hydrolysis rate can be easily controlled by changing the temperature of the reaction.[47] The rate constant of the hydrolysis reaction increases approximately 200 times when the reaction temperature is increased from 60 to 100 ºC.[48] The mechanism of urea hydrolysis comprises the formation of ammonium cyanate as the rate determining step, followed by the rapid hydrolysis of the cyanate to ammonium carbonate.[48] The final conversion of ammonium to ammonia and carbonate to hydrogen carbonate results in a pH of about 8.5 – 9.0, suitable for the precipitation of a large number of LDHs.[47]

As an alternative to urea, hexamethylenetetramine (HMT) has also been used as an ammonia releasing reagent (ARR).[49,50] Since its first application to LDH synthesis,[47] the homogeneous precipitation method using either ARR has been applied to the synthesis of a wide variety of LDHs, either under refluxing[51,52] or hydrothermal conditions.[50,53-56]

1.2.3 Other methods of synthesis

Aside from the LDH synthetic methods described above, other procedures have been used, including anion exchange,[2,31,57] rehydration method,[2,31] reverse micelle

microemulsion method,[12,40] sol-gel method,[58] and separate nucleating and ageing steps (SNAS) method.[12]

In the SNAS method, the different LDH metal salt precursors are mixed together rapidly in a colloidal mill, which induces a rapid nucleation of the LDH particles. The resultant slurry is subsequently aged in a separate step. Thus, the SNAS method allows all the particles to begin forming at the same time and, consequently, the ageing and growth time are the same for all particles. This results in a narrower particle size distribution and a more uniform particle morphology, particularly when compared to the standard co-precipitation method, where particles precipitate out at different times and therefore have a range of different ageing times.[12,59,60]

1.3 Semiconductor photocatalysis

Harnessing solar energy for the catalysis of industrially and pharmaceutically important chemical reactions is an attractive option, as it uses a sustainable, environmentally friendly energy source and can reduce the need for harsh chemicals, such as hydrogen peroxide. Semiconductor photocatalysts have been of interest since the late 1960s, when the activity of TiO_2 in environmental photocatalysis was discovered.[61] In 1972, Fujishima and Honda discovered that water could be split (simultaneously oxidised and reduced) by illuminating a TiO_2 single-crystal electrode to which a small electrochemical bias had been applied.[62] Since then, a significant amount of research has been done into TiO_2 photocatalysis due its chemical stability, non-toxicity, high photocatalytic activity and relatively low cost.[61,63]

The photocatalytic mechanism of TiO_2 and other semiconductor photocatalysts, by which solar energy is converted into chemical energy, involves the promotion of an electron (e^-) from the valence to the conduction band following the absorption of a photon, where the energy of the photon needs to exceed the band gap energy of the photocatalyst (so-called "ultrabandgap illumination"). At the same time, an electronic vacancy or a "hole" (h^+) is generated in the valence band.[63,64] This photogenerated charge carrier pair is typically located in the outer surface region of the photocatalyst due to the short penetration depth of UV and visible light. The charge carrier pair may then undergo a series of processes, including recombination, trapping and interfacial redox reactions, as summarised graphically in Figure 1.2.[63]

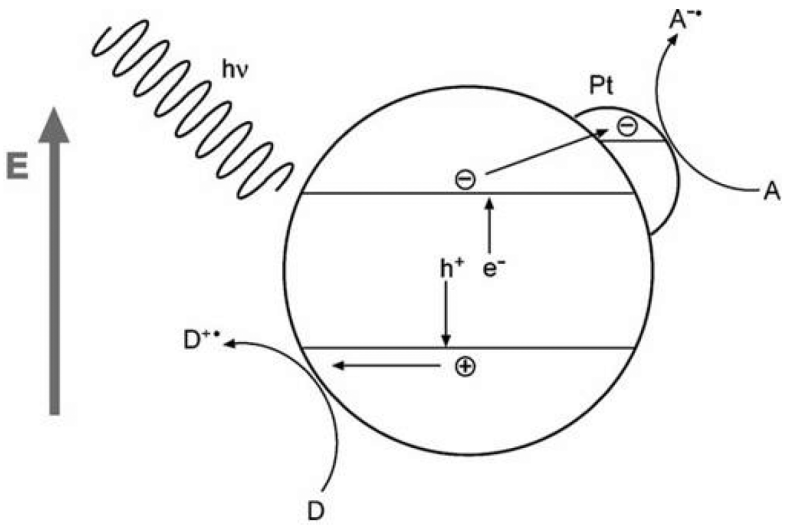


Figure 1.2 Electron (e^-) – hole (h^+) pair generation by photon absorption in a semiconductor photocatalyst. The diffusion of charge carriers to the surface competes with their recombination, which leads to heat generation. At the surface, the charge carriers are trapped by acceptors (A) and donors (D). Trapping of the electrons by acceptors from the semiconductor conduction band is enhanced by platinum "islands", which reduces recombination by improving charge separation.[61] (Reproduced from reference 61.)

Charge carrier recombination is one of the primary mechanisms of inhibiting photocatalyst activity. Immediately after their formation, the recombination of the electron-hole pair is retarded as the charge carriers move in different directions due to a near surface electric field.[63] Continuous illumination destroys this electric field, increasing the likelihood of recombination taking place. The recombination can occur via either non-irradiative pathways (resulting in heat evolution) or irradiative routes (resulting in light emission), depending on whether the semiconductor has a direct or an indirect bad gap, as well as on the presence of trap states. The latter refers to sites of hole, electron or charge carrier pair trapping, which can form on the catalyst surface or in the bulk material.[63]

The photogenerated electrons and holes can be transferred to electron and hole receptors, respectively, weakly adsorbed to the photocatalyst surface, provided the energetic requirements are fulfilled.[62] These are typically quantified by the reduction and oxidation (redox) potentials of the charge carriers and receptor molecules. Specifically, the

reduction potential of the receptor molecule should be lower than the bottom edge of the semiconductor catalyst's conduction band (for reduction) and the oxidation potential of the receptor should be higher than the top edge of the catalyst's valence band (for oxidation).[65] The transfer of an electron or hole to the receptor molecule results in the formation of an anion ($A^{\bullet-}$) or cation ($D^{\bullet+}$) radical, respectively. These radicals can participate in several pathways: (1) reacting chemically between themselves, (2) recombining by back electron transfer to form the excited state of one of the reactants or to dissipate the excitation energy by a non-radiative pathway, or (3) diffusing from the semiconductor catalyst surface into the bulk solution, where they participate in further chemical reactions. Which of these occurs depends on the kinetics of each of the three main pathways and the rate of diffusion of the receptor molecules into the bulk solution.[62]

If the charge carrier receptors are molecules or materials of industrial or pharmaceutical interest, this can be harnessed to catalyse important chemical transformations. Consequently, any photocatalyst development and optimisation should involve adjustments that suppress charge carrier recombination, while promoting the interfacial redox reactions. One method by which the recombination rate can be decreased is the formation of heterojunctions, for instance by doping TiO_2 nanoparticles with noble metals (Figure 1.2).[63]

Because of its high photocatalytic activity, TiO_2 is the most widely studied and industrially used photocatalayst to date. It is also the benchmark photocatalyst against which photocatalytic activity is usually measured.[62] Comparing its three main polymorphic forms, it has been found that anatase exhibits a higher photocatalytic activity than rutile and brookite. This has been ascribed to the charge carriers that are excited deeper in the bulk contributing to surface reactions in anatase than in rutile.[66] Additionally, anatase is an indirect band gap semiconductor, whereas rutile and brookite

belong to the direct band gap semiconductor category. Consequently, anatase exhibits a longer lifetime of photoexcited electrons and holes, as the direct transition of the photogenerated electrons from the conduction back to the valence band is not formally allowed in the case of an indirect band gap.[67]

Other notable semiconductor photocatalysts include metal oxides, nitrides or sulfides, such as CdS, MoS_2 and ZnO, as well as metal-free materials, such as carbon nitride (C_3N_4).[62,65] Within the metal semiconductor catalyst category, the most effective catalysts comprise d^0 or d^{10} metal elements, such as Ti, V, Zr, Zn, Ga and Ge, where the conduction band usually consists of the d (for d^0 elements) or sp orbitals (for d^{10} elements), while the valence band is composed of the 2p orbitals of oxygen or nitrogen atoms, or of the 3p orbitals of sulfur atoms.[65] In comparison to many other metal semiconductors, TiO_2 and ZnO have the advantage of long term stability in the presence of other chemicals, unlike WO_3, CdS, GaP, CdSe and GaAs, which are degraded during the repeated catalytic cycles of heterogeneous photocatalysis.[68] An advantage of TiO_2 over ZnO, however, is its stability in acidic solution where ZnO tends to dissolve.

The most widely researched metal-free semiconductor is graphitic carbon nitride, g-C_3N_4, which has the advantage of a smaller band gap compared to many metal semiconductors. Consequently, it can be used as a visible light photocatalyst.[65]

Semiconductor photocatalysts have been used for a wide range of chemical transformations, including but not limited to overall water splitting, water splitting with focus on one of the half reactions (hydrogen or oxygen evolution), CO_2 reduction, ammonia synthesis and photocatalytic organic pollutant degradation and removal.[65]

1.4 Photo-oxidation of organic reactants

Although the bulk of research into semiconductor photocatalysis has been made in the areas of water splitting, CO_2 reduction and pollutant removal, the photo-oxidation of organic reactants such as benzhydrol (diphenylmethanol),[69,70] benzyl alcohol,[71,72] cyclooctanol,[73] and benzylamine has also been explored.[74-76]

Although metal oxides, such as TiO_2, can acts as high-temperature thermal oxidation catalysts, better conversions and selectivities are observed for room temperature photocatalytic oxidations.[62] For instance, the oxidation of cyclohexane by oxygen over TiO_2 is thermodynamically permissible, but its rate at room temperature is very slow in the absence of irradiation. Even at higher temperatures in the absence of irradiation, little oxidation is observed. In contrast, notable photo-oxidation is observed in the presence of TiO_2, producing 83% cyclohexanone, 5% cyclohexanol and 12% CO_2.[62]

1.4.1 Diphenylmethanol (benzhydrol) photo-oxidation

The photo-oxidation of diphenylmethanol to benzophenone in the presence of TiO_2 photocatalysts has been reported in literature with little side product formation. Vijaikumar *et al.* observed significant conversion to benzophenone under irradiation by a medium pressure mercury lamp with light emission above 350 nm.[70] For a fixed amount of diphenylmethanol, increasing the amount of TiO_2 catalyst increases the amount of oxidised product present up to 0.1 w/v% TiO_2. Similarly, the amount of benzophenone formed was observed to vary linearly with the initial concentration of diphenylmethanol. The importance of a photo-inactive solvent has also been highlighted, with photo-reactions in acetonitrile resulting only in benzophenone formation. Photo-reactions in methanol and ethanol, on the other hand, showed no benzophenone formation and instead

resulted in solvent oxidation.[70] Mohamed *et al.* reported a 95% conversion of diphenylmethanol to benzophenone with anatase TiO_2 after 6 hours of UV irradiation in an acetonitrile solution saturated by bubbling oxygen through it, with minor side product formation of benzoic acid.[69]

1.4.2 Benzyl alcohol photo-oxidation

In comparison to diphenylmethanol (a secondary alcohol), the photo-oxidation of benzyl alcohol is more complex because of its primary alcohol nature. The primary photo-oxidation product, benzaldehyde, can thus be oxidised further to benzoic acid, which in turn allows ester formation via a condensation reaction between benzoic acid and any unreacted benzyl alcohol present.

Nonetheless, TiO_2 has been successfully used in the selective photocatalytic oxidation of benzyl alcohol and its derivatives in the presence of molecular oxygen and either visible or UV light irradiation. Higashimoto *et al.* reported conversions >99% with high selectivities (>99%) for the photo-oxidation of benzyl alcohol to benzaldehyde after 4 hours of irradiation with UV and visible light under an oxygen atmosphere.[72] Similar results were observed for the 4-substituted benzyl alcohol derivatives, including 4-chlorobenzyl, 4-methoxybenzyl, 4-nitrobenzyl and 4-methylbenzyl alcohol. The visible light response was attributed to a surface complex formed by the adsorption of a benzyl alcoholic compound onto the TiO_2 surface.[72] By measuring the UV-vis absorption spectra of TiO_2 on its own and benzyl-alcohol-adsorbed TiO_2, it was observed that unlike pure TiO_2 (which shows absorption only in the UV region), the benzyl-alcohol-adsorbed TiO_2 shows absorption also in the visible region. This was ascribed to the formation of a surface complex and consequently to a charge transfer from benzyl alcohol to TiO_2.[72] A similar hypothesis of a visible-light-absorbing benzyl alcohol-TiO_2 complex was also

suggested by Li *et al.*, who used single-crystalline rutile TiO_2 nanorods to achieve a 99% selectivity in the partial photocatalytic oxidation of benzyl alcohol to benzaldehyde.[77]

The photocatalytic oxidation of aryl alcohols in acetonitrile under UV irradiation by TiO_2 (anatase) has also been investigated by Mohamed *et al.* with 60% photo-oxidation of benzyl alcohol observed after 4 hours of irradiation with a 125 W medium pressure UV lamp.[69] After 6 hours of irradiation with a 450 W medium pressure UV lamp, the total conversion observed was 92%, with a selectivity for benzaldehyde of 48%. Benzoic acid (29%) was formed as a secondary photo-oxidation product. In the kinetic studies with the 125 W lamp, it was shown that the concentration of the over-oxidation product (benzoic acid) increases with prolonged irradiation time.[69]

The proposed mechanism of the benzyl alcohol (and derivatives) photo-oxidation proceeds via photogenerated charge carrier formation **[1]**, followed by the adsorption of oxygen molecules to the catalyst surface **[2]** where they act as electron receptors to form superoxide radical anions **[3]**.[69] The adsorbed alcohol species are likely receptors for holes, resulting in radical cation formation **[4]**. The oxidation process then proceeds via the interaction with the superoxide radical anions **[5.1]** or oxygen molecules **[5.2]**. Competing reactions include electron back transfer to re-form the reactant **[6]** and recombination reactions **[7]**.

$$TiO_2 + h\nu \rightarrow [TiO_2^*] \rightarrow TiO_2^{\bullet-} + e^-_{CB} + h^+_{VB} \quad \textbf{[1]}$$

$$O_2 \text{ (solution)} \rightleftharpoons O_2 \text{ (ads)} \quad \textbf{[2]}$$

$$O_2 \text{ (ads)} + e^- \rightarrow O_2^{\bullet-} \text{ (ads)} \quad \textbf{[3]}$$

$$\text{ArRH-C-OH (ads)} + h^+ \rightarrow (\text{ArRH-C-OH})^{\bullet+} \text{ (ads)} \quad \textbf{[4]}$$

$$(\text{ArRH-C-OH})^{\bullet+} \text{ (ads)} + O_2^{\bullet-} \text{ (ads)} \rightarrow \text{oxidation products} \quad \textbf{[5.1]}$$

$$(\text{ArRH-C-OH})^{\bullet+} \text{ (ads)} + O_2 \text{ (ads)} \rightarrow \text{oxidation products} \quad \textbf{[5.2]}$$

$$(ArRH\text{-}C\text{-}OH)^{\bullet+}\ (ads) + e^- \rightarrow ArRH\text{-}C\text{-}OH \quad \textbf{[6]}$$

$$e^- + h^+ \rightarrow kT \quad \textbf{[7]}$$

Beyond TiO_2, other semiconductor photocatalysts have also been used in benzyl alcohol photo-oxidation, including ZnO, CdS and g-C_3N_3. Jeena *et al*. reported the photo-oxidation of benzyl alcohol using dye-sensitised ZnO in combination with $AgNO_3$ and TEMPO in an aqueous solution with an 82% yield after 2 hours of irradiation with > 450 nm light.[78] In comparison, the equivalent reaction with TiO_2 produced a yield of only 8%, which was ascribed to a strong back electron transfer that reduces the photocatalytic activity of the TiO_2 system. Mixed-phase CdS nanocrystals have also been used in the photo-oxidation of benzyl alcohol to benzaldehyde, with a conversion of about 68% and a benzaldehyde selectivity of 94% after 1 hour of visible light irradiation under an O_2 atmosphere.[79] Cerdan *et al.* have used graphitic carbon nitride, g-C_3N_3, enriched with ZnO or Fe_2O_3 in the selective photo-oxidation of benzyl alcohol. The most active catalyst was Fe_2O_3/g-C_3N_3, which gave a 20% conversion and a 70% benzaldehyde selectivity after 4 hours of irradiation with a 125 W medium pressure mercury UV lamp (main emission at 365 nm) in the presence of air.[71]

1.4.3 Aliphatic alcohol photo-oxidation

The photo-oxidation of aliphatic reactants such as cyclooctanol does not have the added driving force of extending the conjugated system via carbonyl group formation, as compared to aromatic reagents. Consequently, the conversions observed under comparable photocatalytic conditions are lower, with more side product formation. For instance, the reported conversion of cyclohexanol to oxidation products was 72% (with a 64% selectivity for cyclohexanone formation) after 20 hours of irradiation with a 450 W medium pressure UV lamp with a TiO_2 P25 photocatalyst in acetonitrile .[73]

1.4.4 Benzylamine photo-oxidation

The selective photo-oxidation of amines into imines has been explored with a variety of semiconductor photocatalysts, including TiO_2,[74-76] g-C_3N_3,[80] and Nb_2O_5.[81] Unlike in benzyl alcohol photo-oxidation, where benzaldehyde is usually the primary product, benzylamine photo-oxidation does not result in the formation of the pure imine. Instead, *N*-benzylidenebenzylamine is formed *in situ* via the condensation reaction between the imine and the amine starting material.

Higashimoto *et al.* reported the selective photo-oxidation of benzylamine into *N*-benzylidenebenzylamine by TiO_2 under visible light irradiation in the presence of oxygen with a high conversion of over 80%. The visible light response was ascribed to the excitation of the charge transfer surface complex formed by the interaction between benzyl amine and the TiO_2 surface.[75]

1.5 Layered double hydroxides in photocatalysis

In recent years, LDHs have emerged as promising candidates to replace TiO_2-based photocatalysts in applications such as water splitting, CO_2 reduction and organic dye decomposition in pollutant removal. Their layered structure, compositional flexibility, controllable particle size and morphology, low preparation costs and ease of synthesis have resulted in ever-increasing amount of research into LDH photocatalysis.[8,32,82-85]

Incorporation of different photoactive cations into LDHs allows variable band gap photocatalysts to be prepared, with band gap energies ranging from 2.0 to 5.0 eV.[86] In comparison, TiO_2 has band gap energies of 3.0, 3.2 and 3.3 eV for rutile, anatase and brookite polymorphic forms, respectively.[85] Therefore, while TiO_2 acts primarily as a UV-active photocatalyst (unless visible-light-active complexes with the reactant are formed), LDHs can be used as both UV and visible light photocatalysts. The electronic properties of LDHs can be further fine-tuned by the systematic introduction of surface defects.[85] Additionally, the –OH groups of the LDH surface can react with the photogenerated holes to form hydroxyl radicals, $OH^{\bullet}$.[86] These radicals have a high oxidising potential and consequently play an important role as reactive oxygen species in photo-oxidation reactions.

To date, the research into LDHs as semiconductor photocatalysts has focused mainly on three areas: (1) photocatalytic degradation of organic pollutants, (2) photocatalytic water splitting, and (3) photo-reduction of CO_2 into hydrocarbon feedstocks and fuels.[85] Very little research has been done in the area of controlled organic molecule photo-oxidation, where the oxidation is stopped at an intermediate stage rather than proceeding until the degradation products are obtained.

1.5.1 Photocatalytic degradation of organic pollutants

The demand for the removal of organic pollutants, primarily dyes and phenols, from chemical and pharmaceutical industries is ever-growing. Beyond photocatalysis, LDHs have been of interest in the removal of anionic pollutant species from solution by either surface adsorption, interlayer anion exchange or reconstruction of the calcined LDHs.[82] However, LDHs have also shown promise in the photocatalytic pollutant removal via the degradation of organic compounds, such as Orange II,[87,88] methylene blue,[89-91] acridine orange,[92] and Rhodamine B,[93,94] which have been chosen as model pollutants.

ZnTi- and ZnFe-LDHs have attracted attention in this area due to their excellent visible light absorbing abilities, and they have shown good visible-light-induced photocatalytic performance in the degradation and removal of organic pollutants.[8] Similarly, CuCr- and NiCr-LDHs have been found to be 20-times more active than a standard P25 titania catalyst in the decomposition of dyes and phenols under visible light irradiation, as well as having an excellent recycling ability.[8] The ability of a carbonate-intercalated ZnCr-LDH to photodegrade organic pollutants has been ascribed to the ligand-to-metal charge transfer (LMCT) transitions of CrO_6 octahedra that have been observed in the UV-vis spectra of the material.[95]

1.5.2 Photocatalytic water splitting

LDHs have been used primarily in water splitting with focus on one of the half reactions, i.e. with focus on hydrogen or oxygen gas evolution. For instance, a carbonate-intercalated ZnCr-LDH has been found to be a visible-light-active photocatalyst for water splitting to generate hydrogen.[8] Its activity has been explained by the carbonate anions being oxidised to carbonate radicals by the photogenerated holes, which improves the

charge carrier separation. Further replacing part of the Zn^{2+} with Ni^{2+} results in additional metal-to-metal charge transfer (MMCT) transitions, and therefore in an enhanced photocatalytic activity for hydrogen evolution.[96]

In the solar-driven water splitting reaction, it is the water oxidation step that is unfavourable both kinetically and thermodynamically, since it occurs through several steps requiring four positive holes and the formation of O-O bonds.[8] Nonetheless, ZnCr-LDH photocatalysts have been reported to have an apparent quantum yield for O_2 generation of 61%.[97] This is one of the highest values ever reported for a bifunctional chromophore-catalyst material without the involvement of a foreign photosensitiser.[8] Ti-containing LDHs have also shown good water oxidation activity, with the high surface area NiTi-LDH showing a higher oxygen generation rate than CuTi-LDH.[14]

NiTi-LDH nanosheets with highly controlled size and morphology have been prepared by Zhao *et al*. using the reverse micelle microemulsion method, in order to fine-tune and ultimately increase the surface density of Ti^{3+} defects.[40] These LDH photocatalysts showed a very high photocatalytic activity for oxygen evolution using visible light, and have been reported to be one of the most active visible-light-active photocatalysts for oxygen evolution to date.[8] The proposed catalyst energy structure and a simplified mechanism of the photocatalytic oxygen evolution process are shown in Figure 1.3.

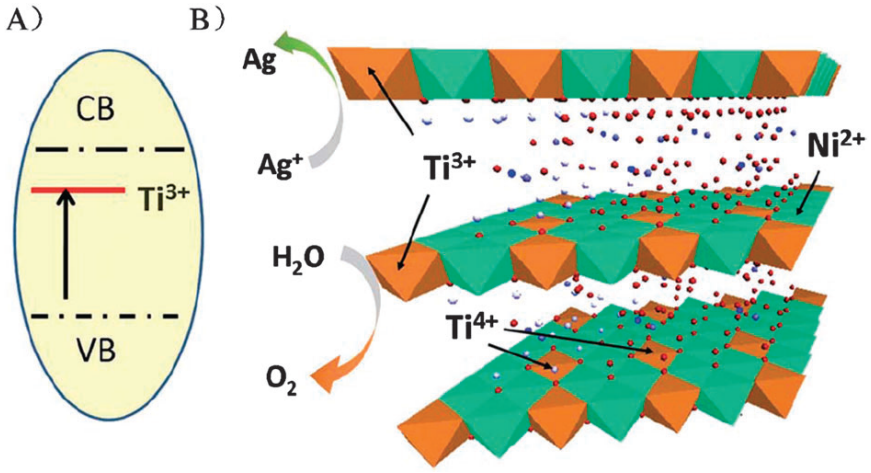


Figure 1.3 (A) The proposed structural model of the energy states for a NiTi-LDH photocatalyst and (B) the schematic illustration of the oxygen evolution process over NiTi-LDH nanosheets under visible light irradiation.[40] (Reproduced from reference 40).

1.5.3 Photo-reduction of CO_2

A highly selective CO_2 photo-reduction to methanol was reported using H_2 and a ZnCuGa-LDH photocatalyst. The high catalytic selectivity has been primarily attributed to the binding of CO_2 at the Cu-O-Zn and Cu-O-Ga sites to form hydrogen carbonate species.[98-100] Tanaka *et al.* further suggested that the surface basic sites of LDHs with a high water tolerance act not only as CO_2 adsorbents, but also as active sites for the activation of CO_2 under irradiation. They observed successful photo-reduction of CO_2 over various LDHs, including NiAl-, ZnAl-, NiGa- and ZnIn-LDHs.[101]

1.5.4 Photo-oxidation of organic reactants

Although LDH photocatalysts have been extensively used in water splitting, CO_2 reduction and complete degradation of organic molecules, limited research has been done on their application in the controlled oxidation of organic reactants, where the oxidation is stopped at an intermediate stage so as to obtain industrially or pharmaceutically relevant products (as opposed to proceeding to complete degradation products). This is especially true for reactions where the LDH metal hydroxide layers are the source of the

photocatalytic activity, as opposed to intercalated molecules or foreign photosensitisers. To the best of the author's knowledge, only four reports of such photocatalytic applications of LDHs exist to date.[24,86,102,103]

Pigot *et al.* have used a 4-benzoylbenzoate intercalated MgAl-LDH in the photo-oxidation of sulfides, where the intercalation of the photosensitiser in between the LDH layers has been shown to improve selectivity towards sulfoxide formation.[104] However, 4-benzoylbenzoate is the photocatalytically active species in this case, rather than the LDH layers.

Research by Teramura *et al.* has shown that a MgAl-LDH supported iron(III) porphyrin exhibits photocatalytic activity in the aerobic epoxidation of cyclohexene.[105] The LDH plays a more active role in this photocatalytic reaction as the iron(III) porphyrin is photocatalytically inactive in its absence. However, the reaction does not proceed without the porphyrin being present in the reaction mixture.

In 2014, the first application of LDHs as photocatalysts in the transformation of primary aromatic amines to their corresponding imines was reported.[24] Zn_6Ti-LDH (i.e. with a Zn:Ti molar ratio of 6:1) has been successfully used to oxidise a wide variety of aromatic and heteroaromatic amines with conversions as high as 100% and selectivities of up to 97% after 5 hours of UV irradiation under aerobic conditions in acetonitrile.[24] Figure 1.4 shows the suggested mechanism of the benzylamine photo-oxidation.

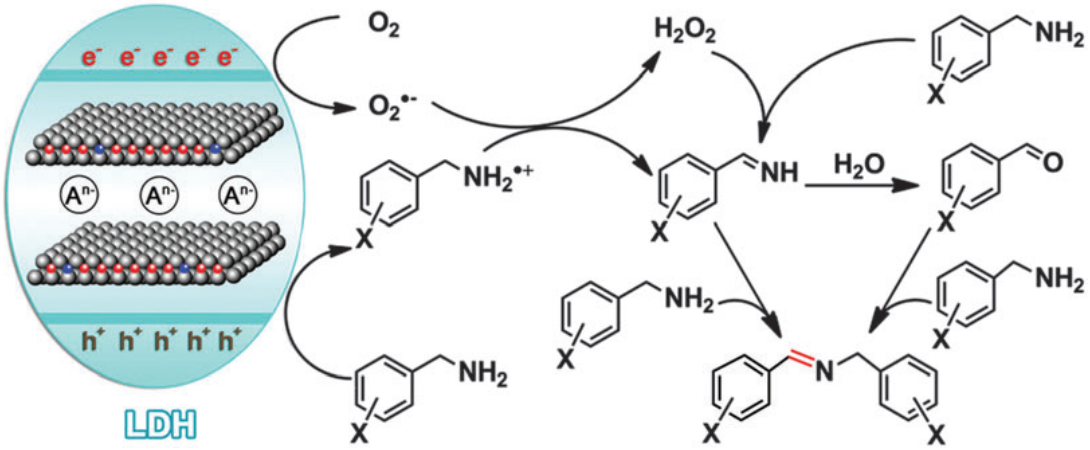


Figure 1.4 The suggested benzylamine aerobic photo-oxidation reaction pathway.[24] (Reproduced from reference 24.)

Control reactions showed that the Zn_6Ti-LDH photocatalyst, air (oxygen) and light are all essential for the reaction to take place. Zn_6Ti-LDH gave a better photocatalytic performance in the photo-oxidation of benzylamine than P25 TiO_2 and ZnO, which gave *N*-benzylidenebenzylamine yields of 85% and 78%, respectively. It was suggested that the superior performance of the Zn_6Ti-LDH catalyst stems from a better dispersion of the photocatalytically active TiO_6 units.[24]

Yang *et al.* have further investigated the effect of the ZnTi-LDH composition on the photocatalytic activity, observing that a lower Ti content (i.e. a higher Zn:Ti ratio) results in a higher photocatalytic activity. This was ascribed to a higher crystallinity and purity of Zn_6Ti-LDH as compared to Zn_5Ti- and Zn_4Ti-LDHs. The Zn_6Ti-LDH was also found to be recyclable, with the photo-oxidation conversion staying the same for four runs.[24]

The role of oxygen and the oxygen active species involved in the amine photo-oxidation reaction have been investigated by adding superoxide dismutase (SOD) radical trapping agent to the reaction mixture. SOD is a superoxide radical anion ($O_2^{\bullet-}$) scavenger. On the addition of SOD, the reaction yield decreases significantly, indicating that $O_2^{\bullet-}$ plays an important role in the amine photo-oxidation mechanism (Figure 1.4).[24] The presence of

H_2O_2 in the reaction was confirmed by adding a starch/KI/CH_3COOH mixture into the system after 1 hour of irradiation, as the colour of the solution changed from white to dark purple.

In 2016, Ni_3Al-LDHs with supported gold nanoparticles (Au/Ni_3Al-LDHs) were used in the selective aerobic photo-oxidation of benzyl alcohol and its derivatives under visible light.[103] A range of pure MgAl-, NiAl-, and NiMgAl-LDHs was also tested in the benzyl alcohol photo-oxidation reaction, under an oxygen atmosphere and with an irradiation time of 24 hours. Photocatalytic activity was observed in all cases, with the highest benzyl alcohol conversion reported for MgAl-LDH (15%). The conversion for NiAl-LDHs varies with the Ni:Al ratio, with the ratio of 3:1 giving the best conversion of 7%. Introducing Au nanoparticles into the system increases the photocatalytic conversion in all cases, with Au/Ni_3Al-LDH showing the best performance (41% conversion and >99% benzaldehyde selectivity).[103]

Figure 1.5 shows the mechanism proposed based on the experimental observations. The high conversion and selectivity of the Au/Ni_3Al-LDH photocatalyst were explained by the effect of localised surface plasmon resonance (LSPR) of Au nanoparticles and the synergy of the transition metal ion Ni(II).[103] Although the mechanism focuses on the Au nanoparticles as the main centres of photocatalytic activity, the reactions carried out with the pure LDHs (without the Au nanoparticles) clearly indicate that the LDH metal hydroxide layers are photocatalytically active in their own right.

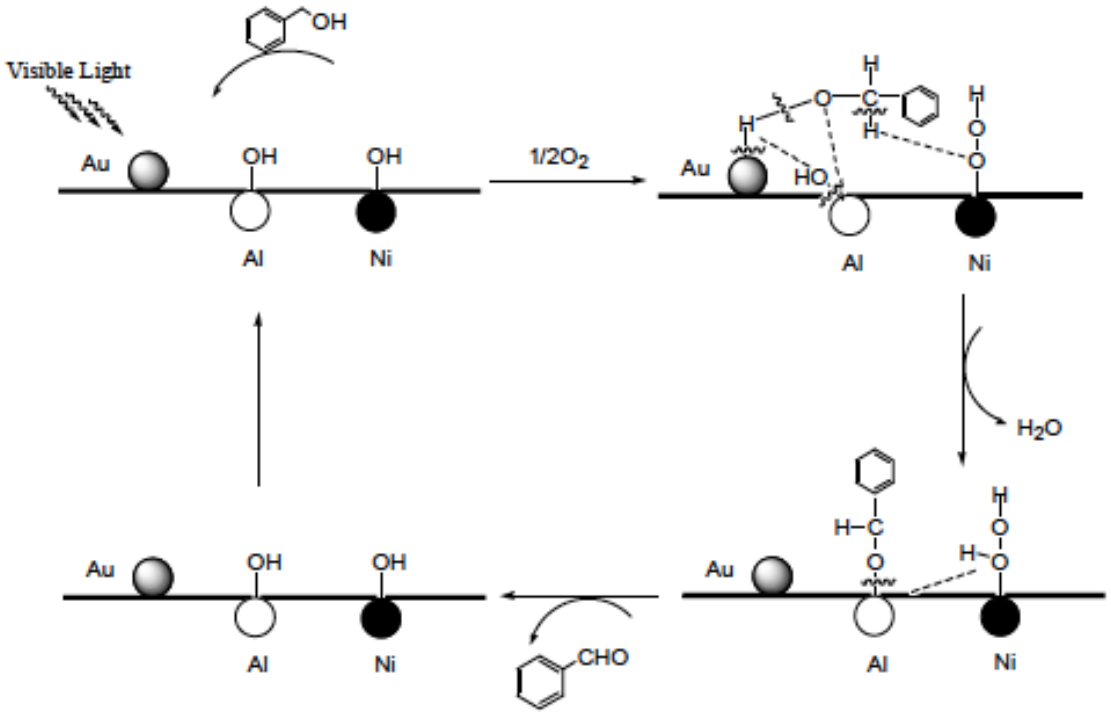


Figure 1.5 The proposed mechanism for the photocatalytic aerobic oxidation of benzyl alcohol using Au/Ni_3Al-LDH.[103] (Reproduced from reference 103.)

In 2018, Wang *et al.* reported the successful application of an Au-Pd/LDH photocatalyst in the selective photo-oxidation of benzyl alcohol under visible light irradiation.[106] An impregnation-reduction method was used to prepare MgAl-LDHs with supported Au-Pd bimetallic alloy nanoparticles of different Au:Pd ratios (Au-Pd/MgAl-LDHs). These photocatalysts showed significantly higher activity than Au/MgAl-LDH and Pd/LDH, as well as Au-Pd/TiO_2. Superoxide radical anions ($O_2^{\bullet-}$) were found to be the main reactive species. Benzyl alcohol can be activated at the surface base sites of MgAl-LDH via surface coordination to form a metal-alkoxide intermediate, which can then be more easily oxidised by $O_2^{\bullet-}$ to form benzaldehyde.[106]

Figure 1.6 summarises a possible mechanism based on the cooperation effect between the alloy nanoparticles and the surface basic sites of MgAl-LDH. As seen from the mechanism, the LDH metal hydroxide layers act only as basic sites that facilitate benzyl

alcohol activation, rather than actual sites of photocatalytic activity. Instead, that is restricted to Au-Pd alloy nanoparticles. Similarly, a report by Yu *et al.* in 2014 also showed that while Au/MgAl-LDHs show good photocatalytic activity in the aerobic oxidation of benzyl alcohol under visible light, no activity is observed in the absence of the Au nanoparticles.[107]

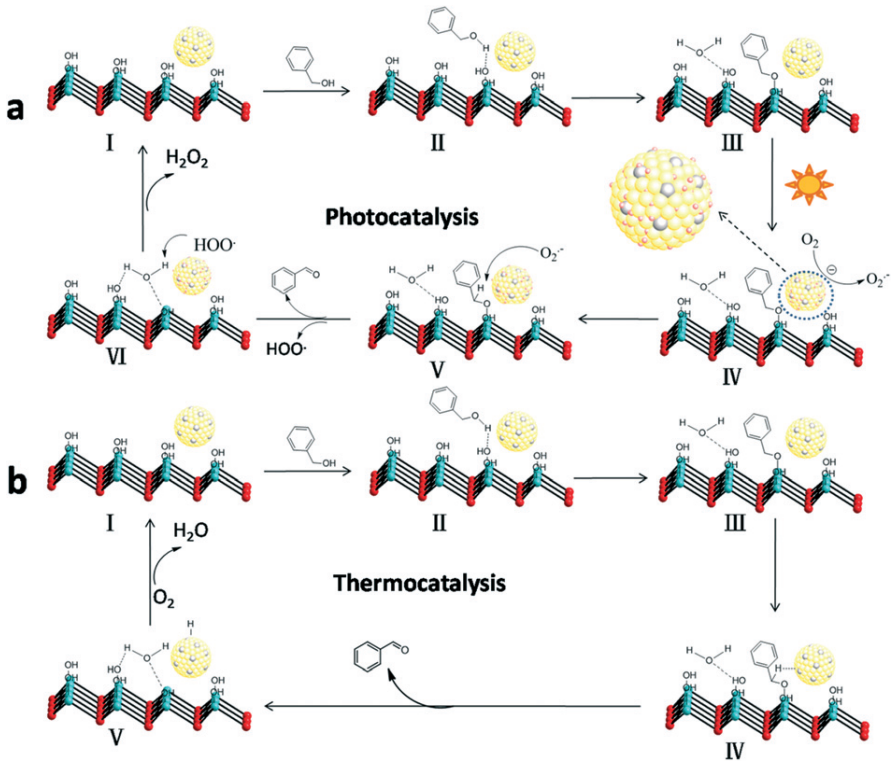


Figure 1.6 Possible mechanisms for the selective oxidation of benzyl alcohol to benzaldehyde over Au-Pd/MgAl-LDH via (a) photocatalysis and (b) thermocatalysis. Blue spheres: Mg/Al atoms, red spheres: oxygen atoms, yellow spheres: Au-Pd alloy nanoparticles.[106] (Reproduced from reference 106.)

In 2020, Li *et al*. used Zn_2Ti-LDHs in the selective photocatalytic oxidation of benzene to phenol in an aqueous solution under UV-visible irradiation.[86] The one-step photo-oxidation proceeds with a benzene conversion of 6% and a high phenol selectivity of 81% after 3 hours of irradiation. This makes ZnTi-LDHs superior to ZnO, TiO_2 and P25, which give phenol selectivities of 72%, 22% and 26%, respectively. The photocatalytic activity of Zn_2Ti-LDH was ascribed to the presence of oxygen vacancies on the LDH surface, which enhance the photogenerated charge carrier separation and consequently result in a

greater formation of superoxide radical anions that play a central role in the oxidation reaction. Additionally, the valence band energy of Zn_2Ti-LDH is a better match for the oxidation potential of benzene as compared to commercial ZnO, TiO_2 and P25 photocatalysts (Figure 1.7).

Density functional theory (DFT) calculations of the band structure gave band gap energies of 3.08, 3.42 and 3.32 eV for Zn_2Ti-LDH, ZnO and anatase TiO_2, respectively, which is in good agreement with experimental results from diffuse reflectance spectroscopy measurements.[86] Partial density of states (PDOS) further showed that for anatase TiO_2, Ti 3d and O 2p orbitals contribute to the conduction and valence bands, respectively. Similarly, Ti 3d orbitals contribute to the conduction band of Zn_2Ti-LDH, while Zn 3d and O 2p orbitals are the main components of its valence band. After oxygen vacancies are introduced ("doped") into the Zn_2Ti-LDH system, a new defect level forms in the middle of the band gap, which reduces the effective band gap energy from 3.08 eV for the undoped Zn_2Ti-LDH to 2.98 eV for the doped system.

These additional defect energy states can potentially act as electron trapping sites that promote electron transfer from the LDH to water or O_2 and therefore facilitate $O_2^{\bullet-}$ formation. This was confirmed by *in situ* experiments, which showed that $O_2^{\bullet-}$ radical anions form on the LDH surface through the photocatalytic water oxidation and play an important role in the benzene photo-oxidation reaction.[86]

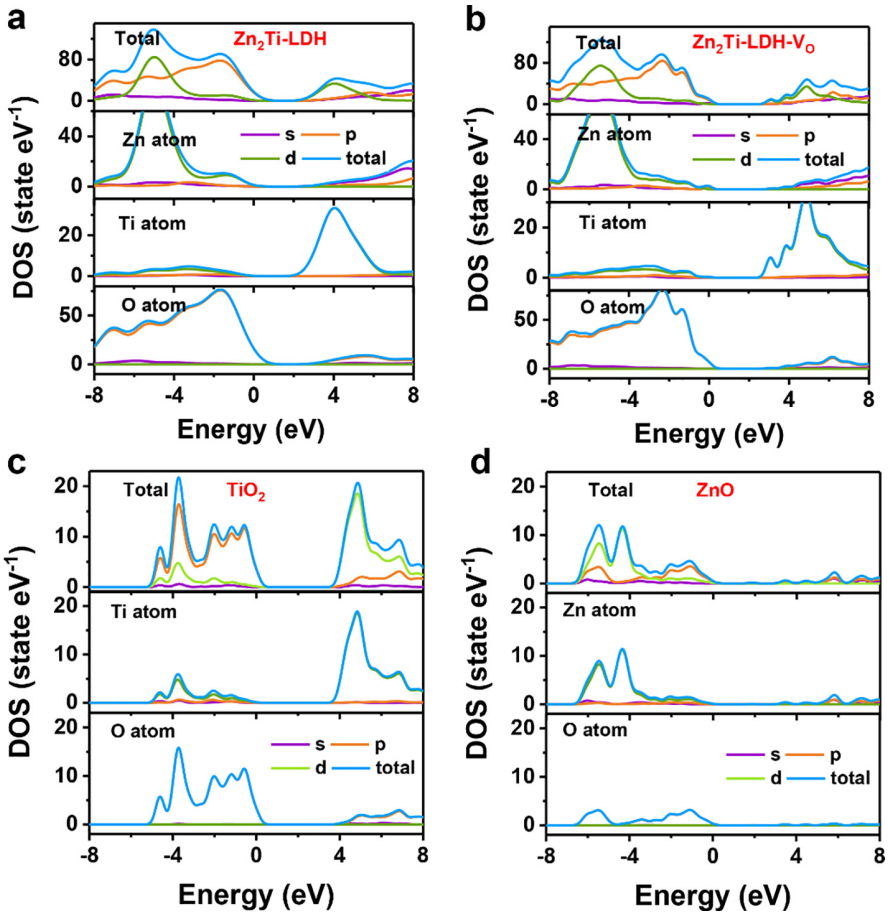


Figure 1.7 Total (TDOS) and partial density of stated (PDOS) of (a) Zn_2Ti-LDH, (b) Zn_2Ti-LDH-V_O with "doped" oxygen vacancies (Vo), (c) TiO_2 and (d) ZnO.[86] (Reproduced from reference 86.)

The reusability and recyclability of the Zn_2Ti-LDH photocatalyst was also investigated. The catalyst was recycled and tested for three cycles with no noticeable degradation in performance (conversion and selectivity).[86] Other LDHs, including NiTi-, CoAl-, NiAl-. ZnAl-, CoCr-, NiCr-, ZnCr-, CuCr-, MgFe-, CuFe-, NiFe-, CoMn-, and NiCo-LDHs, have also been used for the photocatalytic oxidation of benzene to phenol, but no product was detected.[86] Li *et al.* accredited these results to the unique band and electronic structure of Zn_2Ti-LDH.

Control experiments showed that the Zn_2Ti-LDH photocatalyst, air and light were all essential for the effective photo-oxidation of benzene to phenol. Whereas the catalysis cannot proceed in the absence of the photocatalyst and light, phenol can be formed under

a N_2 atmosphere as active oxygen species are formed *in situ* from water under irradiation. Nonetheless, the phenol yield is significantly reduced compared to the reaction in the presence of air.[86] The addition of radical trapping agents, including tetramethylpiperidine *N*-oxide (TEMPO, a radical scavenger), $K_2S_2O_4$ (an electron scavenger), tert-butyl alcohol (TBA, a hydroxyl radical scavenger), and superoxide dismutase (SOD, a superoxide radical anion scavenger), confirmed that $O_2^{\bullet-}$ radical anions play a key role in the photo-oxidation process.

Finally, also in 2020, ZnTi-LDHs have been used in the selective photocatalytic oxidation of benzyl alcohol to benzaldehyde under visible light irradiation in the presence of O_2.[102] Much like with TiO_2,[72,77] the visible light response of the photocatalyst system was attributed to the formation of a surface coordination complex via the chemisorption and activation of benzyl alcohol on the ZnTi-LDH surface. The importance of oxygen vacancies has also been highlighted, as they serve as electron trapping sites and therefore enhance photocatalytic activity.[102]

ZnTi-LDHs with a Zn:Ti ratio of 2:1 (i.e. Zn_2Ti-LDHs) were found to exhibit the best photocatalytic performance – a finding that goes against the observations of Yang *et al.*, who found Zn_6Ti-LDH to be the superior photocatalyst in the photo-oxidation of aromatic amines.[24] This activity trend was correlated to the proportion of exposed –OH groups, which is larger for Zn_2Ti-LDH than for other ZnTi-LDHs.[102] These exposed –OH groups act as coordination sites for benzyl alcohol and allow the formation of the activated surface complex. The latter has in turn been linked to the introduction of a greater number of oxygen vacancies in the Zn_2Ti-LDH structure, which results in an enhanced O_2 adsorption and consequently an enhanced $O_2^{\bullet-}$ active species formation, which ultimately leads to a greater photocatalytic activity. Figure 1.8 shows the proposed mechanism for the selective photo-oxidation of benzyl alcohol over Zn_2Ti-LDH.[102]

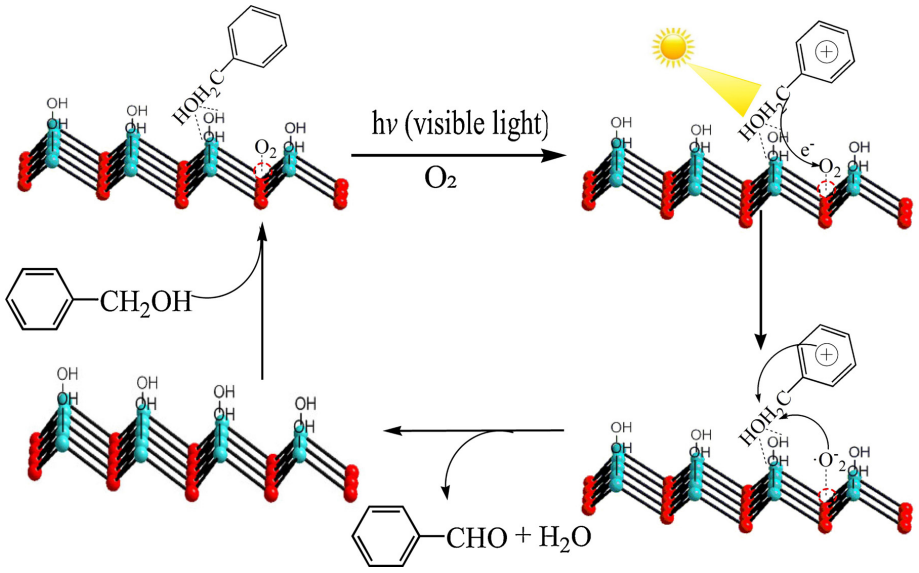


Figure 1.8 Possible mechanism for the selective photocatalytic oxidation of benzyl alcohol to benzaldehyde over ZnTi-LDH under visible light. Light blue spheres: Zn/Ti atoms, red spheres: oxygen atoms, red dotted circle: oxygen vacancy.[102] (Reproduced from reference 102.)

1.5.5 The role of titanium-LDHs in photocatalysis

While different LDH compositions have been investigated for photocatalytic applications,[87,89,90,96,108,109] a significant amount of research has been done on titanium-containing LDHs (Ti-LDHs).[13,14,20,40,42,110-112] A study of TiO_2-SiO_2 binary oxides has revealed that isolated Ti species form the sites of the highest activity in the photo-epoxidation of propene.[113] By extrapolation, this should result in a high photocatalytic activity of Ti-LDHs, as the LDH metal hydroxide layer composition necessitates a high dispersion of the cation with the higher charge.[2]

The role that the degree of dispersion of TiO_6 octahedra plays in photocatalytic activity has been investigated by Zhao *et al*.[112] A family of photocatalysts for water splitting with focus on hydrogen evolution was prepared by distributing TiO_6 units in an M(II)Ti-LDH matrix, where M = Ni, Zn or Mg. High-angle annular dark-field scanning transmission electron microscopy (HAADF-STEM) mapping and X-ray photoelectron spectroscopy (XPS) measurements showed that the TiO_6 octahedra are highly dispersed within the

LDH layers. In comparison, the TiO_6 units are highly aggregated in the inorganic layered material $K_2Ti_4O_9$, which is also photocatalytically active. The high dispersion of TiO_6 units in the LDHs results in a reduced electron-hole recombination rate compared to bulk TiO_2 and $K_2Ti_4O_9$. This is aided also by the large number of Ti^{3+}-O defects that serve as trapping sites and therefore further improve electron-hole separation.[8] The high dispersion of TiO_6 octahedra and the formation of the M(II)-O-Ti framework also decreases the M(II)Ti-LDH band gap, extending the range of wavelengths that can be absorbed.[112] As a result of all these factors, Ti-containing LDHs can show extremely high photocatalytic activity. For instance, the photocatalytic hydrogen production of ZnTi-LDHs is 18-times higher than that of the control $K_2Ti_4O_9$ sample, where the TiO_6 centres are aggregated.[112]

1.6 Thesis overview

This work aims to show that titanium-containing layered double hydroxides, Ti-LDHs, can be used as efficient semiconductor photocatalysts in the photo-oxidation of simple organic molecules. Firstly, a series of NiTi- and MgAlTi-LDHs was prepared using different synthetic methods and with a range of different metal compositions. Secondly, the activity of the prepared Ti-LDHs in the photo-oxidation of organic reagents was investigated and compared to anatase TiO_2 as the baseline photocatalyst. The organic reactants include simple aromatic and aliphatic molecules, specifically diphenylmethanol (benzhydrol), benzyl alcohol, cyclooctanol and benzylamine. Therefore, the reactants considered allow the comparison between aromatic and aliphatic systems, primary and secondary alcohols, and alcohol and amine functional groups. Finally, the TiO_2 and Ti-LDH photocatalysts were combined into a single photocatalytic hybrid material, core-shell TiO_2@Ti-LDH, so as to investigate possible synergistic and heterojunction effects.

Chapter 2 outlines the five different synthetic methods for Ti-LDH preparation and their viability in the synthesis of pure NiTi- and MgAlTi-LDHs with different Ni:Ti and Al:Ti ratios, respectively. The crystallinity, morphology, structure and composition of the prepared Ti-LDHs are analysed. Chapter 3 looks at the application of the synthesised Ti-LDHs in the photo-oxidation of diphenylmethanol to benzophenone, and compares the performance of the Ti-LDHs to that of TiO_2. Chapter 4 examines the effect of changing the photo-oxidation reactant from diphenylmethanol (secondary aromatic alcohol) to benzyl alcohol (primary aromatic alcohol), cyclooctanol (secondary aliphatic alcohol) and benzylamine (primary aromatic amine). Chapter 5 details the synthesis and characterisation of TiO_2@Ti-LDH core-shell hybrid materials, and looks at their application in the photo-oxidation of diphenylmethanol.

1.7 References

1 A. I. Khan and D. O'Hare, *J. Mater. Chem.*, 2002, **12**, 3191–3198.
2 F. Cavani, F. Trifirò and A. Vaccari, *Catal. Today*, 1991, **11**, 173–301.
3 W. Reichle, *Solid State Ionics*, 1986, **22**, 135–141.
4 L. Pesic, S. Salipurovic, V. Markovic, D. Vucelic, W. Kagunya and W. Jones, *J. Mater. Chem.*, 1992, **2**, 1069–1073.
5 G. Marcelin, N. J. Stockhausen, J. F. M. Post and A. Schutz, *J. Phys. Chem.*, 1989, **93**, 4646–4650.
6 S. Miyata, *Clays Clay Miner.*, 1980, **28**, 50–56.
7 P. P. Kumar, A. G. Kalinichev and R. J. Kirkpatrick, *J. Phys. Chem. C*, 2007, **111**, 13517–13523.
8 G. Fan, F. Li, D. G. Evans and X. Duan, *Chem. Soc. Rev.*, 2014, **43**, 7040–7066.
9 G. W. Brindley and S. Kikkawa, *Am. Mineral.*, 1979, **64**, 836–843.
10 F. Peng, T. Luo and Y. Yuan, *New J. Chem.*, 2014, **38**, 4427–4433.
11 A. Sotiles, N. Gomez, S. da Silva and F. Wypych, *J. Braz. Chem. Soc.*, 2019.
12 G. R. Williams and D. O'Hare, *J. Mater. Chem.*, 2006, **16**, 3065–3074.
13 C.-M. Puscasu, E. M. Seftel, M. Mertens, P. Cool and G. Carja, *J. Inorg. Organomet. Polym.*, 2014, **25**, 259–266.
14 Y. Lee, J. H. Choi, H. J. Jeon, K. M. Choi, J. W. Lee and J. K. Kang, *Energy Environ. Sci.*, 2011, **4**, 914–920.
15 J. Poonoosamy, F. Brandt, M. Stekiel, P. Kegler, M. Klinkenberg, B. Winkler, V. Vinograd, D. Bosbach and G. Deissmann, *Appl. Clay Sci.*, 2018, **151**, 54–65.
16 D. Tichit, N. Das, B. Coq and R. Durand, *Chem. Mater.*, 2002, **14**, 1530–1538.
17 X. Zheng and P. A. Cusack, *Fire Mater.*, 2011, **37**, 35–45.
18 S. Velu, K. Suzuki, T. Osaki, F. Ohashi and S. Tomura, *Mater. Res. Bull.*, 1999, **34**, 1707–1717.
19 I. C. Chisem and W. Jones, *J. Mater. Chem.*, 1994, **4**, 1737–1744.
20 K. Hosni, O. Abdelkarim, N. Frini-Srasra and E. Srasra, *Korean J. Chem. Eng.*, 2014, **32**, 104–112.
21 M. Shao, J. Han, M. Wei, D. G. Evans and X. Duan, *Chem. Eng. J.*, 2011, **168**, 519–524.
22 X. Shu, W. Zhang, J. He, F. Gao and Y. Zhu, *Solid State Sci.*, 2006, **8**, 634–639.
23 W. H. Zhang, X. D. Guo, J. He and Z. Y. Qian, *Journal of the European Ceramic Society*, 2008, **28**, 1623–1629.
24 X.-J. Yang, B. Chen, X.-B. Li, L.-Q. Zheng, L.-Z. Wu and C.-H. Tung, *Chem. Commun.*, 2014, **50**, 6664–6667.
25 S. Miyata, *Clays Clay Miner.*, 1983, **31**, 305–311.
26 Q. He, S. Yin and T. Sato, *J. Phys. Chem. Solids*, 2004, **65**, 395–402.
27 A. A. Tsukanov and S. G. Psakhie, *Sci. Rep.*, 2016, **6**, 19986.
28 M. Meyn, K. Beneke and G. Lagaly, *Inorg. Chem.*, 1990, **29**, 5201–5207.
29 Z. P. Xu and P. S. Braterman, *J. Phys. Chem. C*, 2007, **111**, 4021–4026.
30 B. Wang, H. Zhang, D. G. Evans and X. Duan, *Mater. Chem. Phys.*, 2005, **92**, 190–196.
31 S. P. Newman and W. Jones, *New J. Chem.*, 1998, **22**, 105–115.
32 C. Li, M. Wei, D. G. Evans and X. Duan, *Small*, 2014, **10**, 4469–4486.
33 K.-H. Goh, T.-T. Lim and Z. Dong, *Water Res.*, 2008, **42**, 1343–1368.
34 S. Omwoma, W. Chen, R. Tsunashima and Y.-F. Song, *Coord. Chem. Rev.*, 2014, **258-259**, 58–71.

35 D. G. Evans and X. Duan, *Chem. Commun.*, 2006, 485–496.
36 L. Shi, D. Li, J. Wang, S. Li, D. G. Evans and X. Duan, *Clays Clay Miner.*, 2005, **53**, 294–300.
37 Z. Wang, E. Han and W. Ke, *Prog. Org. Coat.*, 2005, **53**, 29–37.
38 Y. Wang and D. Zhang, *Mater. Res. Bull.*, 2011, **46**, 1963–1968.
39 A. I. Khan, L. Lei, A. J. Norquist and D. O'Hare, *Chem. Commun.*, 2001, 2342–2343.
40 Y. Zhao, B. Li, Q. Wang, W. Gao, C. J. Wang, M. Wei, D. G. Evans, X. Duan and D. O'Hare, *Chem. Sci.*, 2014, **5**, 951–958.
41 H. Zhao, J. Xu, L. Liu, G. Rao, C. Zhao and Y. Li, *Journal of CO2 Utilization*, 2016, **15**, 15–23.
42 S.-J. Xia, F.-X. Liu, Z.-M. Ni, W. Shi, J.-L. Xue and P.-P. Qian, *Appl. Catal., B*, 2014, **144**, 570–579.
43 W. Feitknecht and M. Gerber, *Helv. Chim. Acta*, 1942, **25**, 131–137.
44 W. Feitknecht, *Helv. Chim. Acta*, 1942, **25**, 555–569.
45 A. Faour, V. Prévot and C. Taviot-Guého, *J. Phys. Chem. Solids*, 2010, **71**, 487–490.
46 H. W. Olfs, L. O. Torres-Dorante, R. Eckelt and H. Kosslick, *Appl. Clay Sci.*, 2009, **43**, 459–464.
47 U. Costantino, F. Marmottini, M. Nocchetti and R. Vivani, *Eur. J. Inorg. Chem.*, 1998, **1998**, 1439–1446.
48 W. H. R. Shaw and J. J. Bordeaux, *J. Am. Chem. Soc.*, 1955, **77**, 4729–4733.
49 N. Iyi, T. Matsumoto, Y. Kaneko and K. Kitamura, *Chem. Lett.*, 2004, **33**, 1122–1123.
50 N. Iyi, K. Tamura and H. Yamada, *J. Colloid Interface Sci.*, 2009, **340**, 67–73.
51 F. R. Costa, A. Leuteritz, U. Wagenknecht, D. Jehnichen, L. Häußler and G. Heinrich, *Appl. Clay Sci.*, 2008, **38**, 153–164.
52 C. Yilmaz, U. Unal and H. Yagci Acar, *J. Solid State Chem.*, 2012, **187**, 295–299.
53 M. Kayano and M. Ogawa, *Clays Clay Miner.*, 2006, **54**, 382–389.
54 Y. Yang, G. Fan and F. Li, *Mater. Lett.*, 2014, **116**, 203–205.
55 H. Sun, Z. Chu, D. Hong, G. Zhang, Y. Xie, L. Li and K. Shi, *J. Alloys Compd.*, 2016, **658**, 561–568.
56 J. Zhang, X. Xie, C. Li, H. Wang and L. Wang, *RSC Adv.*, 2015, **5**, 29757–29765.
57 S. Carlino, *Solid State Ionics*, 1997, **98**, 73–84.
58 F. Prinetto, G. Ghiotti, P. Graffin and D. Tichit, *Microporous Mesoporous Mater.*, 2000, **39**, 229–247.
59 X. Guo, F. Zhang, D. G. Evans and X. Duan, *Chem. Commun.*, 2010, **46**, 5197–5210.
60 J. Han, Y. Dou, M. Wei, D. G. Evans and X. Duan, *Angew. Chem., Int. Ed.*, 2010, **49**, 2171–2174.
61 A. Fujishima, T. N. Rao and D. A. Tryk, *J. Photochem. Photobiol., C*, 2000, **1**, 1–21.
62 M. A. Fox and M. T. Dulay, *Chem. Rev.*, 1993, **93**, 341–357.
63 J. Schneider, M. Matsuoka, M. Takeuchi, J. Zhang, Y. Horiuchi, M. Anpo and D. W. Bahnemann, *Chem. Rev.*, 2014, **114**, 9919–9986.
64 K. Nakata and A. Fujishima, *J. Photochem. Photobiol., C*, 2012, **13**, 169–189.
65 L. Wang, J. Zhao, H. Liu and J. Huang, *Journal of the Taiwan Institute of Chemical Engineers*, 2018, **93**, 590–602.

66 T. Luttrell, S. Halpegamage, J. Tao, A. Kramer, E. Sutter and M. Batzill, *Sci. Rep.*, 2014, **4**, 515–8.
67 J. Zhang, P. Zhou, J. Liu and J. Yu, *Phys. Chem. Chem. Phys.*, 2014, **16**, 20382–20386.
68 F. A.-Z. G. Gassim, A. N. Alkhateeb and F. H. Hussein, *Desalination*, 2007, **209**, 342–349.
69 O. S. Mohamed, A. E.-A. M. Gaber and A. A. Abdel-Wahab, *J. Photochem. Photobiol., A*, 2002, **148**, 205–210.
70 S. Vijaikumar, N. Somasundaram and C. Srinivasan, *Appl. Catal., A*, 2002, **223**, 129–135.
71 K. Cerdan, W. Ouyang, J. C. Colmenares, M. J. Muñoz-Batista, R. Luque and A. M. Balu, *Chem. Eng. Sci.*, 2019, **194**, 78–84.
72 S. Higashimoto, N. Kitao, N. Yoshida, T. Sakura, M. Azuma, H. Ohue and Y. Sakata, *J. Catal.*, 2009, **266**, 279–285.
73 O. S. Mohamed, S. A. Ahmed, M. F. Mostafa and A.-M. A. Abdel-Wahab, *International Journal of Photoenergy*, 2008, **2008**, 1–11.
74 J. Dai, J. Yang, X. Wang, L. Zhang and Y. Li, *Appl. Surf. Sci.*, 2015, **349**, 343–352.
75 S. Higashimoto, Y. Hatada, R. Ishikawa, M. Azuma, Y. Sakata and H. Kobayashi, *COC*, 2013, **17**, 2374–2381.
76 X. Lang, H. Ji, C. Chen, W. Ma and J. Zhao, *Angew. Chem., Int. Ed.*, 2011, **50**, 3934–3937.
77 C.-J. Li, G.-R. Xu, B. Zhang and J. R. Gong, *Appl. Catal., B*, 2012, **115-116**, 201–208.
78 V. Jeena and R. S. Robinson, *Chem. Commun.*, 2012, **48**, 299–301.
79 H. She, L. Li, Y. Sun, L. Wang, J. Huang, G. Zhu and Q. Wang, *Appl. Surf. Sci.*, 2018, **457**, 1167–1173.
80 Y. Wang, J. Zhou, X. Hao, Y. Wang and Z. Zou, *Appl. Surf. Sci.*, 2018, **456**, 861–870.
81 S. Furukawa, Y. Ohno, T. Shishido, K. Teramura and T. Tanaka, *ACS Catal.*, 2011, **1**, 1150–1153.
82 J. Liu and G. Zhang, *Phys. Chem. Chem. Phys.*, 2014, **16**, 8178–8192.
83 L. Mohapatra and K. Parida, *J. Mater. Chem. A*, 2016, **4**, 10744–10766.
84 Z. P. Xu, J. Zhang, M. O. Adebajo, H. Zhang and C. Zhou, *Appl. Clay Sci.*, 2011, **53**, 139–150.
85 Y. Zhao, X. Jia, G. I. N. Waterhouse, L.-Z. Wu, C.-H. Tung, D. O'Hare and T. Zhang, *Adv. Energy Mater.*, 2015, **6**, 1501974.
86 J. Li, Y. Xu, Z. Ding, A. H. Mahadi, Y. Zhao and Y.-F. Song, *Chem. Eng. J.*, 2020, **388**, 124248.
87 S. Kim, J. Fahel, P. Durand, E. André and C. Carteret, *Eur. J. Inorg. Chem.*, 2017, **2017**, 669–678.
88 L. Sobhana, M. Sarakha, V. Prévot and P. Fardim, *Appl. Clay Sci.*, 2016.
89 M. Dinari, M. M. Momeni and Y. Ghayeb, *J. Mater. Sci.: Mater. Electron.*, 2016, **27**, 9861–9869.
90 M. Dinari, M. M. Momeni, Z. Bozorgmehr and S. Karimi, *J. Iran. Chem. Soc.*, 2016, **14**, 695–701.
91 Z. Timár, G. Varga, S. Muráth, Z. Kónya, Á. Kukovecz, V. Havasi, A. Oszkó, I. Pálinkó and P. Sipos, *Catal. Today*, 2017, **284**, 195–201.
92 R. Kun, M. Balázs and I. Dékány, *Colloids Surf., A*, 2005, **265**, 155–162.
93 J. Sun, Y. Zhang, J. Cheng, H. Fan, J. Zhu, X. Wang and S. Ai, *Journal of*

Molecular Catalysis A: Chemical, 2014, **382**, 146–153.
94 J. Zhu, Z. Zhu, H. Zhang, H. Lu, Y. Qiu, L. Zhu and S. Küppers, *J. Colloid Interface Sci.*, 2016, **481**, 144–157.
95 K. Parida and L. Mohapatra, *Dalton Trans.*, 2012, **41**, 1173–1178.
96 N. Baliarsingh, L. Mohapatra and K. Parida, *J. Mater. Chem. A*, 2013, **1**, 4236–4243.
97 C. G. Silva, Y. Bouizi, V. Fornés and H. Garcia, *J. Am. Chem. Soc.*, 2009, **131**, 13833–13839.
98 N. Ahmed, Y. Shibata, T. Taniguchi and Y. Izumi, *J. Catal.*, 2011, **279**, 123–135.
99 N. Ahmed, M. Morikawa and Y. Izumi, *Catal. Today*, 2012, **185**, 263–269.
100 M. Morikawa, Y. Ogura, N. Ahmed, S. Kawamura, G. Mikami, S. Okamoto and Y. Izumi, *Catal. Sci. Technol.*, 2014, **4**, 1644–1651.
101 K. Teramura, S. Iguchi, Y. Mizuno, T. Shishido and T. Tanaka, *Angew. Chem., Int. Ed.*, 2012, **51**, 8008–8011.
102 J. Zou, Z. Wang, W. Guo, B. Guo, Y. Yu and L. Wu, *Appl. Catal., B*, 2020, **260**, 118185.
103 D. Guo, Y. Wang, P. Zhao, M. Bai, H. Xin, Z. Guo and J. Li, *Catalysts*, 2016, **6**, 64.
104 T. Pigot, T. Arbitre, H. Martinez and S. Lacombe, *Tetrahedron Lett.*, 2004, **45**, 4047–4050.
105 K. Teramura, H. Tsuneoka, K. Ogura, T. Sugimoto, T. Shishido and T. Tanaka, *ChemCatChem*, 2014, **6**, 2276–2281.
106 Z. Wang, Y. Song, J. Zou, L. Li, Y. Yu and L. Wu, *Catal. Sci. Technol.*, 2018, **8**, 268–275.
107 J. Yu, J. Li, H. Wei, J. Zheng, H. Su and X. Wang, *Journal of Molecular Catalysis A: Chemical*, 2014, **395**, 128–136.
108 Á. Patzkó, R. Kun, V. Hornok, I. Dékány, T. Engelhardt and N. Schall, *Colloids Surf., A*, 2005, **265**, 64–72.
109 Y. Fu, F. Ning, S. Xu, H. An, M. Shao and M. Wei, *J. Mater. Chem. A*, 2016, **4**, 3907–3913.
110 R. Li, W. Gao, J. He and J. Hu, *Optoelectron. Adv. Mat.*, 2013, **7**, 279–284.
111 R. K. Sahu, B. S. Mohanta and N. N. Das, *J. Phys. Chem. Solids*, 2013, **74**, 1263–1270.
112 Y. Zhao, P. Chen, B. Zhang, D. S. Su, S. Zhang, L. Tian, J. Lu, Z. Li, X. Cao, B. Wang, M. Wei, D. G. Evans and X. Duan, *Chem. Eur. J.*, 2012, **18**, 11949–11958.
113 C. Murata, H. Yoshida, J. Kumagai and T. Hattori, *J. Phys. Chem. B*, 2003, **107**, 4364–4373.

Chapter 2 Synthesis and characterisation of NiTi- and MgAlTi-layered double hydroxides

2.1 Introduction

The properties of LDHs, such as their morphology, particle size distribution, crystallinity and degree of aggregation, are highly dependent on the choice of the synthetic method and the specific reaction conditions, such as pH, temperature and ageing time. Strict control of these properties and the ability to fine-tune them is required for the intended application in photocatalytic oxidation reactions. The choice of the synthetic method also affects the distribution of Ti centres in the LDH particles and the amount of Ti^{3+} defect sites on the particle surface. The latter have been linked to a higher photocatalytic activity in the visible-light-driven oxygen evolution from water.[1]

In the conventional co-precipitation method, a dilute solution of the metal salts is typically added dropwise to a Na_2CO_3 solution and the pH is kept constant with the addition of a NaOH solution.[2-4] This method usually generates poorly crystalline and highly aggregated LDHs with poor control over the particle size and its distribution, and very low specific surface areas.[5-8]

An alternative synthetic route that allows better control over the LDH particle size and morphology is the homogeneous precipitation method (under either refluxing or hydrothermal conditions), which yields well-defined LDH particles with a narrow particle size distribution.[9] In the this method, an ammonia releasing reagent (such as urea or hexamethylenetetramine, HMT) is used to increase the pH of the reaction mixture, which results in the precipitation of the LDH product.[6,10,11]

Although the synthesis of LDHs usually proceeds in an aqueous medium, non-aqueous synthetic methods have also been explored; these include the reverse microemulsion method,[1] the sol-gel method,[12] and the synthesis of single-layer LDH nanosheets in formamide.[13] In general, the non-aqueous methods allow a high degree of control over the LDH composition and structure, as well as giving rise to LDH properties that are often inaccessible by conventional aqueous synthetic methods.

In this Chapter, the effects of the synthetic conditions on LDH properties will be discussed. A series of NiTi- and MgAlTi-LDHs were prepared using five different synthetic methods: aqueous co-precipitation at constant and variable pH, organic co-precipitation in ethanol, aqueous homogeneous precipitation under reflux (urea reflux) and hydrothermal conditions (urea hydrothermal). The effect of LDH metal composition on LDH properties was also investigated by varying the Ni:Ti and Al:Ti ratios in NiTi- and MgAlTi-LDHs, respectively.

2.2 Synthetic methods and characterisation techniques

NiTi- and MgAlTi-LDHs were prepared by five different synthetic methods: aqueous co-precipitation at constant and variable pH, organic co-precipitation in ethanol, and aqueous homogeneous precipitation under reflux (urea reflux) and hydrothermal conditions (urea hydrothermal). The optimised synthetic conditions are outlined below.

In all cases, titanium(IV) isopropoxide, $Ti(O^iPr)_4$, was chosen as the Ti^{4+} source due to its lower reactivity compared to $TiCl_4$ and therefore a reduced tendency to precipitate out of solution in the form of insoluble oxides and hydroxides. All other metal cations were introduced into the reaction mixture in the form of hydrated nitrate salts.

In all synthetic methods, Ti^{4+} precipitation was prevented by dissolving $Ti(O^iPr)_4$ in concentrated hydrochloric acid (~37% HCl) under an inert nitrogen atmosphere.[1] Subsequent addition of aqueous solutions or hydrated salts dissolved in ethanol proceeded cleanly without any solid precipitating.

The constant pH aqueous co-precipitation method used follows an adapted literature procedure,[14,15] where a solution of metal salts and a solution of 4 M NaOH are added dropwise to a solution of Na_2CO_3, keeping the pH constant at a value of 10. In the variable pH aqueous co-precipitation, a solution of NaOH and Na_2CO_3 was added dropwise to the metal salt solution up to a final pH of 10. The NiTi- and MgAlTi-LDH products prepared by both aqueous co-precipitation methods were aged for 18 hours at 60 ºC and room temperature, respectively.

The organic co-precipitation was carried out in ethanol, using NaOEt as the base alternative to NaOH. The method was designed as a novel, non-aqueous equivalent to the variable pH aqueous co-precipitation, with the amount of NaOEt determined by

calculation based on NaOH requirements in the aqueous method. The addition of a small amount of water (5 mL per 100 mL ethanol) was found to increase the yield of the reaction by about 70%. The products of the organic co-precipitation method were aged for 24 hours at 80 ºC or room temperature for NiTi- and MgAlTi-LDHs, respectively.

The homogeneous precipitation methods used urea as the ammonia releasing reagent (ARR), with the [urea]:[metal salts] ratio of 3:1 for NiTi-LDH products prepared by both methods.[6,9] For the MgAlTi-LDH products, the [urea]:[metal salts] ratios were 6:1 and 4:1 for the urea reflux and urea hydrothermal methods, respectively. The products of both homogeneous precipitation methods were aged at 100 ºC for 18 hours under reflux or hydrothermal conditions for urea reflux and urea hydrothermal methods, respectively.

For NiTi-LDHs, the Ni:Ti ratio was varied between 2:1, 3:1, 4:1, 5:1 and 6:1, while keeping the total metal salt concentration in the reaction mixture constant. For MgAlTi-LDHs, the Mg:(Al+Ti) ratio was kept constant at 3:1, and the Al:Ti ratio was varied between 3:1, 1:1 and 1:3, with the total metal concentration in the reaction mixture being kept constant.

All five synthetic methods (where viable) and all different metal ratios produced free-flowing green and white powders for NiTi- and MgAlTi-LDHs, respectively. More detailed synthetic method descriptions can be found in Chapter 7.

The purity, crystallinity and crystallographic parameters of the LDH products were investigated by powder X-ray diffraction (PXRD). The nature of the intercalated anions was explored using Fourier transform infra-red spectroscopy (FTIR). The morphology, size and aggregation of the LDH particles were investigated with transmission (TEM) and scanning electron microscopy (SEM). The dispersion of Ti centres within the LDH

particles was analysed using energy dispersive X-ray spectroscopy (TEM-EDX and SEM-EDX).

The specific surface areas of the LDH powders were determined with gas adsorption measurements in combination with the Brunauer-Emmett-Teller (BET) method. The composition of the LDH products, specifically the metal content and metal ratios, was determined using inductively coupled plasma mass spectrometry (ICP-MS) in combination with thermogravimetric analysis (TGA), which was used to estimate the amounts of intercalated anions, as well as intercalated and adsorbed water molecules.

The band gaps of the LDH semiconductor photocatalysts were estimated using diffuse reflectance UV-visible spectroscopy (DRUV-vis) together with the Tauc plot graphical method.[16-18] More detailed analysis of selected LDHs included high-angle annular dark-field imaging (HAADF) with elemental mapping and ^{1}H, ^{27}Al and $^{47/49}Ti$ solid state nuclear magnetic resonance (ssNMR) measurements.

More detailed information regarding all analytical methods is listed in Chapter 7.

Furthermore, all the properties of the synthesised Ti-LDHs, including the PXRD peak positions, full width at half maximum (FWHM) data for the (003) and (110) PXRD reflections, d-spacings, lattice parameters, crystallite domain lengths, product yields, BET specific surface areas and FTIR band positions have been summarised in Tables 7.4 – 7.7 in Chapter 7.

2.3 Variation and optimisation of synthetic methods

To investigate the effect of the synthetic method on NiTi- and MgAlTi-LDH properties, the Ni:Ti and Al:Ti ratios were fixed at 4:1 and 3:1, respectively.

The constant pH aqueous co-precipitation and urea hydrothermal methods were found to be unsuitable for NiTi-LDH synthesis; the former due to poorly defined, small and irregular particle morphology (Figure A.1 in Appendix A) and the latter due to proposed $[Ni(NH_3)_6]^{2+}$ complex formation in the closed autoclave system, which leaches Ni^{2+} from the LDH structure and results in significant impurity formation (Figure A.2b in Appendix A). All five methods were found to be suitable for MgAlTi-LDH synthesis, with a wide range of different product crystallinities and particle morphologies observed.

Previous reports of NiTi-LDH synthesis in literature include the use of the urea reflux,[19-22] aqueous co-precipitation at constant pH,[23] aqueous co-precipitation at variable pH,[24,25] and reverse microemulsion methods.[1] MgAlTi-LDHs have been previously synthesised using the aqueous co-precipitation at constant pH,[26,27] aqueous co-precipitation at variable pH,[28] and sol-gel methods.[29] To the best of the author's knowledge, MgAlTi-LDHs have never been prepared by the urea hydrothermal method and neither Ti-LDH has been prepared by a method similar to the newly developed organic co-precipitation method.

The NiTi- and MgAlTi-LDHs prepared and reported in literature to date have also been summarised in Tables 2.1 and 2.2.

Table 2.1 An overview of NiTi-LDHs reported in literature to date, with different Ni:Ti ratios and prepared with different synthetic methods.

Ni:Ti ratio	Synthetic method	References
1.5:1[a]	Aqueous urea reflux	[20]
2:1	Aqueous urea reflux	[22,30]
2.5:1[b]	Aqueous urea reflux	[20]
2.7:1	Aqueous urea reflux	[21]
3:1	Aqueous urea reflux	[22]
4:1	Aqueous urea reflux	[1,22]
5:1	Aqueous urea reflux	[20,22]
6:1	Aqueous urea reflux	[19]
2:1	Variable pH aqueous co-precipitation	[25]
3:1	Variable pH aqueous co-precipitation	[25]
4:1	Variable pH aqueous co-precipitation	[25]
5:1	Variable pH aqueous co-precipitation	[25]
4:1	Reverse micelle with urea reflux	[1]

[a] Recalculated from 3:2 for clarity.
[b] Recalculated from 5:2 for clarity.

Table 2.2 An overview of MgAlTi-LDHs reported in literature to date, with different Mg:(Al+Ti) and Al:Ti ratios, and prepared with different synthetic methods.

Mg:(Al+Ti) ratio	Al:Ti ratio	Synthetic method	References
3:1	1:3	Constant pH aqueous co-precipitation	[26]
3:1	1:1	Constant pH aqueous co-precipitation	[26]
3:1	2:1	Constant pH aqueous co-precipitation	[26]
3:1	3:1	Constant pH aqueous co-precipitation	[26]
3:1	9:1	Constant pH aqueous co-precipitation	[26]
3:1.05	20:1	Sol-gel	[29]
3:1.1	10:1	Sol-gel	[29]
3:1.3	3.3:1	Sol-gel	[29]
6:5	2:3	Variable pH aqueous co-precipitation	[28]
3:1[a]	9:1[a]	Constant pH aqueous co-precipitation	[27]
3:1[a]	7:1[a]	Constant pH aqueous co-precipitation	[27]
3:1[a]	1:1[a]	Constant pH aqueous co-precipitation	[27]
2:1[a]	3:1[a]	Constant pH aqueous co-precipitation	[27]

[a] Rounded up to the nearest whole number for clarity.

The PXRD patterns in Figure 2.1 show that both Ni_4Ti- and $Mg_{12}Al_3Ti$-LDHs can be prepared in their pure form without any Ti-containing impurities, such as TiO_2, present. However, $Mg_{12}Al_3Ti$-LDH synthesised by the urea hydrothermal method contains crystalline magnesite, $MgCO_3$, impurities as a consequence of CO_2 formation by the decomposition of urea in the closed autoclave system.

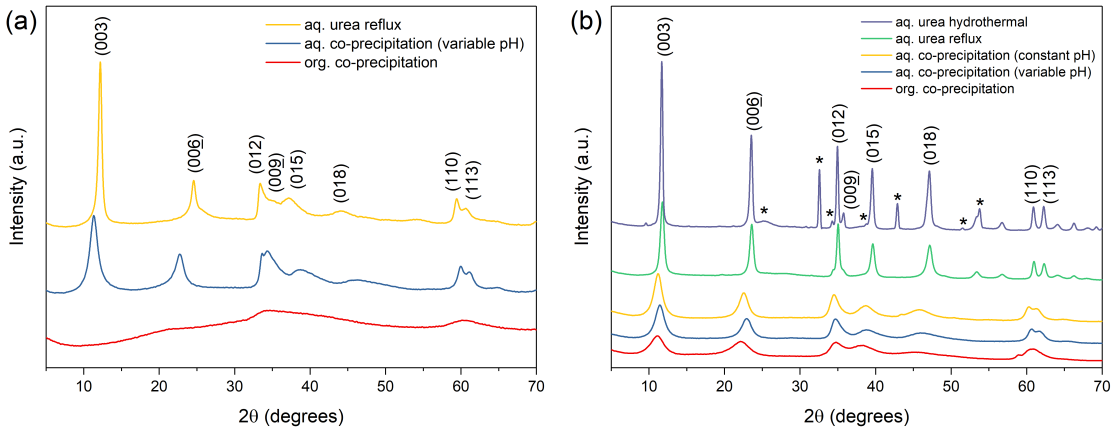


Figure 2.1 PXRD patterns of (a) Ni_4Ti-LDHs and (b) $Mg_{12}Al_3Ti$-LDHs prepared by different synthetic methods. * denotes magnesite, $MgCO_3$, impurity PXRD reflections.

Although the $MgCO_3$ impurity is unlikely to interfere with the LDH photocatalytic performance, a series of reactions with varying [urea]:[metal salts] ratios were attempted in order to try and eliminate it. However, the $MgCO_3$ impurity was present even in products prepared with a [urea]:[metal salts] ratio of 2:1, as shown in Figure 2.2. Rather than reducing the amount of impurities in the $Mg_{12}Al_3Ti$-LDH product, decreasing the [urea]:[metal salts] ratio from 4:1 to 2:1 only resulted in a reduced product yield. The urea hydrothermal $Mg_{12}Al_3Ti$-LDH products also show the presence of an unknown crystalline impurity with a PXRD reflection peak at ~10º.

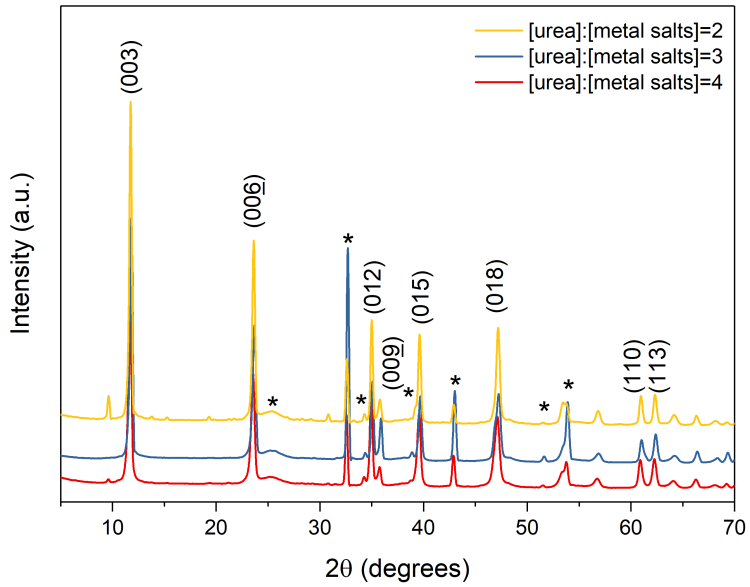


Figure 2.2 PXRD patterns of $Mg_{12}Al_3Ti$-LDHs prepared by the urea hydrothermal synthetic method with different [urea]:[metal salts] ratios. * denotes magnesite, $MgCO_3$, impurity PXRD reflections.

With the exception of the Ni_4Ti-LDH prepared by the organic co-precipitation method, all products show PXRD patterns characteristic of LDHs, with three major (00*l*) basal reflections in the 0 – 35° 2θ region, (003), (006) and (009). The peaks at ~62° can be assigned to (110) and (113) non-basal reflections.[1,26]

The d_{003}-spacing of all the $Mg_{12}Al_3Ti$-LDHs and the Ni_4Ti-LDH synthesised by the aqueous co-precipitation method is ~7.6 – 7.9 Å, which is typical of carbonate intercalated LDHs.[22,26,27] This is confirmed by the FTIR spectra in Figure 2.3, which show characteristic carbonate stretching bands around 1,500 cm^{-1}.[19] In addition to the carbonate bands, the FTIR spectra are typical of LDHs, with the O-H stretching band in the 3,200 – 3,700 cm^{-1} region due to the interlayer and adsorbed water molecules, as well as the LDH layer hydroxyl groups,[26] and a water bending band around 1,600 cm^{-1}.[26] The bands in the fingerprint region below 1,000 cm^{-1} can be ascribed to the various vibration modes of M-O, M-O-M and O-M-O bonds in the metal hydroxide layers.[26]

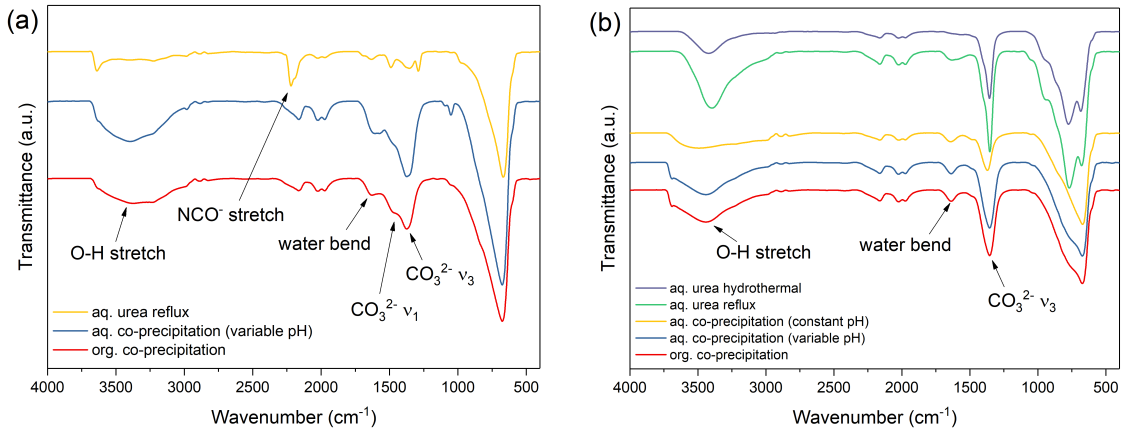


Figure 2.3 FTIR spectra of (a) Ni_4Ti-LDHs and (b) $Mg_{12}Al_3Ti$-LDHs prepared by different synthetic methods. The bands in the 2,000 – 2,250 cm^{-1} range are a consequence of the apparatus setup and not a feature of the LDH samples.

The Ni_4Ti-LDH prepared by the urea reflux method shows a reduced d_{003}-spacing of only ~7.3 Å (Figure 2.1a). This is due to cyanate, NCO^-, rather than carbonate, being the predominant intercalated anion, as confirmed by the presence of FTIR bands around 2,200 and 2,250 cm^{-1} (Figure 2.3a).[19,20,22] Accordingly, the intensity of the carbonate stretching bands around 1,500 cm^{-1} is noticeably reduced. The presence of cyanate is a consequence of the incomplete decomposition of urea, which has been observed before in NiAl- and NiTi-LDHs.[19,20,31] The splitting of the O-H band, typically centred around 3,500 cm^{-1}, into two bands has been previously attributed to the presence of the NCO^- group near the hydroxyl group.[20] As no such cyanate intercalation has been observed for MgAlTi-LDHs or other LDH metal compositions, it is likely that the presence of Ni^{2+} in the LDH metal hydroxide layers plays a crucial role.

In terms of crystallinity, as estimated from the PXRD reflection sharpness and intensity, the homogeneous precipitation methods yield the most crystalline products for both Ti-LDH metal compositions. This is consistent with previous literature reports, where LDHs prepared by homogenous precipitation methods exhibited a higher degree of crystallinity than those prepared by aqueous co-precipitation.[6] In comparison, the organic co-

precipitation results in products with notably less intense PXRD peaks, or in the case of Ni_4Ti-LDH, in the complete absence of distinct (00*l*) basal reflections (Figure 2.1a).

This is attributed to the complete delamination of the LDH particles, such that the organic co-precipitation Ni_4Ti-LDH exists in the form of nanosheets that are so thin that there is insufficient coherence along the platelet stacking axis (*c*-axis) to observe any (00*l*) Bragg reflection intensity.[15] By synthesising the Ni_4Ti-LDHs in a non-aqueous environment, the water molecules are partially replaced by ethanol molecules, which reduces the hydrogen bonding capacity of the LDH layers. This decreases the tendency for layer stacking, allowing dispersion into thin nanosheets or even single layers.

In addition to delamination, the decreased hydrogen bonding capacity also reduces particle aggregation, which carries through to the dry powder and results in a very high specific surface area of 326 m^2g^{-1} (Table 2.3). The delamination and concomitant increase in surface area is reminiscent of the aqueous miscible organic solvent treatment (AMOST) method, where an aqueous miscible solvent (e.g. acetone or ethanol) dispersion step results in high surface areas of above 400 m^2g^{-1}.[32,33]

The organic co-precipitation method achieves nearly the same degree of delamination and increase in surface area for Ni_4Ti-LDH, in what is essentially a one-step process as opposed to separate synthesis and post-treatment steps. However, in comparison to the Ni_4Ti-LDH, the $Mg_{12}Al_3Ti$-LDH prepared by the same method shows a smaller degree of delamination, with better resolved (00*l*) basal PXRD reflections. It also shows a lower surface area of 107 m^2g^{-1}.

Table 2.3 The BET specific surface areas (in m^2g^{-1}) of Ni_4Ti- and $Mg_{12}Al_3Ti$-LDHs prepared by different synthetic methods.

Synthetic method/LDH	**Ni_4Ti-LDH**	**$Mg_{12}Al_3Ti$-LDH**
Organic co-precipitation	326	107
Aqueous co-precipitation at constant pH	/	44
Aqueous co-precipitation at variable pH	65	0.5
Aqueous urea reflux	153	128
Aqueous urea hydrothermal	/	64

As seen in Table 2.3, the two aqueous co-precipitation methods give LDH products with the lowest surface areas, which is consistent with literature findings.[32,33] The aqueous urea reflux method results in comparably higher surface areas. The lower surface area of the urea hydrothermal $Mg_{12}Al_3Ti$-LDH can be attributed to the individual hexagonal platelet morphology (Figure 2.5e), since the absence of stacking and flower-like platelet aggregates reduces the total pore volume.

In terms of the morphology, all Ni_4Ti-LDH particles are irregularly shaped thin sheets with varying degrees of aggregation, irrespective of the synthetic method, as shown in Figure 2.4. The products of the variable pH aqueous co-precipitation and the urea reflux methods have an average particle diameter of about 100 nm. In comparison, the particles synthesised by the organic co-precipitation method are smaller, with diameters in the 10 – 50 nm range.

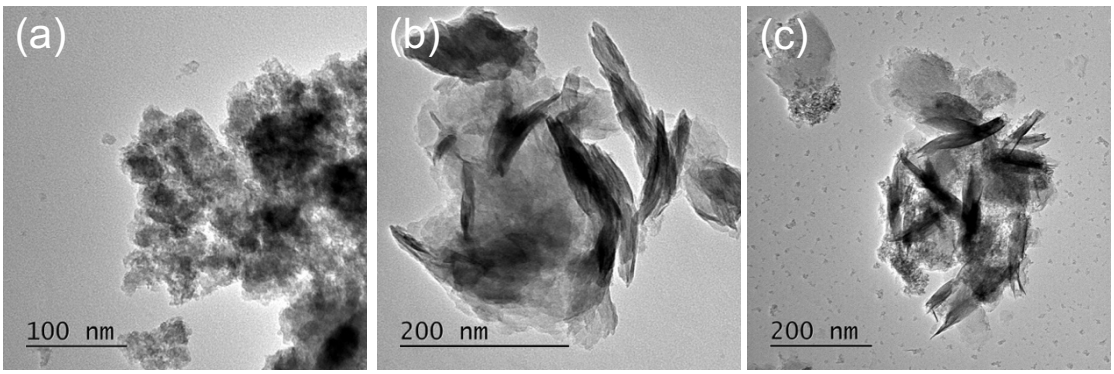


Figure 2.4 TEM images of Ni_4Ti-LDHs prepared by the (a) organic co-precipitation, (b) aqueous co-precipitation at variable pH and (c) urea reflux methods.

In comparison to Ni_4Ti-LDHs, the morphology of $Mg_{12}Al_3Ti$-LDHs varies greatly with the synthetic method, as seen in Figures 2.5 and 2.6.

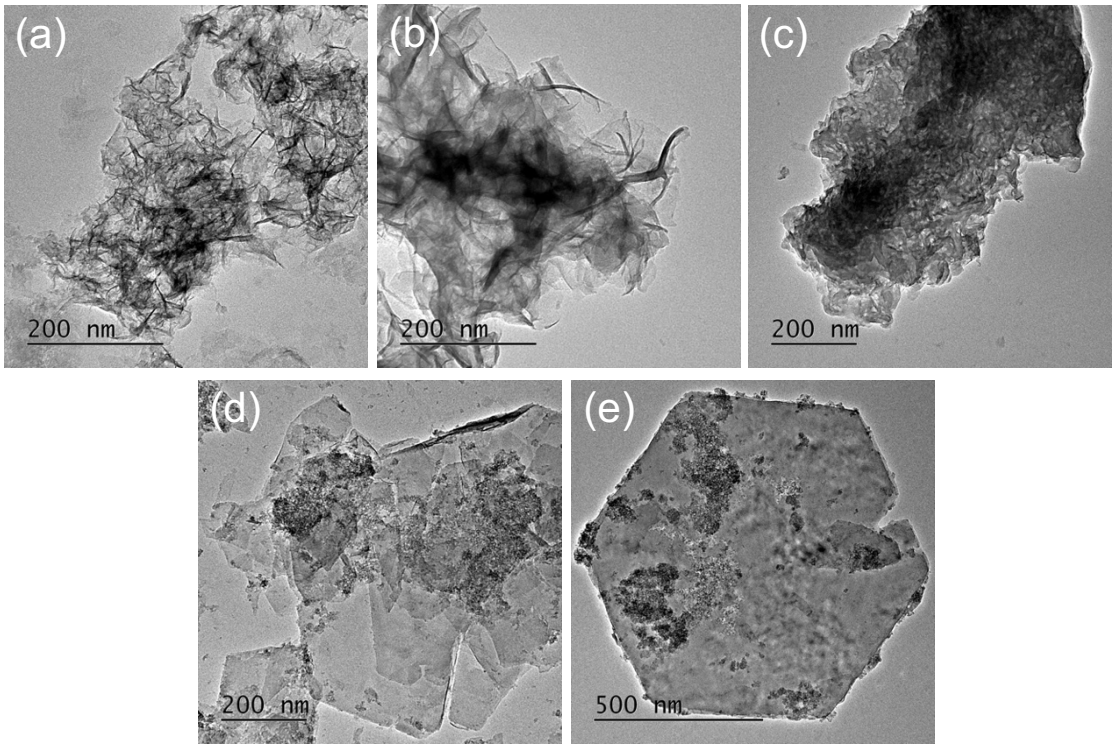


Figure 2.5 TEM images of $Mg_{12}Al_3Ti$-LDHs prepared by the (a) organic co-precipitation, (b) aqueous co-precipitation at constant pH, (c) aqueous co-precipitation at variable pH, (d) urea reflux and (e) urea hydrothermal methods.

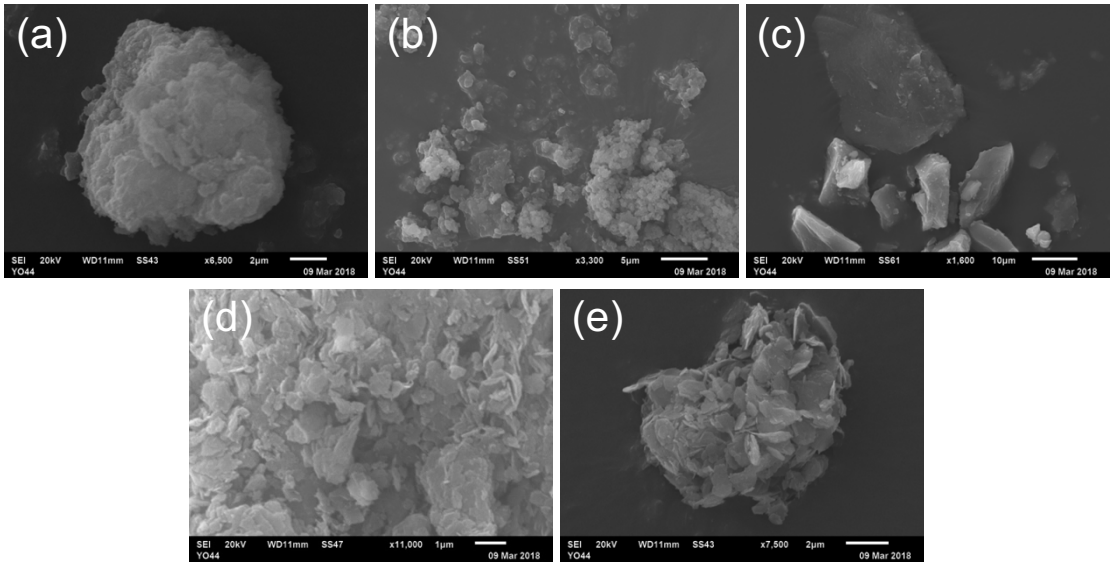


Figure 2.6 SEM images of $Mg_{12}Al_3Ti$-LDHs prepared by the (a) organic co-precipitation, (b) aqueous co-precipitation at constant pH, (c) aqueous co-precipitation at variable pH, (d) urea reflux and (e) urea hydrothermal methods.

The products of the organic co-precipitation and constant pH aqueous co-precipitation methods consist of thin sheet-like particles with curved and irregular contours, similar to Ni_4Ti-LDHs. The product of the variable pH aqueous co-precipitation method comprises smaller particles and shows a higher degree of aggregation.

The greatest difference in morphology is seen with the homogeneous precipitation products, which take the form of large platelets (Figures 2.5d,e and 2.6d,e). Whereas the platelets in the urea reflux product are thin and irregularly shaped, those of the urea hydrothermal product have a much more well-defined hexagonal shape.

This is indicative of a high degree of crystallinity and order within the $Mg_{12}Al_3Ti$-LDH structure, which translates into a regular hexagonal particle shape. This significant change in particle morphology between the urea reflux and urea hydrothermal methods highlights the importance of pressure in increasing the LDH product crystallinity and particle size, which has been noted previously.[34]

The dispersion of Ti centres within the Ni_4Ti- and $Mg_{12}Al_3Ti$-LDH particles was analysed using TEM-EDX (Figure 2.7) and SEM-EDX (Figure 2.8), respectively. In the case of Ni_4Ti-LDHs, there is a clear trend with the organic co-precipitation method giving the best and the aqueous urea reflux method giving the poorest dispersion, where a 'good dispersion' is taken to mean an even distribution of Ti centres within the LDH particles, with no notable areas of localised high or low Ti concentration (accordingly, a 'poor dispersion' refers to an uneven distribution of Ti centres with localised areas of high and low Ti concentration). This can be attributed to two factors: the rate at which the pH increases during the synthesis, and the greater tendency of Ti^{4+} to precipitate out of aqueous solution (as compared to non-aqueous solutions).

The urea reflux method, in which the pH increase is gradual over the period of 18 hours and which is carried out in an aqueous solution, shows areas of isolated high and low Ti atom density. In comparison, the organic co-precipitation method involves the addition of base, NaOEt, over only 1 hour and a significantly smaller amount of water added (5 mL of water per 100 mL ethanol). Consequently, the Ni_4Ti-LDH product synthesised by the organic co-precipitation method shows a fairly even distribution of Ti centres across the particle (Figure 2.7a).

In comparison to Ni_4Ti-LDHs, there is no clear trend between the synthetic method and the distribution of Ti centres for $Mg_{12}Al_3Ti$-LDHs (Figure 2.8). The Ti centres appear evenly dispersed in all samples. This might be the consequence of the low Ti content (Al:Ti = 3:1), which results the higher average crystallinity of $Mg_{12}Al_3Ti$-LDHs in comparison to Ni_4Ti-LDHs (especially in the case of the homogeneous precipitation products), which necessitates a high order within the LDH structure.

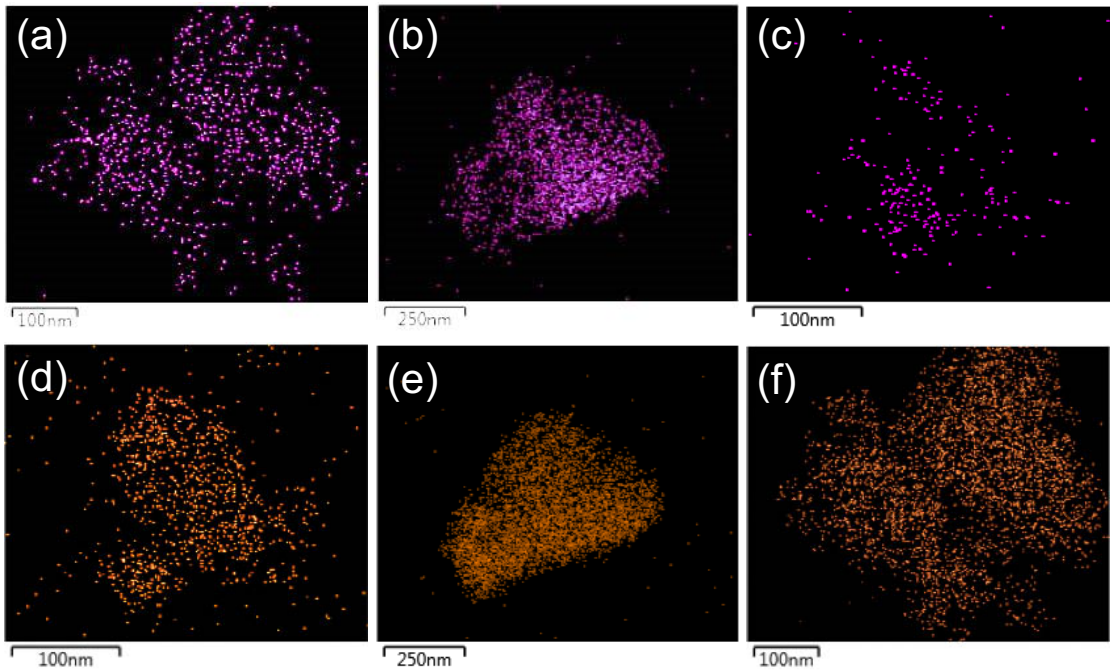


Figure 2.7 TEM-EDX images of Ni_4Ti-LDHs prepared by (a,d) organic co-precipitation, (b,e) aqueous co-precipitation at variable pH and (c,f) aqueous urea reflux method. The purple dots (a-c) show the distribution of Ti atoms and the orange dots (d-f) show the distribution of Ni atoms.

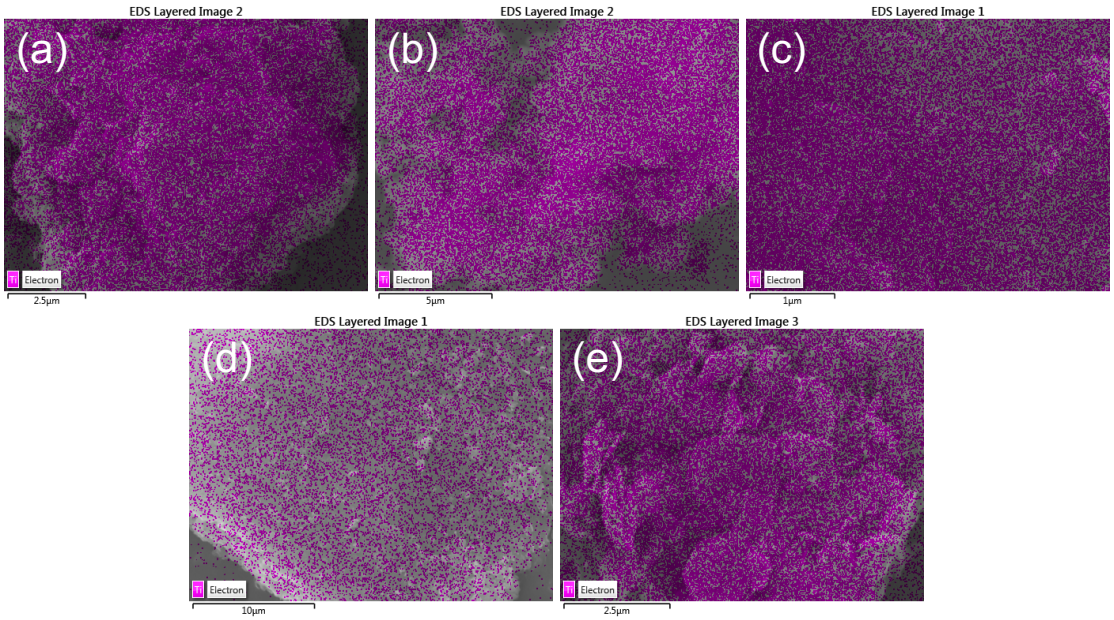


Figure 2.8 SEM-EDX images of $Mg_{12}Al_3Ti$-LDHs prepared by (a) organic co-precipitation, (b) aqueous co-precipitation at constant pH, (c) aqueous co-precipitation at variable pH, (d) aqueous urea reflux and (e) aqueous urea hydrothermal method. The purple dots represent the location of Ti atoms.

2.4 Variation of metal ratios

To study the effects of changing the metal ratios on the LDH properties, the total metal salt concentration in the reaction mixture was kept constant while the metal ratios were varied under optimised reaction conditions. In the case of NiTi-LDHs, the Ni:Ti ratio was varied from 2:1 to 6:1 in integer steps. For MgAlTi-LDHs, the Mg:(Al+Ti) ratio was kept constant at 3:1, and the Al:Ti ratio was varied between 3:1, 1:1 and 1:3. It should be noted that pure MgTi-LDHs (i.e. where Al:Ti=0:1) cannot be synthesised according to literature findings,[26] except by a sol-gel method.[35]

Tables 2.4 and 2.5 summarise the obtained metal ratios, as determined by ICP-MS, and compare them to the theoretical metal ratios for NiTi- and MgAlTi-LDH, respectively. A more detailed compositional analysis of the Ti-LDHs is summarised in Tables A.5 and A.6 in Appendix A. For NiTi-LDHs (Table 2.4), the trend of how the experimental metal ratios deviate from the theoretical ones follows the trend of how the Ti dispersion varies with synthetic method.

The urea reflux method products show the greatest deviation from the theoretically expected Ni:Ti ratios, with deviations of up to about 30%. In comparison, the organic co-precipitation products show the lowest deviations of below 10%. Nonetheless, most experimental Ni:Ti ratios increase roughly from 2:1 to 6:1 in incremental amounts, indicating that a good degree of control over the LDH composition is possible by varying the ratios of the metal salt reactants in the reaction mixture.

In the case of MgAlTi-LDHs (Table 2.5), the Mg:(Al+Ti) ratio is notably reduced from the theoretically expected value of 3:1 in most cases, with the exception of the urea hydrothermal products. There, the experimental ratio determined by ICP-MS indicates

that the Mg content in the products is close to or even greater than expected, possibly due the formation of the magnesite, $MgCO_3$, impurity seen in the PXRD patterns in Figures 2.1b and 2.2. In all other MgAlTi-LDH samples, the reduced Mg content could be due to the preferential precipitation and incorporation of the more highly charged Al^{3+} and Ti^{4+} into the LDH structure.

Table 2.4 The theoretical and experimental Ni:Ti metal ratios for NiTi-LDHs prepared by different synthetic methods.

Synthetic method/Ni:Ti ratio	**Theoretical**	**Experimental (from ICP-MS)**
Aqueous urea reflux	2:1	2.6:1
	3:1	3.8:1
	4:1	4.8:1
	5:1	6.5:1
	6:1	6.1:1
Aqueous co-precipitation at variable pH	2:1	1.9:1
	3:1	2.9:1
	4:1	3.6:1
	5:1	4.5:1
	6:1	6.0:1
Organic co-precipitation	2:1	1.8:1
	3:1	3.1:1
	4:1	4.0:1
	5:1	4.6:1
	6:1	6.2:1

Unlike the Mg:(Al+Ti) ratio, the Al:Ti ratio is significantly closer to the theoretically predicted value for all MgAlTi-LDH samples. Any discrepancies are minor, and it follows that the relative amounts of Al^{3+} and Ti^{4+} within the LDH metal hydroxide layers can be controlled by tuning the relative amounts of $Al(NO_3)_3 \cdot 9H_2O$ and $Ti(O^iPr)_4$ in the reaction mixture, respectively.

It should be noted that while the values in Tables 2.4 and 2.5 show a deviation of the actual metal ratios from the theoretically predicted ones (based on the amounts of metal salt reactants added to the reaction mixture), the LDHs will still be referred to according to their theoretical metal ratios in all of the following.

Table 2.5 The theoretical and experimental Mg:(Al+Ti) and Al:Ti metal ratios for MgAlTi-LDHs prepared by different synthetic methods.

Synthetic method/metal ratio	**Mg:(Al+Ti) theoretical**	**Mg:(Al+Ti) experimental**	**Al:Ti theoretical**	**Al:Ti experimental**
Aqueous urea hydrothermal	3:1	1.8:1	3:1	3.2:1
		3.3:1	1:1	1.3:1
		4.0:1	1:3	1:2.2
Aqueous urea reflux	3:1	0.9:1	3:1	3.3:1
		0.8:1	1:1	1.3:1
		0.6:1	1:3	1:4.2
Aqueous co-precipitation at variable pH	3:1	1.1:1	3:1	2.5:1
		1.1:1	1:1	1:1.2
		1.0:1	1:3	1:3.6
Aqueous co-precipitation at constant pH	3:1	1.4:1	3:1	2.5:1
		1.2:1	1:1	1:1.3
		1.1:1	1:3	1:3.5
Organic co-precipitation	3:1	1.4:1	3:1	2.3:1
		1.4:1	1:1	1:1.3
		1.4:1	1:3	1:3.6

The amount of Ti in both NiTi- and MgAlTi-LDHs has a large impact on the LDH crystallinity, as seen in Figures 2.9 and 2.10, as well as in Figures A.2c,d and A.3 in Appendix A. Specifically, a larger the amount of Ti (i.e. lower Ni:Ti and Al:Ti ratios) corresponds to a reduction in product crystallinity, as evidenced by the reduced intensity and sharpness of (00*l*) basal PXRD reflections. The reduced crystallinity with an increasing amount of Ti in the LDH metal hydroxide layers has been reported

before,[20,26,27] and can be ascribed to the larger size and higher charge of Ti^{4+} cations, as discussed in Section 1.1 of Chapter 1.

Nonetheless, the PXRD patterns show that NiTi- and MgAlTi-LDHs with a wide range of different compositions can be prepared with high sample purity. The exception to this is the Ni_2Ti-LDH product (Figure 2.9a), which shows minor impurity formation through the appearance of PXRD reflections in the 2θ region around 15º and 20º. The MgAlTi-LDHs prepared by the urea hydrothermal method (Figure 2.10) also show the presence of impurity – however, this is independent of the Al:Ti ratio.

The magnesite, $MgCO_3$, impurity was observed previously and it was shown that it cannot be removed by varying the [urea]:[metal salts] ratio (Figure 2.2). Although the proportion of this impurity appears to increase with decreasing Al:Ti ratio (Figure 2.10), the relative intensities of the MgAlTi-LDH and $MgCO_3$ PXRD reflections actually change due to the decreasing MgAlTi-LDH crystallinity. Although it has been reported that varying the amount of Ti in Ti-LDH metal hydroxide layers can affect the lattice parameter a and consequently the position of the (110) reflection (since $a = 2d_{110}$),[20,27,29] no clear trend in the variation of the position of the (110) reflection with the Ti content has been observed for the prepared NiTi- and MgAlTi-LDHs in this work.

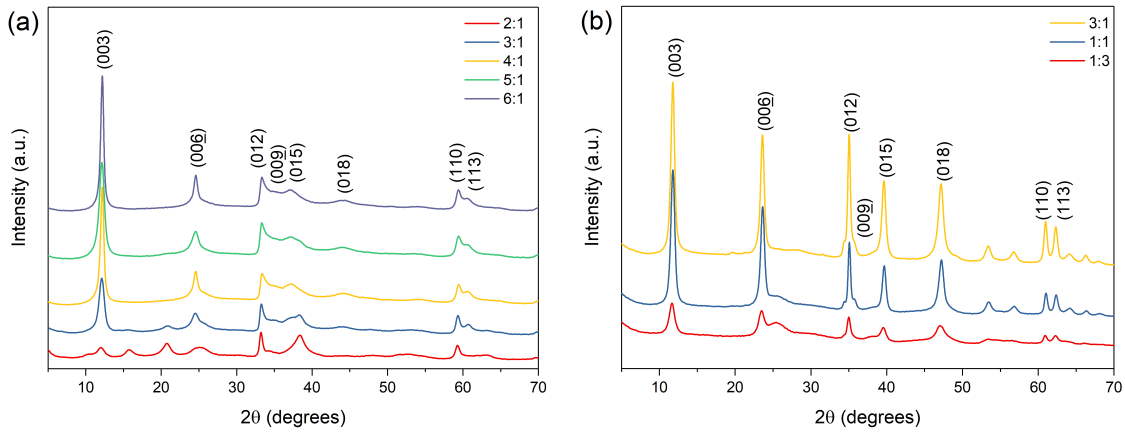


Figure 2.9 PXRD patterns of (a) NiTi-LDHs and (b) MgAlTi-LDHs prepared by the urea reflux method with different Ni:Ti and Al:Ti ratios, respectively.

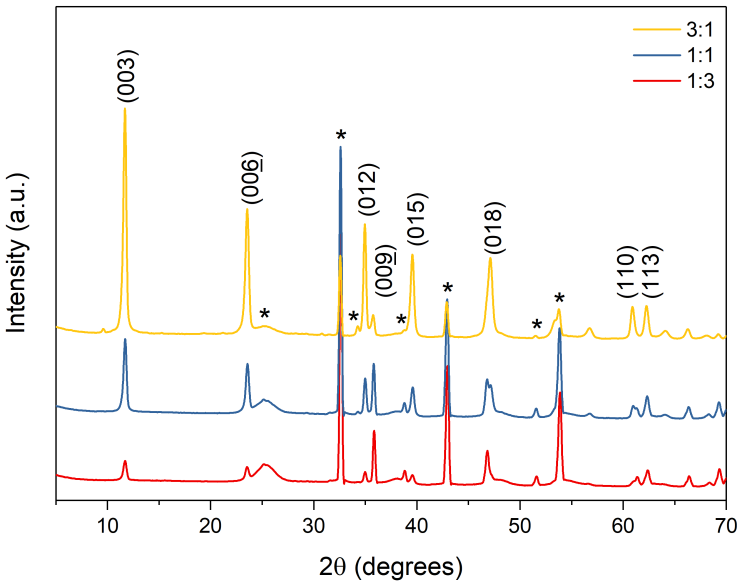


Figure 2.10 PXRD patterns of MgAlTi-LDHs prepared by the urea hydrothermal method with different Al:Ti ratios. * denotes magnesite, $MgCO_3$, impurity PXRD reflections.

The FTIR spectra of all the NiTi- and MgAlTi-LDHs prepared with different Ti content and using different synthetic methods are shown in Figures A.4 and A.5 of Appendix A, respectively. Similarly, the BET specific surface areas of all the Ti-LDHs are summarised in Table A.1 in Appendix A.

The morphology of the NiTi-LDHs prepared by the urea reflux method is largely unchanged with varying Ni:Ti ratio (Figure 2.11), with all products comprising thin, sheet-like nanoparticles with irregular contours. The minimal impact that the amount of Ti has on the particle morphology of NiTi-LDHs extends also to the other two methods, as can be seen in Figures A.6 and A.7 in Appendix A.

In comparison, the Al:Ti ratio has a large effect on the morphology of MgAlTi-LDHs prepared by the two homogeneous precipitation methods (Figures 2.12 and 2.13). A larger amount of Ti directly correlates to a less well-defined particle morphology. In the case of the urea reflux products, the Al:Ti = 3:1 product comprises large platelets (Figure 2.12a), whereas the Al:Ti = 1:3 product shows the presence of smaller, irregularly shaped nanosheets (Figure 2.12c).

This trend is especially noticeable for the products of the urea hydrothermal method, where the particles go from a very well-defined regular hexagon morphology (Figure 2.13a) to a less well-defined, irregular disk morphology (Figure 2.13c) with an increasing amount of Ti present.

The TEM images of MgAlTi-LDHs prepared with varying Al:Ti ratio using the constant pH aqueous co-precipitation, variable pH aqueous co-precipitation and organic co-precipitation methods are shown in Figures A.8, A.9 and A.10 of Appendix A, respectively.

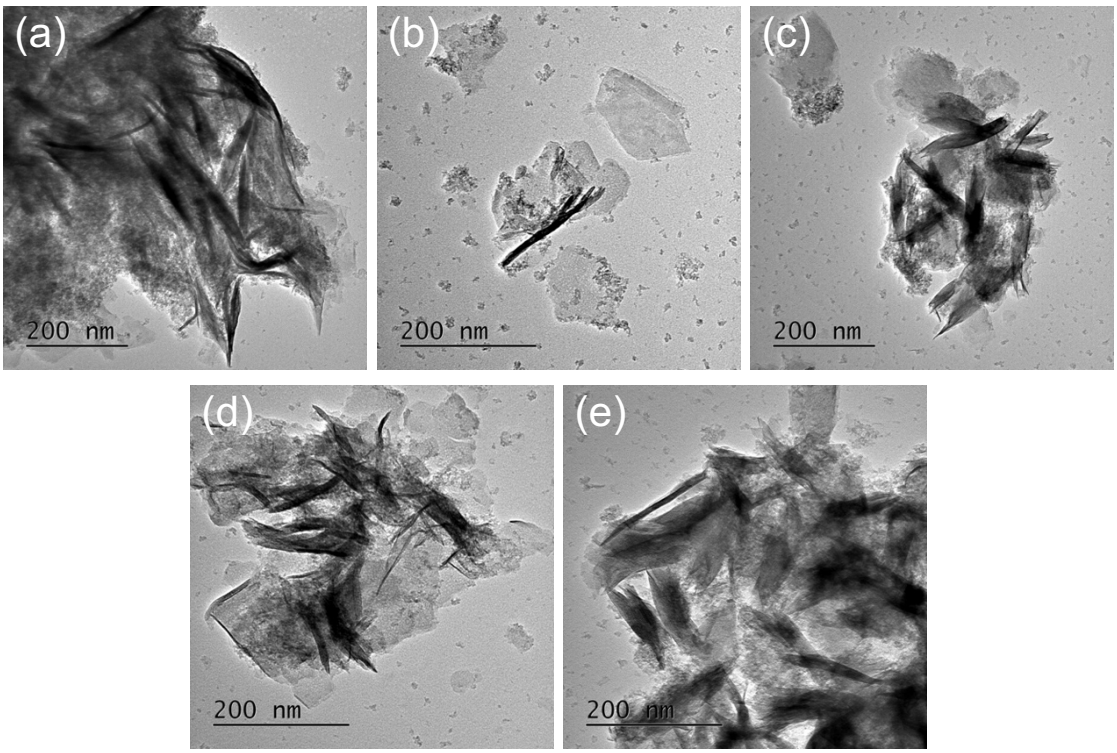


Figure 2.11 TEM images of urea reflux NiTi-LDHs with Ni:Ti ratios of (a) 2:1, (b) 3:1, (c) 4:1, (d) 5:1 and (e) 6:1.

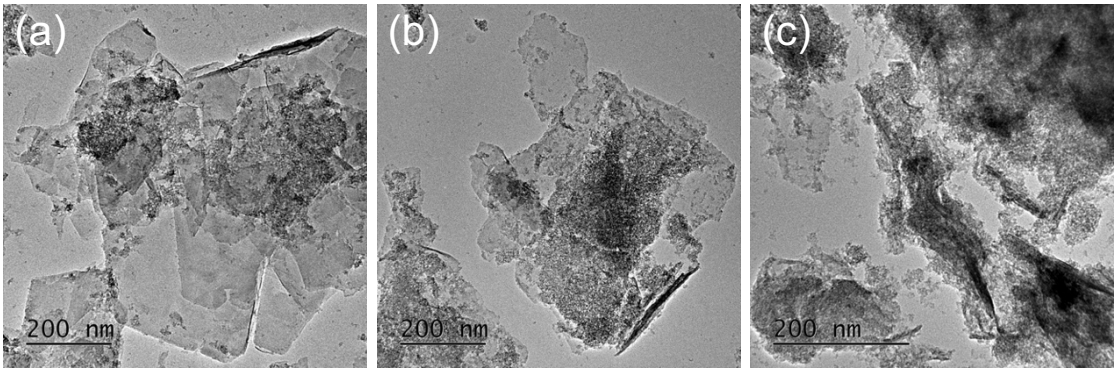


Figure 2.12 TEM images of urea reflux MgAlTi-LDHs with Al:Ti ratios of (a) 3:1, (b) 1:1 and (c) 1:3.

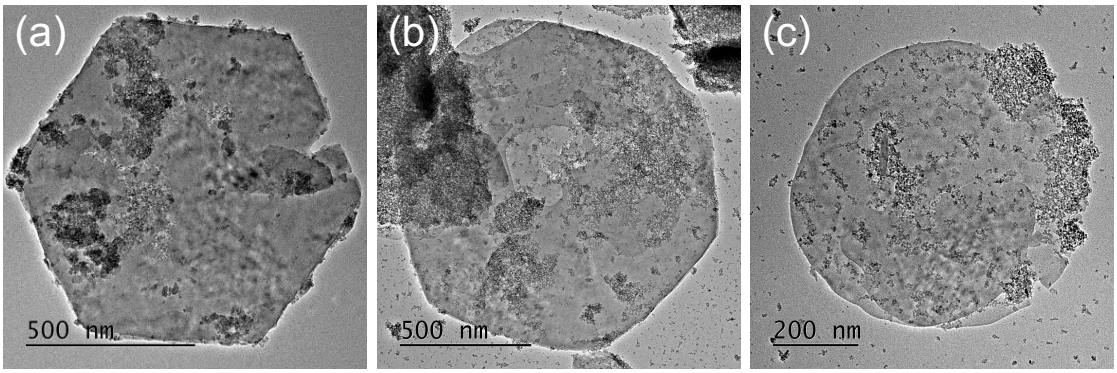


Figure 2.13 TEM images of urea hydrothermal MgAlTi-LDHs with Al:Ti ratios of (a) 3:1, (b) 1:1 and (c) 1:3.

2.5 Thermogravimetric analysis and chemical formulae

The chemical formulae of the synthesised NiTi- and MgAlTi-LDHs were determined using a combination of ICP-MS data (Tables 2.4 and 2.5) and thermogravimetric analysis (TGA). Representative plots of TGA and dTGA curves for the Ni_4Ti- and $Mg_{12}AlTi_3$-LDHs prepared by the aqueous co-precipitation method at variable pH are shown in Figure 2.14. The TGA and dTGA plots of all the other Ti-LDHs are shown in Figures A.11 – A.18 in Appendix A.

The TGA and dTGA curves shown in Figure 2.14 are characteristic of an LDH with the weight loss up to about 200 °C corresponding to the loss of the adsorbed and intercalated water (and solvent) molecules, and the dTGA peak in the 250 – 450 °C region corresponding to combined metal hydroxide layers dehydroxylation and intercalated anion decomposition.[20,32]

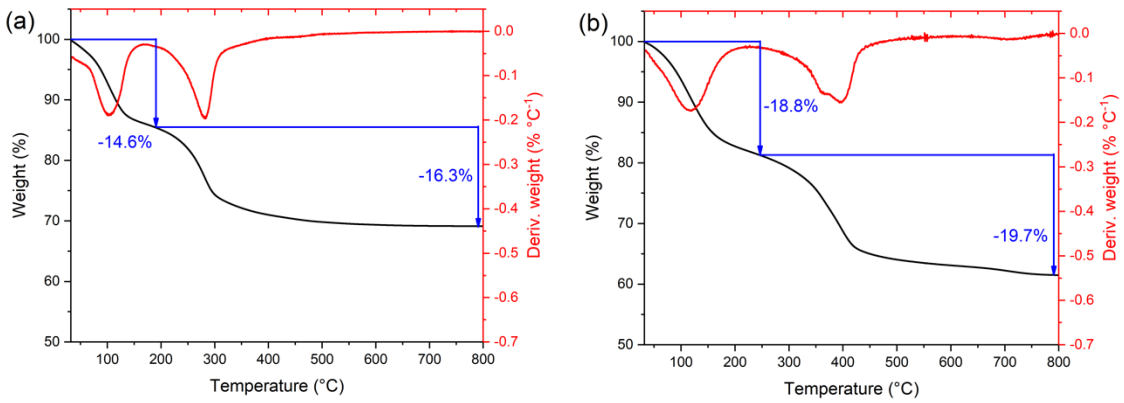


Figure 2.14 TGA (black) and dTGA (red) curves for (a) Ni_4Ti- and (b) $Mg_{12}AlTi_3$-LDHs prepared by the aqueous co-precipitation method at variable pH.

When using the ICP-MS and TGA data to estimate the chemical formulae, several assumptions were made in order to be able to calculate the amounts of anions and intercalated or adsorbed solvent molecules within a formula unit. Any deviations from

typical values reported in literature or discrepancies between values determined from ICP-MS and from TGA can be largely attributed to those assumptions.

It was assumed that the only solvent present is water, which is not strictly true for LDHs prepared by the organic co-precipitation method, which are likely to contain traces of ethanol molecules, as previously observed in LDHs treated with an AMO solvent.[32] Further, it was assumed that the only anion species present is carbonate, CO_3^{2-}. Considering that many reagents used in LDH synthesis are nitrate salts and that concentrated hydrochloric acid was used to prevent the precipitation of Ti^{4+} out of solution, the presence of other anions is probable. In the case of NiTi-LDHs synthesised by the urea reflux method, FTIR spectroscopy has also shown the presence of cyanate, NCO^-, anions (Figure 2.3a**)**. Finally, it was assumed that no defects are present in the LDH structure, and that all Ti centres carry a 4+ charge.

The estimated chemical formulae for Ni_4Ti-LDHs prepared by three different synthetic methods, $Mg_{12}AlTi_3$-LDHs prepared by five different synthetic methods and MgAlTi-LDHs prepared by the urea hydrothermal method with different theoretical Al:Ti ratios are shown in Tables 2.6, 2.7 and 2.8, respectively. All chemical formulae can be found in Tables A.3 and A.4 in Appendix A. All the formulae are listed using the $M(II)_{1-x}M(IV)_x(OH)_2$ or $M(II)_{1-x-y}M(III)_xM(IV)_y(OH)_2$ terminology (where all the chemical formulae are normalised to two hydroxyl groups per formula unit), so as to allow facile comparison between the different LDHs.

The slightly larger number of water molecules per formula unit for the Ni_4Ti-LDH prepared by the organic co-precipitation method is likely a consequence of ethanol molecules being present, both in the interlayer region and adsorbed on the LDH particle

surface. Since it was assumed that water is the only solvent present, the value of 1.3 also includes these ethanol molecules.

Interestingly, no such trend is observed for $Mg_{12}AlTi_3$-LDHs, as the organic co-precipitation product contains a smaller number of water molecules per formula unit than the aqueous co-precipitation and urea reflux products. In comparison, the aqueous urea hydrothermal product contains a notably smaller amount of water. The water content of MgAlTi- and NiTi-LDHs is similar, with approximately one water molecule per formula unit on average. The notable exception to this are the urea hydrothermal MgAlTi-LDH products, with contain as little as 0.3 water molecules per formula unit.

Table 2.6 Estimated chemical formulae of NiTi-LDHs prepared by three different synthetic methods, all with a theoretical Ni:Ti ratio of 4:1.

Synthetic method	Estimated chemical formula
Aqueous urea reflux	$[Ni_{0.83}Ti_{0.17}(OH)_2](CO_3)_{0.17} \bullet 0.6H_2O$
Aqueous co-precipitation at variable pH	$[Ni_{0.78}Ti_{0.22}(OH)_2](CO_3)_{0.22} \bullet 1.0H_2O$
Organic co-precipitation	$[Ni_{0.80}Ti_{0.20}(OH)_2](CO_3)_{0.20} \bullet 1.3H_2O$

Table 2.7 Estimated chemical formulae of MgAlTi-LDHs prepared by five different synthetic methods, all with a theoretical Al:Ti ratio of 1:3.

Synthetic method	Estimated chemical formula
Aqueous urea hydrothermal	$[Mg_{0.80}Al_{0.06}Ti_{0.14}(OH)_2](CO_3)_{0.17} \bullet 0.3H_2O$
Aqueous urea reflux	$[Mg_{0.37}Al_{0.12}Ti_{0.51}(OH)_2](CO_3)_{0.57} \bullet 1.5H_2O$
Aqueous co-precipitation at var. pH	$[Mg_{0.51}Al_{0.11}Ti_{0.38}(OH)_2](CO_3)_{0.44} \bullet 1.2H_2O$
Aqueous co-precipitation at const. pH	$[Mg_{0.53}Al_{0.11}Ti_{0.36}(OH)_2](CO_3)_{0.42} \bullet 1.3H_2O$
Organic co-precipitation	$[Mg_{0.59}Al_{0.09}Ti_{0.32}(OH)_2](CO_3)_{0.37} \bullet 1.0H_2O$

Table 2.8 Estimated chemical formulae of MgAlTi-LDHs prepared by the aqueous urea hydrothermal method, with different theoretical Al:Ti ratios.

Theoretical Al:Ti ratio	Estimated chemical formula
3:1	$[Mg_{0.65}Al_{0.27}Ti_{0.08}(OH)_2](CO_3)_{0.22} \bullet 0.6H_2O$
1:1	$[Mg_{0.77}Al_{0.13}Ti_{0.10}(OH)_2](CO_3)_{0.17} \bullet 0.5H_2O$
1:3	$[Mg_{0.80}Al_{0.06}Ti_{0.14}(OH)_2](CO_3)_{0.17} \bullet 0.3H_2O$

2.6 Band gaps and Ti oxidation states

The band gaps of the synthesised Ti-LDHs were analysed by diffuse reflectance UV-visible spectroscopy (DRUV-vis) in conjunction with the graphical Tauc plot method.[16-18] Representative DRUV-vis spectra of NiTi- and MgAlTi-LDHs and a Tauc plot of the MgAlTi-LDH sample are shown in Figure 2.15. DRUV-vis spectra of all NiTi- and MgAlTi-LDHs are shown in Figures A.19 and A.20 in Appendix A, respectively.

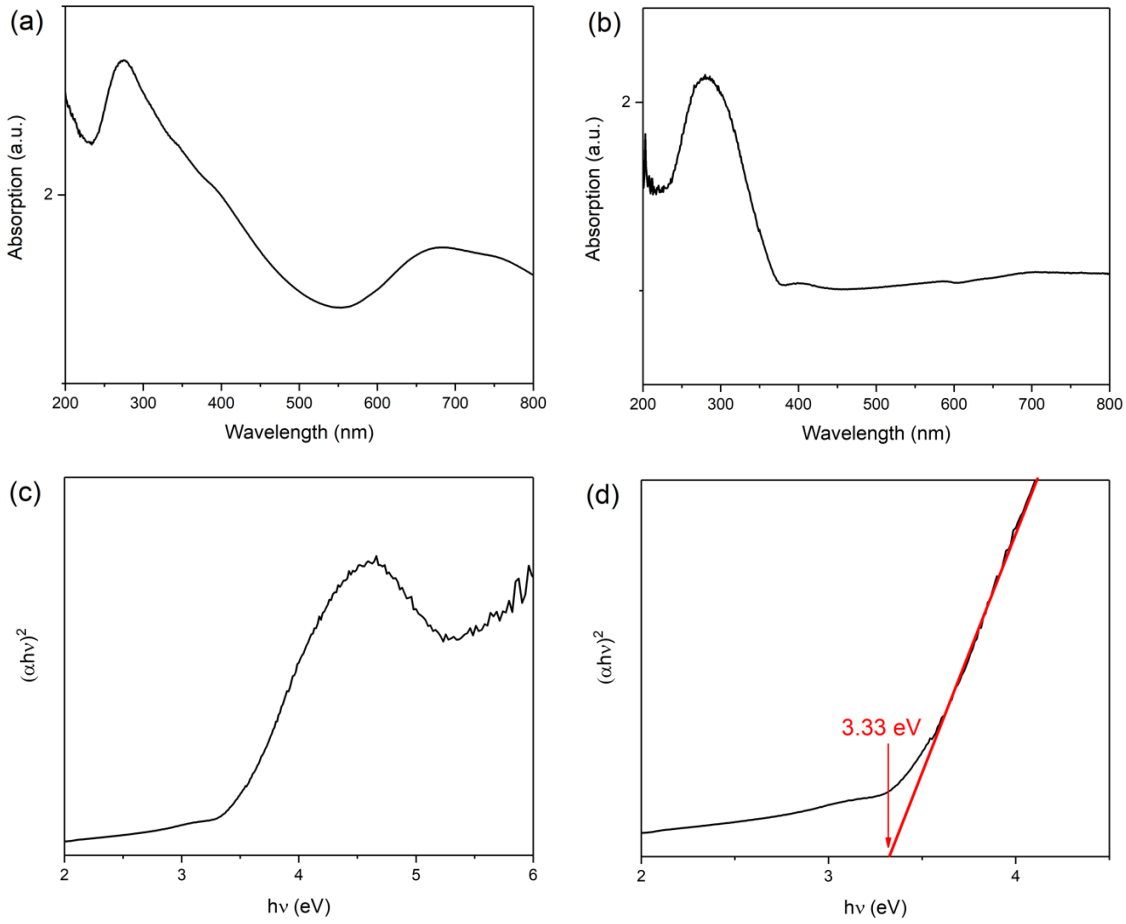


Figure 2.15 Representative DRUV-vis spectra of (a) NiTi- and (b) MgAlTi-LDHs, and (c,d) the Tauc plot of the MgAlTi-LDH sample with the extrapolation of the approximately linear part shown. The *x*-intercept at 3.33 eV corresponds to the estimated band gap energy of the sample.

The NiTi-LDH DRUV-vis spectrum comprises two broad absorption bands in the 250 – 450 nm and 600 – 800 nm regions. The former can be attributed to the ligand-to-metal charge transfer that involves the octahedral coordination of Ti atoms in the metal

hydroxide sheets.[22] The latter band in the blue region is a consequence of the presence of Ni^{2+} cations in the metal hydroxide layers. Accordingly, it is not present in the DRUV-vis spectrum of the MgAlTi-LDH (Figure 2.15b).

In the graphical Tauc plot method, the determination of band gap energy relies on the correct extrapolation of the approximately linear part of the $(\alpha h\nu)^2$ vs $h\nu$ graph and the determination of the *x*-intercept. Consequently, the band gap energies are best treated as estimates. For example, the band gap energy of anatase, known from literature to have a value of 3.2 eV,[36] can be estimated from an experimental Tauc plot to have a value anywhere in the range of 2.8 – 3.2 eV, depending on the choice of the linear part from which to extrapolate. Therefore, emphasis is placed on relative trends and approximate agreement with literature, rather than the absolute values listed in Tables 2.9 and 2.10.

The band gap energies of NiTi-LDHs listed in Table 2.9 show that while there is no clear trend between their values and the Ni:Ti ratio, the synthetic method has a larger effect. Specifically, NiTi-LDHs prepared by the aqueous co-precipitation method at variable pH have an average band gap energy of 2.30 eV. In comparison, aqueous urea reflux and organic co-precipitation methods give NiTi-LDHs with lower average band gap energies of 2.19 and 2.20 eV, respectively. These values are all in good agreement with literature findings, which report NiTi-LDH band gap energies in the 2.1 – 2.4 eV range.[1,22,30] Because the values are below 3.1 eV, NiTi-LDHs can act both as visible-light- and UV-active photocatalysts.

Previously reported density functional theory (DFT) calculations show that for an ideal NiTi-LDH system, the valence band (VB) top primarily comprises the occupied Ni 3d and O 2p orbitals, while the conduction band (CB) bottom is dominated by the unoccupied Ti 3d orbitals.[1,22] The band gap transition from the VB top to the CB bottom

corresponds to about 2.1 eV, which is in good agreement with the experimental values estimated from the DRUV-vis measurements (Table 2.9). Introducing Ti^{3+} states has been proposed to include removing oxygen atoms from the central surface, forming V_{Ti}^{3+} defect states.[1] The result of these defect states is the hybridisation of the CB bottom to include both Ti 3d orbitals and O 2p orbitals. Consequently, the theoretical DFT band gap energy is calculated to be much lower, about 1.8 eV. However, this reduction in the band gap energy is likely to be minimal for NiTi-LDHs where Ti centres are primarily in the 4+ oxidation state.

The band gap energies of MgAlTi-LDHs in Table 2.10 show a notably different trend, with all five synthetic methods giving LDHs with an average band gap energy of about 3.4 eV. Contrary to NiTi-LDHs, the Al:Ti metal ratio has a larger effect, with the band gap energy decreasing with an increasing amount of Ti (i.e. lower Al:Ti ratio). The values in excess of 3.1 eV mean that MgAlTi-LDHs can only act as UV-active photocatalysts, unless they form an active complex with reactant molecules, which has been reported to extend the activity range into the visible spectrum.[37-39] The estimated band gap energies are in good agreement with literature findings,[22,28] with the Mg_6AlTi-LDH prepared by aqueous co-precipitation at variable pH and $Mg_{12}AlTi_3$-LDHs prepared by aqueous urea hydrothermal and aqueous urea reflux methods, respectively, showing slightly lower band gap energies than the typically reported 3.4 – 3.5 eV.To the best of the author's knowledge, DFT calculations that predict the orbitals that contribute to the VB and CB of MgAlTi-LDHs have not been reported in literature to date. Nonetheless, based on the data available for NiTi-LDHs,[1,22] as well as other transition-metal-based LDHs,[30] it is likely that the VB top comprises primarily O 2p orbitals, while the CB bottom consists predominantly of unoccupied Ti 3d orbitals, with negligible contributions from empty Mg 3s and Al 3s and 3p orbitals.

Table 2.9 Estimated band gap energies of NiTi-LDHs prepared by different synthetic methods and with different Ni:Ti ratios.

Synthetic method	**Ni:Ti ratio**	**Band gap energy (eV)**
Aqueous urea reflux	2:1	2.23
	3:1	2.18
	4:1	2.20
	5:1	2.19
	6:1	2.16
Aqueous co-precipitation at variable pH	2:1	2.31
	3:1	2.33
	4:1	2.34
	5:1	2.27
	6:1	2.27
Organic co-precipitation	2:1	2.18
	3:1	2.20
	4:1	2.21
	5:1	2.21
	6:1	2.19

Table 2.10 Estimated band gap energies of MgAlTi-LDHs prepared by different synthetic methods and with different Al:Ti ratios.

Synthetic method	**Al:Ti ratio**	**Band gap energy (eV)**
Aqueous urea hydrothermal	3:1	3.39
	1:1	3.42
	1:3	3.33
Aqueous urea reflux	3:1	3.42
	1:1	3.41
	1:3	3.25
Aqueous co-precipitation at variable pH	3:1	3.38
	1:1	3.34
	1:3	3.36
Aqueous co-precipitation at constant pH	3:1	3.59
	1:1	3.39
	1:3	3.35
Organic co-precipitation	3:1	3.41
	1:1	3.40
	1:3	3.38

2.7 Advanced analysis of high crystallinity MgAlTi-LDHs

As evidenced by the intense and sharp PXRD peaks in Figures 2.1b and 2.10, as well as the well-defined morphology of the particles shown in Figure 2.13, the urea hydrothermal method gives MgAlTi-LDHs with a high degree of order within their structure and consequently a high crystallinity.

If this highly organised structure reduces electron-hole recombination while also forming suitable active sites on the particle surface to facilitate the targeted photo-oxidation reactions, it can result in a high photocatalytic activity. Therefore, these high crystallinity MgAlTi-LDHs were further analysed using high-angle annular dark-field imaging (HAADF) with elemental mapping and solid state nuclear magnetic resonance (ssNMR) spectroscopy. Particular attention was given to the $Mg_{12}AlTi_3$-LDH, since its high Ti content is likely to correlate with a higher photocatalytic activity. The HAADF images of urea hydrothermal $Mg_{12}AlTi_3$- and $Mg_{12}Al_3Ti$-LDHs are shown in Figure 2.16**.**

Crucially, the elemental mapping (Ti K signal) shows that the Ti centres are not evenly dispersed within the LDH platelets, but rather cluster together in areas of high Ti density. However, these areas do not form a separate crystallographic entity, since the PXRD patterns of these samples (Figure 2.10) only show the presence of the respective LDHs and the magnesite impurity, without any PXRD reflections that could be assigned to a Ti impurity phase. The high crystallinity of these samples further suggests that there is notable ordering of the metal cations also within these areas of Ti clustering.

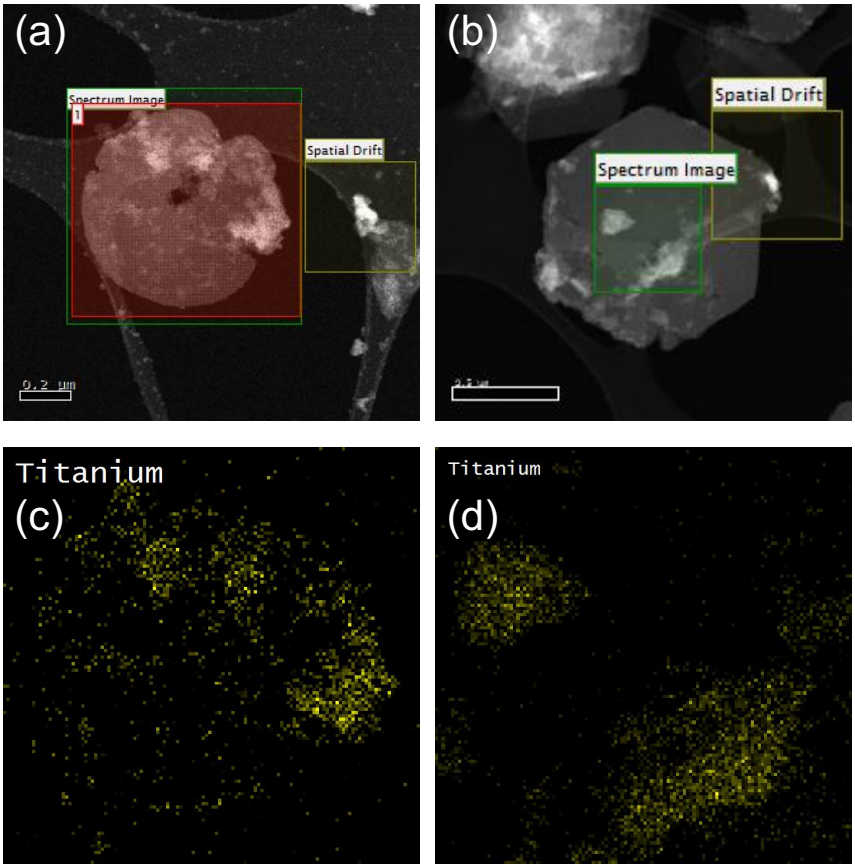


Figure 2.16 (a and b) HAADF images and (c and d) Ti K signal mapping of urea hydrothermal $Mg_{12}AlTi_3$- and $Mg_{12}Al_3Ti$-LDHs, respectively. The yellow dots in the Ti K signal mapping images represent Ti centres.

To the best of the author's knowledge, the Ti environments of Ti-LDHs have not been directly probed by $^{47/49}$Ti ssNMR spectroscopy to date. The two NMR-active isotopes, ^{47}Ti (I = 5/2) and ^{49}Ti (I = 7/2), both have small gyromagnetic ratios (γ) and low natural abundances (7.3% for ^{47}Ti and 5.5% for ^{49}Ti).[40,41] This results in a very low intrinsic detection sensitivity. Additionally, both isotopes have moderately large quadrupole moments, which give rise to broad ssNMR signals.[42] All these unfavourable NMR characteristics typically make the observation of the broad $^{47/49}$Ti ssNMR spectra difficult.[40] However, the symmetrical octahedral (O_h) and tetrahedral (T_d) Ti local environments within the MgAlTi-LDH metal hydroxide matrix make their detection possible, with reasonably good intensity and resolution.

Comparing the $^{47/49}$Ti dynamic ssNMR spectra of $Mg_{12}AlTi_3$- and $Mg_{12}Al_3Ti$-LDHs prepared by the urea hydrothermal method, the former gives a significantly more intense spectrum due to the higher Ti content (Figure 2.17a). Furthermore, the $Mg_{12}AlTi_3$-LDH $^{47/49}$Ti ssNMR spectrum shows a better resolution, with more distinct resonances.

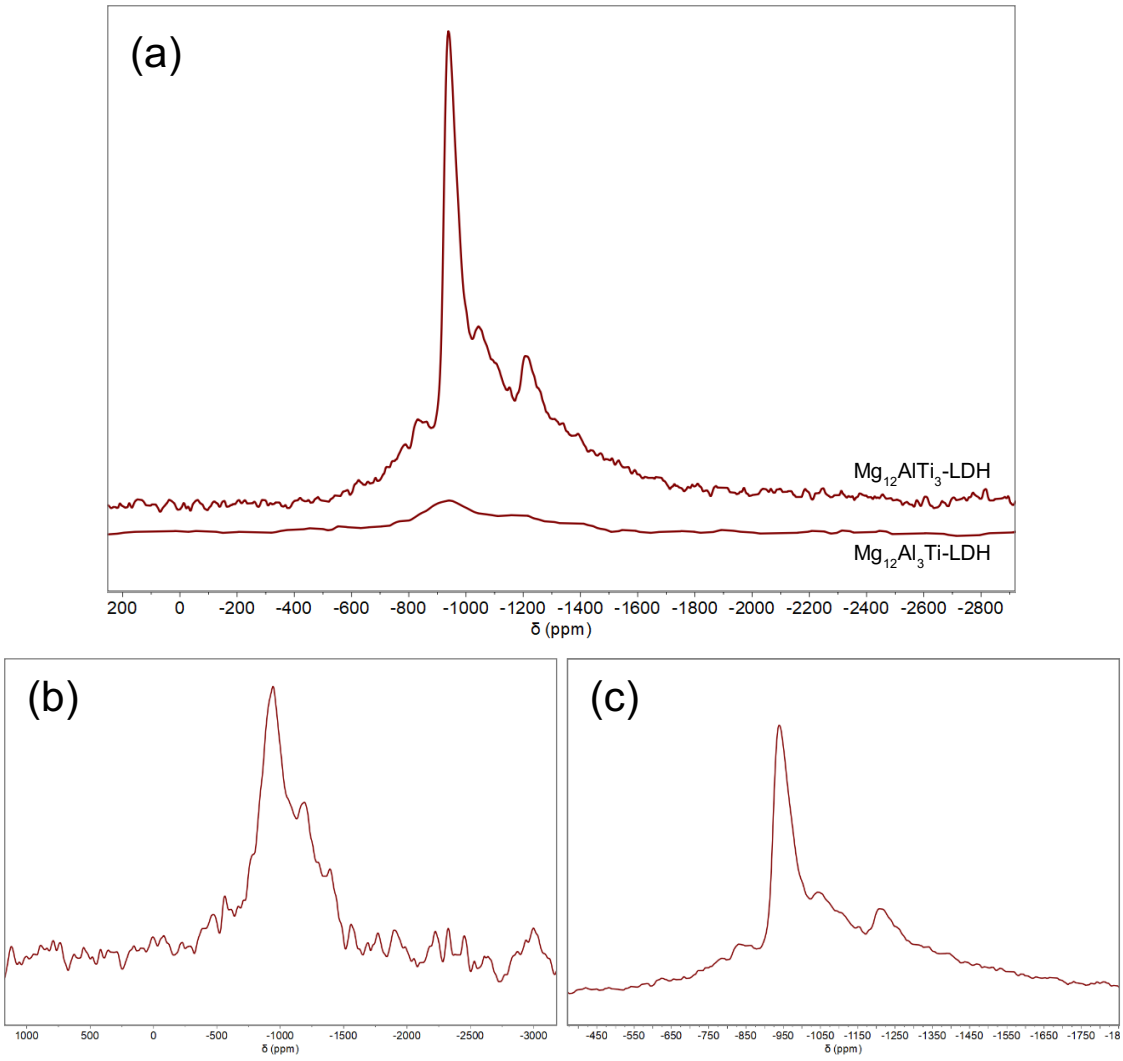


Figure 2.17 (a) The comparison of the $^{47/49}$Ti dynamic ssNMR spectra of $Mg_{12}Al_3Ti$- and $Mg_{12}AlTi_3$-LDHs prepared by the urea hydrothermal method, as well as the separate spectra of the two samples (b and c, respectively).

The peak fitting analysis of the $^{47/49}$Ti ssNMR spectrum of the $Mg_{12}AlTi_3$-LDH sample in Figure 2.18 shows four different Ti local environments (taking into account that each environment corresponds to two isotope peaks). Because the two Ti two isotopes have very similar γ's, the resonance frequencies differ only by a small amount.[41] Consequently,

the resonances due to the two different isotopes very nearly overlap in the ssNMR spectrum, as seen in the peak fitting profile.

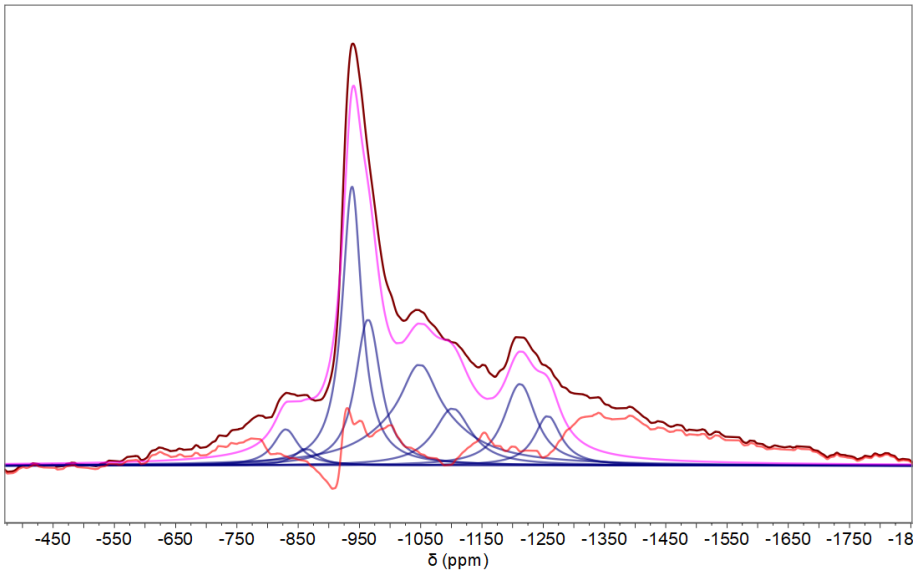


Figure 2.18 Peak fitting analysis of the $^{47/49}$Ti dynamic ssNMR spectrum of $Mg_{12}AlTi_3$-LDH prepared by the urea hydrothermal method.

Although the exact nature of the four different Ti local environments is difficult to determine without detailed computational simulations, it is possible to hypothesise that they are the result of different coordination modes of the Ti centres (octahedral or tetrahedral) and/or different cation nearest-neighbours in the LDH metal hydroxide matrix with both Mg^{2+} and Al^{3+} cations present in addition to Ti^{4+}.[43] A further level of complexity is added by considering that Ti can exists in the urea hydrothermal $Mg_{12}AlTi_3$-LDH also in the 3+ oxidation state,[1] which can also affect the Ti local environment.

Nonetheless, the $^{47/49}$Ti ssNMR spectrum in Figure 2.18 shows that the $Mg_{12}AlTi_3$-LDH does indeed have a highly ordered structure with a high level of complexity. This is further confirmed by the ^{1}H ssNMR spectrum shown in Figure 2.19, which shows an above average number of well-resolved resonances. In addition to the broad water resonance between about –1 and 7 ppm and the HCO_3^- resonance at 10.4 ppm,[44] the

^{1}H ssNMR spectrum has eight further resonances, which correspond to eight unique local environments of the hydroxyl groups, –OH, in the metal hydroxide layers.

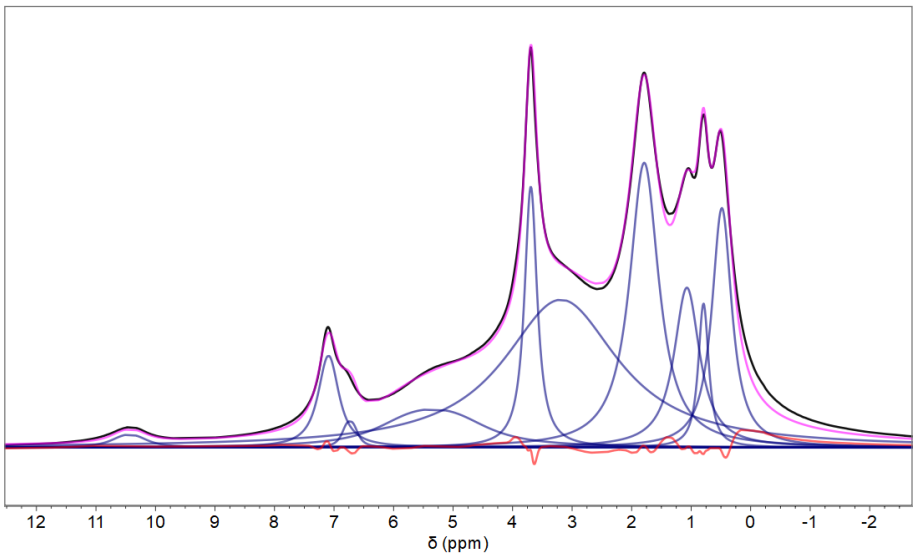


Figure 2.19 Peak fitting analysis of the ^{1}H ssNMR spectrum of $Mg_{12}AlTi_3$-LDH prepared by the urea hydrothermal method.

Typical LDH ^{1}H ssNMR spectra of MgAl-, ZnAl- and other M(II)M'(III)-LDHs comprise a maximum of three resonances associated with unique hydroxyl group proton environments.[45,46] Each hydroxyl group within the LDH metal hydroxide layers is typically located above a triangle formed by three cationic sites. For MgAl-LDHs, this gives three possible local environments: Mg_3–OH, Mg_2Al–OH and $MgAl_2$–OH, with the latter being the result of small amounts of Al clustering in an otherwise perfectly ordered cation arrangement.[45] Similarly, for ZnAl-LDHs, the local proton environments are Zn_3–OH, Zn_2Al–OH and $ZnAl_2$–OH, although the resonance ascribed to the Zn_3–OH moiety could also correspond to ZnAl□–OH, where □ is a cation vacancy.[46]

The complexity of ^{1}H ssNMR spectra increases with the introduction of a third cation into the LDH matrix, such as with MgAlTi-LDHs. Here, the number of possible Mg/Al/Ti–OH permutations is much larger, especially considering the possibility of two different oxidation states of the Ti centres. Much like with the $^{47/49}$Ti ssNMR spectra

above, detailed assignment of the individual resonances is impossible without computational simulations. This is especially true knowing from the HAADF images in Figure 2.16c that the $Mg_{12}AlTi_3$-LDH particles contain areas of lower and higher Ti density.

Based on literature reports of the different $M(II)_{3-y}M'(III)_y$–OH environments,[45,46] the possible local proton environments in MgAlTi-LDHs include: Mg_3–OH, Mg_2Al–OH, $MgAl_2$–OH, MgAlTi(IV)–OH, MgAlTi(III)–OH, Mg_2Ti(IV)–OH and Mg_2Ti(III)–OH, with the resonances at higher frequencies (higher ppm values) corresponding to hydroxyl groups adjacent to metal cations with higher electronegativities and higher positive charges.[45] In addition to these seven possible environments, the presence of defects (such as cation vacancies) can add further resonances.

The complexity of the urea hydrothermal $Mg_{12}AlTi_3$-LDH structure is evident also in the ^{27}Al ssNMR spectrum (Figure 2.20). The ^{27}Al resonance positions are highly sensitive to the coordination number, making it easy to distinguish the different coordination geometries of Al^{3+} centres within the LDH metal hydroxide layers. Octahedral 6-coordinate $Al(OM)_6$ sites usually occupy the –5 to 15 ppm range, while tetrahedral 4-coordinate $Al(OM)_4$ sites fall in the 60 to 90 ppm range.[47] Therefore, the three peaks in Figure 2.20 between 2 and 7 ppm correspond to 6-coordinate octahedral Al^{3+} centres, whereas the peaks around 31.4 and 66.9 ppm correspond to 5- and 4-coordinate Al^{3+}, respectively.[45]

In typical ^{27}Al ssNMR spectra of MgAl-LDHs, the peak around 10 ppm can be attributed to $Al(OMg)_6$ moieties and the peaks at lower ppm values (around 0 ppm) are ascribed to $Al(OMg)_5(OAl)$ and $Al(OMg)_4(OAl)_2$ moieties resulting from defects in the cation ordering.[45] The exact determination of the Al^{3+} environments in $Mg_{12}AlTi_3$-LDH is more

complex than in MgAl-LDHs due to the presence of the third cation species (with two possible oxidation states), and requires additional computational simulations. However, considering that the Ti content is notably higher than the Al content (and that consequently the probability of Al-O-Al connections is low), the most likely 6-coordinate Al^{3+} environments correspond to the $Al(OMg)_6$, $Al(OMg)_5(OTi)_2$ and $Al(OMg)_4(OTi)_2$ moieties.[48]

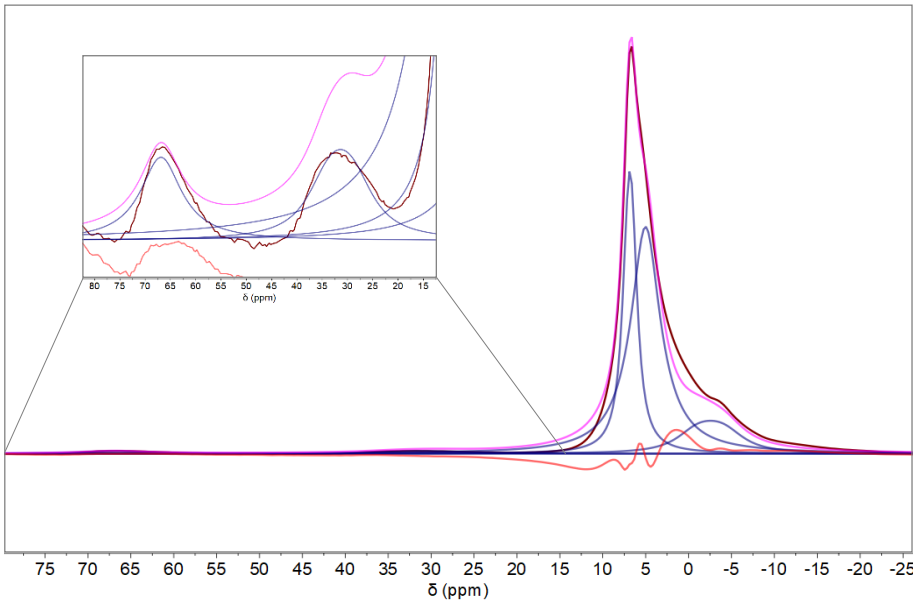


Figure 2.20 Peak fitting analysis of the ^{27}Al ssNMR spectrum of $Mg_{12}AlTi_3$-LDH prepared by the urea hydrothermal method, with a zoomed-in view at the two peaks at about 31.4 and 66.9 ppm (inset).

In an ideal LDH structure, all Al^{3+} cations would only be present in octahedral coordination, i.e. in 6-coordinate environments. However, tetrahedral (4-coordinate) Al^{3+} centres have been observed previously, primarily in calcined-rehydrated LDH samples.[47,49] Although it is not clear why the $Mg_{12}AlTi_3$-LDH product prepared in this work shows the presence of tetrahedrally coordinated Al^{3+} in the absence of a calcination-rehydration process, the previous findings reported in literature indicate that suitable tetrahedral interstitial sites are present in the LDH structure to give rise to 4-coordinate Al^{3+} centres. The 5-coordinate Al^{3+} centres are a likely consequence of the presence of additional defects.

2.8 Conclusions

Thirty NiTi- and MgAlTi-LDHs were synthesised with five different synthetic methods: aqueous co-precipitation at constant and variable pH, organic co-precipitation, and homogeneous precipitation under reflux and hydrothermal conditions, with different Ni:Ti and Al:Ti ratios, respectively. The choice of synthetic method was found to have a significant effect on the LDH crystallinity and degree of Ti dispersion, with organic co-precipitation giving LDH particles with an even distribution of Ti centres, whereas homogeneous precipitation products show clustering of Ti centres. The M(II/III):Ti ratio was similarly shown to have a large effect on the LDH properties, with a larger Ti content corresponding to a lower crystallinity and a less well-defined particle morphology.

Thermogravimetric analysis (TGA) and inductively coupled plasma mass spectrometry (ICP-MS) were used to determine the chemical formulae of the synthesised LDHs. Their band gap energies were estimated using diffuse reflectance UV-visible spectroscopy (DRUV-vis) in conjunction with the graphical Tauc plot method. The band gap energies of NiTi- and MgAlTi-LDHs were found to be about 2.3 and 3.4 eV, respectively, in good agreement with previous literature reports. Finally, the properties of the highly crystalline urea hydrothermal MgAlTi-LDHs were further analysed, as it can be anticipated that the high degree of order within their structure can result in a high photocatalytic activity.

In summary, it has been shown that a wide variety of Ti-LDHs can be synthesised with high purity and good control over their properties, such as morphology and composition. The newly developed organic co-precipitation method was found to allow the synthesis of delaminated Ti-LDH nanosheets with high Ti dispersion, whereas the urea hydrothermal method gives highly crystalline >1 μm large hexagonal platelets with an uneven dispersion of Ti in the form of areas of high and low Ti concentration.

2.9 References

1 Y. Zhao, B. Li, Q. Wang, W. Gao, C. J. Wang, M. Wei, D. G. Evans, X. Duan and D. O'Hare, *Chem. Sci.*, 2014, **5**, 951–958.
2 F. Cavani, F. Trifirò and A. Vaccari, *Catal. Today*, 1991, **11**, 173–301.
3 W. Feitknecht and M. Gerber, *Helv. Chim. Acta*, 1942, **25**, 131–137.
4 W. Feitknecht, *Helv. Chim. Acta*, 1942, **25**, 555–569.
5 D. G. Evans and X. Duan, *Chem. Commun.*, 2006, 485–496.
6 U. Costantino, F. Marmottini, M. Nocchetti and R. Vivani, *Eur. J. Inorg. Chem.*, 1998, **1998**, 1439–1446.
7 M. Adachi-Pagano, C. Forano and J.-P. Besse, *J. Mater. Chem.*, 2003, **13**, 1988–1993.
8 F. Malherbe, C. Forano and J.-P. Besse, *Microporous Mat.*, 1997, **10**, 67–84.
9 M. Ogawa and H. Kaiho, *Langmuir*, 2002, **18**, 4240–4242.
10 N. Iyi, T. Matsumoto, Y. Kaneko and K. Kitamura, *Chem. Lett.*, 2004, **33**, 1122–1123.
11 N. Iyi, K. Tamura and H. Yamada, *J. Colloid Interface Sci.*, 2009, **340**, 67–73.
12 J. Prince, A. Montoya, G. Ferrat and J. S. Valente, *Chem. Mater.*, 2009, **21**, 5826–5835.
13 J. Yu, J. Liu, A. Clearfield, J. E. Sims, M. T. Speiegle, S. L. Suib and L. Sun, *Inorg. Chem.*, 2016, **55**, 12036–12041.
14 Q. Wang, X. Zhang, J. Zhu, Z. Guo and D. O'Hare, *Chem. Commun.*, 2012, **48**, 7450–7452.
15 Q. Wang and D. O'Hare, *Chem. Commun.*, 2013, **49**, 6301–6303.
16 B. D. Viezbicke, S. Patel, B. E. Davis and D. P. Birnie III, *Phys. Status Solidi B*, 2015, **252**, 1700–1710.
17 N. Baliarsingh, L. Mohapatra and K. Parida, *J. Mater. Chem. A*, 2013, **1**, 4236–4243.
18 R. Lu, X. Xu, J. Chang, Y. Zhu, S. Xu and F. Zhang, *Appl. Catal., B*, 2012, **111-112**, 389–396.
19 Y. Lee, J. H. Choi, H. J. Jeon, K. M. Choi, J. W. Lee and J. K. Kang, *Energy Environ. Sci.*, 2011, **4**, 914–920.
20 X. Shu, W. Zhang, J. He, F. Gao and Y. Zhu, *Solid State Sci.*, 2006, **8**, 634–639.
21 X. Shu, J. He, D. Chen and Y. Wang, *J. Phys. Chem. C*, 2008, **112**, 4151–4158.
22 Y. Zhao, P. Chen, B. Zhang, D. S. Su, S. Zhang, L. Tian, J. Lu, Z. Li, X. Cao, B. Wang, M. Wei, D. G. Evans and X. Duan, *Chem. Eur. J.*, 2012, **18**, 11949–11958.
23 R. Li, W. Gao, J. He and J. Hu, *Optoelectron. Adv. Mat.*, 2013, **7**, 279–284.
24 V. Solovov, V. Kovalenko, N. Nikolenko, V. Kotok and E. Vlasova, *EEJET*, 2017, **1**, 16–22.
25 W. H. Zhang, X. D. Guo, J. He and Z. Y. Qian, *Journal of the European Ceramic Society*, 2008, **28**, 1623–1629.
26 K. Hosni, O. Abdelkarim, N. Frini-Srasra and E. Srasra, *Korean J. Chem. Eng.*, 2014, **32**, 104–112.
27 N. Das and A. Samal, *Microporous Mesoporous Mater.*, 2004, **72**, 219–225.
28 H. Zhao, J. Xu, L. Liu, G. Rao, C. Zhao and Y. Li, *Journal of CO2 Utilization*, 2016, **15**, 15–23.
29 G. Mendoza-Damián, F. Tzompantzi, A. Mantilla, A. Barrera and L. Lartundo-Rojas, *Journal of Hazardous Materials*, 2013, **263**, 67–72.
30 S.-M. Xu, H. Yan and M. Wei, *J. Phys. Chem. C*, 2017, **121**, 2683–2695.

31 B. Mavis and M. Akinc, *Chem. Mater.*, 2006, **18**, 5317–5325.
32 C. Chen, M. Yang, Q. Wang, J.-C. Buffet and D. O'Hare, *J. Mater. Chem. A*, 2014, **2**, 15102–15110.
33 C. Chen, A. Wangriya, J.-C. Buffet and D. O'Hare, *Dalton Trans.*, 2015, **44**, 16392–16398.
34 L. Hickey, J. T. Kloprogge and R. L. Frost, *J. Mater. Sci.*, 2000, **35**, 4347–4355.
35 U. Sharma and P. Jeevanandam, *J. Nanosci. Nanotechnol.*, 2018, **18**, 264–278.
36 Y. Zhao, X. Jia, G. I. N. Waterhouse, L.-Z. Wu, C.-H. Tung, D. O'Hare and T. Zhang, *Adv. Energy Mater.*, 2015, **6**, 1501974.
37 S. Higashimoto, N. Kitao, N. Yoshida, T. Sakura, M. Azuma, H. Ohue and Y. Sakata, *J. Catal.*, 2009, **266**, 279–285.
38 C.-J. Li, G.-R. Xu, B. Zhang and J. R. Gong, *Appl. Catal., B*, 2012, **115-116**, 201–208.
39 J. Zou, Z. Wang, W. Guo, B. Guo, Y. Yu and L. Wu, *Appl. Catal., B*, 2020, **260**, 118185.
40 J. Zhu, N. Trefiak, T. K. Woo and Y. Huang, *J. Phys. Chem. C*, 2009, **113**, 10029–10037.
41 C. Gervais, M. E. Smith, A. Pottier, J. P. Jolivet and F. Babonneau, *Chem. Mater.*, 2001, **13**, 462–467.
42 A. Labouriau and W. L. Earl, *Chemical Physics Letters*, 1997, **270**, 278–284.
43 J. Xu, B. E. G. Lucier, Z. Lin, A. Sutrisno, V. V. Terskikh and Y. Huang, *J. Phys. Chem. C*, 2014, **118**, 27353–27365.
44 P. J. Sideris, F. Blanc, Z. Gan and C. P. Grey, *Chem. Mater.*, 2012, **24**, 2449–2461.
45 S. Cadars, G. Layrac, C. Gérardin, M. Deschamps, J. R. Yates, D. Tichit and D. Massiot, *Chem. Mater.*, 2011, **23**, 2821–2831.
46 S. S. C. Pushparaj, C. Forano, V. Prévot, A. S. Lipton, G. J. Rees, J. V. Hanna and U. G. Nielsen, *J. Phys. Chem. C*, 2015, **119**, 27695–27707.
47 A. Vyalikh, D. Massiot and U. Scheler, *Solid State Nucl. Magn. Reson.*, 2009, **36**, 19–23.
48 N. D. Jensen, C. Forano, S. S. C. Pushparaj, Y. Nishiyama, B. Bekele and U. G. Nielsen, *Phys. Chem. Chem. Phys.*, 2018, **20**, 25335–25342.
49 A. Béres, I. Pálinkó, J. C. Bertrand, J. B. Nagy and I. Kiricsi, *Journal of Molecular Structure*, 1997, **410-411**, 13–16.

Chapter 3 Photo-oxidation of diphenylmethanol

3.1 Introduction

In order to probe the photocatalytic activity of the prepared NiTi- and MgAlTi-LDHs in the photo-oxidation of simple organic molecules, diphenylmethanol (benzhydrol) was chosen as the primary reactant, for a number of reasons outlined below. The reaction is shown in Figure 3.1.

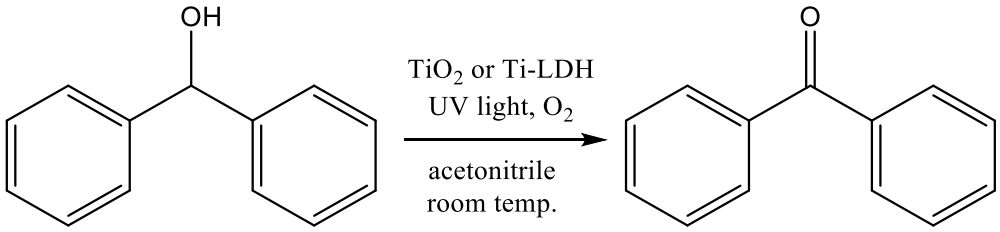


Figure 3.1 Reaction scheme for the photo-oxidation of diphenylmethanol.

Firstly, diphenylmethanol is a suitable simple model compound for secondary alcohols and the absence of any other functional groups minimises the chances of side reactions and therefore side product formation, which could otherwise complicate the analysis of the product mixture. Secondly, as a secondary alcohol, diphenylmethanol cannot over-oxidise to a carboxylic acid unlike primary alcohols (unless C-C bond cleavage occurs), which means that the expected photo-oxidation reaction involves only one reactant and one main product, with minimal anticipated side product formation.

Thirdly, diphenylmethanol is an important intermediate in the synthesis of a large number of organic compounds, including pharmaceuticals, perfumes and agrochemicals.[1] Benzophenones, the products of diphenylmethanol oxidation, are also useful synthons for fullerenes, bioactive oxygen heterocycles, dyes and medicines.[2] Finally, the conversion of diphenylmethanol to benzophenone can be easily followed by ^{1}H NMR, with the

resonances of interest being the 5.9 ppm peak of diphenylmethanol (corresponding to the Ph_2-C<u>H</u>OH proton) and the 7.8 ppm peak of benzophenone (corresponding to the four *ortho* protons on the aromatic rings).

The non-photocatalytic diphenylmethanol oxidation has been previously reported with a wide variety of oxidising agents, such as 2,2'-bipyridyl-Cu(II) permanganate, pyridinium chlorochromate, *N*-bromosuccinimide and tributylammonium chlorochromate.[2]

The photo-oxidation of diphenylmethanol to benzophenone using TiO_2 as the photocatalyst has been previously reported in literature with little side product formation. Vijaikumar *et al.* observed significant conversion to benzophenone under irradiation with a medium pressure mercury lamp with $\lambda > 350$ nm.[3] Similarly, Mohamed *et al.* reported a 95% conversion of diphenylmethanol to benzophenone with anatase TiO_2 after 6 hours of UV irradiation in an acetonitrile solution saturated by bubbling oxygen through it, with minor side product formation of benzoic acid.[4] Doped TiO_2 has also been used – for example, Shali *et al.* used lanthanum-modified TiO_2 to photo-oxidise diphenylmethanol with low-energy UV radiation ($\lambda > 350$ nm) in acetonitrile.[5] They observed a conversion of up to 96% (with 100% benzophenone selectivity) after 80 minutes of irradiation.

The photocatalytic activity of LDHs in both simple molecule photo-oxidation and beyond has been reported previously, as discussed in more detail in Chapter 1. Broadly, the research into LDHs as semiconductor photocatalysts has focused on three main areas: photocatalytic degradation of organic pollutants,[6-9] photocatalytic water splitting,[10-13] and photo-reduction of CO_2 into hydrocarbon feedstocks and fuels.[14-17] Focusing on Ti-LDHs, NiTi-LDHs have shown high activity for the photocatalytic oxygen evolution from water,[13,18,19] whereas MgAlTi-LDHs have been successfully used in the photo-degradation of methylene blue and 2,4-dichlorophenol,[20,21] and in CO_2 photo-reduction.[22]

In comparison to these three areas of LDH photocatalysis, only a limited amount of research has been done into the activity of LDH photocatalysts in the photo-oxidation of organic molecules, where the oxidation is stopped at an intermediate stage as opposed to proceeding to complete degradation products. Yang *et al.* used ZnTi-LDHs in the successful photo-oxidation of benzylamine and its derivatives, with high conversions and selectivities of up to 100 and 99%, respectively.[23] Guo *et al.* used NiAl-LDHs, doped with gold nanoparticles, to photo-oxidise benzyl alcohol with high conversion and selectivity,[24] whereas Zou *et al.* used pure ZnTi-LDHs to carry out the same photocatalytic reaction with a conversion of up to 52% and a high selectivity.[25]

However, to the best of the author's knowledge, LDHs have not been previously used in the diphenylmethanol photo-oxidation reaction. Nonetheless, previously reported studies into the photocatalytic activity of LDHs outlined above give a good indication that Ti-LDHs, and more specifically NiTi- and MgAlTi-LDHs, should be active also in the diphenylmethanol photo-oxidation reaction.

3.2 Photo-reactor setup and reaction conditions

All photocatalytic reactions were carried out in an immersion well photo-reactor with a 125 W medium pressure mercury lamp (Figure 3.2). The lamp emits radiation primarily in the UV region of the electromagnetic spectrum, with the most intense emission peak at 365 nm. In the photo-reactor, the lamp is positioned in the centre of the reaction setup, thus ensuring maximum irradiation of the reaction mixture. A jacketed immersion well allows the circulation of cooling water (set at 15 °C), which keeps the reaction mixture at a constant temperature and prevents the UV lamp from over-heating. Keeping the reaction mixture temperature low and constant is crucial in preventing the occurrence of any thermally induced side reactions.

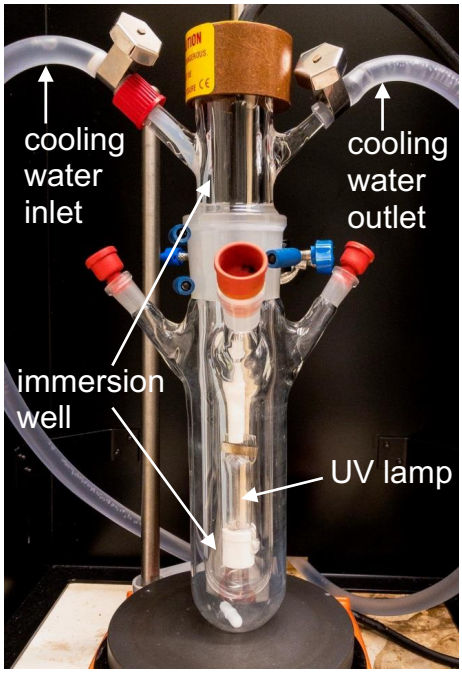


Figure 3.2 Photo-reactor setup: immersion well photo-reactor with 125 W medium pressure UV lamp.

Because the reaction mixture is separated from the lamp by the immersion well in this photo-reactor setup, the material that the immersion well is made of is an important consideration, as it determines the range of wavelengths emitted by the UV lamp that reach the reaction. Two different immersion wells were used in the photocatalytic studies:

a quartz immersion well that transmits the whole range of wavelengths generated, and a borosilicate immersion well that eliminates the wavelengths below 300 nm.

In all of the below photocatalytic reactions, acetonitrile was used as the solvent of choice, as it cannot be photo-oxidised in the presence of a catalyst such as TiO_2. In comparison, using methanol or ethanol instead can result in preferential solvent oxidation.[3,5] Pure oxygen gas was bubbled through the reaction mixture at a gas flow rate of 70 cm^3min^{-1} and the reaction mixture was stirred at 1,000 rpm, so as to prevent sedimentation and keep the solid catalysts evenly dispersed for the whole duration of the irradiation. Before every reaction, the reaction mixture was sonicated for 15 minutes to achieve optimal catalyst dispersion. During the irradiation, the reaction flask of the immersion well reactor was wrapped in aluminium foil to reflect the maximum amount of UV light back into the reaction. The reactor was further enclosed in a black metal box.

Existing studies often report pre-treating the photocatalysts before their introduction into the reaction mixture. For example, Mohamed *et al.* dried TiO_2 at 120 ºC for 12 hours before using it in the photo-oxidation of selected aryl alcohols.[4] In this work, however, all catalysts are used without pre-treatment and are likely to contain trace amounts of adsorbed or absorbed water. Nonetheless, all Ti-LDHs were dried in a vacuum oven for a minimum of 18 hours at room temperature after synthesis and then kept in airtight containers, which minimises contact with air and the possibility of coming into contact with ambient moisture.

With the exception of the kinetic studies and recycling experiments, all photocatalytic reactions were carried out with an irradiation time of 1 hour. In the kinetic studies, the irradiation period was varied between 15 minutes and 6 hours. In the recycling experiments, the irradiation time was kept constant at 2 hours. The acetonitrile solvent

volume in all reactions was 100 mL. The catalyst loading was kept constant at 5 mg in all initial photocatalytic reactions, with the exception of the catalyst loading studies, where the amount of catalyst was varied between 5 and 50 mg. Subsequently, the optimal catalyst loadings were used. Similarly, the reactant (diphenylmethanol) concentration was kept constant at of 100 mM, with the exception of the reactant concentration studies, where it was varied between 5 and 100 mM, after which the optimised concentration was used.

For completeness, the reactant concentrations and the catalyst loadings used (both in terms of weight, mg, and in terms of concentration, wt%) are listed in Table B.1 in Appendix B.

In all reactions, the catalyst was removed from the product mixture using a syringe filter. The acetonitrile was then removed from the product mixture using rotary evaporation.

More detailed information regarding all photo-oxidation reaction conditions is outlined in Chapter 7.

3.3 Characterisation techniques and product mixture analysis

The output of the UV lamp was determined and monitored over time (to ensure consistency in irradiation conditions between reactions) using actinometry with potassium ferrioxolate as the actinometer of choice.[26] The presence of the anticipated products, the conversion and the selectivity of the photo-reactions were quantified by ^{1}H NMR spectroscopy in $CDCl_3$.

In all of the reactions outlined below, the only compounds present in the product mixture after irradiation, as detectable by ^{1}H NMR spectroscopy, were diphenylmethanol (the reactant), benzophenone (the oxidation product) and benzaldehyde (the side product formed by C-C bond cleavage). However, benzaldehyde was present only in negligibly small amounts (<1%) and is therefore not included in any of the conversion calculations. Similarly, it is assumed that any other potential side products form in negligible amounts (as they are not detectable by ^{1}H NMR) and they are equally omitted from the conversion calculations.

Consequently, the conversion of diphenylmethanol to benzophenone was determined based on the integration of the 5.9 ppm ^{1}H NMR resonance of diphenylmethanol (corresponding to the Ph_2-C<u>H</u>OH proton) and the 7.8 ppm resonance of benzophenone (corresponding to the four *ortho* protons on the aromatic rings). A representative ^{1}H NMR spectrum of the diphenylmethanol photo-oxidation product mixture is shown in Figure 3.3.

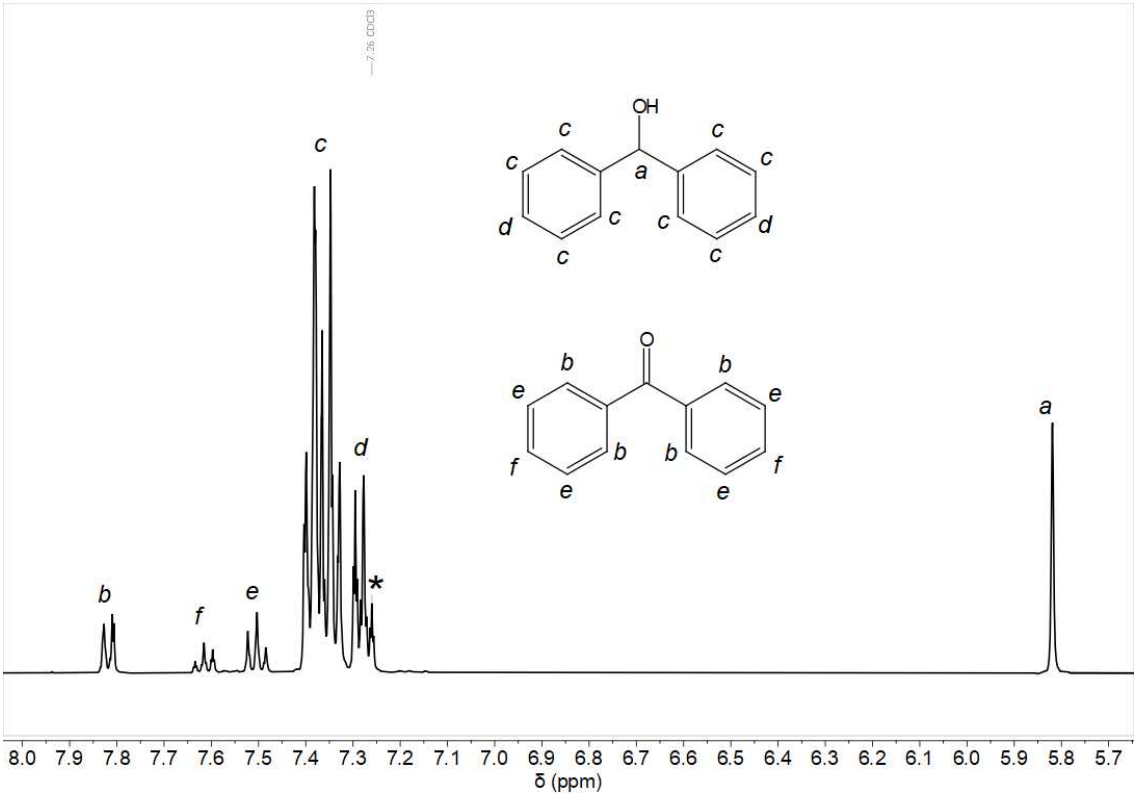


Figure 3.3 Representative ^{1}H NMR spectrum of the diphenylmethanol photo-oxidation product mixture after 1 hour of UV irradiation with 25 mg of urea hydrothermal $Mg_{12}AlTi_3$-LDH photocatalyst, with resonances assigned to diphenylmethanol and benzophenone. * denotes the residual protio-solvent resonance in the deuterated chloroform, $CDCl_3$.

In all of the below, the conversion (expressed as a percentage, %) of diphenylmethanol to benzophenone refers to the proportion of the total diphenylmethanol initially present before reaction (the total amount of reactant) that was photo-oxidised to benzophenone during the reaction.

Specifically:

$$Conversion\ (\%) = \frac{n(benzophenone)_{final}}{n(diphenylmethanol)_{final} + n(benzophenone)_{final}} \times 100\%$$

where $n(A)_{final}$ refers to the amount of compound A in the product mixture, as inferred from the integration of ^{1}H NMR resonances outlined above.

The transparency of the relevant catalyst dispersions or reaction mixtures was analysed using UV-visible spectroscopy, with focus on the transmission of the dispersion at 365 nm, which is the main emission wavelength of the UV lamp used in this work.

More detailed analysis method descriptions and parameters can be found in Chapter 7.

3.4 The effect of short-wavelength UV radiation

In the control reaction for the photo-oxidation of diphenylmethanol in the absence of a catalyst using the quartz immersion well in the photo-reactor setup, significant conversion to the oxidised product benzophenone was observed (41% after 1 hour of UV irradiation). Contrary to literature reports,[4,5,27] this conversion decreased on the addition of a catalyst into the photocatalytic system. For example, on adding 25 mg (1.4 wt%) TiO_2 or NiTi-LDHs into the reaction mixture, the conversion of diphenylmethanol to benzophenone after 1 hour decreased from 41 to 34 or 38%, respectively. Furthermore, a correlation between the cloudiness/opaqueness of the reaction mixture (due to the dispersion of the catalyst) and the decrease in conversion was observed. Thus, the TiO_2 dispersion with a lower transparency resulted in a greater reduction in conversion as compared to NiTi-LDHs that give a dispersion with a higher transparency.

While the high photocatalytic activity of TiO_2 has been widely investigated and reported on, it acts effectively as an inhibitor in this set of photocatalytic reactions. However, when the quartz immersion well is replaced by the borosilicate immersion well, the conversion in the absence of a catalyst drastically decreases to only 6% after 1 hour of irradiation. The addition of TiO_2 or NiTi-LDHs is then accompanied by the expected increase in conversion to oxidised products (14 or 11%, respectively). The difference between the two setups is solely the absence of the short wavelength UV radiation ($\lambda < 300$ nm) interacting with the reaction mixture when the borosilicate immersion well is used.

It is therefore proposed that when the quartz immersion well is used, the short-wavelength (high-energy) UV radiation is sufficient to cause the oxidation of the organic reactant even in the absence of a catalyst, either through the activation of molecular oxygen gas or through the activation of the reactant molecules themselves. On the addition of a

catalyst, the reduced transparency of the resulting dispersion limits the effects of the short-wavelength (high-energy) photons. While the solid catalyst is likely to act in its photocatalytic capacity even in this case, the results indicate that the kinetics of the catalytic reaction are slower than the kinetics of the reaction involving the short-wavelength photons alone.

To the best of the author's knowledge, such findings have not been reported previously, with most literature on the photo-oxidation of organic molecules observing little to no reaction in the absence of a catalyst under all reported reaction conditions.[5,23,28,29] Similarly, all reports observed an increase in conversion to the oxidised product when a photocatalyst was introduced into the system. However, all of these studies used either visible light irradiation or irradiation with $\lambda > 300$ nm.

In light of these results, the borosilicate immersion well was used in all subsequent reactions, as it allows effective screening of the different Ti-LDH photocatalysts and their photocatalytic performance. Nonetheless, some photo-oxidation still takes place without a catalyst even with the borosilicate immersion well, indicating that enough high-energy photons remain to oxidise a small proportion of the reactant molecules.

3.5 Control reactions and TiO_2 baseline reactions

While the photo-oxidation of diphenylmethanol can take place in the absence of a catalyst (6% conversion to benzophenone after 1 hour of irradiation with O_2 gas flow, as discussed above), no reaction was observed in the absence of light/irradiation and when the reaction was carried out in an inert N_2 atmosphere, without O_2 bubbling through the reaction mixture. It is therefore evident that both irradiation and the presence of oxygen are paramount for the photo-oxidation of diphenylmethanol to take place. These observations are consistent with previous literature findings, which confirmed the importance of light and oxygen or air in achieving the photo-oxidation of a variety of simple organic molecules.[5,23,29]

To establish a baseline for subsequent photo-oxidations with Ti-LDHs and compare the performance of the photocatalytic system in this work (including the photo-reactor setup and reaction conditions such as reaction volume, irradiation intensity and time, etc.) with previous literature reports,[3,4] the anatase form of TiO_2 was studied in the photo-oxidation of diphenylmethanol. The anatase polymorphic form was chosen because it exhibits a higher photocatalytic activity than rutile and brookite.[30]

Firstly, the effect of the TiO_2 catalyst loading on the conversion of diphenylmethanol to benzophenone was studied, keeping all other variables constant: the irradiation period at 1 hour, the O_2 flow rate at 70 cm^3min^{-1} and the reactant concentration at 100 mM (Figure 3.4). The conversion increases from 6% in the absence of the catalyst to 14% at a loading of 5 mg, and then shows a marked decrease when the catalyst loading is further increased to 10, 25 and 50 mg. This decrease in conversion with increasing catalyst loading has been observed before for benzyl alcohol photo-oxidation using TiO_2,[28] and can be attributed to the decreased transparency of the reaction mixture as the amount of

TiO_2 increases. The transparency of the reaction mixture was quantified with UV-visible transmittance measurements at 365 nm, which is the most prominent emission of the UV lamp used in the photo-reactor setup. The results are shown in Figure 3.4.

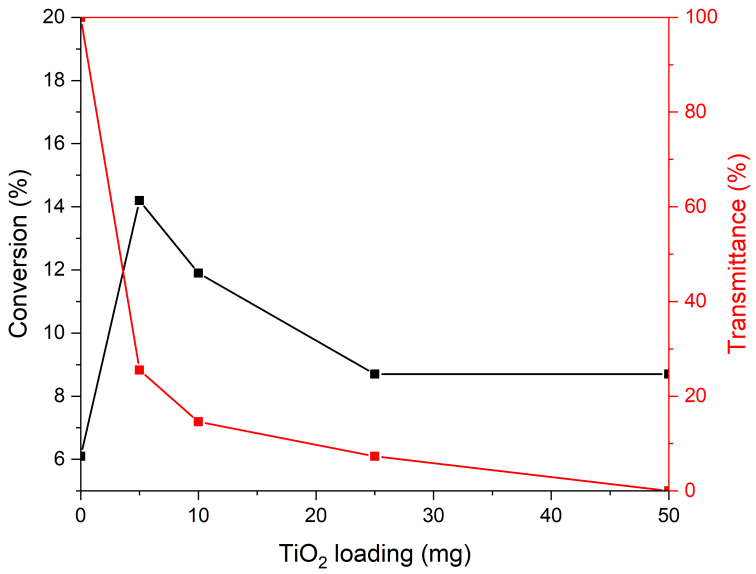


Figure 3.4 The variation of the photocatalytic conversion of diphenylmethanol to benzophenone (black) and the reaction mixture transparency quantified as transmittance at 365 nm (red) with TiO_2 catalyst loading.

At higher catalyst loadings, TiO_2 forms a very cloudy, opaque, white dispersion in acetonitrile, which prevents the incident photons from penetrating into the reaction mixture and interacting with catalyst particles due to scattering effects.[31] One previous study of diphenylmethanol photo-oxidation with TiO_2 does report an increased conversion with increased catalyst loading, with the maximum conversion obtained with the highest loading of 10 mg per 10 mL of solvent.[3] This amount of catalyst is equivalent to 100 mg per 100 mL of solvent, as scaled up to the reaction volumes used in this work. It is therefore unclear why Vijaikumar *et al.* have observed such a profoundly different trend, as such a concentrated catalyst dispersion should have a negligible transparency and should therefore exhibit a very low conversion to oxidised products (as evident from Figure 3.4).

Secondly, the effect of reactant concentration on the photo-oxidation conversion was studied, keeping all other reaction parameters constant as above, using the optimal TiO_2 loading of 5 mg. The results are summarised in Figure 3.5. The variation of conversion with reactant concentration is unusual in that it decreases from 5 to 25 mM, followed by an increase for concentrations of 50 and 100 mM, the latter giving the highest conversion of 14%.

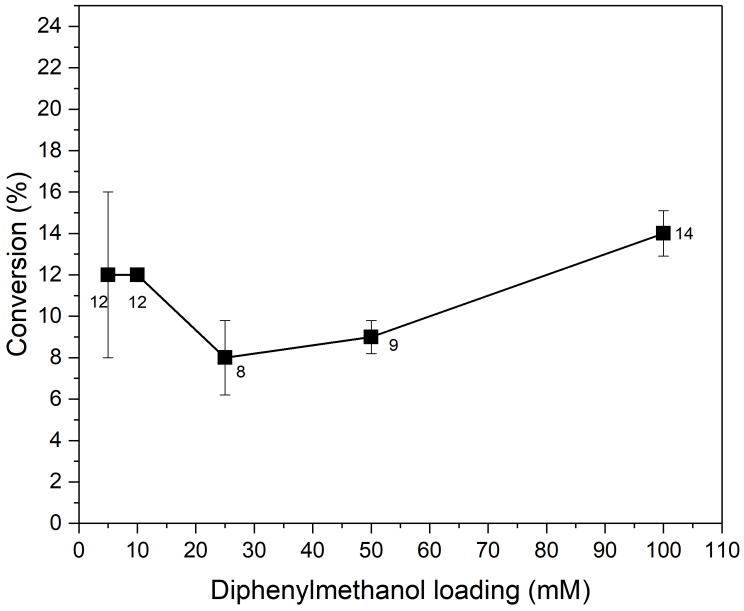


Figure 3.5 The variation of the photocatalytic conversion of diphenylmethanol to benzophenone with reactant concentration for TiO_2 (anatase). (Error bars denote standard deviation. For each data point, three independent experiments were performed.)

The typical effect of varying the amount of reactant in a catalytic reaction involves an initial increase in the reaction rate as more reactant molecules are adsorbed onto the available active sites and thus converted to the oxidised product, followed by a plateau once active site saturation is reached. Vijaikumar *et al.* have found, for example, that the amount of benzophenone formed varies linearly with the initial concentration of diphenylmethanol up to a reactant concentration of 1.6 mM (a value that is below the lowest reactant concentration considered in this work).[3] In terms of conversion, this would correspond to an approximately constant conversion up to where the reactant

concentration matches the amount of available active sites, followed by a decrease in conversion as the reactant concentration is increased further. The results summarised in Figure 3.5 show a large deviation from this typical trend and, to the best of the author's knowledge, have not been observed previously in any similar photocatalytic oxidation system using TiO_2 or other photocatalysts.

The two separate trends (an initial decrease in conversion, followed by an increase with increasing reactant concentration) indicate the presence of two different photo-oxidation mechanisms, with different rate determining steps, operating above and below the 25 mM reactant concentration.[32]

Finally, the kinetics of the diphenylmethanol photo-oxidation in the presence of TiO_2 were studied using the best catalyst loading and reactant concentration of 5 mg and 100 mM, respectively. The irradiation time was varied between 15 minutes and 6 hours, as shown in Figure 3.6.

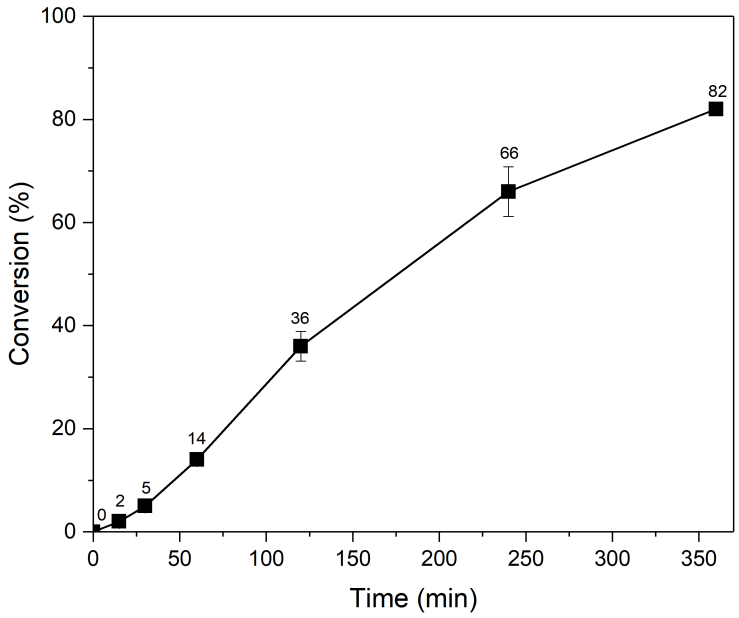


Figure 3.6 The time variation of the photocatalytic conversion of diphenylmethanol to benzophenone for TiO_2 (anatase) under optimised conditions of catalyst loading and reactant concentration. (Error bars denote standard deviation. For each data point, three independent experiments were performed.)

The yield of benzophenone and therefore the conversion increases with time in an approximately linear fashion for up to 2 hours, after which a deviation from linearity is observed, with the conversion lower than expected from a linear trend. This deviation is the likely result of two factors: firstly, the progressively smaller proportion of diphenylmethanol molecules in the reaction mixture and therefore a progressively smaller likelihood of their adsorption to the catalyst particles and their active sites, and secondly, possible catalyst poisoning or degradation. A similar time variation of the conversion was observed previously by Vijaikumar *et al.*.[3]

To the best of the author's knowledge, only two reports of diphenylmethanol photo-oxidation in the presence of pure TiO_2 exist,[3,4] as discussed in Chapter 1 and in the introduction to this Chapter. Comparing the conversion values in Figure 3.6 with those found in literature is difficult due to the different photo-reactor setups, reaction volumes, reactant concentrations, catalyst loadings, the nature of the irradiation (visible or UV light, or a combination of the two) and vastly different lamp intensities. For example, Vijaikumar *et al.* observed a 23% conversion after 2 hours of irradiation with a 250 W lamp with emission above 350 nm (i.e. primarily in the low energy UV and visible region of the electromagnetic spectrum), using 10 mg TiO_2 in 10 mL of a 1 mM diphenylmethanol solution.[3] In comparison, Mohamed *et al.* reported a 95% conversion after 6 hours of irradiation with a 450W UV lamp, using 100 mg TiO_2 in 400 mL of a 10 mM diphenylmethanol solution.[4]

While a direct comparison with literature is therefore impossible, it is nonetheless evident that a conversion of about 82% after 6 hours of irradiation with a lower-intensity UV lamp (125 W) is relatively high, and it can be concluded that the photocatalytic setup and reaction conditions in this work are comparable to those previously reported in literature.

3.6 The effect of Ti-LDH composition and synthetic method

The effects of the metal composition (specifically, the Ni:Ti ratio of NiTi-LDHs and the Al:Ti ratio of MgAlTi-LDHs) and synthetic method on Ti-LDH properties have been discussed in Chapter 2. The prepared Ti-LDHs span a wide range of properties in terms of different Ti content, Ti dispersion, morphology and degree of crystallinity, all of which can have a large influence on the photocatalytic activity.[18,23]

To study how the metal composition and synthetic method affect the photocatalytic conversion of diphenylmethanol to benzophenone, and based on the observations from TiO_2 experiments outlined above, the catalyst loading was fixed at 5 mg, the reactant concentration was kept constant at 100 mM and the irradiation period was 1 hour. As shown in Figure 3.7 for Ti-LDHs prepared using the urea reflux method, the conversion decreases with decreasing Ti content (i.e. increasing Ni:Ti and Al:Ti ratios), indicating that the Ti centres are crucial to active site formation and photocatalytic activity. The same trend was observed also for MgAlTi-LDHs prepared by the urea hydrothermal method (Figure 3.8).

Previously reported studies of how the photocatalytic activity changes with varying Ti content of Ti-LDHs often show opposing trends. For example, Yang *et al.* have shown that Zn_6Ti-LDHs have a higher activity in the photocatalytic oxidation of primary aromatic amines than Zn_4Ti- and Zn_5Ti-LDHs.[23] Similarly, Zhao *et al.* have observed that Ni_4Ti-LDHs display the highest photocatalytic activity in the water-splitting reaction, as compared to Ni_2Ti- and Ni_3Ti-LDHs.[19] However, they also report that Ni_4Ti-LDHs are more active than Ni_5Ti-LDHs, which was attributed to the higher crystallinity of the former product. Overall, they concluded that a lower amount of Ti in conjunction with

high crystallinity results in a superior dispersion of TiO_6 units and therefore a higher photocatalytic activity.

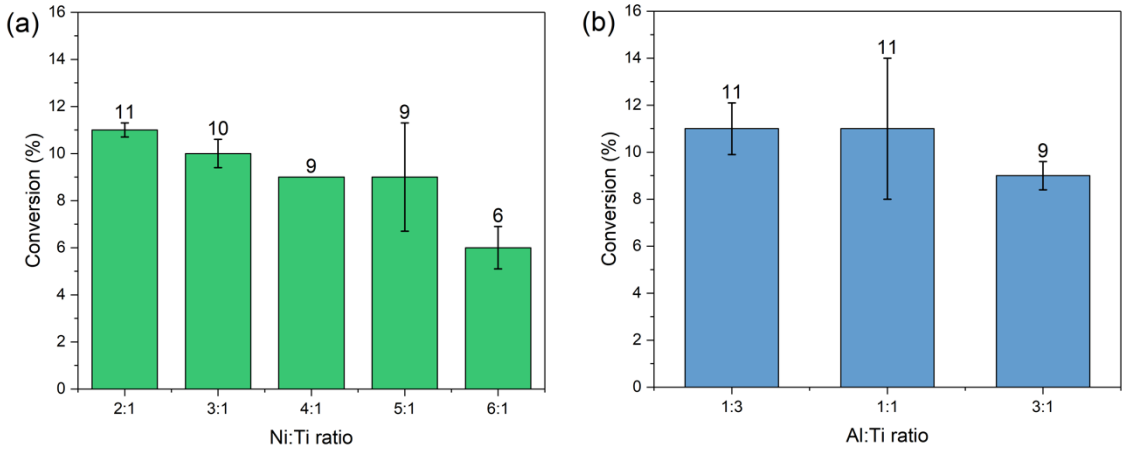


Figure 3.7 Photocatalytic conversion of diphenylmethanol to benzophenone for a series of Ti-LDHs prepared by the aqueous urea reflux method: (a) NiTi-LDHs prepared with Ni:Ti ratios from 2:1 to 6:1 and (b) MgAlTi-LDHs prepared with Al:Ti ratios varying between 1:3, 1:1 and 3:1. (Error bars denote standard deviation. For each data point, three independent experiments were performed.)

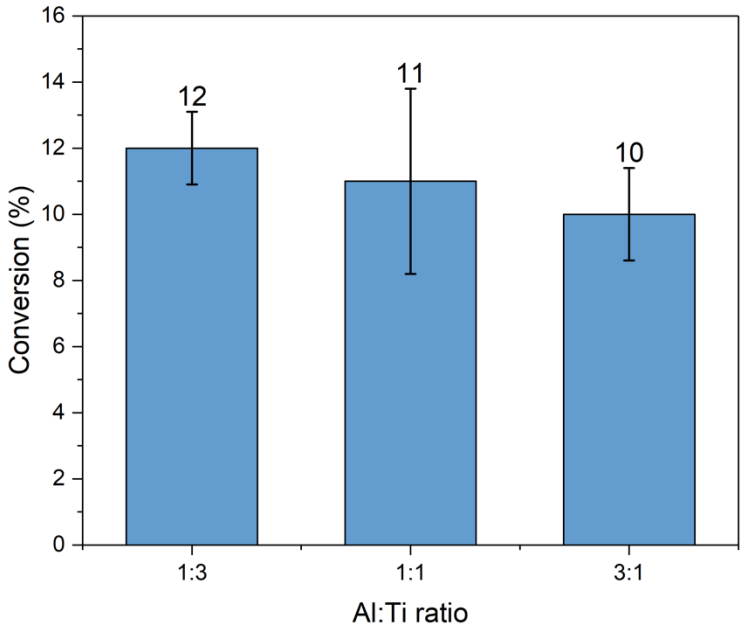


Figure 3.8 Photocatalytic conversion of diphenylmethanol to benzophenone for a series of MgAlTi-LDHs, prepared by the aqueous urea hydrothermal method with different Al:Ti ratios varying between 1:3, 1:1 and 3:1. (Error bars denote standard deviation. For each data point, three independent experiments were performed.)

On the other hand, Zou *et al.* have observed that the photocatalytic activity in the photo-oxidation of benzyl alcohol decreases with decreasing Ti content of ZnTi-LDHs, with the

conversion decreasing from 61 to 28% with Zn_2Ti- and Zn_4Ti-LDH, respectively.[25] They attributed this to a decreasing amount of surface –OH groups with decreasing Ti content. With Zn_2Ti-LDH, the largest number of surface –OH groups is exposed, and these have been proposed to correlate to a larger amount of surface oxygen vacancies, which act as active sites for enhanced O_2 adsorption and activation in the benzyl alcohol photo-oxidation reaction.

More detailed analysis, possibly in conjunction with computational modelling, would be required to determine whether the trends observed for the NiTi- and MgAlTi-LDHs in this work are due to a similar trend in the number of surface –OH groups. Whereas Zou *et al.* observed relatively clear differences in FTIR O-H stretching band intensities for ZnTi-LDHs with different Zn:Ti ratios,[25] no such clear trends were observed for the prepared NiTi- and MgAlTi-LDHs (Figures A.4 and A.5 in Appendix A). Additionally, the facts that the O-H FTIR stretching bands in the 3,100 – 3,500 cm^{-1} region correlate not just to surface –OH groups but also to the adsorbed and intercalated water molecules and that the intensity of bands in FTIR spectra depends on several different factors beyond just the number of the relevant functional groups further prevent any conclusive interpretation.

It is therefore unclear why the results summarised in Figures 3.7 and 3.8 show the opposite activity trend to those anticipated based on reports by Yang *et al.* and Zhao *et al.*.[19,23] In addition to surface –OH groups, it can be hypothesised that Ti centres (specifically, those located at the catalyst particle surface) are crucial in the formation of the active sites where diphenylmethanol photo-oxidation takes place. Further, it is possible that, especially in MgAlTi-LDHs that contain no other photo-active metals, the presence of Ti results in the formation of defect impurity states that alter the band gap

structure of the photocatalysts and thus improve the charge carrier separation and/or charge carrier transfer to the oxygen gas and diphenylmethanol molecules.

Based on these observations, only NiTi-LDHs with a Ni:Ti ratio of 2:1 and MgAlTi-LDHs with an Al:Ti ratio of 1:3 were used in subsequent photocatalytic studies. The effects of the synthetic method on the photocatalytic activity are summarised in Figure 3.9.

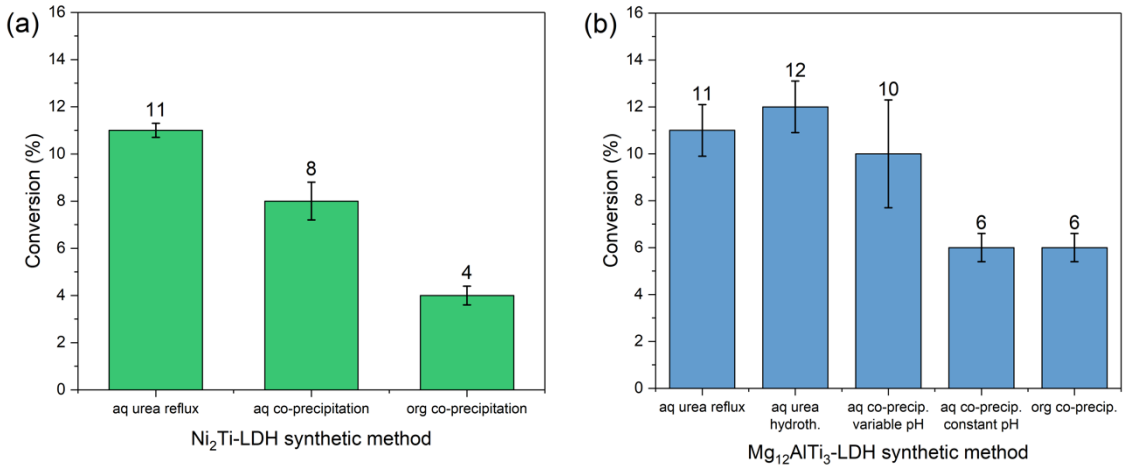


Figure 3.9 Photocatalytic conversion of diphenylmethanol to benzophenone for a series of (a) Ni_2Ti-LDHs prepared by three different synthetic methods and (b) $Mg_{12}AlTi_3$-LDHs prepared by five different synthetic methods. (Error bars denote standard deviation. For each data point, three independent experiments were performed.)

Contrary to literature findings, which predict a higher photocatalytic activity for Ti-LDHs with the highest dispersion of Ti centres,[19] the trend observed here is exactly the opposite. The synthetic methods that give the poorest Ti dispersion (the homogeneous precipitation methods: urea reflux and urea hydrothermal) give the highest photocatalytic activity. On the other hand, the organic co-precipitation method that gives Ti-LDHs with the highest degree of Ti dispersion, results in the lowest photo-oxidation conversion, which is comparable to or even lower than that obtained in the absence of a catalyst (6%).

Instead, the photocatalytic activity follows the crystallinity trend – with the urea hydrothermal method giving the most crystalline and the organic co-precipitation method

the least crystalline Ti-LDH products, as evident from the PXRD patters in Figure 2.1. This suggests that a high degree of crystallinity allows the formation of highly ordered or structured active sites where the photo-oxidation of reactant molecules takes place. In this respect (and contrary to the Ti content and Ti dispersion trends), the results are in good agreement with literature findings that highlight the correlation between good crystallinity and high photocatalytic activity.[19] Furthermore, a high degree of crystallinity is also likely to affect the electron-hole separation, thus suggesting that the homogeneous precipitation products have a reduced charge carrier recombination rate.

Different synthetic methods are also likely to produce LDHs with different amounts of surface defects, such as oxygen vacancies or Ti–O surface defects. The oxygen vacancies have been linked to a high photocatalytic activity in the selective photo-oxidation of benzyl alcohol over ZnTi-LDHs.[25] Specifically, the oxygen vacancies have been proposed to serve as centres for capturing photo-electrons from the photo-excited surface-coordinated reactants and also act as active sites for enhanced O_2 adsorption and activation. The Ti–O surface defects, on the other hand, can serve as trapping sites to improve electron-hole separation.[18]

Interestingly, there is no clear correlation between the photocatalytic activity (as shown in Figure 3.9) and the specific surface area of the Ti-LDH catalysts (Tables A.1 and A.2 in Appendix A) or their particle size. Based purely on the accessibility and number of active sites, photocatalysts with the highest specific surface area and/or smallest particle size might be expected to have the highest photocatalytic activity. Thus, the organic co-precipitation Ni_2Ti-LDH product (relatively small particle size, specific surface area of 274 m^2g^{-1}) should have the highest activity among the Ni_2Ti-LDHs. Instead, it shows the lowest conversion of only 4%, which is lower than the conversion in the absence of a photocatalyst. Similarly, the urea hydrothermal $Mg_{12}AlTi_3$-LDH (large particle size,

specific surface area of 76 m^2g^{-1}) should have one of the lowest photocatalytic activities. Instead, it gives the highest conversion of diphenylmethanol to benzophenone of 12%. Therefore, it can be concluded that the specific surface area and the particle sizes of the Ti-LDH products are not a significant contributing factor to their photocatalytic activity.

Therefore, the urea reflux Ni_2Ti-LDH and the urea hydrothermal $Mg_{12}AlTi_3$-LDH were chosen as the most active representative Ti-LDH photocatalysts and used in all subsequent photo-oxidation reactions. The comparison of the two representative Ti-LDH catalysts with TiO_2, which is the most widely used and studied photocatalyst and therefore a suitable benchmark, is shown in Figure 3.10. All three conversions refer to the product mixture after 1 hour of irradiation with a 5 mg catalyst loading and a 100 mM reactant concentration. It is evident that although TiO_2 gives the highest conversion (14%), the $Mg_{12}AlTi_3$-LDH catalyst gives a comparable result (12%). The performance of the Ni_2Ti-LDH catalyst is slightly worse (11%).

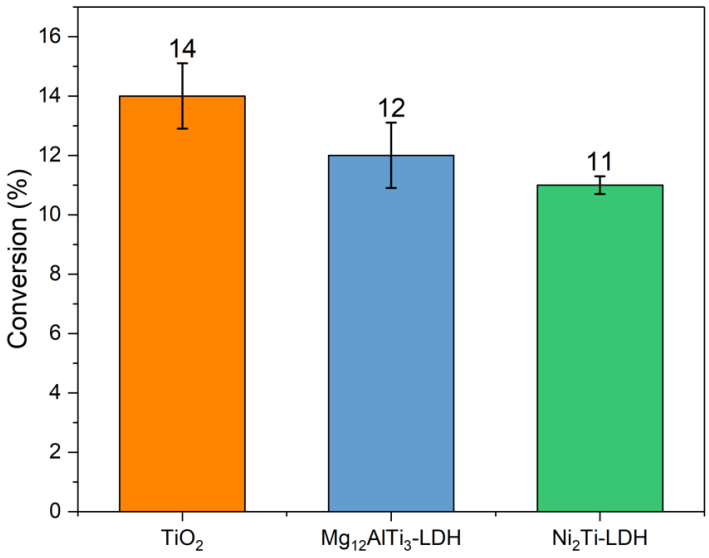


Figure 3.10 Photocatalytic conversion of diphenylmethanol to benzophenone with three different photocatalysts at 5 mg loading after 1 hour of UV irradiation. (Error bars denote standard deviation. For each data point, three independent experiments were performed.)

However, it was shown above that the Ti content plays a crucial role in determining the photocatalytic activity of Ti-LDHs (Figure 3.7), suggesting that Ti centres are highly important to active site formation. Therefore, it is more informative to calculate the activity per Ti centre for these three catalysts, so as to normalise their photocatalytic performance relative to their Ti content. The results are shown in Figure 3.11.

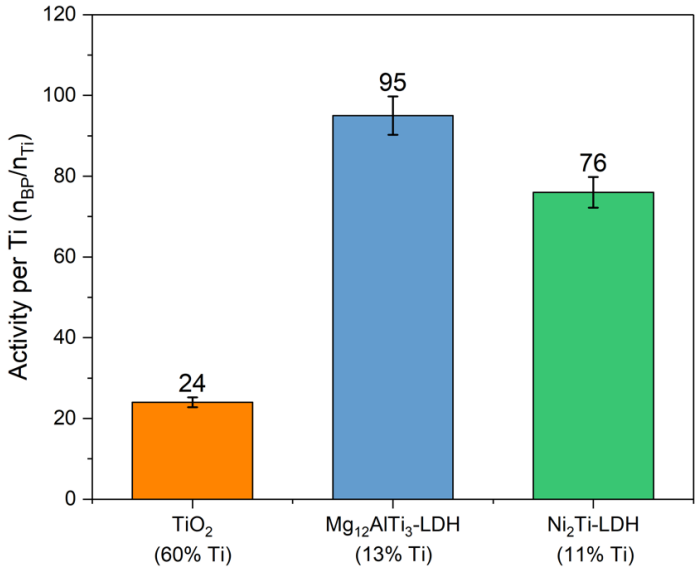


Figure 3.11 Activity per Ti centre for the photocatalytic conversion of diphenylmethanol to benzophenone with three different photocatalysts at 5 mg loading after 1 hour of UV irradiation. (Error bars denote standard deviation. For each data point, three independent experiments were performed.)

In terms of activity per Ti centre, the Ti-LDHs exhibit a significantly higher photocatalytic activity than TiO_2, with $Mg_{12}AlTi_3$-LDH being more active than Ni_2Ti-LDH. This indicates that the Ti-containing active sites of Ti-LDHs have a notably higher turnover frequency than the analogous active sites of TiO_2. This might be due to the different composition of and ordering within the active sites of the Ti-LDHs as compared to TiO_2.

However, for an in-depth understanding of the higher activity per Ti centre of the Ti-LDHs, more analysis is required, for example determining which metal cations other than Ti^{4+} (or Ti^{3+}) contribute to the active site formation and the crystallographic position of

the active sites (e.g. edge or corner sites, and the proportion of each in the different photocatalysts).

Additionally, the Ti content is also likely to affect the exact nature of the valence and conduction band positions (and any potential defect impurity states), as well as the efficiency of charge carrier separation and therefore the charge carrier recombination rates. All of these factors and their magnitude (in relation to the amount of Ti incorporated) will affect the photocatalytic activity of the catalysts and will therefore be reflected in the activity per Ti centre, as well as the difference between the NiTi- and MgAlTi-LDHs.

The photocatalytic activities of NiTi- and MgAlTi-LDHs, prepared by the aqueous co-precipitation method, have been compared previously in the water splitting reaction under a combination of UV and visible irradiation.[19] It was found that NiTi-LDHs display a notably higher activity than MgAlTi-LDHs, contrary to the observations of this work. However, this could be because NiTi-LDHs can absorb both UV and visible light, whereas MgAlTi-LDHs are restricted to only the UV part of the irradiation used in the reaction setup of Zhao *et al.*[19] As the photo-reactor setup in this work used only UV light, all the prepared NiTi- and MgAlTi-LDHs can absorb the whole range of the irradiation. The activity trends in this work therefore more accurately reflect the differences in active site performance and charge carrier recombination, rather than being influenced by different amounts of irradiation absorbed.

3.7 Variation of catalyst loading and reactant concentration

In Section 3.5, it was shown how varying the catalyst loading and reactant concentration affects the conversion of diphenylmethanol to benzophenone when TiO_2 is used as the photocatalyst. To study whether Ti-LDHs show similar trends, the catalyst loading vas varied between 5 and 50 mg, and the reactant concentration was varied between 5 and 100 mM, keeping the irradiation time constant at 1 hour. Only the most active representative Ti-LDH photocatalysts, urea reflux Ni_2Ti-LDH and urea hydrothermal $Mg_{12}AlTi_3$-LDH, were considered. Figure 3.12 shows how the conversion varies with catalyst loading for the two Ti-LDHs and compares the results with TiO_2 as the benchmark photocatalyst (the reactant concentration was kept constant at 100 mM). Whereas Ni_2Ti-LDH gives a similar result to TiO_2, with the conversion rapidly decreasing when the catalyst loading is increased above 5 mg, the $Mg_{12}AlTi_3$-LDH shows markedly different behaviour. For the $Mg_{12}AlTi_3$-LDH, the conversion increases when the catalyst loading is increased from 5 to 25 mg, where it reaches a maximum value of 19%, followed by a slight decrease when the loading is increased further.

This difference in behaviour between TiO_2 and $Mg_{12}AlTi_3$-LDH can be ascribed to the difference in how the reaction mixture transparency varies with catalyst loading, as seen in Figures 3.4 and 3.13. The overall conversion is a balance of two effects: the inherent photocatalytic activity of the catalyst (which is expected to contribute an approximately linear increase in activity with catalyst loading) and the transparency or opaqueness of the catalyst dispersion (which acts to decrease the conversion with increased loading).[28,31]

Whereas for TiO_2 the transparency of the reaction mixture decreases rapidly with catalyst loading (Figure 3.4), the decrease in transparency is slower for $Mg_{12}AlTi_3$-LDH (Figure 3.13). Therefore, the opaqueness of the reaction mixture does not outweigh the

inherent photocatalytic activity of the $Mg_{12}AlTi_3$-LDH catalyst until the catalyst loading is as high as 50 mg.

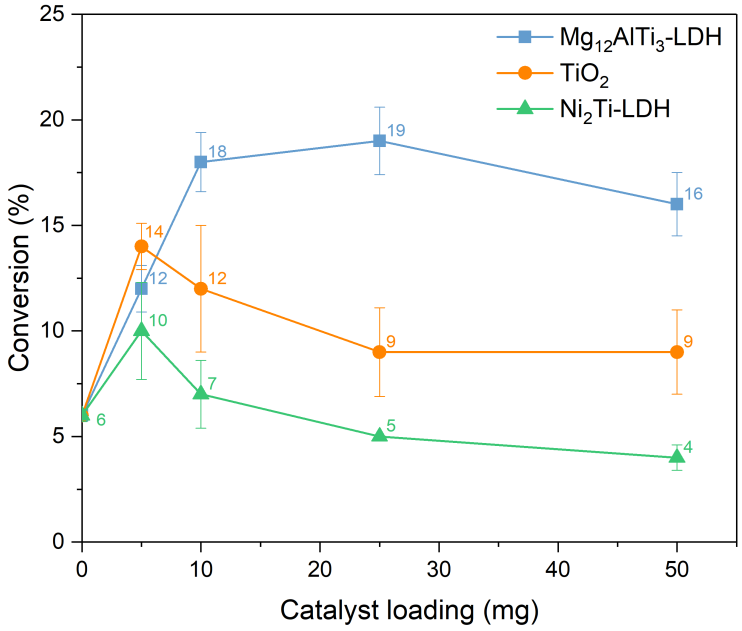


Figure 3.12 The variation of the photocatalytic conversion of diphenylmethanol to benzophenone with catalyst loading for TiO_2 (anatase), urea hydrothermal $Mg_{12}AlTi_3$-LDH and urea reflux Ni_2Ti-LDH. (Error bars denote standard deviation. For each data point, three independent experiments were performed.)

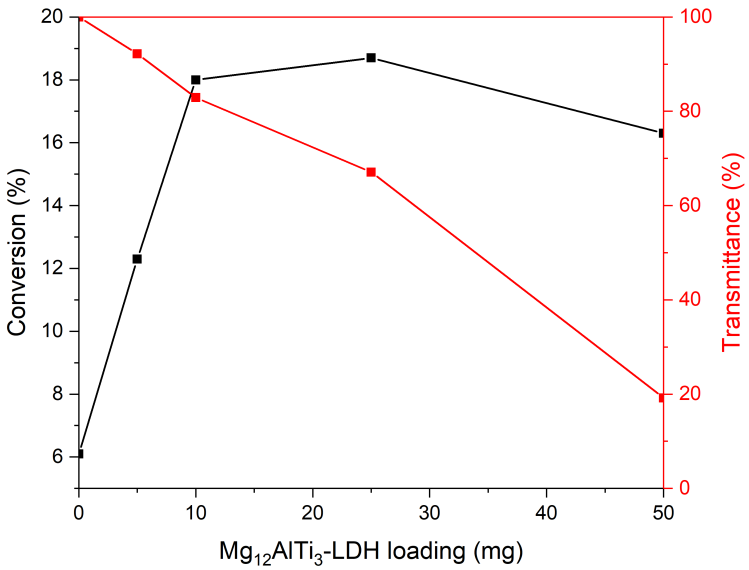


Figure 3.13 The variation of the photocatalytic conversion of diphenylmethanol to benzophenone (black) and the reaction mixture transparency, quantified as transmittance at 365 nm (red), with catalyst loading for urea hydrothermal $Mg_{12}AlTi_3$-LDH.

Therefore, the TiO_2 and Ni_2Ti-LDH systems reach peak activity at a catalyst loading of 5 mg, whereas the $Mg_{12}AlTi_3$-LDH system is at its most active with a catalyst loading of

25 mg. Because of this, and because the $Mg_{12}AlTi_3$-LDH has been shown to be more active than the Ni_2Ti-LDH catalyst (Figures 3.10), only TiO_2 and $Mg_{12}AlTi_3$-LDH at their optimal loadings have been considered in all subsequent reactions.

Keeping the $Mg_{12}AlTi_3$-LDH loading fixed at its optimal value of 25 mg and varying the reactant concentration shows a trend in conversion that is very similar to that of TiO_2, as seen in Figure 3.14. As with TiO_2, the origins of this unusual trend are not well understood, but they can be ascribed to the presence of two different photo-oxidation mechanisms (with different rate-determining steps) that operate below and above the 25 mM reactant concentration.[32] The highest conversion of 19% was observed for a reactant concentration of 100 mM, which was therefore used all subsequent reactions.

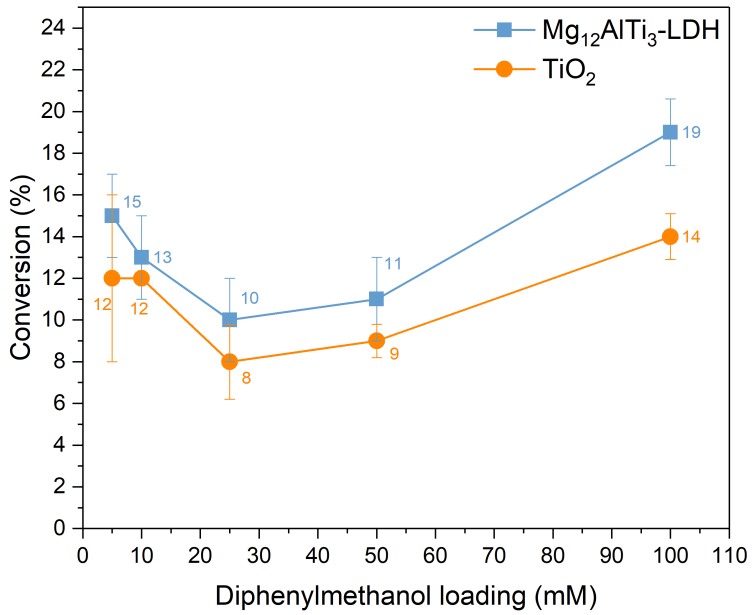


Figure 3.14 The variation of the photocatalytic conversion of diphenylmethanol to benzophenone with reactant concentration for TiO_2 (5 mg loading) and urea hydrothermal $Mg_{12}AlTi_3$-LDH (25 mg loading). (Error bars denote standard deviation. For each data point, three independent experiments were performed.)

3.8 Kinetic studies and catalyst re-cycling

When the UV irradiation time is varied between 15 minutes and 6 hours under optimised conditions for each catalyst, $Mg_{12}AlTi_3$-LDH shows a nearly identical conversion vs time profile as TiO_2, as shown in Figure 3.15. This implies a similar photocatalytic activity of the two catalyst systems under optimised conditions of catalyst loading and reactant concentration. The two systems differ only in the nature of the catalyst and its loading: 5 mg for TiO_2 (60% Ti content) and 25 mg for $Mg_{12}AlTi_3$-LDH (13% Ti content).

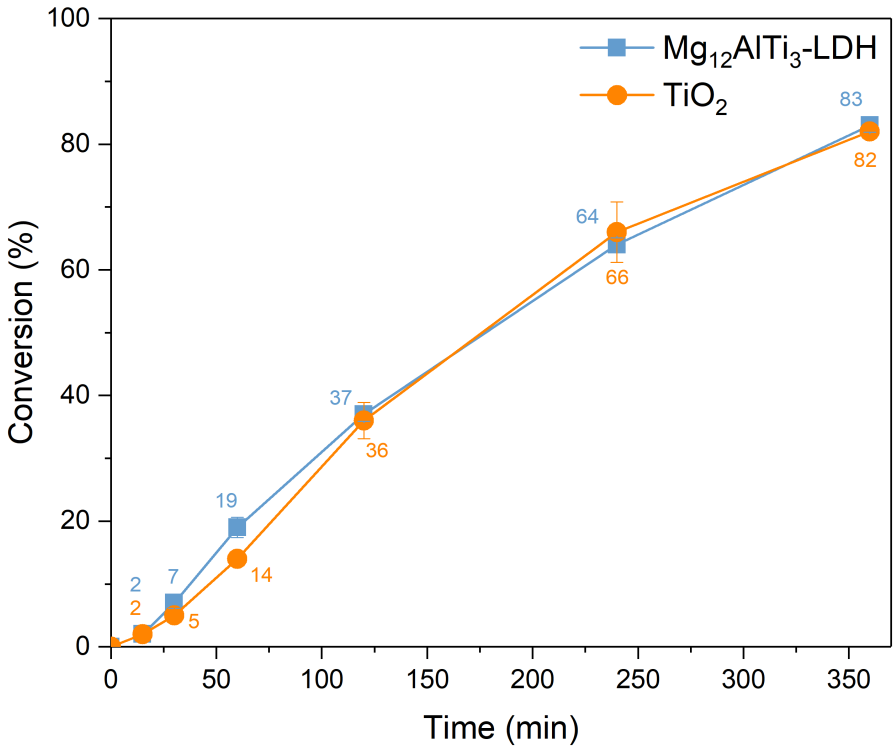


Figure 3.15 The time variation of the photocatalytic conversion of diphenylmethanol to benzophenone for TiO_2 (anatase) and urea hydrothermal $Mg_{12}AlTi_3$-LDH, under optimised conditions of catalyst loading and reactant concentration for both catalysts. (Error bars denote standard deviation. For each data point, three independent experiments were performed.)

Simplistically, the similar kinetic profiles of the two catalysts could be ascribed to the fact that 5 mg of TiO_2 and 25 mg of $Mg_{12}AlTi_3$-LDH contain similar amounts of titanium, as it has been shown above that the Ti content plays an important role in determining the photocatalytic activity. However, this does not take into account the different proportion

of Ti centres located on the surface and in a suitable environment so as to form an active site. Further, as discussed above, the transparency and opaqueness of the reaction mixture also affect the conversion, and the transparency of the catalyst dispersion differs notably between the two catalysts (the transmittance at 365 nm being about 67 and 26% for dispersions containing 25 mg $Mg_{12}AlTi_3$-LDH and 5 mg TiO_2, respectively).

Therefore, a detailed interpretation of the kinetic plot in Figure 3.15 would require further experimentation and analysis. Nonetheless, it can be concluded that under optimised conditions, the highly crystalline urea hydrothermal $Mg_{12}AlTi_3$-LDH gives a similar photocatalytic performance as TiO_2, with a conversion of 83% after 6 hours of UV irradiation.

The recyclability of the $Mg_{12}AlTi_3$-LDH catalyst was also investigated. Catalyst recyclability is an important consideration for heterogeneous photocatalysis – any efficient and successful photocatalyst needs to maintain a high activity over several photocatalytic cycles.[33] Due to the small catalyst loadings used in this work, attempting to carry out a filtration to separate out the catalyst during successive cycles would result in too much catalyst loss. Therefore, the recycling experiments were carried out as follows. Each cycle involved 2 hours of UV irradiation, and afterwards, the solvent was removed by rotary evaporation to give a dispersion of the solid catalyst in the product mixture. A <0.1 mL aliquot was removed to be analysed by ^{1}H NMR spectroscopy. Then, a solution of diphenylmethanol (specifically, 100 mL of 100 mM diphenylmethanol solution in acetonitrile) was added to the catalyst dispersion in the product mixture and irradiated. This process was repeated three times to give a total of four cycles. The results are summarised in Figure 3.16.

Interestingly, the photocatalytic activity was observed to increase after the first two cycles: it is 1.6-times better after the first cycle and 1.7-times better after the second cycle as compared to the first cycle. More commonly, photocatalysts lose some of their activity in successive catalytic cycles, with conversion decreasing by as much as 80 – 90% over the course of 8 – 10 cycles.[34] Photocatalyst recovery and re-use have been deemed effective for catalysts where the conversion decreases by about 10% or less over the course of 10 cycles.[34,35]

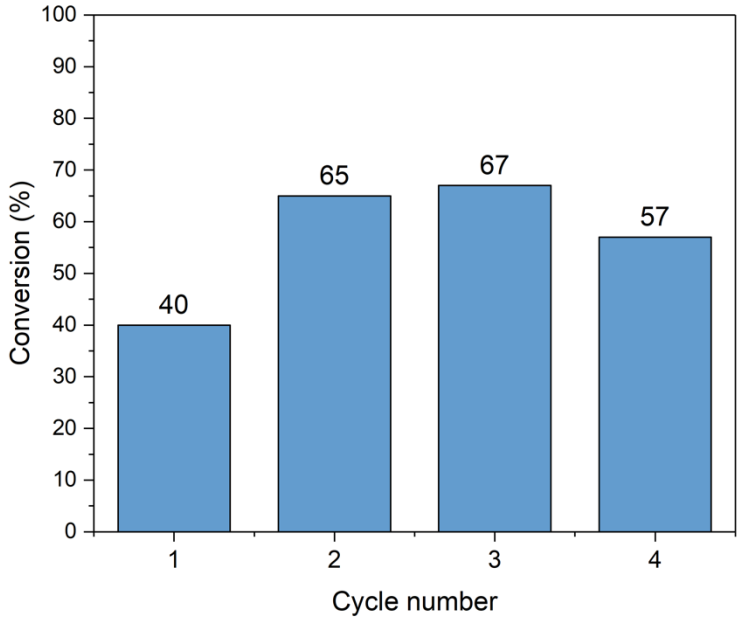


Figure 3.16 The conversion of diphenylmethanol to benzophenone in successive photocatalytic cycles with re-cycled urea hydrothermal $Mg_{12}AlTi_3$-LDH photocatalyst at 25 mg loading.

However, a similar increase in photocatalytic activity in successive cycles has been observed before in the degradation of model pollutants (phenol and Rhodamine B) under visible light irradiation using nanorods of TiO_2 doped with a controlled amount of tungsten.[33] There, the increase in activity was predominantly attributed to the gradual diffusion of tungsten from the surface into the TiO_2 lattice. It is possible that an analogous structural change occurs in successive cycles in the case of the $Mg_{12}AlTi_3$-LDH, with a possible diffusion of Ti towards the LDH surface. As it has been shown that Ti centres

are important for photocatalytic activity and active site formation (Figure 3.7), a greater proportion of Ti on the catalyst surface after the first cycle could explain the observed increase in conversion. It is also possible that prolonged dispersion of the $Mg_{12}AlTi_3$-LDH particles in acetonitrile results in their reduced aggregation and/or partial delamination in a manner similar to the AMOST method,[36,37] resulting in an increased surface area and therefore a greater accessibility of the surface active sites. Alternatively, the cause of the increased activity could be the formation of an LDH-reactant complex during the first catalytic cycle, which then improves the photocatalytic activity of the system in subsequent cycles.

3.9 Conclusions

The NiTi- and MgAlTi-LDHs, whose synthesis and characterisation were outlined in Chapter 2, were used in the photocatalytic oxidation of diphenylmethanol using an immersion well photo-reactor with a 125 W medium pressure mercury UV lamp, with acetonitrile used as the solvent and oxygen gas bubbling through the reaction mixture. It was found that the high-energy, short-wavelength radiation ($\lambda < 300$ nm) can cause the photo-oxidation of diphenylmethanol even in the absence of a photocatalyst. Consequently, a borosilicate immersion well was used to eliminate radiation below 300 nm, which allowed the effective screening of the Ti-LDH photocatalysts.

Both the metal composition (Ti content) and synthetic method of the LDHs were shown to affect their photocatalytic activity. Specifically, a larger Ti content and a high crystallinity (obtained by using the urea hydrothermal method) result in the highest conversion of diphenylmethanol to benzophenone, comparable to that of anatase TiO_2. Varying the catalyst loading showed that the observed photo-oxidation conversion is the balance of two effects: the inherent photocatalytic activity of the photocatalyst and the reduced transparency of the reaction mixture as the amount of catalyst is increased. The conversion with the urea hydrothermal $Mg_{12}AlTi_3$-LDH was found to increase with catalyst loading up to 25 mg to a final value of 19%, whereas the conversion with TiO_2 decreased when the loading was increased beyond 5 mg.

In summary, it has been shown that the crystalline urea hydrothermal $Mg_{12}AlTi_3$-LDH is a highly active photocatalyst for the photo-oxidation of diphenylmethanol, giving a conversion of 83% after 6 hours of UV irradiation with negligible side product formation. Importantly, it can be recycled and even shows an enhanced photocatalytic activity in successive catalytic cycles.

3.10 References

1 S. P. M. Menachery, T. P. Nguyen, P. Gopinathan, U. K. Aravind and C. T. Aravindakumar, *Chemical Physics*, 2018, **513**, 201–208.
2 S. Sheik Mansoor and S. Syed Shafi, *React. Kinet., Mech. Catal.*, 2010, **75**, 1886–31.
3 S. Vijaikumar, N. Somasundaram and C. Srinivasan, *Appl. Catal., A*, 2002, **223**, 129–135.
4 O. S. Mohamed, A. E.-A. M. Gaber and A. A. Abdel-Wahab, *J. Photochem. Photobiol., A*, 2002, **148**, 205–210.
5 N. B. Shali and S. Sugunan, *J Sol-Gel Sci Technol*, 2007, **42**, 101–105.
6 S. Kim, J. Fahel, P. Durand, E. André and C. Carteret, *Eur. J. Inorg. Chem.*, 2017, **2017**, 669–678.
7 L. Sobhana, M. Sarakha, V. Prévot and P. Fardim, *Appl. Clay Sci.*, 2016.
8 J. Sun, Y. Zhang, J. Cheng, H. Fan, J. Zhu, X. Wang and S. Ai, *Journal of Molecular Catalysis A: Chemical*, 2014, **382**, 146–153.
9 J. Zhu, Z. Zhu, H. Zhang, H. Lu, Y. Qiu, L. Zhu and S. Küppers, *J. Colloid Interface Sci.*, 2016, **481**, 144–157.
10 G. Fan, F. Li, D. G. Evans and X. Duan, *Chem. Soc. Rev.*, 2014, **43**, 7040–7066.
11 N. Baliarsingh, L. Mohapatra and K. Parida, *J. Mater. Chem. A*, 2013, **1**, 4236–4243.
12 C. G. Silva, Y. Bouizi, V. Fornés and H. Garcia, *J. Am. Chem. Soc.*, 2009, **131**, 13833–13839.
13 Y. Lee, J. H. Choi, H. J. Jeon, K. M. Choi, J. W. Lee and J. K. Kang, *Energy Environ. Sci.*, 2011, **4**, 914–920.
14 Y. Zhao, X. Jia, G. I. N. Waterhouse, L.-Z. Wu, C.-H. Tung, D. O'Hare and T. Zhang, *Adv. Energy Mater.*, 2015, **6**, 1501974.
15 N. Ahmed, Y. Shibata, T. Taniguchi and Y. Izumi, *J. Catal.*, 2011, **279**, 123–135.
16 N. Ahmed, M. Morikawa and Y. Izumi, *Catal. Today*, 2012, **185**, 263–269.
17 M. Morikawa, Y. Ogura, N. Ahmed, S. Kawamura, G. Mikami, S. Okamoto and Y. Izumi, *Catal. Sci. Technol.*, 2014, **4**, 1644–1651.
18 Y. Zhao, B. Li, Q. Wang, W. Gao, C. J. Wang, M. Wei, D. G. Evans, X. Duan and D. O'Hare, *Chem. Sci.*, 2014, **5**, 951–958.
19 Y. Zhao, P. Chen, B. Zhang, D. S. Su, S. Zhang, L. Tian, J. Lu, Z. Li, X. Cao, B. Wang, M. Wei, D. G. Evans and X. Duan, *Chem. Eur. J.*, 2012, **18**, 11949–11958.
20 K. Hosni, O. Abdelkarim, N. Frini-Srasra and E. Srasra, *Korean J. Chem. Eng.*, 2014, **32**, 104–112.
21 G. Mendoza-Damián, F. Tzompantzi, A. Mantilla, A. Barrera and L. Lartundo-Rojas, *Journal of Hazardous Materials*, 2013, **263**, 67–72.
22 H. Zhao, J. Xu, L. Liu, G. Rao, C. Zhao and Y. Li, *Journal of CO2 Utilization*, 2016, **15**, 15–23.
23 X.-J. Yang, B. Chen, X.-B. Li, L.-Q. Zheng, L.-Z. Wu and C.-H. Tung, *Chem. Commun.*, 2014, **50**, 6664–6667.
24 D. Guo, Y. Wang, P. Zhao, M. Bai, H. Xin, Z. Guo and J. Li, *Catalysts*, 2016, **6**, 64.
25 J. Zou, Z. Wang, W. Guo, B. Guo, Y. Yu and L. Wu, *Appl. Catal., B*, 2020, **260**, 118185.
26 E. W. Vitz, *J. Chem. Educ.*, 1981, **58**, 655.
27 O. S. Mohamed, S. A. Ahmed, M. F. Mostafa and A.-M. A. Abdel-Wahab,

International Journal of Photoenergy, 2008, **2008**, 1–11.
28 F. A.-Z. G. Gassim, A. N. Alkhateeb and F. H. Hussein, *Desalination*, 2007, **209**, 342–349.
29 S. Higashimoto, N. Kitao, N. Yoshida, T. Sakura, M. Azuma, H. Ohue and Y. Sakata, *J. Catal.*, 2009, **266**, 279–285.
30 T. Luttrell, S. Halpegamage, J. Tao, A. Kramer, E. Sutter and M. Batzill, *Sci. Rep.*, 2014, **4**, 515–8.
31 R. Marotta, I. Di Somma, D. Spasiano, R. Andreozzi and V. Caprio, *Chem. Eng. J.*, 2011, **172**, 243–249.
32 J. O. Schreck, *J. Chem. Educ.*, 1971, **48**, 103.
33 K. Sorathiya, B. Mishra, A. Kalarikkal, K. P. Reddy, C. S. Gopinath and D. Khushalani, *Sci. Rep.*, 2016, **6**, 2893–9.
34 A. G. S. Prado, L. B. Bolzon, C. P. Pedroso, A. O. Moura and L. L. Costa, *Appl. Catal., B*, 2008, **82**, 219–224.
35 L. L. Costa and A. G. S. Prado, *J. Photochem. Photobiol., A*, 2009, **201**, 45–49.
36 C. Chen, M. Yang, Q. Wang, J.-C. Buffet and D. O'Hare, *J. Mater. Chem. A*, 2014, **2**, 15102–15110.
37 C. Chen, A. Wangriya, J.-C. Buffet and D. O'Hare, *Dalton Trans.*, 2015, **44**, 16392–16398.

Chapter 4 Photo-oxidation of benzyl alcohol, cyclooctanol and benzylamine

4.1 Introduction

The study of the photocatalytic properties of Ti-LDHs was extended beyond diphenylmethanol photo-oxidation to also include benzyl alcohol, cyclooctanol and benzylamine as additional reactants, so as to determine whether Ti-LDHs can be used to photo-oxidise a wider range of functional groups as part of either aromatic or aliphatic systems. The three photo-oxidation reactions are shown in Figure 4.1.

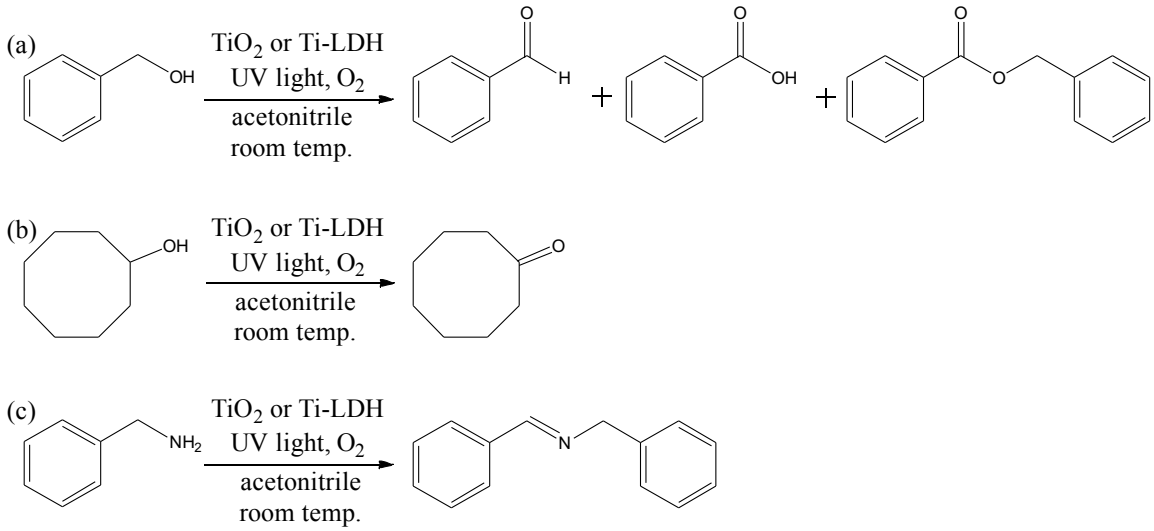


Figure 4.1 Reaction schemes for the photo-oxidation of (a) benzyl alcohol, (b) cyclooctanol and (c) benzylamine.

Thus, both alcohol and amine functional groups have been considered, as well as the photo-oxidation of aliphatic reactants in comparison with aromatic compounds. The latter have the benefit of an additional driving force of an extended conjugated system when photo-oxidised. Additionally, using benzyl alcohol as a photo-oxidation reactant allows the comparison between secondary (diphenylmethanol) and primary alcohols (benzyl

alcohol). In the latter case, the possibility of over-oxidation to benzoic acid introduces the additional complexity of selectivity.[1,2]

In addition to being useful model compounds for a theoretical study of the photocatalytic activity of the prepared NiTi- and MgAlTi-LDHs, the three new reactants also represent groups of compounds that are important intermediates in the synthesis of a large number of useful organic compounds.

For example, benzaldehyde obtained through the (photo-)oxidation of benzyl alcohol is a highly demanded compound due to its wide variety of applications in food, pharmaceutical and perfumery industries.[3] Commercial benzaldehyde is produced by the partial oxidation of toluene in the presence of a vanadyl pyrophosphate catalyst.[2]

The oxidation of cyclooctanol has not been as extensively studied. Magnetically recyclable core-shell Pd nanocatalysts have been used to oxidise a wide range of cycloalkanols, including cyclopentanol, cyclohexanol and cyclooctanol with high yields in the 70 – 95% range.[3] Cyclooctanol was chosen as the reactant in this work because of its higher boiling point (b.p. 209 ºC) in comparison to other cycloalkanols such as cyclohexanol (b.p. 160 ºC) or cycloheptanol (b.p. 185 ºC). This allows solvent removal by rotary evaporation in the work-up step without the concern that any of the reactant would be simultaneously evaporated from the product mixture.

Finally, imine derivatives obtained through amine oxidation are an important class of compounds with broad applications in organic synthesis – useful in reactions such as nucleophilic addition, condensation, and cycloadditions. Imines are also key intermediates in the synthesis of various biologically active nitrogen-containing heterocycles.[4] Traditionally, imines are prepared by the condensation of amines with carbonyl compounds in the presence of dehydrating agents and Lewis acid catalysts.[5]

More recently, effort has been devoted to a more facile, direct synthesis of imines via one-pot procedures with a variety of catalysts, including metal-based, metal-free, photo- and bio-inspired catalysts.[5] For example, hydrogen peroxide, H_2O_2, has been used successfully to oxidise benzylamines in an aqueous solution in the presence of V_2O_5 with high yields.[6]

4.2 Photo-reactor setup and reaction conditions

The photo-reactor setup used in all of the photocatalytic reactions in this Chapter was the same as that outlined in Chapter 3: an immersion well photo-reactor with a 125 W medium pressure mercury UV lamp, separated from the reaction mixture by a borosilicate immersion well that eliminates all irradiation below 300 nm (Figure 3.2). All reaction mixtures were sonicated for 15 minutes before reaction and stirred at 1,000 rpm throughout the irradiation period to ensure proper dispersion of the solid catalysts and prevent sedimentation. The oxygen flow rate through the reaction mixture was kept constant at 70 cm^3min^{-1} and the solvent used was acetonitrile, with the solvent volume kept constant at 100 mL.

The reactant (benzyl alcohol, cyclooctanol and benzylamine) concentration was kept constant at 100 mM, as that was determined to be the optimal reactant concentration for diphenylmethanol photo-oxidation in Chapter 3. Only the two most active representative Ti-LDH photocatalysts, urea reflux Ni_2Ti-LDH and urea hydrothermal $Mg_{12}AlTi_3$-LDH (as determined in Chapter 3) and anatase TiO_2 as the benchmark photocatalyst were considered in this Chapter. To compare the performance of the three photocatalysts in the photo-oxidation reactions of the three different reactants, the catalyst loading was kept constant at 5 mg. The optimal $Mg_{12}AlTi_3$-LDH loading of 25 mg was also included, as it was found in Chapter 3 that it gives the best Ti-LDH photocatalytic performance.

For completeness, the reactant concentrations and the catalyst loadings used (both in terms of weight, mg, and in terms of concentration, wt%) are listed in Table C.1 in Appendix C.

In all control reactions and photocatalyst comparison experiments, the irradiation time was 1 hour. In the kinetic (time variation) experiments, the irradiation period was varied between 15 minutes and 6 hours for benzyl alcohol and benzylamine, and between 1 and 6 hours for cyclooctanol.

As in the reactions outlined in Chapter 3, the catalyst was removed from the product mixture using a syringe filter following the photo-oxidation reactions. The acetonitrile was then removed from the product mixture using rotary evaporation.

More detailed information regarding all photo-oxidation reaction conditions is outlined in Chapter 7.

4.3 Characterisation techniques and product mixture analysis

The presence of oxidised products, as well as the conversion and selectivity of the photo-oxidation reactions were analysed using ^{1}H NMR spectroscopy in $CDCl_3$.

In the benzyl alcohol photo-oxidation reactions, the only compounds present in the product mixture after irradiation, as detectable by ^{1}H NMR spectroscopy, were benzyl alcohol (the reactant), benzaldehyde, benzoic acid and benzyl benzoate ester. Similarly, the only compounds in the cyclooctanol photo-oxidation product mixture were the reactant and cyclooctanone. The benzylamine photo-oxidation product mixture comprised the reactant and *N*-benzylidenebenzylamine. It is therefore assumed that any other potential side products in any of the three photo-oxidation reactions form in negligible amounts and are therefore not included in the conversion calculations.

The conversion of benzyl alcohol to photo-oxidation products was determined based on the integration of the 4.7 ppm ^{1}H NMR resonance of benzyl alcohol (corresponding to the two Ph-C$\underline{H_2}$OH protons), the 10.0 ppm benzaldehyde resonance (corresponding to the Ph-C$\underline{H}$O proton), the 8.1 ppm benzoic acid resonance (corresponding to the two *ortho* protons on the aromatic ring) and the 4.3 ppm benzyl benzoate resonance (corresponding to the two Ph-COO-C$\underline{H_2}$-Ph protons).

The conversion of cyclooctanol to cyclooctanone was similarly determined by integrating the 3.8 ppm cyclooctanol resonance (corresponding to the R_2-C$\underline{H}$-OH proton) and the 2.4 ppm cyclooctanone resonance (corresponding to the four R-C$\underline{H_2}$-CO-C$\underline{H_2}$-R protons).

Finally, the conversion of benzylamine to its photo-oxidation product was calculated based on the integrations of the 3.8 ppm benzylamine resonance (corresponding to the

two Ph-C<u>H$_2$</u>-NH$_2$ protons) and the 8.5 ppm *N*-benzylidenebenzylamine resonance (corresponding to the Ph-C<u>H</u>-N-CH$_2$-Ph proton).

The representative ^{1}H NMR spectra of the benzyl alcohol, cyclooctanol and benzylamine photo-oxidation product mixtures are shown in Figures 4.2, 4.3 and 4.4, respectively.

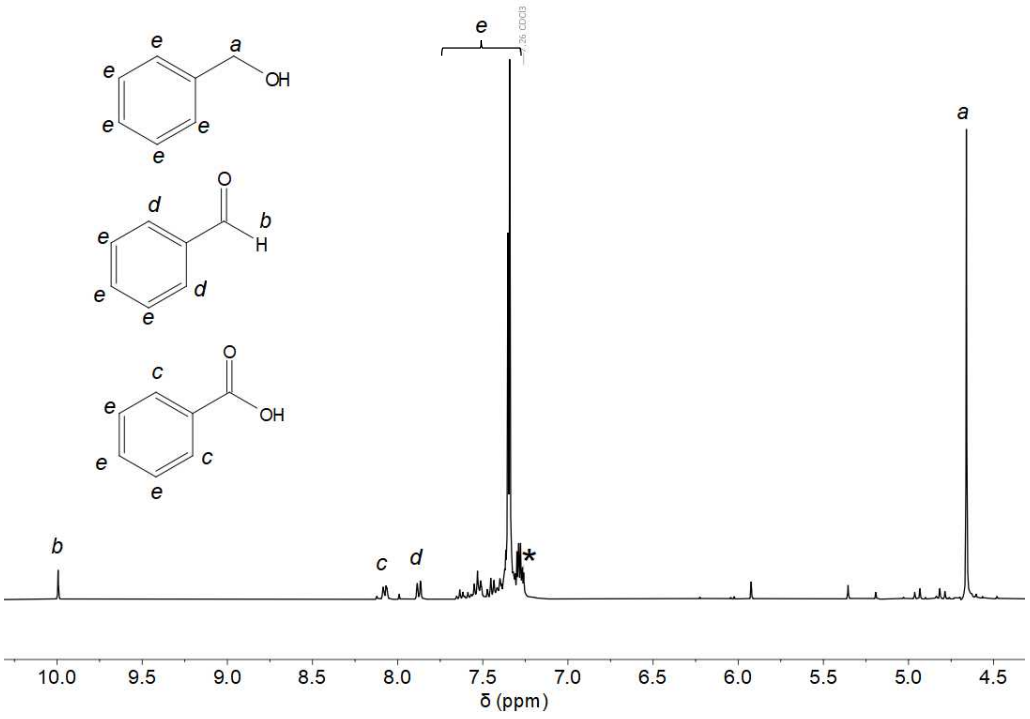


Figure 4.2 Representative ^{1}H NMR spectrum of the benzyl alcohol photo-oxidation product mixture after 1 hour of UV irradiation with 25 mg of urea hydrothermal $Mg_{12}AlTi_3$-LDH photocatalyst, with ^{1}H resonances assigned to benzyl alcohol, benzaldehyde and benzoic acid. * denotes the residual protio-solvent resonance in the deuterated chloroform, $CDCl_3$.

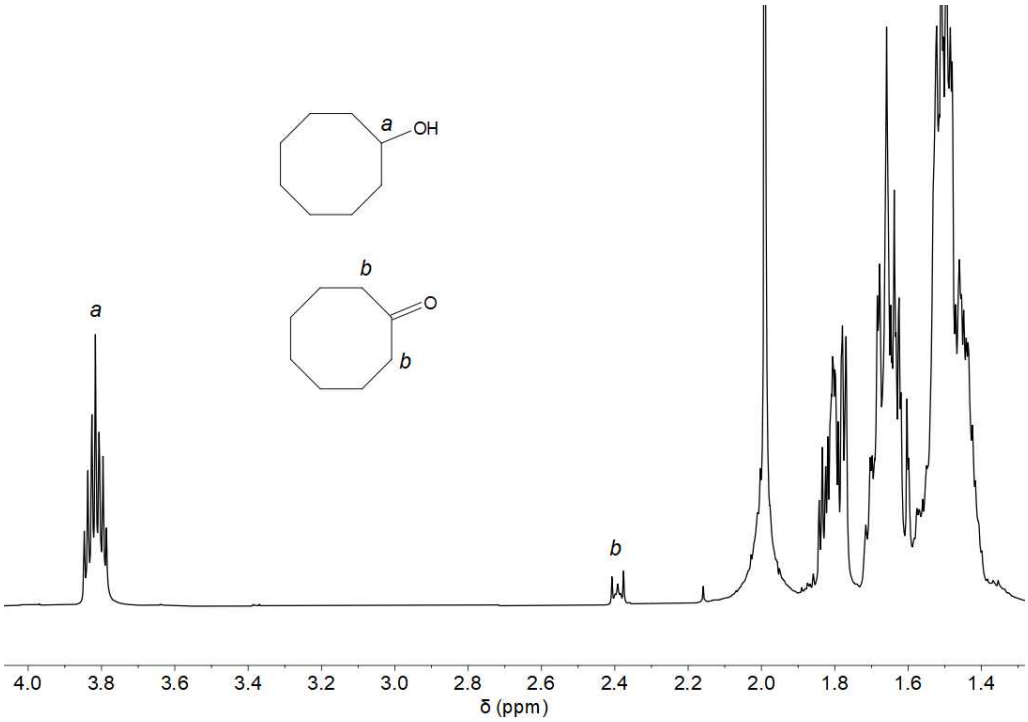


Figure 4.3 Representative ^{1}H NMR spectrum of the cyclooctanol photo-oxidation product mixture after 6 hours of UV irradiation with 25 mg of urea hydrothermal $Mg_{12}AlTi_3$-LDH photocatalyst, with ^{1}H resonances assigned to cyclooctanol and cyclooctanone. The resonances below 2.2 ppm correspond to the unlabelled protons of the –C<u>H$_2$</u>– groups of the two C8 rings.

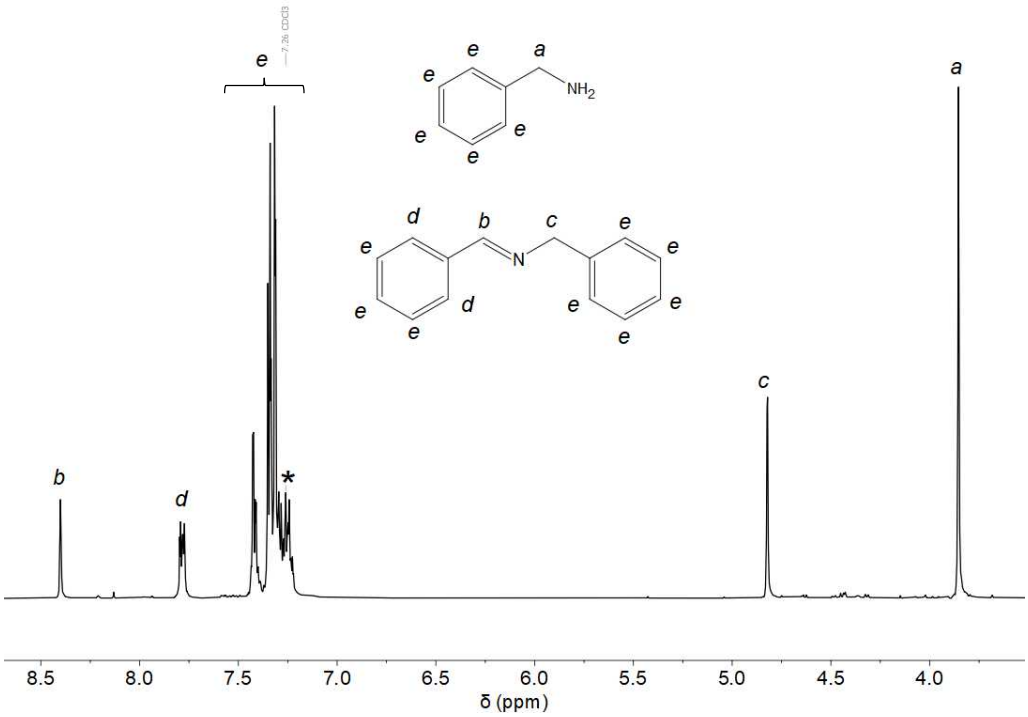


Figure 4.4 Representative ^{1}H NMR spectrum of the benzylamine photo-oxidation product mixture after 6 hours of UV irradiation with 25 mg of urea hydrothermal $Mg_{12}AlTi_3$-LDH photocatalyst, with ^{1}H resonances assigned to benzylamine and *N*-benzylidenebenzylamine. * denotes the residual protio-solvent resonance in the deuterated chloroform, $CDCl_3$.

In all of the below, the conversion (expressed as a percentage, %) of the relevant photo-oxidation reaction refers to the proportion of the total reactant initially present that is converted to oxidised products during the reaction. In cases where compounds like benzyl benzoate or *N*-benzylidenebenzylamine are formed, only the oxidised part of the molecule is considered to contribute to the conversion – so that the conversion accurately reflects the amount of oxidation actually taking place and allows facile comparison between the different reactants.

Specifically, for benzyl alcohol photo-oxidation, the conversion is defined as follows:

$$Conversion\ (\%) = \frac{n(benzaldehyde) + n(benzoic\ acid) + n(benzyl\ benzoate)}{n(benzyl\ alcohol) + n(benzaldehyde) + n(benzoic\ acid) + 2{\times}n(benzyl\ benzoate)} \times 100\%$$

For cyclooctanol photo-oxidation, the conversion is defined as follows:

$$Conversion\ (\%) = \frac{n(cyclooctanone)_{final}}{n(cyclooctanol)_{final} + n(cyclooctanone)_{final}} \times 100\%$$

And for benzylamine photo-oxidation, the conversion is defined as follows:

$$Conversion\ (\%) = \frac{n(N-benzylidenebenzylamine)_{final}}{n(benzylamine)_{final} + 2{\times}n(N-benzylidenebenzylamine)_{final}} \times 100\%$$

In all of the conversion calculations, $n(A)_{final}$ refers to the amount of compound A in the product mixture, as inferred from the integration of ^{1}H NMR resonances outlined above.

4.4 Photo-oxidation of benzyl alcohol

As with the diphenylmethanol photo-oxidation reactions in Chapter 3, no conversion to oxidised products was observed for the photo-oxidation of benzyl alcohol when the reaction was carried out in the dark or without O_2 under an inert N_2 atmosphere. This is consistent with previous literature findings on benzyl alcohol photo-oxidation with both TiO_2 and LDHs, which observed either a drastic reduction in activity or no conversion at all in the absence of irradiation and/or oxygen.[1,7-10]

However, contrary to literature reports,[1,10] the photo-oxidation does take place in the absence of a catalyst when the reaction mixture is irradiated with UV light and O_2 is bubbled through it, giving a conversion of 4% after 1 hour. Additionally, some of the initially formed benzaldehyde is oxidised further to benzoic acid (without any ester formation), resulting in a selectivity of 76% for benzaldehyde. These observations are in line with the findings in Chapter 3, where although the borosilicate immersion well blocks out the high-energy photons corresponding to $\lambda < 300$ nm, some of the remaining photons still possess sufficient energy to activate the reactant and/or oxygen gas molecules to result in benzyl alcohol photo-oxidation.

The comparison of the three representative photocatalysts (TiO_2, urea reflux Ni_2Ti-LDH and urea hydrothermal $Mg_{12}AlTi_3$-LDH at 5 mg loading, and also urea hydrothermal $Mg_{12}AlTi_3$-LDH at the optimal 25 mg loading) is shown in Figure 4.5. All conversions refer to the product mixture after 1 hour of irradiation. For all three photocatalysts, a notable degree of over-oxidation to benzoic acid takes place – however, no benzyl benzoate ester presence was detected by ^{1}H NMR spectroscopy. In all cases, the conversion increases on the addition of a catalyst.

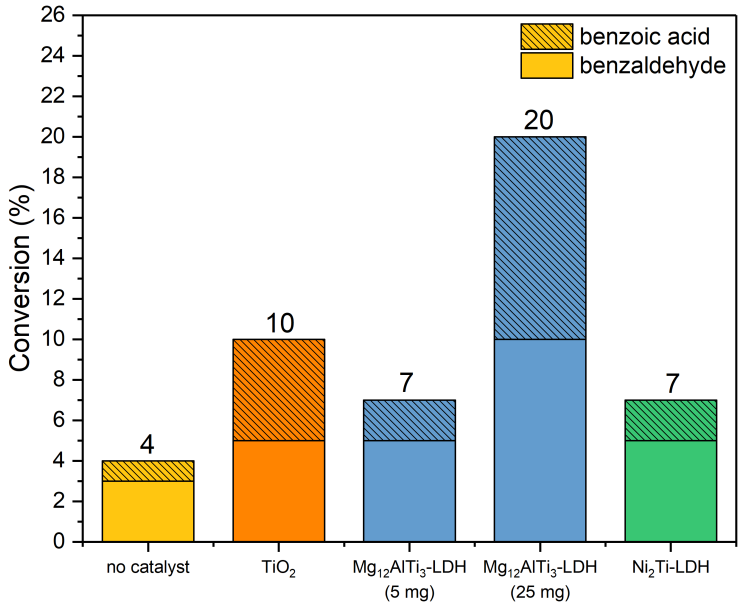


Figure 4.5 Photocatalytic conversion of benzyl alcohol to the corresponding oxidised products (benzaldehyde and benzoic acid) after 1 hour of UV irradiation with three different photocatalysts, including the comparison to the reaction without a catalyst. Unless specified, all catalyst loadings are 5 mg.

Comparing the conversions for the catalyst loading of 5 mg, the TiO_2 anatase catalyst gives the best conversion of 10% and, contrary to the results for diphenylmethanol photo-oxidation in Chapter 3, the conversion with Ni_2Ti-LDH is equal to that with $Mg_{12}AlTi_3$-LDH (7% after 1 hour of irradiation). Increasing the $Mg_{12}AlTi_3$-LDH loading to 25 mg increases the conversion to the highest value of 20%. This 5-fold increase in catalyst loading does not result in an equivalent 5-fold increase in conversion due to the decreased reaction mixture transparency, as shown previously in Figure 3.13.

In terms of selectivity, the Ti-LDHs at 5 mg loading give a benzaldehyde selectivity of 72 and 76% for Ni_2Ti- and $Mg_{12}AlTi_3$-LDHs, respectively. The more active TiO_2, on the other hand, gives an approximately 50:50 mixture of benzaldehyde and benzoic acid, performing worse than the Ti-LDHs in that respect. When the $Mg_{12}AlTi_3$-LDH loading is increased to 25 mg, it gives a similar result of an approximately 50:50 mixture of aldehyde and acid, suggesting that a higher conversion (and therefore a higher activity) corresponds to a higher degree of over-oxidation. That is, rather than oxidising more

benzyl alcohol to benzaldehyde, the more active photocatalyst (or a larger amount of catalyst) works to preferentially oxidise the benzaldehyde further to benzoic acid.

The over-oxidation to benzoic acid is likely to be a consequence of the presence of water in the reaction mixture, introduced in the form of adsorbed or intercalated water molecules in the catalysts or formed *in situ* as a side product of the photo-oxidation reaction (e.g. following a mechanism similar to the one shown in Figure 1.4).[11] Specifically, any water molecules present in the reaction mixture can react with the initially formed benzaldehyde to form a 1,1-geminal diol (a 'hydrate'), which can then be oxidised further to benzoic acid.[12,13] To test this hypothesis, the reaction was carried out using a sample of urea hydrothermal $Mg_{12}AlTi_3$-LDH that was dried at 120 ºC for 12 hours prior to reaction, at 25 mg catalyst loading. While the conversion decreased slightly (from 20 to 16%), the benzaldehyde selectivity increased from 49 to 59% when the dried catalyst was used, indicating a reduced degree of over-oxidation. This confirms the hypothesis that the water content of the catalyst does to some extent contribute to the over-oxidation to benzoic acid.

The $Mg_{12}AlTi_3$-LDH catalyst at its best loading of 25 mg was used further to study the kinetics of benzyl alcohol photo-oxidation by varying the irradiation time between 15 minutes and 6 hours, as shown in Figures 4.6 and 4.7. The time variation of the composition of this reaction is more complex than that of diphenylmethanol photo-oxidation (Figure 3.15) due to the possibility of over-oxidation and ester side product formation. From Figure 4.6, it can be seen that the benzyl alcohol photo-oxidation with $Mg_{12}AlTi_3$-LDH proceeds via initial benzaldehyde formation, which is then rapidly oxidised further to benzoic acid. As the amount of benzoic acid in the reaction mixture builds up, it reacts with the remaining reactant present to form benzyl benzoate ester. This

reduces the amount of free benzyl alcohol in the reaction mixture, and prevents the photo-oxidation from proceeding until a conversion of 100% is reached (Figure 4.6).

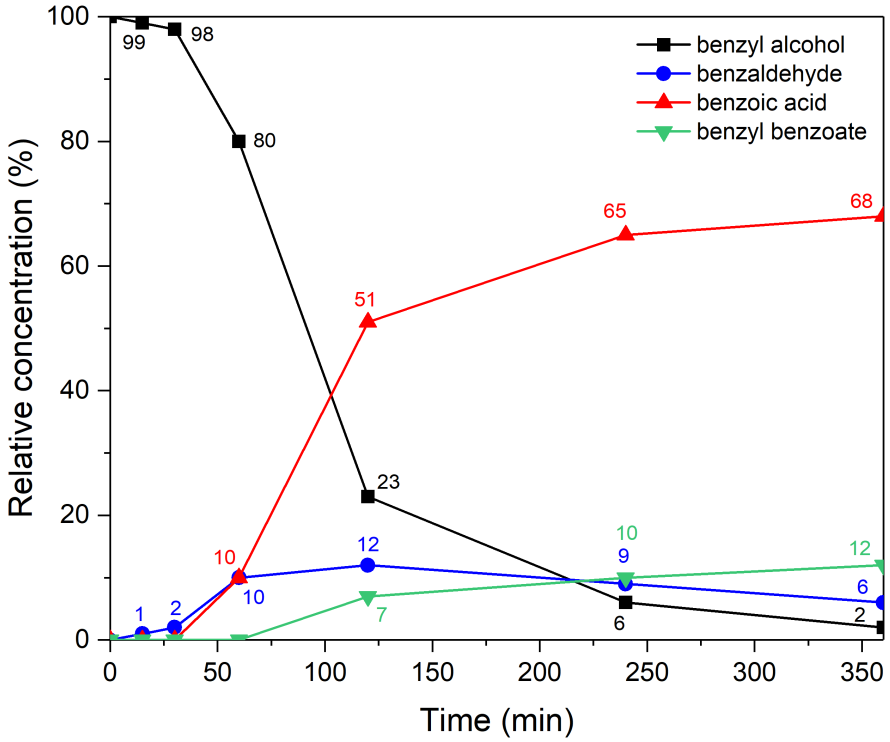


Figure 4.6 The composition of the benzyl alcohol photo-oxidation product mixture at different time intervals for urea hydrothermal $Mg_{12}AlTi_3$-LDH at 25 mg catalyst loading.

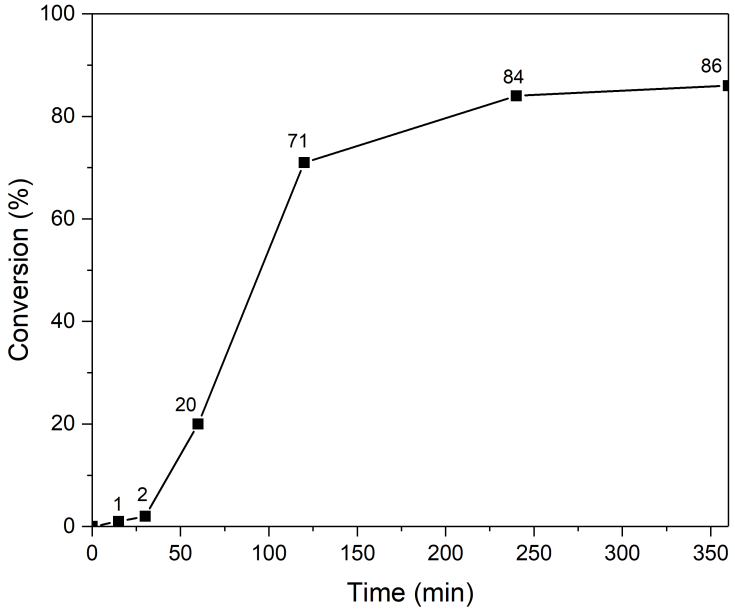


Figure 4.7 The time variation of the photocatalytic net conversion of benzyl alcohol to the corresponding oxidised products for urea hydrothermal $Mg_{12}AlTi_3$-LDH at 25 mg catalyst loading.

After 6 hours, the conversion to photo-oxidised products is 86%, with a very low benzaldehyde selectivity of only 7%. Thus, benzoic acid is the main product of the benzyl alcohol photo-oxidation with urea hydrothermal $Mg_{12}AlTi_3$-LDH.

Comparing the results of the benzyl alcohol photo-oxidation reactions in this work with literature findings is complicated because of different photo-reactor setups and reaction conditions, as previously outlined in Section 3.5. Mohamed *et al.* used a 125 W medium pressure mercury lamp, similar to the one in this work, to study the kinetics of benzyl alcohol photo-oxidation with TiO_2 and observed an approximately 20% conversion after 1 hour, with about 100% selectivity for benzaldehyde.[1]

This is notably different from the findings of this work, where TiO_2 gives a conversion that is only half of the reported conversion after the same period of irradiation, with a much lower selectivity. In this respect, the $Mg_{12}AlTi_3$-LDH photocatalyst at the 25 mg loading comes closer to literature findings, albeit with a lower selectivity. Even after 14 hours of irradiation, Mohamed *et al.* still observed only small amounts of benzoic acid formed, making up only about 10% of the final product mixture (with a conversion of about 90%).[1] A possible reason for this is that they used a dried TiO_2 catalyst, although it has been shown above that drying the photocatalyst does not have a large enough impact on the selectivity to fully explain this discrepancy.

However, when they used a 450 W medium pressure mercury lamp to carry out the benzyl alcohol photo-oxidation with TiO_2, they observed a much poorer benzaldehyde selectivity of only about 48% after 6 hours (with a conversion of 92%). This can be attributed to the higher light intensity and a relatively long irradiation time, which allows the initially formed benzaldehyde to be oxidised further.

Higashimoto *et al.* observed a conversion of about 50% after 1 hour of irradiation with an LED lamp in the presence of TiO_2 with a benzyl alcohol selectivity of about 100%.[7] After 4 hours of irradiation, they observed a nearly 100% conversion with little to no over-oxidation product formation.

Zou *et al.* used Zn_2Ti-LDH in the photocatalytic oxidation of benzyl alcohol.[10] They reported a 61% conversion with a 77% benzaldehyde selectivity after 4 hours of UV-visible irradiation. In comparison, the $Mg_{12}AlTi_3$-LDH system gives an 84% conversion with a 10% benzaldehyde selectivity after 4 hours of UV irradiation.

Overall, it can therefore be concluded that although the urea hydrothermal $Mg_{12}AlTi_3$-LDH photocatalytic system performs worse than previous literature reports in terms of benzaldehyde selectivity, it nonetheless gives a similar degree of overall benzyl alcohol photo-oxidation as previous TiO_2 studies and outperforms the Zn_2Ti-LDH catalyst used by Zou *et al*. in terms of conversion.

4.5 Photo-oxidation of cyclooctanol

With cyclooctanol photo-oxidation, no conversion to cyclooctanone was observed in the absence of irradiation, the catalyst or oxygen (when the reaction was carried out in an inert N_2 atmosphere). It is therefore evident that all three are essential for cyclooctanol photo-oxidation to take place. This is consistent with previous literature reports of cycloalkanol photo-oxidations.[14]

The comparison of conversions using the three representative catalysts at 5 or 25 mg catalyst loading after 1 hour of UV irradiation is shown in Figure 4.8. All conversions are much lower than those of the diphenylmethanol and benzyl alcohol photo-oxidation, likely due to the absence of the additional driving force of extended conjugation in the aliphatic system of the cyclooctanone product.

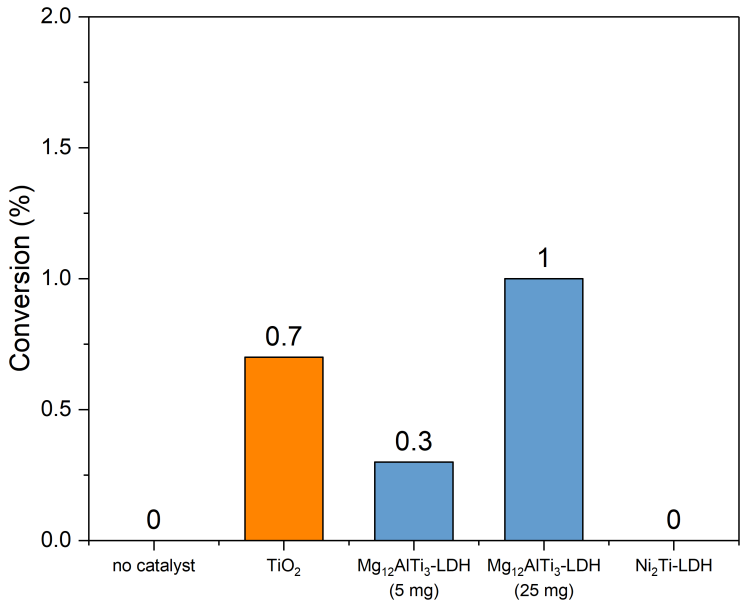


Figure 4.8 Photocatalytic conversion of cyclooctanol to cyclooctanone after 1 hour of UV irradiation with three different photocatalysts, including the comparison to the reaction without a catalyst. Unless specified, all catalyst loadings are 5 mg.

Comparing the three catalysts at 5 mg loading, TiO_2 gives the highest conversion, which is 2.3-times higher than that of urea hydrothermal $Mg_{12}AlTi_3$-LDH. Unlike in

diphenylmethanol and benzyl alcohol photo-oxidation reactions, no reaction takes place when urea reflux Ni_2Ti-LDH is used, indicating either that it is unsuitable for the photo-oxidation of aliphatic reactants or that it requires a different set of reaction conditions.

The conversion increases when the $Mg_{12}AlTi_3$-LDH loading is increased from 5 to 25 mg to about 1%. As observed previously, although the catalyst loading is increased 5-fold, the conversion does not increase by the same factor due to the decreased transparency of the reaction mixture when a larger amount of catalyst is dispersed in it (Figure 3.13).

$Mg_{12}AlTi_3$-LDH at 25 mg was used further to study the kinetics of cyclooctanol photo-oxidation, as shown in Figure 4.9. Since no side product formation was detected by ^1H NMR spectroscopy, the time variation of the cyclooctanol photo-oxidation is less complex than that of benzyl alcohol photo-oxidation, with cyclooctanone being the only product formed.

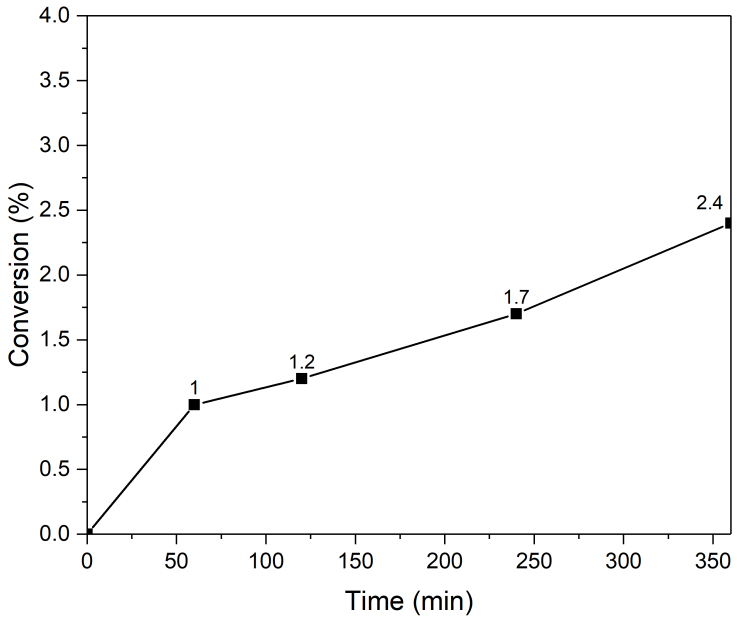


Figure 4.9 The time variation of the photocatalytic conversion of cyclooctanol to cyclooctanone for urea hydrothermal $Mg_{12}AlTi_3$-LDH at 25 mg catalyst loading.

Due to the low conversion observed after 1 hour of irradiation (Figure 4.8), the time of reaction was varied in the 1 – 6 hours range, as opposed to the 15 minutes – 6 hours range for the other reactants. Even after 6 hours of UV irradiation, the conversion is only 2.4%. This is significantly lower than the values in the literature report on cycloalkanol photo-oxidation with TiO_2 nanoparticles by Mohamed *et al.*.[14] Although their studies do not include cyclooctanol, they observed a 72% conversion for the photo-oxidation of cyclohexanol with a 46% selectivity for cyclohexanone after 20 hours of UV irradiation in acetonitrile with a 450 W medium pressure mercury lamp. For cycloheptanol, they observed an even higher conversion of 100% with an 80% cycloheptanone selectivity.

It is unclear why the photocatalytic system used in this work gives a much lower conversion for cyclooctanol photo-oxidation for both TiO_2 and Ti-LDH catalysts than might be expected based on the literature findings for similar cycloalkanol photo-oxidations. It is possible that the reaction conditions used in the cyclooctanol photo-oxidation were unsuitable, as they were optimised for the photo-oxidation of an aromatic compound (as outlined in Chapter 3). Therefore, the suitability of the Ti-LDHs, and especially the urea hydrothermal $Mg_{12}AlTi_3$-LDH, for the successful photo-oxidation of cyclooctanol should not be discarded altogether. Instead, further experiments and reaction condition optimisation is required to gain a more accurate understanding.

4.6 Photo-oxidation of benzylamine

Similarly to benzyl alcohol and diphenylmethanol photo-oxidations, when benzylamine was used as the reactant, no conversion was observed in the dark or in the absence of oxygen, when the reaction was carried out under an inert N_2 atmosphere. Much like with the two alcohol reactants, some oxidation did occur even when no catalyst was present in the reaction mixture – the conversion after 1 hour was 1%.

Whereas most literature findings report no conversion in the absence of light, oxygen/air and catalyst for TiO_2 photocatalysts,[15-17] Yang *et al.* have observed a 3% yield of *N*-benzylidenebenzylamine in the absence of a catalyst after 5 hours of irradiation with a 500 W high pressure mercury lamp ($\lambda > 300$ nm) under an atmosphere of air.[11] The latter observation is consistent with the findings of this work, in that while the borosilicate immersion well eliminates all irradiation with $\lambda < 300$ nm, the remaining high-energy photons are still sufficient to cause a small amount of oxidation even in the absence of a catalyst (although the conversion is notably lower than that observed when a quartz immersion well is used, as outlined in Section 3.4).

The comparison of the two most active representative Ti-LDH photocatalysts (urea reflux Ni_2Ti-LDH and urea hydrothermal $Mg_{12}AlTi_3$-LDH) with TiO_2 and a no-catalyst reaction for the benzylamine photo-oxidation conversion is shown in Figure 4.10, with either 5 or 25 mg catalyst loading. For both TiO_2 and $Mg_{12}AlTi_3$-LDH, the conversion is higher than in the absence of a catalyst. Interestingly, the conversion to *N*-benzylidenebenzylamine stayed approximately the same as in the absence of a catalyst on the addition of Ni_2Ti-LDH into the reaction mixture. This suggests that the reduced transparency of the reaction mixture on its introduction outweighs or balances out its inherent photocatalytic activity, indicating that it is an unsuitable photocatalyst for benzylamine photo-oxidation.

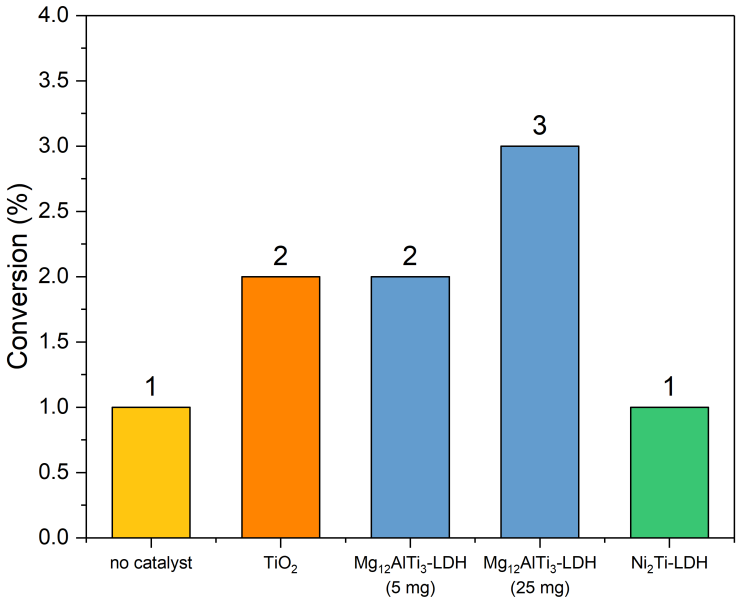


Figure 4.10 Photocatalytic conversion of benzylamine to *N*-benzylidinebenzylamine after 1 hour of UV irradiation with three different photocatalysts, including the comparison to the reaction without a catalyst. Unless specified, all catalyst loadings are 5 mg.

$Mg_{12}AlTi_3$-LDH at the 25 mg catalyst loading was used further to study the kinetics of benzylamine photo-oxidation, as shown in Figure 4.11. Similarly to cylcooctanol, no side product formation was observed, with the only product detected by ^{1}H NMR spectroscopy being *N*-benzylidenebenzylamine. Consequently, the time variation of the benzylamine photo-oxidation reaction is less complex than that of the benzyl alcohol photo-oxidation.

It should be noted that the presence of the direct oxidation product of benzylamine, i.e. of the corresponding imine, cannot be detected due to the fast *in situ* condensation with the unreacted reactant to form *N*-benzylidenebenylamine. This is consistent with literature findings, which only report the presence of *N*-benzylidenebenzylamine or the substituted equivalents after irradiation in the presence of photocatalysts.[11]

The time variation plot in Figure 4.11 shows an approximately linear trend in conversion. However, the conversion values observed are notably lower than those expected based

on previous literature reports. For example, Yang *et al.* have observed a 100% conversion of benzylamine to *N*-benzylidenebenzylamine after 5 hours of UV irradiation ($\lambda > 300$ nm) with a 500 W high pressure mercury lamp, using ZnTi-LDHs.[11]

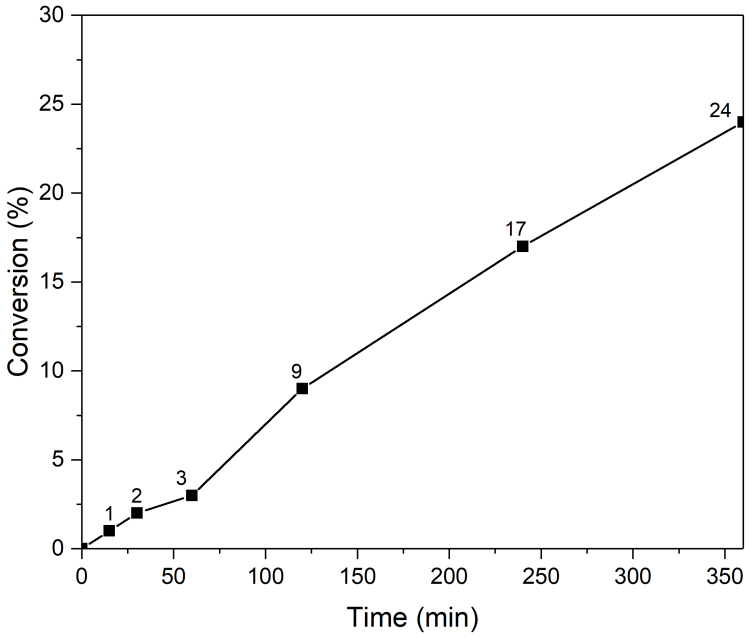


Figure 4.11 The time variation of the photocatalytic conversion of benzylamine to *N*-benzylidenebenzylamine for urea hydrothermal $Mg_{12}AlTi_3$-LDH at 25 mg catalyst loading.

The higher conversion can be partially attributed to the higher-intensity UV lamp, and therefore a larger number of photons emitted and absorbed within the irradiation period. Considering that the lamp used by Yang *et al*. is 4-times as intense as the one used in this work, and assuming a 1:1 correlation between the lamp intensity and the conversion, the estimated conversion using the reaction conditions in this work (catalyst, reaction volume, etc.) with a 500 W lamp after 6 hours would correspond to 96% (= 4 x 24%, as per Figure 4.11).

This roughly estimated value indicates that the urea hydrothermal $Mg_{12}AlTi_3$-LDH can be successfully used as a photocatalyst in the oxidation of benzylamine, with a similar

level of performance as other Ti-LDHs that have been previously used in the same reaction.

However, a more detailed comparison with literature would require the use of the same type of 500 W UV lamp and an irradiation time of 5 hours, especially in order to be able to directly compare the viability of the $Mg_{12}AlTi_3$-LDH catalyst used in this work with the ZnTi-LDH used in literature.

4.7 Comparison of the four different reactants

Finally, the kinetic profiles of the photo-oxidation reactions with the four different reactants (diphenylmethanol, benzyl alcohol, cyclooctanol and benzylamine) with the urea hydrothermal $Mg_{12}AlTi_3$-LDH at 25 mg catalyst loading were compared, as shown in Figure 4.12. This allows the determination of the effects that the different functional groups and the presence of aromaticity have on the conversion. To the best of the author's knowledge, such a study of a single photocatalyst applied to the photo-oxidation of a range of different organic reactants has not been reported previously.

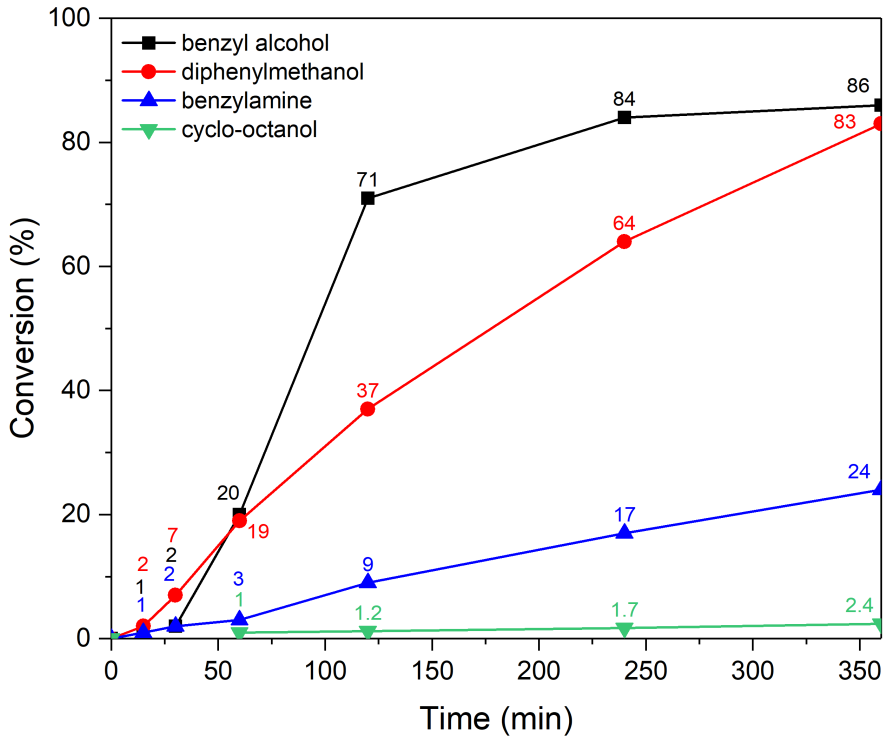


Figure 4.12 Comparison of the time variation of the photocatalytic conversion with urea hydrothermal $Mg_{12}AlTi_3$-LDH (at 25 mg catalyst loading) for the four different reactants considered in this work.

Firstly, it can be seen that the presence of an aromatic system in diphenylmethanol, benzyl alcohol and benzylamine drastically increases the conversion and the rate of conversion in comparison to the aliphatic system of cyclooctanol. This can be ascribed to the additional diving force of extending the conjugated system of the former three molecules

on oxidation through the formation of a carbonyl, C=O, or an imine, C=N, functional group, respectively.

Secondly, by comparing the two alcohols with the imine functionality, it is evident that the photocatalytic system used in this work, and specifically the urea hydrothermal $Mg_{12}AlTi_3$-LDH, is more active for the photo-oxidation of the alcohol functional groups. Part of the reason might be that the catalytic system used was originally optimised for the photo-oxidation of diphenylmethanol (as outlined in Chapter 3). Nonetheless, the $Mg_{12}AlTi_3$-LDH photocatalyst shows promise also for the photo-oxidation of amines, although a longer reaction time or a higher-intensity UV lamp might be required.

Finally, the comparison of the primary (benzyl alcohol) with the secondary alcohol (diphenylmethanol) shows that although the initial rate of photo-oxidation is faster for the former, the end conversion after 6 hours of UV irradiation is very similar. The initial higher rate of benzyl alcohol photo-oxidation can be ascribed to the rapid oxidation of 1,1-geminal diols (formed through the hydration of the aldehyde molecules).[12,13,18] This can also be seen in Figure 3.5, where benzaldehyde is preferentially oxidised to benzoic acid (rather than benzyl alcohol to benzaldehyde).

Nonetheless, the two different aromatic alcohols give a similar conversion after 6 hours of irradiation despite the difference in initial photo-oxidation rates because the photo-oxidation of benzyl alcohol is limited by the fact that part of the reactant is used to form the benzyl benzoate side product and is therefore unavailable for oxidation.

4.8 Conclusions

The optimised reaction conditions, as determined in Chapter 3 for the diphenylmethanol photo-oxidation, were used further to investigate the effectiveness of the two most active representative Ti-LDHs (urea reflux Ni_2Ti-LDH and urea hydrothermal $Mg_{12}AlTi_3$-LDH) in photo-oxidising other simple aromatic and aliphatic reactants, specifically benzyl alcohol, cyclooctanol and benzylamine. Thus, both alcohol and amine functional groups were considered, as well as the photo-oxidation of both aliphatic and aromatic compounds.

The photo-oxidation of benzyl alcohol is the most complex out of the three new reactants due to the over-oxidation to benzoic acid, which then further reacts with the benzyl alcohol present in the reaction mixture to form benzyl benzoate. This ester formation limits the conversion to 86% after 6 hours of UV irradiation. The conversion of cyclooctanol to cyclooctanone was notably lower at only 2.4% after 6 hours, as consistent with the absence of the additional driving force of extending the conjugation on oxidation. Although the urea hydrothermal $Mg_{12}AlTi_3$-LDH was found to also be active in the benzylamine photo-oxidation, the conversion was lower than that for the two aromatic alcohol reactants at only 24% after 6 hours.

Overall, the comparison of the three new photo-oxidation reactants with diphenylmethanol allowed the following conclusions to be made: (1) aromatic reactants show a higher conversion to photo-oxidised products due to the additional driving force of extending the conjugated system, (2) primary alcohols have a higher initial rate of photo-oxidation than secondary alcohols, and (3) the photocatalytic system used in this work is better suited to the photo-oxidation of alcohols than to that of amines.

4.9 References

1 O. S. Mohamed, A. E.-A. M. Gaber and A. A. Abdel-Wahab, *J. Photochem. Photobiol., A*, 2002, **148**, 205–210.
2 L. Amori, T. D. Giacco, C. Rol and G. V. Sebastiani, *J. Chem. Res.*, 1998, 644–645.
3 K. Cerdan, W. Ouyang, J. C. Colmenares, M. J. Muñoz-Batista, R. Luque and A. M. Balu, *Chem. Eng. Sci.*, 2019, **194**, 78–84.
4 X.-F. Wu, A. Petrosyan, T. V. Ghochikyan, A. S. Saghyan and P. Langer, *Tetrahedron Lett.*, 2013, **54**, 3158–3159.
5 B. Chen, L. Wang and S. Gao, *ACS Catal.*, 2015, **5**, 5851–5876.
6 G. Chu and C. Li, *Org. Biomol. Chem.*, 2010, **8**, 4716–4719.
7 S. Higashimoto, N. Kitao, N. Yoshida, T. Sakura, M. Azuma, H. Ohue and Y. Sakata, *J. Catal.*, 2009, **266**, 279–285.
8 S. Higashimoto, K. Okada, T. Morisugi, M. Azuma, H. Ohue, T.-H. Kim, M. Matsuoka and M. Anpo, *Top Catal*, 2010, **53**, 578–583.
9 J. Yu, J. Li, H. Wei, J. Zheng, H. Su and X. Wang, *Journal of Molecular Catalysis A: Chemical*, 2014, **395**, 128–136.
10 J. Zou, Z. Wang, W. Guo, B. Guo, Y. Yu and L. Wu, *Appl. Catal., B*, 2020, **260**, 118185.
11 X.-J. Yang, B. Chen, X.-B. Li, L.-Q. Zheng, L.-Z. Wu and C.-H. Tung, *Chem. Commun.*, 2014, **50**, 6664–6667.
12 R. J. Ouellette and J. D. Rawn, in *Organic Chemistry*, Elsevier, 2018, pp. 463–505.
13 S. E. Davis, M. S. Ide and R. J. Davis, *Green Chem.*, 2013, **15**, 17–45.
14 O. S. Mohamed, S. A. Ahmed, M. F. Mostafa and A.-M. A. Abdel-Wahab, *International Journal of Photoenergy*, 2008, **2008**, 1–11.
15 J. Dai, J. Yang, X. Wang, L. Zhang and Y. Li, *Appl. Surf. Sci.*, 2015, **349**, 343–352.
16 X. Lang, W. Ma, Y. Zhao, C. Chen, H. Ji and J. Zhao, *Chem. Eur. J.*, 2012, **18**, 2624–2631.
17 X. Lang, H. Ji, C. Chen, W. Ma and J. Zhao, *Angew. Chem., Int. Ed.*, 2011, **50**, 3934–3937.
18 T. Mallat and A. Baiker, *Chem. Rev.*, 2004, **104**, 3037–3058.

Chapter 5 Core-shell titanium dioxide@Ti-LDH hybrid materials

5.1 Introduction

In the previous two Chapters, it was shown that both TiO_2 (specifically, its anatase polymorphic form) and Ti-LDHs (specifically, NiTi- and MgAlTi-LDHs) show good photocatalytic activity for the photo-oxidation of simple organic molecules.

In the chemistry of LDHs, core-shell hybrid materials (as shown schematically in Figure 5.1) have been of considerable interest as they allow the combination of features of two different materials (the core and the shell), and frequently show a synergistic effect between the two, such that the catalytic activity of the core-shell material is higher than that of the equivalent mechanical mixture.[1-4] The vertical growth of LDH platelets on the core nanoparticles also reduces *ab*-face aggregation, potentially increasing the surface area, as well as the number and accessibility of active sites.[5,6] Additionally, the interior architecture of the hybrid materials can be further tuned to form core-shell, yolk-shell and hollow structures (Figure 5.1).[3]

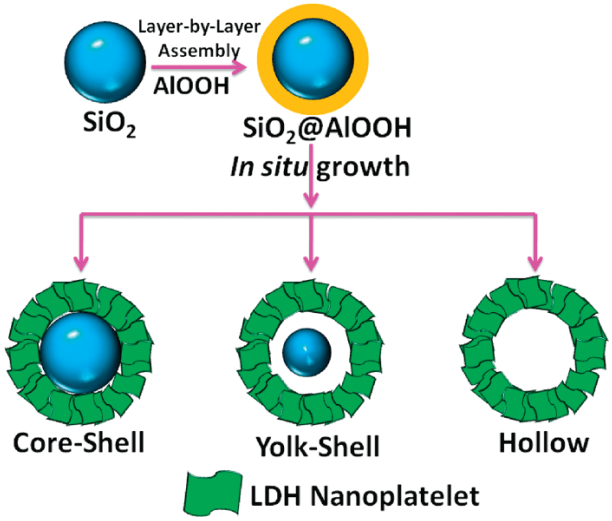


Figure 5.1 Schematic preparation of core@LDH microspheres with tuneable interior architecture.[3]

A variety of core materials have been explored to date, including SiO_2,[5,7,8] TiO_2,[9,10] ZnO,[6,11,12] Cu_2O,[13] Fe_3O_4,[2] zeolites,[1,14] and carbon.[4] Such core@LDH materials have a wide range of possible applications, for example in advanced electrodes for supercapacitors,[15] in electrocatalytic oxygen evolution reactions,[4] as magnetic nanocatalysts in organic reactions,[2] and in photocatalysis.[6,9-11,13]

In photocatalysis, most of the work has been done on core@LDH materials where the core is TiO_2,[9,10,16] ZnO,[6,11,12] or Cu_2O.[13] That is, the choice of the core materials has been restricted to compounds that are highly efficient photocatalysts in their own right. For example, Dou *et al.* have used TiO_2@CoAl-LDH core-shell nanospheres in the photocatalytic water splitting reaction with focus on oxygen generation.[9] They observed an extraordinarily high photocatalytic activity towards oxygen evolution under full sunlight (> 200 nm, i.e. including both UV and visible irradiation) and under visible light (> 420 nm).

This high activity was attributed to the incorporation of visible-light-active CoAl-LDH shell with the UV-light-responsive TiO_2 core, which promotes the utilisation of a wider range of wavelengths. Furthermore, the combined experimental results and computational simulations showed that a strong donor-acceptor coupling and suitable band matching between the TiO_2 core and the LDH shell (i.e. the formation of a 'heterojunction') facilitate the separation of the photoinduced electron-hole pairs.[9] Similarly, Kumar *et al.* have ascribed the photocatalytic activity of P25@CoAl-LDHs in the photo-reduction of CO_2 to the matching of the semiconductor band structures and therefore the formation of a heterojunction.[17]

The possibility of establishing a heterojunction is a definite advantage of core@LDH photocatalysts, as heterojunctions allow better electron-hole separation and consequently

a reduced charge carrier recombination rate.[6,11,18-20] Similar heterojunctions can also be formed by doping or impregnating the LDH particles with smaller nanoparticles, such as Ag_2CO_3 or TiO_2,[21,22] or by alternating cationic LDH layers and anionic layered titanate nanosheets.[23]

In addition to the formation of a heterojunction, Guo *et al.* have attributed the enhanced photocatalytic activity of ZnO@CuZnAl-LDHs for CO_2 reduction to an increase in the surface area, which increases the number of active sites where CO_2 can adsorb to.[6]

Core@LDH composites can be prepared by a variety of different synthetic methods. For example, Shao *et al.* used a layer-by-layer (LbL) deposition followed by an *in situ* growth technique to form SiO_2@NiAl-LDHs – specifically, the silica microspheres were coated with an ultrathin AlOOH film, followed by a washing step and, finally, a reaction with an alkaline solution containing Ni^{2+} cations.[3] Chen *et al.*, on the other hand, prepared SiO_2@MgAl-LDHs using a simple aqueous co-precipitation method without any pre-treatment.[8] They further tuned the LDH composition and the thickness of the LDH shell by varying the Mg:Al ratio of the reaction mixture. Zeolites@MgAl-LDHs have been prepared by similar co-precipitation methods.[1]

TiO_2@CoAl-LDHs have been prepared by Dou *et al.* using an aqueous urea hydrothermal method,[9] whereas He *et al.* prepared TiO_2@CoAl-LDHs using the urea reflux method.[10] Recently, Jo *et al.* synthesised TiO_2@NiAl-LDHs also using the urea hydrothermal method.[16] To the best of the author's knowledge, no examples of core-shell TiO_2@Ti-LDHs have been reported to date. Similarly, no TiO_2@LDH composites – or, more generally, no core@LDH hybrid materials – have been used in the photocatalytic oxidation of simple organic molecules. Instead, core-shell TiO_2@LDHs have been used in the photocatalytic CO_2 reduction,[16,17,20] the photo-degradation of organic molecules

and dyes,[24,25] and the photocatalytic water splitting reaction with emphasis on O_2 generation.[9]

In this Chapter, five different synthetic methods were considered for the synthesis of TiO_2@Ti-LDHs, and their properties (such as structure, morphology, composition, and band gaps) were studied. Finally, selected TiO_2@Ti-LDHs were used in the photocatalytic oxidation of diphenylmethanol, and their photocatalytic activity was compared to that of the equivalent mechanical mixture of TiO_2 and Ti-LDHs.

5.2 Synthetic methods and characterisation techniques

All the synthetic methods used in this Chapter to prepare the TiO_2@Ti-LDH core-shell materials are based on the synthetic methods developed, optimised and used to prepare the NiTi- and MgAlTi-LDHs, as outlined in Chapter 2. For the shell layer of these hybrid materials, only NiTi-LDHs with a Ni:Ti ratio of 4:1 (i.e. Ni_4Ti-LDHs) and MgAlTi-LDHs with an Al:Ti ratio of 3:1 (i.e. $Mg_{12}Al_3$Ti-LDHs) were considered. These materials, while not exhibiting the highest photocatalytic activity, show a high degree of crystallinity, and are therefore more likely to form well-defined shell layers on the TiO_2 cores than the less crystalline, albeit more photocatalytically active, Ti-LDHs with a higher Ti content. The reaction mixture (specifically, the amounts of reactants: TiO_2 and metal salt LDH precursors) was initially prepared so as to achieve a theoretical TiO_2:LDH ratio of 1:1 in the core-shell materials, where the ratio refers to the relative weights of the two components rather than their molar ratio. The required amounts of the metal salt LDH precursors in the reaction mixture were calculated based on the yields of the reactions used to prepare the pure Ti-LDHs, as outlined in Chapter 2. This ratio was subsequently also changed to 2:1 for selected synthetic methods.

Based on the findings in Chapter 2, five different synthetic methods were used to prepare TiO_2@$Mg_{12}Al_3$Ti-LDHs: aqueous co-precipitation at constant and variable pH, organic co-precipitation in ethanol and homogeneous precipitation under reflux (urea reflux) and hydrothermal conditions (urea hydrothermal). Similarly, four different synthetic methods were used to prepare the TiO_2@Ni_4Ti-LDHs: aqueous co-precipitation at constant and variable pH, organic co-precipitation in ethanol and the urea reflux method. Although the constant pH aqueous co-precipitation was previously determined to not be very suitable

for NiTi-LDH synthesis (as discussed in Section 2.3), this method was also used due to its effectiveness at preparing TiO_2@$Mg_{12}Al_3$Ti-LDHs.

Aside from the introduction of anatase TiO_2 into the reaction mixtures, all the synthetic methods were carried out as outlined in Chapter 2, with an initial ageing time of 18 hours, either at room temperature (for the TiO_2@$Mg_{12}Al_3$Ti-LDH products of the three co-precipitation methods), at 60 ºC (for the variable and constant pH aqueous co-precipitation TiO_2@Ni_4Ti-LDHs), at 80 ºC (for the organic co-precipitation TiO_2@Ni_4Ti-LDH) or at 100 ºC (for the two homogeneous precipitation methods). Additionally, the ageing time for selected synthetic methods was varied between 1, 4 and 18 hours to study the effect of ageing time on the formation of the core-shell materials.

All five synthetic methods (where viable) produced free-flowing pale green and white powders for TiO_2@NiTi- and TiO_2@MgAlTi-LDHs, respectively. More detailed synthetic method descriptions can be found in Chapter 7.

The purity and crystallinity of the TiO_2@Ti-LDH products were investigated by powder X-ray diffraction (PXRD). The successful formation of the core-shell materials was determined by transmission electron microscopy (TEM), which was also used to analyse the morphology of the TiO_2@Ti-LDH particles and the presence of any unbound 'free' LDH. The actual TiO_2:Ti-LDH ratios of selected core-shell materials and their discrepancy from the theoretically expected ones were estimated using thermogravimetric analysis (TGA). The band gaps of selected TiO_2@Ti-LDH core-shell materials were estimated using diffuse reflectance UV-visible spectroscopy (DRUV-vis) together with the Tauc plot graphical method.[22,26,27]

More detailed information regarding all analytical methods is listed in Chapter 7.

5.3 TiO_2@Ti-LDH synthesis and characterisation

5.3.1 TiO_2 characterisation

The core material (TiO_2 anatase powder) was analysed by PXRD and TEM, as shown in Figure 5.2. The PXRD pattern shows characteristic anatase reflections with intense 2θ diffraction peaks at 25º and 48º,[28,29] and a high degree of crystallinity as shown by the intense and sharp peaks in Figure 5.2a. In terms of morphology, TiO_2 consists of nanoparticles in the 50 – 200 nm diameter range, which tend to cluster together into small aggregates (Figure 5.2b)

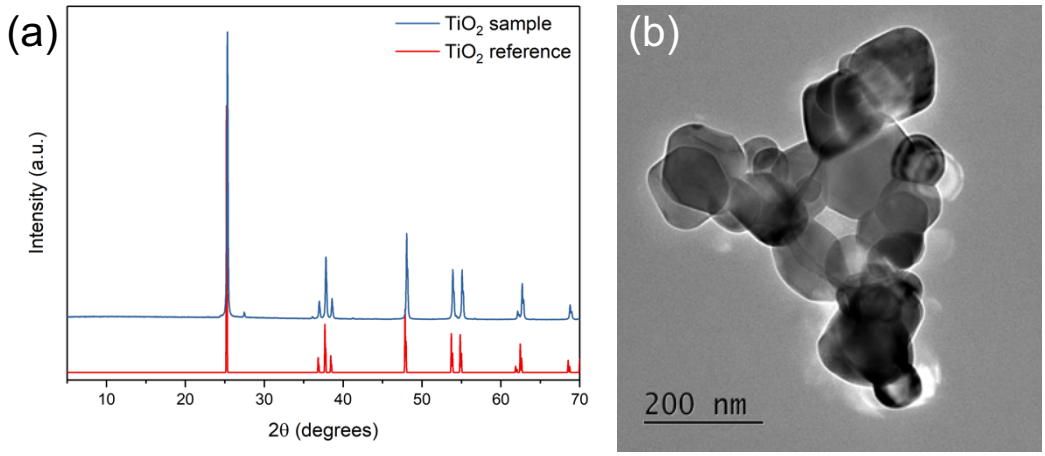


Figure 5.2 (a) The comparison of sample and reference anatase TiO_2 PXRD patterns. The reference pattern was taken from the RRUFF Database (RRUFF ID: R060277.9). (b) TEM image of TiO_2 anatase core material.

5.3.2 The effect of the synthetic method on TiO_2@Ni_4Ti-LDHs

The PXRD patterns of the TiO_2@Ni_4Ti-LDHs prepared by four different methods are shown in Figure 5.3. In all cases, the PXRD patterns show the presence of both TiO_2 and Ni_4Ti-LDHs, with the LDH crystallinity trend following that shown in Chapter 2 (Figure 2.1a). Specifically, the urea reflux method gives Ni_4Ti-LDHs with the highest degree of crystallinity, whereas the absence of the (00*l*) Bragg reflections in the PXRD

pattern of the organic co-precipitation product can be ascribed to both a lower crystallinity of the LDH, as well as its partial delamination during the synthesis in ethanol (Section 2.3).[30] No impurity formation was observed for any of the four samples, as the only PXRD reflections present are those of TiO_2 and NiTi-LDHs.

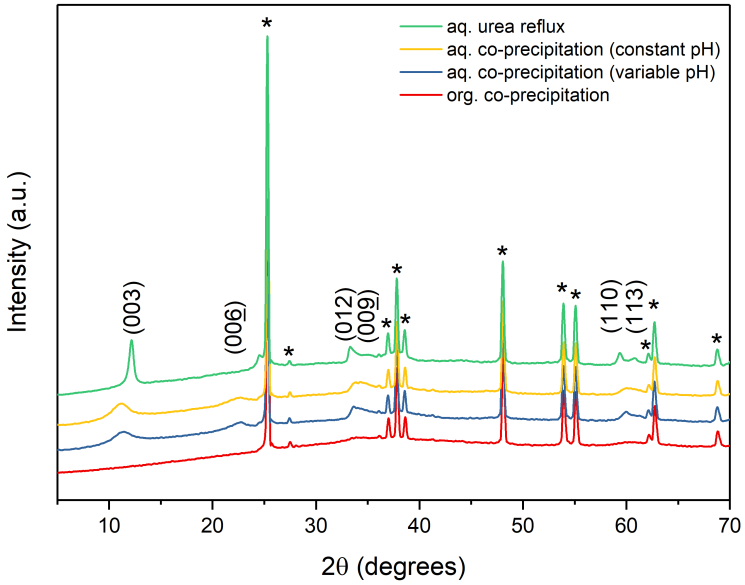


Figure 5.3 PXRD patterns of TiO_2@Ni_4Ti-LDHs prepared by the organic co-precipitation, aqueous co-precipitation at constant pH and variable pH, and urea reflux methods, with an ageing time of 18 hours in all cases. * denotes the TiO_2 anatase phase.

The successful formation of the core-shell TiO_2@Ni_4Ti-LDHs and their morphology was investigated using TEM, as shown in Figure 5.4. The organic co-precipitation and aqueous co-precipitation at constant pH are not suitable for TiO_2@Ni_4Ti-LDH core-shell preparation, as they give products with poor shell formation, with only a small number of Ni_4Ti-LDH sheets or platelets sparsely covering the TiO_2 surface (Figure 5.4a,b). The variable pH aqueous co-precipitation and urea reflux methods, on the other hand, show better results with a successful formation of core-shell particles (Figure 5.4c,d).

However, even the latter two methods give core-shell products with poor coverage, so that the LDH sheets (for variable pH aqueous co-precipitation) or platelets (for urea reflux) are unevenly distributed across the TiO_2 surface, with areas where no LDH particles have formed at all. Furthermore, in both methods, the alignment of the LDH

particles on the core is a mix of vertical and horizontal sheets/platelets, rather than the preferred arrangements where all the particles are vertically aligned on the surface, so as to maximise the surface area and the accessible active sites.[3,5] Additionally, significant amounts of unbound 'free' LDH are present in all four TiO_2@Ni_4Ti-LDH samples.[5]

It can therefore be concluded that the preparation of TiO_2@Ni_4Ti-LDHs core-shell particles with an even coverage of predominantly vertically aligned LDH particles is unfavourable under the synthetic conditions used in this work.

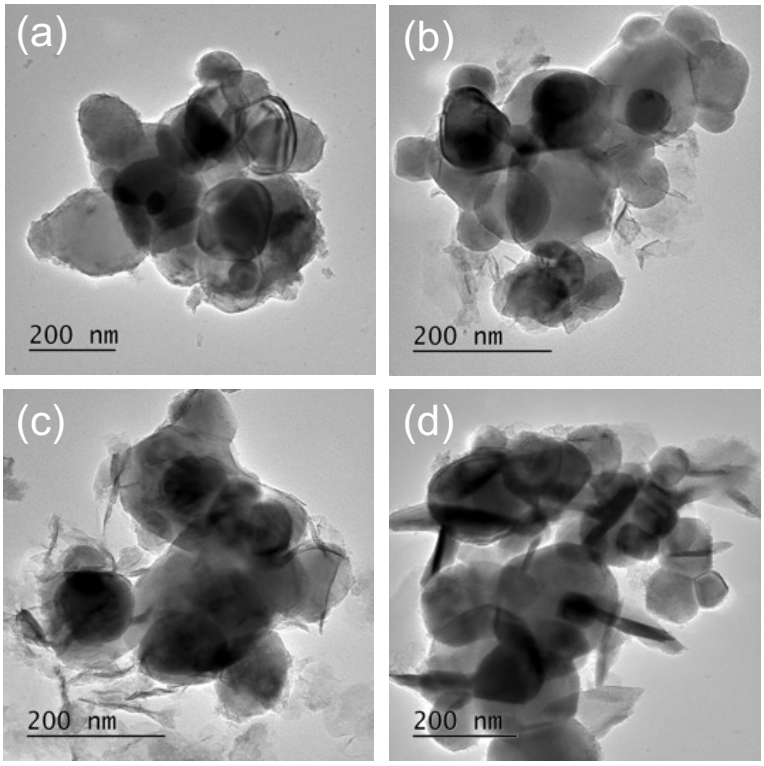


Figure 5.4 TEM images of TiO_2@Ni_4Ti-LDHs prepared by the (a) organic co-precipitation, (b) aqueous co-precipitation at constant pH and (c) variable pH, and (d) urea reflux methods, with an ageing time of 18 hours in all cases.

5.3.3 The effect of the synthetic method on TiO_2@$Mg_{12}Al_3$Ti-LDHs

The PXRD patterns of TiO_2@$Mg_{12}Al_3$Ti-LDHs prepared by five different synthetic methods are shown in Figure 5.5. All five products show the presence of both TiO_2 and MgAlTi-LDHs, with the crystallinity trend of the LDH phase following that of the separately synthesised MgAlTi-LDHs in Figure 2.1b. Specifically, the two homogeneous precipitation methods give LDHs with the highest degree of crystallinity, as evident from the intense and sharp (00*l*) PXRD peaks. The organic co-precipitation method, on the other hand, gives products that are less crystalline and/or partially delaminated, resulting in less intense (00*l*) Bragg diffractions.[30] With the exception of the urea hydrothermal core-shell product, none of the TiO_2@$Mg_{12}Al_3$Ti-LDHs show the presence of any crystalline impurities. The urea hydrothermal product contains a magnesite, $MgCO_3$, impurity phase, which was also observed in the separately synthesised urea hydrothermal MgAlTi-LDHs (Figure 2.10).

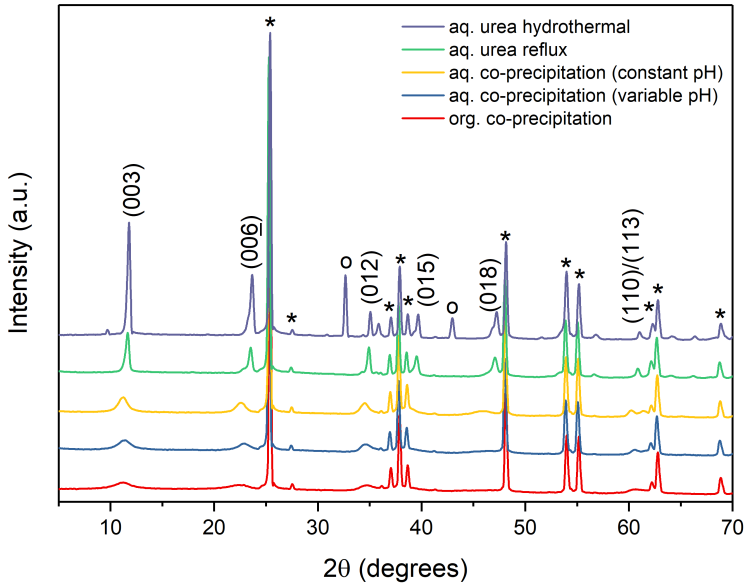


Figure 5.5 PXRD patterns of TiO_2@$Mg_{12}Al_3$Ti-LDHs prepared by the organic co-precipitation, aqueous co-precipitation at constant pH and variable pH, urea reflux and urea hydrothermal methods, with an ageing time of 18 hours in all cases. '*' denotes the TiO_2 anatase phase and 'o' denotes the magnesite, $MgCO_3$, impurity PXRD reflections.

In comparison to TiO_2@Ni_4Ti-LDHs, the $Mg_{12}Al_3$Ti-LDH equivalents on average show better core-shell formation, with a more even coverage of the TiO_2 cores. However, there are significant differences between the products prepared using the different synthetic methods, as seen in Figure 5.6.

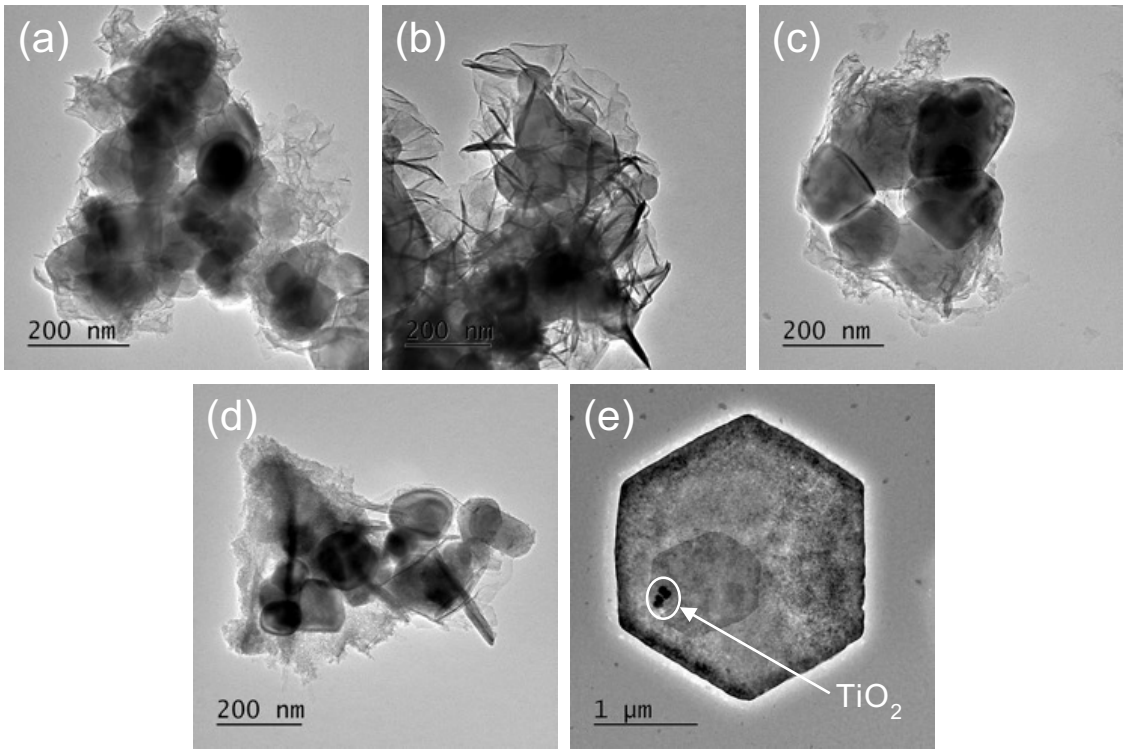


Figure 5.6 TEM images of TiO_2@$Mg_{12}Al_3$Ti-LDHs prepared by the (a) organic co-precipitation, (b) aqueous co-precipitation at constant pH and (c) variable pH, (d) urea reflux and (e) urea hydrothermal methods, with an ageing time of 18 hours in all cases.

The organic co-precipitation, variable pH aqueous co-precipitation and urea reflux methods produce shells predominantly comprised of small, irregularly shaped, thin nanosheets that do not show a regular alignment on the TiO_2 surface. In line with the morphology previously observed for the MgAlTi-LDHs prepared by the urea reflux method (Figure 2.12) and similarly to TiO_2@Ni_4Ti-LDH prepared by the same method, the urea reflux method product also contains some larger and thicker LDH platelets.

The urea hydrothermal TiO_2@$Mg_{12}Al_3$Ti-LDH product (Figure 5.6e), on the other hand, cannot be accurately classified as a core-shell material, due to the size of the large

hexagonal LDH platelets (> 1μm) in comparison to the TiO_2 nanospheres (< 200 nm) Instead, this product can be more accurately described as $Mg_{12}Al_3Ti$-LDH doped with TiO_2 nanoparticles. While this was not the targeted material, it might nonetheless possess interesting photocatalytic properties, as doping/impregnation with nanoparticles can be equally as effective at heterojunction formation and improved charge carrier separation as core-shell hybrid materials.[22,31-33]

The best core-shell formation was observed for the products of the constant pH aqueous co-precipitation (Figure 5.6b), which is the method frequently used to prepare core@LDH hybrid materials.[1,5] The product comprises TiO_2@$Mg_{12}Al_3Ti$-LDH core-shell particles with an even coverage and a shell thickness of about 100 nm. The shell comprises thin, irregularly shaped, thin nanosheets that are predominantly vertically aligned on the TiO_2 surface.

It should be noted that even in the case of the constant pH aqueous co-precipitation product, the analysis and charcterisation of the material is complicated due to the high aggregation of the TiO_2 particles. Therefore, instead of a single TiO_2 sphere or particle forming the core of the core-shell material, the core actually comprises several TiO_2 particles in the form of an aggregate.

5.3.4 The effect of the TiO_2:LDH ratio on TiO_2@$Mg_{12}Al_3Ti$-LDHs

Although it was found that the constant pH aqueous co-precipitation is the most suitable method for TiO_2@$Mg_{12}Al_3Ti$-LDH synthesis and that the product comprises little to no TiO_2 nanospheres that show no shell formation (Figure 5.7a), some unbound 'free' LDH was also observed, as shown in Figure 5.7b. In order to try to minimise the amount of 'free' LDH, the theoretical TiO_2:LDH ratio was changed from 1:1 to 2:1. The comparison of the PXRD patterns of the two products is shown in Figure D.1 in Appendix D.

However, this reduction in the amounts of metal salt LDH precursors in the reaction mixture resulted in a poorer shell formation, with a reduced density of LDH sheets on the TiO_2 surface, as well as TiO_2 nanospheres that show no shell formation at all (Figure 5.7c). Additionally, a small amount of unbound 'free' LDH that has nucleated away from a TiO_2 core was also observed in the sample, as shown in Figure 5.7d. It can therefore be concluded that while increasing the TiO_2:LDH ratio does slightly reduce the amount of 'free' LDH, it also compromises the shell formation of TiO_2@$Mg_{12}Al_3$Ti-LDH particles. Therefore, the initial TiO_2:LDH ratio of 1:1 was used in all subsequent experiments.

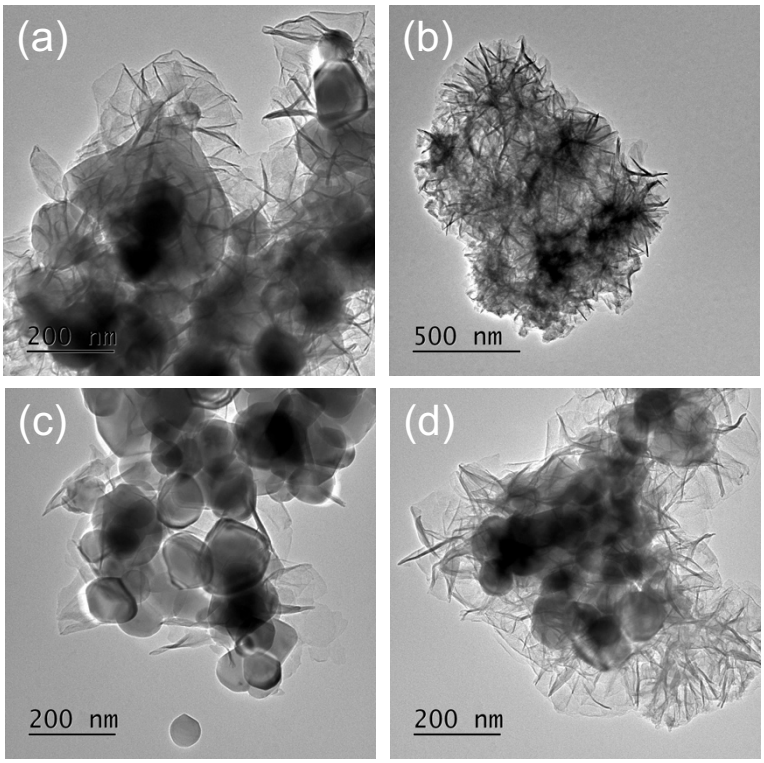


Figure 5.7 TEM images of TiO_2@$Mg_{12}Al_3$Ti-LDHs prepared by the constant pH aqueous co-precipitation method with a theoretical TiO_2:LDH ratio of (a,b) 1:1 and (c,d) 2:1.

5.3.5 The effect of the ageing time on TiO_2@$Mg_{12}Al_3$Ti-LDHs

Finally, the effect of ageing time on the constant pH aqueous co-precipitation TiO_2@$Mg_{12}Al_3$Ti-LDHs was studied. The TEM images of the products after 1, 4 and

18 hours of ageing at room temperature are shown in Figure 5.8 (the corresponding PXRD patterns of the products with different ageing times are shown in Figure D.2 in Appendix D). It can be seen that an ageing time of even just 1 hour is sufficient for the formation of core-shell particles with an even coverage of vertically aligned LDH nanosheets, giving a shell thickness of about 100 nm (Figure 5.8a).

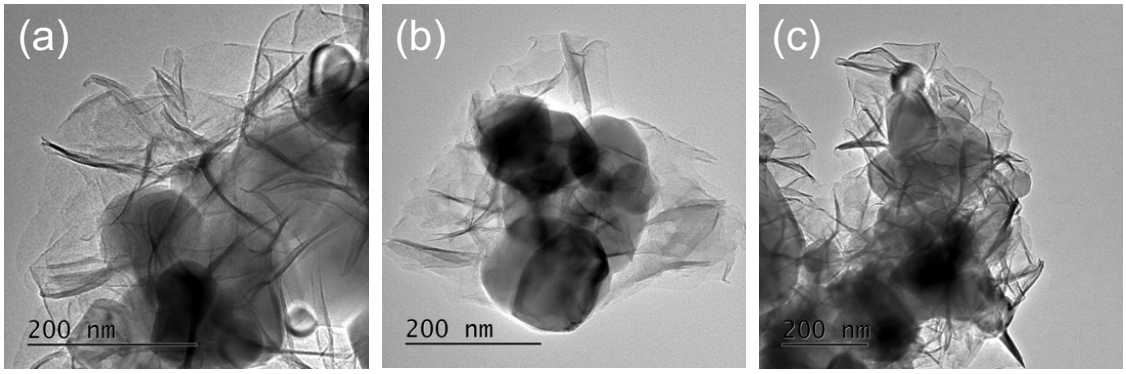


Figure 5.8 TEM images of TiO_2@$Mg_{12}Al_3$Ti-LDHs prepared by the aqueous co-precipitation method at constant pH, with an ageing time of (a) 1 hour, (b) 4 hours and (c) 18 hours.

When LDHs are synthesised in the absence of a core material, relatively long ageing times (12 hours or longer) are typically required to obtain products with a high level of crystallinity and well-defined morphology.[34] The precipitation process of an LDH can be roughly divided into two stages: the nucleation and the particle growth.[35] Specifically, the formation process of typical MgAl-LDH crystallites proceeds via an initial formation of aluminium hydroxide or hydrous oxide aggregates or nanoparticles (nucleation), followed by the formation of the LDH by the migration of Mg^{2+} cations into the structure and subsequent crystallite growth.[34,36] The formation of nuclei is an energetically activated (thermodynamically unfavourable) process and nucleation is frequently the rate determining step in the crystal formation process.[37]

However, when synthesising core-shell hybrid materials, the core particles provide nucleation sites,[1] thereby facilitating the rate determining nucleation step and shortening

the overall reaction time. Therefore, a shorter ageing time of only 1 hour is sufficient for core-shell formation. Prolonging the ageing time to 4 or 18 hours (Figure 5.8b,c) does not noticeably change the morphology of the core-shell particles, with the size of the $Mg_{12}Al_3Ti$-LDH shell particles, the thickness and density of the shell and the coverage staying approximately the same. Equally, the amounts of unbound 'free' LDH do not change significantly with ageing time.

Short ageing times are frequently observed in core@LDH synthesis. For example, Chen *et al.* and Kwok *et al.* all used an ageing time of 1 hour to prepare SiO_2@MgAl-LDHs,[5,8] whereas Lyu *et al.* similarly prepared zeolite@LDH and MOF@LDH hybrid materials with an ageing time of 1 hour.[14] Nonetheless, especially when using a homogeneous precipitation method, the ageing times used can be longer: Dou *et al.* aged the reaction mixture hydrothermally for 24 hour to prepare TiO_2@CoAl-LDHs,[9] and Wang *et al.* used an ageing time of 24 hours in the urea hydrothermal synthesis of TiO_2@MgAl-LDHs.[33]

5.4 Thermogravimetric analysis and composition of TiO_2@$Mg_{12}Al_3$Ti-LDHs

Thermogravimetric analysis (TGA) was used to estimate the composition of two representative TiO_2@$Mg_{12}Al_3$Ti-LDHs, and determine the differences between the theoretically predicted and the actual TiO_2:LDH ratios. Because MgAlTi-LDHs have been shown in Chapter 3 to be more active than NiTi-LDHs in the photo-oxidation of diphenylmethanol, and because the morphology of TiO_2@Ni_4Ti-LDHs is notably less well-defined and more irregular than that of the TiO_2@$Mg_{12}Al_3$Ti-LDHs, TiO_2@Ni_4Ti-LDHs have not been considered in any of the following analyses, nor have they been used in the photo-oxidation of diphenylmethanol (Section 5.6).

The two representative core-shell materials chosen were TiO_2@$Mg_{12}Al_3$Ti-LDHs prepared by the aqueous co-precipitation at constant pH and by the urea reflux method, as they show good coverage and shell formation (Figure 5.6b,d). Both materials chosen were prepared with a theoretical TiO_2:LDH ratio of 1:1 and aged for 18 hours.

The TGA plots of the two core-shell products are shown in Figure 5.9. It can be seen that TiO_2 shows a negligible weight loss in the 30 – 800 ºC range (the exact weight loss is only 0.5%). Accordingly, the weight loss of the core-shell material is predominantly due to the LDH weight loss on heating (which was discussed in Section 2.5, and is labelled in Figure 5.9a),[5] which can be used to estimate the LDH proportion in the core-shell material. This type of TGA plot, where the TGA curve of the core-shell material is intermediate between that of the separate core and shell materials, is typical of core@LDH composites.[1,8]

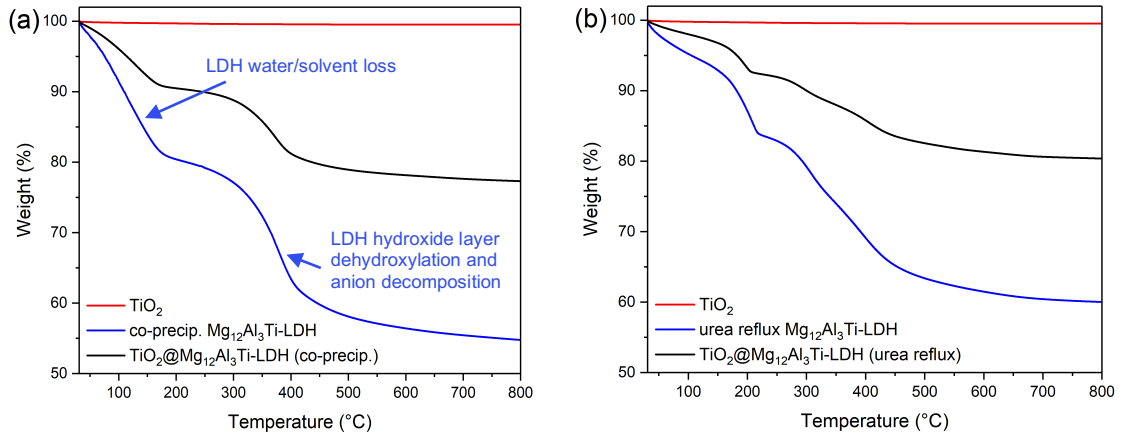


Figure 5.9 TGA plots of TiO_2, $Mg_{12}Al_3Ti$-LDH and the core-shell $TiO_2@Mg_{12}Al_3Ti$-LDH, the latter two prepared by the (a) aqueous co-precipitation at constant pH and (b) aqueous urea reflux method, with a theoretical TiO_2:LDH ratio of 1:1 and an ageing time of 18 hours in both cases.

To simplify the determination of the core-shell composition, it was assumed that the elemental composition of the shell is the same as that of the equivalent $Mg_{12}Al_3Ti$-LDHs synthesised separately, as listed in Table A.4 in Appendix A.

The estimated TiO_2:LDH ratios and core-shell compositions are summarised in Table 5.1. In terms of weight, the TiO_2 and MgAlTi-LDHs are present in the products in an approximately 1:1 ratio. Looking at the molar ratios, the constant pH aqueous co-precipitation product contains a larger amount of LDH, giving a TiO_2:LDH molar ratio of 1:0.78. The aqueous urea reflux product has a TiO_2:LDH molar ratio of 1:0.69.

Table 5.1 Estimated TiO_2:LDH ratios (both in terms of weight and molar ratios) and chemical formulae of $TiO_2@Mg_{12}Al_3Ti$-LDHs prepared by constant pH aqueous co-precipitation and urea reflux methods, both with a theoretical TiO_2:LDH weight ratio of 1:1.

Synthetic method	**TiO_2:LDH weight ratio (molar ratio)**	**Estimated chemical formula**
Co-precipitation	1:0.96 (1:0.78)	$TiO_2@[[Mg_{0.58}Al_{0.30}Ti_{0.12}(OH)_2](CO_3)_{0.27} \cdot 1.1H_2O]_{0.78}$
Urea reflux	1:0.91 (1:0.69)	$TiO_2@[[Mg_{0.46}Al_{0.41}Ti_{0.13}(OH)_2](CO_3)_{0.34} \cdot 0.9H_2O]_{0.69}$

It is therefore evident that the actual TiO_2:LDH ratios, as determined by TGA analysis, are in excellent agreement with the theoretically predicted weight ratio of 1:1, with the observed deviations being lower than 10%. It can therefore be concluded that the composition of the TiO_2@Ti-LDH hybrid core-shell materials, and more specifically the relative proportions of TiO_2 and Ti-LDH in the final product, can be easily controlled just by varying the relative amounts of the TiO_2 core and the LDH shell precursors in the reaction mixture.

It should be noted, however, that the TGA analysis does not differentiate between the LDH particles bound to the TiO_2 core in a core-shell material and the unbound 'free' LDH, the presence of which has been observed by TEM (Figure 5.7b). Therefore, part of the MgAlTi-LDH in the chemical formulae listed in Table 5.1 might actually be 'free' LDH, such that the actual TiO_2:LDH ratio of the core-shell material can be more accurately formulated as 1:(0.96 – x) and 1:(0.91 – x) for the aqueous co-precipitation and urea reflux products, respectively, where x refers to the weight of the 'free' LDH.

Nonetheless, so as to remain consistent with the terminology used in the Chapter up to this point, these core-shell products will be referred to as TiO_2@$Mg_{12}Al_3$Ti-LDHs in subsequent discussion, rather than by their estimated chemical formulae.

5.5 Band gaps of selected TiO_2@MgAlTi-LDHs

The band gap energies of the two representative TiO_2@$Mg_{12}Al_3$Ti-LDH core-shell products (prepared by constant pH aqueous co-precipitation and urea reflux methods, with 18 hours ageing time and a theoretical TiO_2:LDH ratio of 1:1) were analysed using UV-visible diffuse reflectance spectroscopy (DRUV-vis) in conjunction with the Tauc plot graphical method.[22,26,27] The application and the drawbacks of the Tauc plot method have been discussed previously in Section 2.6.

The absorbance DRUV-vis spectra of the core-shell materials, and their comparison to TiO_2 and the separately synthesised $Mg_{12}Al_3$Ti-LDH shell components, are shown in Figure 5.10. Both the absorbance spectra are normalised so that they have the same absorbance at 200 nm, to allow for comparison. The Tauc plots of the two core-shell materials are shown in Figure 5.11.

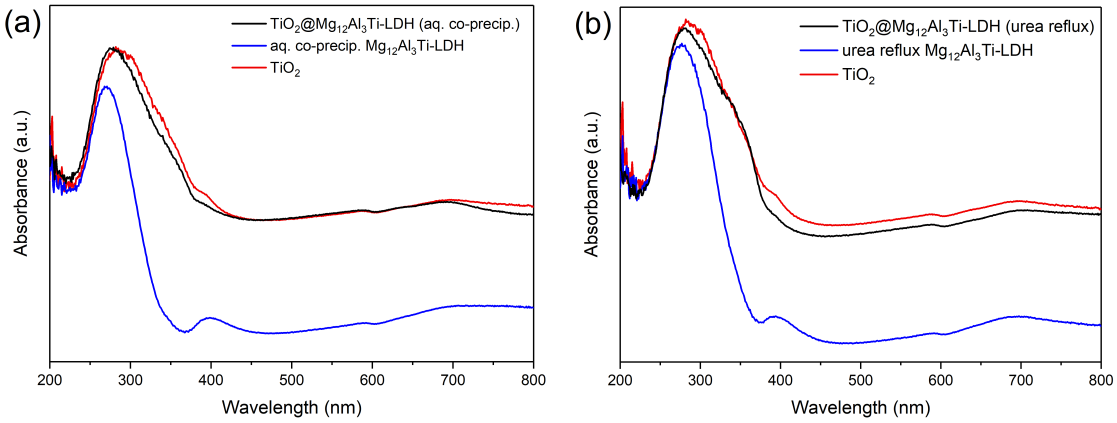


Figure 5.10 DRUV-vis plots of TiO_2, $Mg_{12}Al_3$Ti-LDH and the core-shell TiO_2@$Mg_{12}Al_3$Ti-LDH, the latter two prepared by the (a) aqueous co-precipitation at constant pH and (b) aqueous urea reflux methods, with a theoretical TiO_2:LDH ratio of 1:1 and an ageing time of 18 hours in both cases.

It can be seen that the absorbance of the core-shell materials more closely resembles that of the TiO_2 core than that of the $Mg_{12}Al_3$Ti-LDH shell. Specifically, the absorption profiles of TiO_2 and the two core-shell products are nearly identical both in terms of the

bands present and in terms of the absorption intensity. The two $Mg_{12}Al_3Ti$-LDH spectra, on the other hand, show a notably lower absorption for $\lambda > 350$ nm compared to the core-shell catalysts.

Kumar *et al.* have reported similar findings, with the TiO_2@LDH core-shell products exhibiting DRUV-vis spectra intermediate between those of their constituent components, albeit dominated by the TiO_2 component with its strong UV absorption.[17,20] Nonetheless, they have observed a weak visible light response from the CoAl-LDH shell particles. No such feature can be observed for the TiO_2@$Mg_{12}Al_3Ti$-LDHs in this work, as the pure (separately synthesised) $Mg_{12}Al_3Ti$-LDHs show no prominent bands in the visible spectrum, consistent with their band gap of about 3.4 eV and their appearance as a white powder.

Jo *et al.* have observed a DRUV-vis spectrum of their TiO_2@NiAl-LDH core-shell product which comprises features of the individual spectra of both the TiO_2 core and the NiAl-LDH shell components.[16] However, as above, the composite nature of the DRUV-vis spectrum is more evident for TiO_2@NiAl-LDHs than the core-shell materials in this work as NiAl-LDHs do exhibit intense absorption bands in the visible region, unlike MgAlTi-LDHs.

This similarity in DRUV-vis absorption spectra is carried further to the band gap energies, where the TiO_2@$Mg_{12}Al_3Ti$-LDHs have band gap energies in the 3.0 – 3.1 eV range, close to the band gap energy of TiO_2 anatase of 3.1 eV (Figure 5.12). This is notably lower than the band gap energies of the equivalent $Mg_{12}Al_3Ti$-LDHs for either synthetic method.

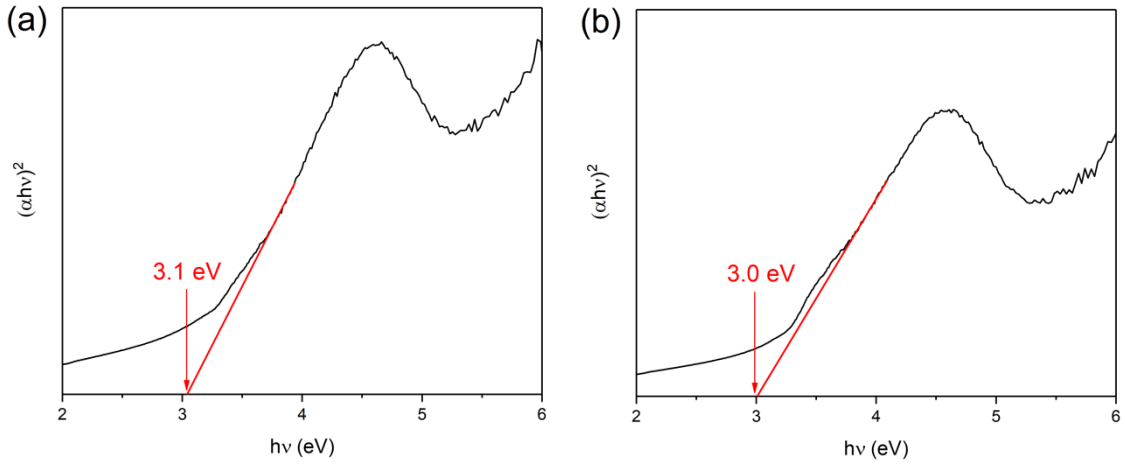


Figure 5.11 Tauc plots of the core-shell TiO_2@$Mg_{12}Al_3$Ti-LDHs prepared by the (a) aqueous co-precipitation at constant pH and (b) aqueous urea reflux methods, with a theoretical TiO_2:LDH ratio of 1:1 and an ageing time of 18 hours in both cases.

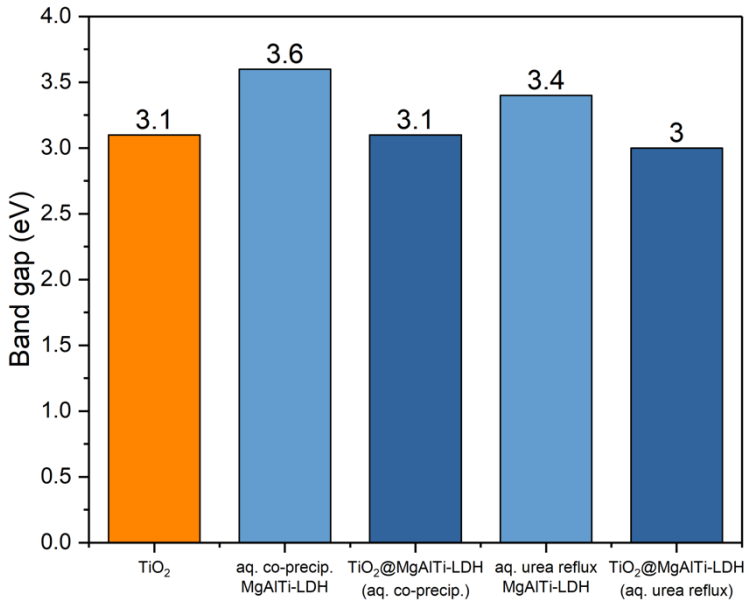


Figure 5.12 The comparison of band gap energies for representative core-shell TiO_2@$Mg_{12}Al_3$Ti-LDHs with those of TiO_2 and the individually synthesised $Mg_{12}Al_3$Ti-LDHs that are equivalent to the LDHs that make up the shell.

5.6 TiO_2@MgAlTi-LDHs in diphenylmethanol photo-oxidation

In order to study any potential synergistic heterojunction effects of the TiO_2@$Mg_{12}Al_3$Ti-LDH core-shell materials, the aqueous co-precipitation and urea reflux products, which were analysed in more detail in Sections 5.4 and 5.5, were used in the photo-oxidation of diphenylmethanol. The conversion to benzophenone with the core-shell photocatalysts was compared to that obtained with the 1:1 mechanical mixture of TiO_2 and $Mg_{12}Al_3$Ti-LDHs, where the 1:1 ratio refers to the weight of the compounds rather than their relative molar amounts (in order to be consistent with the TiO_2:LDH ratio of TiO_2@LDHs). For the best possible comparison, the $Mg_{12}Al_3$Ti-LDH in the mechanical mixture was prepared by the same synthetic method as the TiO_2@$Mg_{12}Al_3$Ti-LDH core-shell catalyst.

The photo-reactor setup used was the same as that outlined in Chapter 3: an immersion well photo-reactor with a 125 W medium pressure mercury UV lamp, separated from the reaction mixture by a borosilicate immersion well that eliminates all irradiation below 300 nm (Figure 3.2). All reaction mixtures were sonicated for 15 minutes before reaction and stirred at 1,000 rpm throughout the irradiation period to ensure proper dispersion of the solid catalysts and prevent sedimentation. The oxygen flow rate through the reaction mixture was kept constant at 70 cm^3min^{-1} and the solvent used was acetonitrile, with the solvent volume kept constant at 100 mL. The irradiation time was 1 hour.

The reactant (diphenylmethanol) concentration was kept constant at 100 mM and the TiO_2@$Mg_{12}Al_3$Ti-LDH catalyst loading was 25 mg, the optimal value found for MgAlTi-LDHs in Chapter 3. Accordingly, the mechanical mixture of the two catalysts comprised 12.5 mg of TiO_2 and 12.5 mg of $Mg_{12}Al_3$Ti-LDH.

The diphenylmethanol photo-oxidation product mixture was analysed by ^{1}H NMR spectroscopy in $CDCl_3$. The conversion of diphenylmethanol to benzophenone was then determined as outlined in Chapter 3, by the integration of the 5.9 ppm ^{1}H NMR resonance of diphenylmethanol (corresponding to the Ph_2-C<u>H</u>OH proton) and the 7.8 ppm resonance of benzophenone (corresponding to the four *ortho* protons on the aromatic rings). As in Chapter 3, the conversion (expressed as a percentage, %) of diphenylmethanol to benzophenone was calculated as follows:

$$Conversion\ (\%) = \frac{n(benzophenone)_{final}}{n(diphenylmethanol)_{final} + n(benzophenone)_{final}} \times 100\%$$

where $n(A)_{final}$ refers to the amount of compound A in the product mixture, as inferred from the integration of the ^{1}H NMR resonances outlined above.

The photocatalytic conversion of diphenylmethanol to benzophenone with the aqueous co-precipitation and urea reflux TiO_2@$Mg_{12}Al_3$Ti-LDH core-shell products is shown in Figure 5.13, and compared to that obtained with a $Mg_{12}Al_3$Ti-LDH + TiO_2 mechanical mixture. It can be seen that while the conversion obtained with the core-shell products is higher than that in the absence of a catalyst, it is nonetheless lower than that obtained with a mechanical mixture of the two separate catalysts.

This indicates that there is no synergy and no heterojunction formation in the particular case of these specific TiO_2@MgAlTi-LDHs. This result is the opposite of many literature findings, where TiO_2@LDH hybrid materials exhibited a greatly enhanced photocatalytic activity compared to the individual components, in reactions such as CO_2 photo-reduction.[16,17,20] In those findings, the enhanced activity was ascribed to a larger surface area, a stronger light-harvesting ability (spanning both the UV and the visible parts of the

electromagnetic spectrum where relevant), and the matching of the semiconductor band structures combined with strong donor-acceptor coupling (i.e. heterojunction formation).

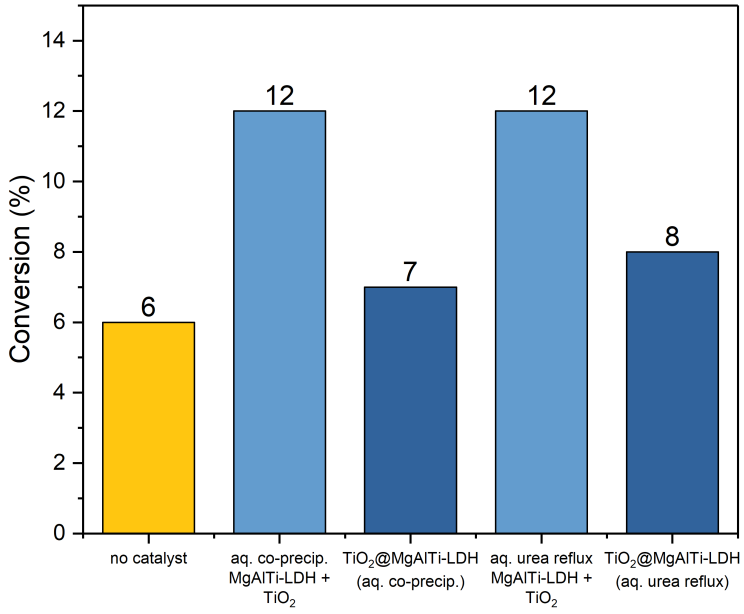


Figure 5.13 Photocatalytic conversion of diphenylmethanol to benzophenone after 1 hour of UV irradiation with aqueous co-precipitation and urea reflux TiO_2@$Mg_{12}Al_3$Ti-LDH core-shell catalysts and the mechanical mixture equivalents, including the comparison to the reaction without a catalyst.

Since no such improvement in the photocatalytic activity was observed in this work, it can be inferred that the band structure of the $Mg_{12}Al_3$Ti-LDH shell was an unsuitable match for the band structure of the TiO_2 core and no heterojunction could be established.[17] More detailed analysis, including the determination of the valence and conduction band edges, would be required to confirm this hypothesis with certainty.

Additionally, core-shell photocatalysts typically show a reduced charge carrier recombination rate as a consequence of heterojunction formation (typically quantified by time-resolved or steady state photoluminescence).[16,17,20] Considering that no improvement in photocatalytic activity on core-shell formation was observed in this work, it is likely that no such reduction in charge carrier recombination occurs for the two TiO_2@$Mg_{12}Al_3$Ti-LDHs used in the photo-oxidation reactions outlined above.

5.7 Conclusions

Nine different TiO_2@Ni_4Ti- and TiO_2@$Mg_{12}Al_3Ti$-LDH core-shell hybrid materials were synthesised using a total of five different synthetic methods: aqueous co-precipitation at constant and variable pH, organic co-precipitation, and homogeneous precipitation under reflux (urea reflux) and hydrothermal conditions (urea hydrothermal). While TiO_2@Ni_4Ti-LDHs largely exhibit poor shell formation, TiO_2@$Mg_{12}Al_3Ti$-LDHs were successfully synthesised with the constant pH aqueous co-precipitation and urea reflux methods. The constant pH aqueous co-precipitation product in particular comprises core-shell particles with an even coverage of predominantly vertically aligned LDH nanosheets.

The effects of the TiO_2:LDH ratio and ageing time were also explored. It was found that the TiO_2:LDH ratio can be used to control the density of the core coverage, although it does not allow the fine-tuning of the amount of unbound 'free' LDH present. Furthermore, it was shown that a shorter ageing time of only 1 hour is sufficient to form core-shell products with a good coverage of vertically aligned, crystalline LDH particles. This was ascribed to the fact that the TiO_2 core particles provide nucleation sites, which facilitate the rate determining nucleation step and thus shorten the overall LDH synthesis reaction time.

The determination of the approximate chemical formulae of selected TiO_2@$Mg_{12}Al_3Ti$-LDHs showed that good control over the core-shell composition is possible, with the experimentally determined TiO_2:LDH ratio being in excellent agreement with the theoretically predicted one.

Finally, the optical properties (DRUV-vis absorption spectra and band gap energies) of the aqueous co-precipitation and urea reflux TiO_2@$Mg_{12}Al_3$Ti-LDH core-shell products were analysed, and the two products were then used in the photocatalytic oxidation of diphenylmethanol. The photocatalytic conversion with the core-shell catalysts was compared to that obtained with the mechanical mixture of the separate core and shell components. It was found that the core-shell catalysts exhibit a lower photocatalytic activity than the mechanical mixture, indicating that no heterojunction synergistic effects are present.

Nonetheless, this Chapter shows the successful synthesis of a novel range of TiO_2@Ti-LDH core-shell compounds which, to the best of the author's knowledge, have not been synthesised to date. The synthetic methods allow good control over the product properties and should enable further research into potential TiO_2@Ti-LDH photocatalysts with a better band structure alignment of the core and shell components, such that an enhanced photocatalytic performance can be obtained.

Specifically, the focus of any subsequent studies into a better band alignment should be, firstly, to analyse the position of the valence band maxima and conduction band minima of the two core-shell components (the Ti-LDH shell and the TiO_2 core) and, secondly, to correctly select the Ti-LDHs that allow the optimal charge carrier separation though heterojunction formation. For example, organic molecule photo-oxidation (which requires the involvement of both charge carriers) would be optimised with a straddling heterojunction, whereas water splitting with focus on either hydrogen or oxygen evolution (where only the electrons or holes are required for the main reaction) would require a staggered heterojunction.[38]

5.8 References

1 C. Chen, C. F. H. Byles, J.-C. Buffet, N. H. Rees, Y. Wu and D. O'Hare, *Chem. Sci.*, 2016, **7**, 1457–1461.
2 H. Zhang, G. Zhang, X. Bi and X. Chen, *J. Mater. Chem. A*, 2013, **1**, 5934–5942.
3 M. Shao, F. Ning, Y. Zhao, J. Zhao, M. Wei, D. G. Evans and X. Duan, *Chem. Mater.*, 2012, **24**, 1192–1197.
4 Y. Ni, L. Yao, Y. Wang, B. Liu, M. Cao and C. Hu, *Nanoscale*, 2017, **9**, 11596–11604.
5 W. L. J. Kwok, D.-G. Crivoi, C. Chen, J.-C. Buffet and D. O'Hare, *Dalton Trans.*, 2018, **47**, 143–149.
6 Q. Guo, Q. Zhang, H. Wang, Z. Liu and Z. Zhao, *Catalysis Communications*, 2016, **77**, 118–122.
7 X. Ji, W. Zhang, L. Shan, Y. Tian and J. Liu, *Sci. Rep.*, 2015, **5**, 6333–10.
8 C. Chen, R. Felton, J.-C. Buffet and D. O'Hare, *Chem. Commun.*, 2015, **51**, 3462–3465.
9 Y. Dou, S. Zhang, T. Pan, S. Xu, A. Zhou, M. Pu, H. Yan, J. Han, M. Wei, D. G. Evans and X. Duan, *Adv. Funct. Mater.*, 2015, **25**, 2243–2249.
10 X. He, F. Wang, H. Liu, L. Niu and X. Wang, *J Am Ceram Soc*, 2018, **38**, 5707.
11 M. Shao, F. Ning, M. Wei, D. G. Evans and X. Duan, *Adv. Funct. Mater.*, 2013, **24**, 580–586.
12 N. T. H. Trang, H. V. Ngoc, N. Lingappan and D. J. Kang, *Nanoscale*, 2014, **6**, 2434–2439.
13 H. Jiang, K.-I. Katsumata, J. Hong, A. Yamaguchi, K. Nakata, C. Terashima, N. Matsushita, M. Miyauchi and A. Fujishima, *Appl. Catal., B*, 2018, **224**, 783–790.
14 M. Lyu, C. Chen, J.-C. Buffet and D. O'Hare, *New J. Chem.*, 2020, **44**, 10095–10101.
15 S. Liu, S. C. Lee, U. Patil, I. Shackery, S. Kang, K. Zhang, J. H. Park, K. Y. Chung and S. Chan Jun, *J. Mater. Chem. A*, 2017, **5**, 1043–1049.
16 W.-K. Jo, S. Moru and S. Tonda, *J. Mater. Chem. A*, 2020, **8**, 8020–8032.
17 S. Kumar, M. A. Isaacs, R. Trofimovaite, L. Durndell, C. M. A. Parlett, R. E. Douthwaite, B. Coulson, M. C. R. Cockett, K. Wilson and A. F. Lee, *Appl. Catal., B*, 2017, **209**, 394–404.
18 J. Schneider, M. Matsuoka, M. Takeuchi, J. Zhang, Y. Horiuchi, M. Anpo and D. W. Bahnemann, *Chem. Rev.*, 2014, **114**, 9919–9986.
19 C. Wang, B. Ma, S. Xu, D. Li, S. He, Y. Zhao, J. Han, M. Wei, D. G. Evans and X. Duan, *Nano Energy*, 2017, **32**, 463–469.
20 S. Kumar, L. J. Durndell, J. C. Manayil, M. A. Isaacs, C. M. A. Parlett, S. Karthikeyan, R. E. Douthwaite, B. Coulson, K. Wilson and A. F. Lee, *Part. Part. Syst. Charact.*, 2017, **35**, 1700317.
21 Y. Ao, D. Wang, P. Wang, C. Wang, J. Hou and J. Qian, *Mater. Res. Bull.*, 2016, **80**, 23–29.
22 R. Lu, X. Xu, J. Chang, Y. Zhu, S. Xu and F. Zhang, *Appl. Catal., B*, 2012, **111-112**, 389–396.
23 B. Lin, P. Sun, Y. Zhou, S. Jiang, B. Gao and Y. Chen, *Journal of Hazardous Materials*, 2014, **280**, 156–163.
24 F. Aoudjit, O. Cherifi and D. Halliche, *Separation Science and Technology*, 2018, **54**, 1095–1105.
25 M. Hadnadjev-Kostic, T. Vulic, R. Marinkovic-Neducin, D. Lončarević, J.

Dostanić, S. Markov and D. Jovanović, *Journal of Cleaner Production*, 2017, **164**, 1–18.
26 B. D. Viezbicke, S. Patel, B. E. Davis and D. P. Birnie III, *Phys. Status Solidi B*, 2015, **252**, 1700–1710.
27 N. Baliarsingh, L. Mohapatra and K. Parida, *J. Mater. Chem. A*, 2013, **1**, 4236–4243.
28 H. Ijadpanah-Saravy, M. Safari, A. Khodadadi-Darban and A. Rezaei, *Analytical Letters*, 2014, **47**, 1772–1782.
29 M. Kong, Y. Li, X. Chen, T. Tian, P. Fang, F. Zheng and X. Zhao, *J. Am. Chem. Soc.*, 2011, **133**, 16414–16417.
30 Q. Wang and D. O'Hare, *Chem. Commun.*, 2013, **49**, 6301–6303.
31 Š. Paušová, J. Krýsa, J. Jirkovský, G. Mailhot and V. Prévot, *Environ Sci Pollut Res*, 2012, **19**, 3709–3718.
32 R. Djeda, G. Mailhot and V. Prévot, *ChemEngineering*, 2020, **4**, 39.
33 L. Wang, X. Gao, Y. Cheng, X. Zhang, G. Wang, Q. Zhang and J. Su, *J. Photochem. Photobiol., A*, 2019, **369**, 44–53.
34 Y. Yang, X. Zhao, Y. Zhu and F. Zhang, *Chem. Mater.*, 2012, **24**, 81–87.
35 M. Adachi-Pagano, C. Forano and J.-P. Besse, *J. Mater. Chem.*, 2003, **13**, 1988–1993.
36 S. K. Sharma, P. K. Kushwaha, V. K. Srivastava, S. D. Bhatt and R. V. Jasra, *Ind. Eng. Chem. Res.*, 2007, **46**, 4856–4865.
37 W. J. Kim, S. D. Kim, H. S. Jung and D. T. Hayhurst, *Microporous Mesoporous Mater.*, 2002, **56**, 89–100.
38 H. Li, Y. Zhou, W. Tu, J. Ye and Z. Zou, *Adv. Funct. Mater.*, 2015, **25**, 998–1013.

Chapter 6 Conclusions and outlook

The work outlined in this thesis has focused on the development of novel titanium-containing layered double hydroxides, Ti-LDHs, and their application in photocatalysis, specifically in the photo-oxidation of simple organic molecules.

Five different synthetic methods were optimised and investigated for their viability in preparing NiTi- and MgAlTi-LDHs. The two different aqueous co-precipitation methods (at constant and variable pH) were based on previously reported literature procedures,[1,2] with adaptations that prevented the precipitation of Ti^{4+} cations in the form of insoluble TiO_2 even in an aqueous solution. A novel non-aqueous equivalent to the variable pH co-precipitation was developed, where the synthesis is carried out in ethanol with sodium ethoxide, NaOEt, used as the base alternative to the commonly used sodium hydroxide, NaOH. This method was found to produce highly delaminated LDHs with a specific surface area as high as 326 m^2g^{-1}, thus presenting a new one-pot method for preparing high-surface-area layered materials.

The crystallinity and morphology of the Ti-LDH products were found to be highly dependent on the synthetic method, with the homogeneous precipitation methods (urea reflux and urea hydrothermal) resulting in LDH products with the highest degree of crystallinity and well-defined particle morphology. The urea hydrothermal MgAlTi-LDHs, in particular, comprise well-defined hexagonal platelets with diameters in excess of 1 μm, which were further analysed by high-angle annular dark-field microscopy (HAADF) and solid state nuclear magnetic resonance spectroscopy (ssNMR). The former showed that although the products are highly crystalline, the dispersion of the Ti centres within their particles is uneven with localised areas of high and low Ti density. ^{1}H, ^{27}Al and $^{49/49}Ti$ ssNMR spectra of the $Mg_{12}AlTi_3$-LDH product also confirmed its highly

ordered structure through the presence of a relatively large number of well-resolved ssNMR peaks. These indicate that the structure of the ternary MgAlTi-LDHs is rather complex, with the number of different ^{1}H, ^{27}Al and $^{47/49}Ti$ chemical environments being larger than expected based on previous literature reports.

The effect of the Ti content was also investigated by varying the Ni:Ti and Al:Ti ratio in NiTi- and MgAlTi-LDHs, respectively. A clear trend was observed, where a higher Ti content results in a lower crystallinity and a less well-defined particle morphology. Overall, it was determined that the developed synthetic methods allow good control over the Ti-LDH properties by means of controlling the reaction conditions and the relative amounts of the LDH precursor metal salts in the reaction mixture.

The application of LDHs as semiconductor photocatalysts in the controlled oxidation of organic molecules has not been extensively studied, with only a very limited number of literature reports available. In order to study the efficiency of NiTi- and MgAlTi-LDHs in organic molecule photo-oxidation, diphenylmethanol was chosen as a simple model compound due to the fact that as a secondary alcohol with only one functional group that can be oxidised, the likelihood of side product formation is very low.

It was found that high-energy, short-wavelength ($\lambda < 300$ nm) UV radiation can result in photo-oxidation taking place even in the absence of a photocatalyst – an observation that, to the best of the author's knowledge, has not been reported previously. Using a borosilicate immersion well in the photo-reactor setup, which eliminates all radiation below 300 nm, allowed effective photocatalyst screening. This, in turn, showed that the homogeneous precipitation methods and a higher Ti content correspond to the highest activity. Consequently, the urea reflux Ni_2Ti-LDH and the urea hydrothermal $Mg_{12}AlTi_3$-LDH were studied further as the best representative photocatalysts.

The Ni_2Ti-LDH was found to be less active than the $Mg_{12}AlTi_3$-LDH, although both gave a conversion of diphenylmethanol to benzophenone that was comparable to that of anatase TiO_2, which was used as a benchmark comparison due to the fact that it is the most widely studied photocatalyst. Looking at the catalytic activity per Ti centre, it was found that Ti-LDHs are significantly more active than TiO_2 when their activity (i.e. the conversion) is normalised relative to their Ti content, which was previously shown to play a crucial role in determining the photocatalytic activity of the Ti-LDHs.

Although tentative hypotheses for the observed activity trends have been suggested, based on the characterisation of the prepared Ti-LDHs and the literature available to date, a deeper understanding of the Ti-LDH activity can be obtained through additional analysis, such as transient fluorescence or photoluminescence measurements (to determine any differences in the charge carrier recombination rate between different Ti-LDHs),[3-5] XPS and XANES analysis (to determine the presence of different Ti oxidation states),[5] valence and conduction band edge determination (e.g. through the Mott-Schottky analysis),[6,7] and computational modelling.

By varying the catalyst loading, it was further determined that the observed photocatalytic activity (in terms of the conversion to benzophenone) of the photocatalysts is a balance of two effects: the inherent photocatalytic activity of the material and the reduced transparency of the reaction mixture as the amount of catalyst is increased. Using the optimised catalyst loading and reactant concentration, the kinetics of diphenylmethanol photo-oxidation with urea hydrothermal $Mg_{12}AlTi_3$-LDH were investigated, with an observed conversion of 83% after 6 hours of UV irradiation.

The same optimised catalyst loadings and reactant concentration were used further to investigate the effectiveness of the urea reflux Ni_2Ti-LDH and urea hydrothermal

$Mg_{12}AlTi_3$-LDH in photo-oxidising other simple aromatic and aliphatic reactants, specifically benzyl alcohol, cyclooctanol and benzylamine. The photo-oxidation of benzyl alcohol was the most complex out of the three due to over-oxidation to benzoic acid, which then further reacts with the benzyl alcohol present in the reaction mixture to form benzyl benzoate.

The comparison of the four different photo-oxidation reactants studied in this thesis allowed the following conclusions to be made: (1) aromatic reactants show a higher conversion to photo-oxidised products due to the additional driving force of extending the conjugated system, (2) primary alcohols have a higher initial rate of photo-oxidation than secondary alcohols, and (3) the photocatalytic system used in this work is better suited to the photo-oxidation of alcohols than to that of amines.

This research can be extended beyond the scope outlined in this thesis, for example by considering reactants with additional functional groups. This should allow the study of the effects of electron-donating and electron-withdrawing groups on the conversion, as well as the study of potential selectivity issues if more than one functional group within a molecule can be oxidised. Furthermore, other functional groups, such as alkenes, could also be considered so as to extend the range of reactants even further.

Finally, the semiconductor photocatalysts TiO_2 and Ti-LDHs were combined into a single hybrid material though the synthesis of TiO_2@Ti-LDH core-shell products, with the aim to investigate possible synergistic heterojunction effects. However, preliminary studies into diphenylmethanol photo-oxidation showed that the specific TiO_2@Ti-LDHs studied in this work gave a lower photocatalytic activity than the corresponding mechanical mixture of TiO_2 and Ti-LDHs. Nonetheless, a novel range of TiO_2@Ti-LDH core-shell materials has been successfully synthesised, with good control over the product

properties. The synthetic methods used should therefore allow the preparation of other potential TiO_2@LDH photocatalysts with better core-shell band structure alignment, such that an enhanced photocatalytic performance can be obtained. The newly developed synthetic methods could also be applied to the synthesis of other core@Ti-LDH hybrid materials, where the core is another semiconductor photocatalyst, such as ZnO.

Many of the photocatalysts synthesised as part of this work (as well as the methods used to obtain them) have not been reported previously. This thesis has explored only a small part of their potential applications in the world of photocatalysis. The research started in this work can thus be extended to also include CO_2 photo-reduction and photocatalytic water splitting, where other LDHs have previously been shown to be active.

In the medium term, the work outlined in this thesis can be used to direct the synthesis of novel photocatalysts. For example, MgAlTi- and NiTi-LDHs with metal compositions that were not prepared as part of this work, Ti-LDHs with other M(II) and/or M(III) cations in the metal hydroxide layers, mixed metal oxides obtained through the calcination of the Ti-LDHs presented in this work, TiO_2@LDH core-shell materials with a variety of different LDH metal compositions (chosen for their appropriate band structure so as to achieve optimal band alignment), core@Ti-LDH core-shell materials with a variety of different photocatalytically active core materials, and more. All of these different photocatalysts can be potentially prepared using the methods outlined in this thesis, and then applied to organic molecule photo-oxidation and other photocatalytic reactions of interest.

References

1 C. Chen, A. Wangriya, J.-C. Buffet and D. O'Hare, *Dalton Trans.*, 2015, **44**, 16392–16398.
2 C. Chen, M. Yang, Q. Wang, J.-C. Buffet and D. O'Hare, *J. Mater. Chem. A*, 2014, **2**, 15102–15110.
3 N. Baliarsingh, L. Mohapatra and K. Parida, *J. Mater. Chem. A*, 2013, **1**, 4236–4243.
4 B. Li, Y. Zhao, S. Zhang, W. Gao and M. Wei, *ACS Appl. Mater. Interfaces*, 2013, **5**, 10233–10239.
5 Y. Zhao, B. Li, Q. Wang, W. Gao, C. J. Wang, M. Wei, D. G. Evans, X. Duan and D. O'Hare, *Chem. Sci.*, 2014, **5**, 951–958.
6 S. Iguchi, S. Kikkawa, K. Teramura, S. Hosokawa and T. Tanaka, *Phys. Chem. Chem. Phys.*, 2016, **18**, 13811–13819.
7 G. Zhang, B. Lin, W. Yang, S. Jiang, Q. Yao, Y. Chen and B. Gao, *RSC Adv.*, 2015, **5**, 5823–5829.

Chapter 7 Experimental details

7.1 Analytical techniques for LDH characterisation

The analytical techniques are listed below in the alphabetical order, not in the order in which they first appear in Chapters 2 – 6.

7.1.1 Diffuse reflectance UV-visible spectroscopy (DRUV-vis)

DRUV-vis spectra were recorded on an Agilent Cary 4000 UV Vis spectrometer fitted with the Pike Veemac Diffuse IR accessory that allows diffuse reflective UV-vis measurements of powder samples. The samples were loaded into a crucible and the instrument was set to record absorption in the 200 – 900 nm range.

7.1.2 Fourier transform infrared (FTIR) spectroscopy

Part of the FTIR spectra were recorded on a ThermoScientific Nicolet iS5 spectrometer fitted with an iD3 ATR accessory. The instrument was set to record transmittance in the 700 – 4,000 cm^{-1} range with 50 scans at 4 cm^{-1} resolution. The other FTIR spectra were recorded on a Bruker VERTEX 80 spectrometer fitted with a DuraSamplIR II diamond ATR (attenuated total reflection) accessory. The instrument was set to record in the 500 – 4,000 cm^{-1} range with 50 scans at 4 cm^{-1} resolution. The diamond accessory gave rise to absorption bands in the 1,800 – 2,300 cm^{-1} range, but they did not interfere with the analysis.

7.1.3 High-angle annular dark-field imaging (HAADF)

The HAADF images were acquired by Dr Christopher Allen (Department of Materials, University of Oxford) at Diamond Light Source on a Jeol ARM200CF microscope with

an accelerating voltage of 200 kV. In all cases, a few milligrams of material were dispersed in ethanol using sonication, and then cast onto carbon films on copper grids (400 mesh, Agar Scientific) and allowed to air dry.

7.1.4 Inductively coupled plasma mass spectrometry (ICP-MS)

ICP-MS analysis was performed by Dr Alaa Abdul-Sada (University of Sussex). The analysis was conducted on 20 – 30 mg samples that were digested in concentrated nitric acid, HNO_3, and diluted. Each solution was analysed three times and the mean value was reported.

7.1.5 Powder X-ray diffraction (PXRD)

PXRD spectra were recorded on a PANalytical X'pert Pro Diffractometer operating at 40 kV/40 mA in reflection mode with Cu K_α radiation ($\alpha1$ = 1.540598 Å, $\alpha1$ = 1.54426 Å, weighted average = 1.541847 Å). Samples were placed into stainless steel sample holders, which were spun at 15 rpm during recording, and analysed in the 2θ range from 5.0100° to 72.9760° with a step size 0.0170º and a slit size of 1°. The stainless-steel holders gave rise to peaks at 2θ = 43.36º, 44.29º and 50.51º, which did not interfere with analysis.

7.1.6 Scanning electron microscopy (SEM) and scanning electron microscopy with energy-dispersive X-ray analysis (SEM-EDX)

SEM and SEM-EDX images were acquired by Dr Dana-Georgiana Crivoi (University of Oxford) at the Harwell Research Complex on a Jeol JSM-6100LV microscope with an accelerating voltage of 200 kV. Samples were prepared by dispersion in ethanol using sonication, and then cast onto carbon tabs and sputter-coated with a 10 nm platinum layer to facilitate imaging.

7.1.7 Solid state nuclear magnetic resonance (ssNMR) spectroscopy

High resolution ^{1}H, ^{27}Al and $^{47/49}Ti$ ssNMR spectra were obtained by Dr Nicholas H. Rees, Dr Jean-Charles Buffet and Dr Zoë R. Turner (all University of Oxford) and Dr Dinu Iuga (University of Warwick) at the UK 850 MHz Solid-State NMR Facility at the University of Warwick using the Bruker Avance Neo 850 MHz solid-state NMR spectrometer. The ^{1}H DP-MAS ssNMR measurements, recorded with background suppression and spin-echo pulse sequences,[1] and ^{27}Al DP-MAS ssNMR measurements used 1.3 mm OD rotors and a MAS rate of 60 kHz at 23 ºC. The $^{47/49}Ti$ ssNMR measurements used 7 mm OD rotors and were carried out at 23 ºC using a double frequency sweep spin-echo sequence either in a static mode or with a MAS rate of 5 kHz.

7.1.8 Surface area analysis

The specific surface area of the samples was determined by the Brunauer-Emmett-Teller (BET) method using the nitrogen (N_2) adsorption and desorption isotherms collected at 77 K on a Micromeritics TriStar II 3030 instrument. The samples were degassed at 110 ºC overnight before analysis.

7.1.9 Thermogravimetric analysis (TGA)

TGA was carried out on a Perkin Elmer TGA7 instrument. A few milligrams of sample were placed in a platinum crucible suspended from a platinum wire, which was weighed empty first. Sample mass was recorded under a continuous flow of N_2 from 30 to 800 °C at a rate of 5 °C/minute. At the start of the program several minutes at 30 °C were included to allow the sample mass to settle, and at the final temperature to ensure mass loss was complete.

7.1.10 Transmission electron microscopy (TEM) and transmission electron microscopy with energy-dispersive X-ray analysis (TEM-EDX)

TEM images were acquired at the Harwell Research Complex on a Jeol JEM-2100 microscope at an accelerating voltage of 200 kV. TEM-EDX images were acquired by Dr Haohong Duan (University of Oxford) at the David Cockayne Centre for Electron Microscopy (Department of Materials, University of Oxford) on a Jeol JEM-2100 microscope with an accelerating voltage of 200 kV. In all cases, a few milligrams of material were dispersed in ethanol using sonication, and then cast onto carbon films on copper grids (400 mesh, Agar Scientific) and allowed to air dry.

7.2 Analytical techniques for photo-oxidation conversion and selectivity calculations

7.2.1 Nuclear magnetic resonance (NMR) spectroscopy

Solution phase NMR spectra were recorded on a 400 MHz Bruker Avance III HD spectrometer. ^{1}H spectra were recorded at 298 K and referenced internally to the residual protio-solvent resonance in the deuterated solvent (deuterated chloroform, $CDCl_3$).

7.2.2 Ultraviolet-visible (UV-vis) spectroscopy

UV-vis measurements were taken on a Cary Series UV-vis spectrometer. The absorbance was measured at 365 nm. The dispersion of the catalyst in acetonitrile was shaken and a small amount transferred into a 1 cm quartz cuvette.

7.3 Experimental details for Chapter 2

7.3.1 Materials

Titanium isopropoxide ($Ti(O^iPr)_4$), nickel nitrate hexahydrate ($Ni(NO_3)_2 \cdot 6H_2O$), magnesium nitrate hexahydrate ($Mg(NO_3)_2 \cdot 6H_2O$), aluminium nitrate nonahydrate ($Al(NO_3)_3 \cdot 9H_2O$), concentrated hydrochloric acid (HCl, 37%), sodium hydroxide (NaOH), sodium carbonate (Na_2CO_3), sodium ethoxide (NaOEt, 21 wt% solution in ethanol), urea ($CO(NH_2)_2$) and ethanol (EtOH, ≥99.8%) were purchased from Sigma Aldrich and used without further purification.

7.3.2 Synthesis of NiTi-LDHs

Ni_4Ti-LDH: aqueous co-precipitation at constant pH

Ni_4Ti-LDH was synthesised by the constant pH aqueous co-precipitation method adapted from Chen *et al.*,[2,3] with adaptations for the synthesis of Ti-LDHs based on the work of Zhao *et al.*.[4] $Ti(O^iPr)_4$ (1.48 mL, 5.0 mmol) was added dropwise to 0.6 mL concentrated HCl under an inert nitrogen atmosphere, with stirring at 400 rpm. $Ni(NO_3)_2 \cdot 6H_2O$ (5.82 g, 20.0 mmol) was dissolved in 50 mL deionised (DI) water and added dropwise to the $Ti(O^iPr)_4$/HCl solution with stirring at 300 rpm.

Na_2CO_3 (1.59 g, 15.0 mmol) was dissolved in 50 mL DI water and the pH was adjusted to 10 by the dropwise addition of 4 M NaOH. The Ni^{2+}/Ti^{4+} solution was added dropwise to the Na_2CO_3 solution over the period of 1 hour with stirring at 500 rpm, and the pH of the precipitation was maintained at ~10 using 4 M NaOH solution. The resulting reaction mixture was aged in an oil bath at 60 °C for 18 hours with stirring at 650 rpm.

Ni_4Ti-LDH: aqueous co-precipitation at variable pH

Ni_4Ti-LDH was synthesised by the variable pH aqueous co-precipitation method adapted from the constant pH equivalent outlined above. $Ti(O^iPr)_4$ (1.48 mL, 5.0 mmol) was added dropwise to 0.6 mL concentrated HCl under an inert nitrogen atmosphere, with stirring at 400 rpm. $Ni(NO_3)_2 \bullet 6H_2O$ (5.82 g, 20.0 mmol) was dissolved in 50 mL DI water and added dropwise to the $Ti(O^iPr)_4$/HCl solution with stirring at 300 rpm.

Na_2CO_3 (1.59 g, 15.0 mmol) and NaOH (1.32 g, 33.0 mmol) were dissolved in 50 mL DI water and the resulting solution was added dropwise to the Ni^{2+}/Ti^{4+} solution over the period of 1 hour with stirring at 500 rpm, up to a final pH of ~10. The resulting reaction mixture was aged in an oil bath at 60 °C for 18 hours with stirring at 650 rpm.

Ni_4Ti-LDH: organic co-precipitation

Ni_4Ti-LDH was synthesised by the organic co-precipitation method adapted from the variable pH aqueous equivalent outlined above. $Ti(O^iPr)_4$ (1.48 mL, 5.0 mmol) was added dropwise to 0.6 mL concentrated HCl under an inert nitrogen atmosphere, with stirring at 400 rpm. $Ni(NO_3)_2 \bullet 6H_2O$ (5.82 g, 20.0 mmol) was dissolved in 50 mL ethanol, and added dropwise to the $Ti(O^iPr)_4$/HCl solution with stirring at 300 rpm.

NaOEt (19.0 mL of 21 wt% solution in ethanol, 50.0 mmol) was dissolved in a mixture of 5 mL DI water and 50 mL ethanol, and the resulting solution was added dropwise to the Ni^{2+}/Ti^{4+} solution over the period of 1 hour with stirring at 500 rpm. The resulting reaction mixture was aged in an oil bath at 80 °C for 18 hours with stirring at 650 rpm.

Ni_4Ti-LDH: aqueous urea reflux

Ni_4Ti-LDH was synthesised by the aqueous urea reflux method adapted from the homogeneous precipitation method used by Costantino *et al.*,[5] with adaptations for the synthesis of Ti-LDHs based on the work of Zhao *et al.*.[4] $Ti(O^iPr)_4$ (1.48 mL, 5.0 mmol) was added dropwise to 0.6 mL concentrated HCl under an inert nitrogen atmosphere, with stirring at 400 rpm. $Ni(NO_3)_2 \bullet 6H_2O$ (5.82 g, 20.0 mmol) was dissolved in 50 mL DI water and added dropwise to the $Ti(O^iPr)_4$/HCl solution with stirring at 300 rpm.

Urea (4.50 g, 75.0 mmol, [urea]:[metal salts] = 3:1) was dissolved in 50 mL DI water and added to the Ni^{2+}/Ti^{4+} solution. The resulting reaction mixture was aged under reflux conditions in an oil bath at 100 °C for 18 hours with stirring at 650 rpm.

Ni_4Ti-LDH: aqueous urea hydrothermal

Ni_4Ti-LDH was synthesised by the aqueous urea hydrothermal method adapted from the homogeneous precipitation method used by Ogawa e*t al*.,[6] with adaptations for the synthesis of Ti-LDHs based on the work of Zhao *et al.*.[4] $Ti(O^iPr)_4$ (1.18 mL, 4.0 mmol) was added dropwise to 0.5 mL concentrated HCl under an inert nitrogen atmosphere, with stirring at 400 rpm. $Ni(NO_3)_2 \bullet 6H_2O$ (4.65 g, 16.0 mmol) was dissolved in 40 mL DI water and added dropwise to the $Ti(O^iPr)_4$/HCl solution with stirring at 300 rpm.

Urea (3.60 g, 60.0 mmol, [urea]:[metal salts] = 3:1) was dissolved in 40 mL DI water and added to the Ni^{2+}/Ti^{4+} solution. The resulting reaction mixture was divided between two 50 mL Teflon inner vessel within a stainless steel outer vessel (40 mL of reaction mixture in each), followed by ageing in an oven at 100 °C for 18 hours.

7.3.3 Synthesis of MgAlTi-LDHs

$Mg_{12}Al_3Ti$-LDH: aqueous co-precipitation at constant pH

$Mg_{12}Al_3Ti$-LDH was synthesised by the constant pH aqueous co-precipitation method adapted from Chen *et al.*,[2,3] with adaptations for the synthesis of Ti-LDHs based on the work of Zhao *et al.*.[4] $Ti(O^iPr)_4$ (0.59 mL, 2.0 mmol) was added dropwise to 0.3 mL concentrated HCl under an inert nitrogen atmosphere, with stirring at 400 rpm. $Mg(NO_3)_2 \cdot 6H_2O$ (6.15 g, 24.0 mmol) and $Al(NO_3)_3 \cdot 9H_2O$ (2.25 g, 6.0 mmol) were dissolved in 50 mL DI water and added dropwise to the $Ti(O^iPr)_4$/HCl solution with stirring at 300 rpm.

Na_2CO_3 (2.12 g, 20.0 mmol) was dissolved in 50 mL DI water and the pH was adjusted to 10 by the dropwise addition of 4 M NaOH. The $Mg^{2+}/Al^{3+}/Ti^{4+}$ solution was added dropwise to the Na_2CO_3 solution over the period of 1 hour with stirring at 500 rpm, and the pH of the precipitation was maintained at ~10 using 4 M NaOH solution. The resulting reaction mixture was aged at room temperature for 18 hours with stirring at 650 rpm.

$Mg_{12}Al_3Ti$-LDH: aqueous co-precipitation at variable pH

$Mg_{12}Al_3Ti$-LDH was synthesised by the variable pH aqueous co-precipitation method adapted from the constant pH equivalent outlined above. $Ti(O^iPr)_4$ (0.59 mL, 2.0 mmol) was added dropwise to 0.3 mL concentrated HCl under an inert nitrogen atmosphere, with stirring at 400 rpm. $Mg(NO_3)_2 \cdot 6H_2O$ (6.15 g, 24.0 mmol) and $Al(NO_3)_3 \cdot 9H_2O$ (2.25 g, 6.0 mmol) were dissolved in 50 mL DI water and added dropwise to the $Ti(O^iPr)_4$/HCl solution with stirring at 300 rpm.

Na_2CO_3 (2.12 g, 20.0 mmol) and NaOH (1.20 g, 30.0 mmol) were dissolved in 50 mL DI water and the resulting solution was added dropwise to the $Mg^{2+}/Al^{3+}/Ti^{4+}$ solution

over the period of 1 hour with stirring at 500 rpm, up to a final pH of ~10. The resulting reaction mixture was aged at room temperature for 18 hours with stirring at 650 rpm.

$Mg_{12}Al_3Ti$-LDH: organic co-precipitation

$Mg_{12}Al_3Ti$-LDH was synthesised by the organic co-precipitation method adapted from the variable pH aqueous equivalent outlined above. $Ti(O^iPr)_4$ (0.59 mL, 2.0 mmol) was added dropwise to 0.3 mL concentrated HCl under an inert nitrogen atmosphere, with stirring at 400 rpm. $Mg(NO_3)_2 \bullet 6H_2O$ (6.15 g, 24.0 mmol) and $Al(NO_3)_3 \bullet 9H_2O$ (2.25 g, 6.0 mmol) were dissolved in 50 mL ethanol, and added dropwise to the $Ti(O^iPr)_4$/HCl solution with stirring at 300 rpm.

NaOEt (24.0 mL of 21 wt% solution in ethanol, 64.0 mmol) was dissolved in a mixture of 5 mL DI water and 50 mL ethanol, and the resulting solution was added dropwise to the $Mg^{2+}/Al^{3+}/Ti^{4+}$ solution over the period of 1 hour with stirring at 500 rpm. The resulting reaction mixture was aged at room temperature for 18 hours with stirring at 650 rpm.

$Mg_{12}Al_3Ti$-LDH: aqueous urea reflux

$Mg_{12}Al_3Ti$-LDH was synthesised by the aqueous urea reflux method adapted from the homogeneous precipitation method used by Costantino *et al.*,[5] with adaptations for the synthesis of Ti-LDHs based on the work of Zhao *et al.*.[4] $Ti(O^iPr)_4$ (0.59 mL, 2.0 mmol) was added dropwise to 0.3 mL concentrated HCl under an inert nitrogen atmosphere, with stirring at 400 rpm. $Mg(NO_3)_2 \bullet 6H_2O$ (6.15 g, 24.0 mmol) and $Al(NO_3)_3 \bullet 9H_2O$ (2.25 g, 6.0 mmol) were dissolved in 50 mL DI water and added dropwise to the $Ti(O^iPr)_4$/HCl solution with stirring at 300 rpm.

Urea (11.53 g, 192.0 mmol, [urea]:[metal salts] = 6:1) was dissolved in 50 mL DI water and added to the $Mg^{2+}/Al^{3+}/Ti^{4+}$ solution. The resulting reaction mixture was aged under reflux conditions in an oil bath at 100 °C for 18 hours with stirring at 650 rpm.

$Mg_{12}Al_3Ti$-LDH: aqueous urea hydrothermal

$Mg_{12}Al_3Ti$-LDH was synthesised by the aqueous urea hydrothermal method adapted from the homogeneous precipitation method used by Ogawa e*t al*.,[6] with adaptations for the synthesis of Ti-LDHs based on the work of Zhao *et al*..[4] $Ti(O^iPr)_4$ (0.47 mL, 1.6 mmol) was added dropwise to 0.2 mL concentrated HCl under an inert nitrogen atmosphere, with stirring at 400 rpm. $Mg(NO_3)_2 \bullet 6H_2O$ (4.92 g, 19.2 mmol) and $Al(NO_3)_3 \bullet 9H_2O$ (1.80 g, 4.8 mmol) were dissolved in 40 mL DI water and added dropwise to the $Ti(O^iPr)_4$/HCl solution with stirring at 300 rpm.

Urea (6.15 g, 102.4 mmol, [urea]:[metal salts] = 4:1) was dissolved in 40 mL DI water and added to the $Mg^{2+}/Al^{3+}/Ti^{4+}$ solution. For the experiments where the [urea]:[metal salts] ratio was changed to 3:1 and 2:1, the quantities of urea used were 4.61 g (76.8 mmol) and 3.08 g (51.2 mmol), respectively. The resulting reaction mixture was divided between two 50 mL Teflon inner vessel within a stainless steel outer vessel (40 mL of reaction mixture in each), followed by ageing in an oven at 100 °C for 18 hours.

7.3.4 Variation of Ni:Ti and Al:Ti metal ratios

For experiments where the Ni:Ti and Al:Ti metal ratios were varied, only the amounts of LDH metal salt precursors were changed, as listed in Tables 7.1, 7.2 and 7.3. The amounts of all other reagents and solvents were kept constant at values outlined in Sections 7.3.2 and 7.3.3.

Table 7.1 Quantities of $Ti(O^iPr)_4$ and $Ni(NO_3)_2 \cdot 6H_2O$ for different Ni:Ti metal ratios.

Ni:Ti ratio	**$Ti(O^iPr)_4$ volume (amount)**	**$Ni(NO_3)_2 \cdot 6H_2O$ mass (amount)**
2:1	2.46 mL (8.3 mmol)	4.86 g (16.7 mmol)
3:1	1.86 mL (6.3 mmol)	5.47 g (18.9 mmol)
4:1	1.48 mL (5.0 mmol)	5.82 g (20.0 mmol)
5:1	1.24 mL (4.2 mmol)	6.11 g (21.0 mmol)
6:1	1.06 mL (3.6 mmol)	6.28 g (21.6 mmol)

Table 7.2 Quantities of $Ti(O^iPr)_4$, $Mg(NO_3)_2 \cdot 6H_2O$ and $Al(NO_3)_3 \cdot 9H_2O$ for different Al:Ti metal ratios, for all synthetic methods except urea hydrothermal.

Al:Ti ratio	**$Ti(O^iPr)_4$ volume (amount)**	**$Mg(NO_3)_2 \cdot 6H_2O$ mass (amount)**	**$Al(NO_3)_3 \cdot 9H_2O$ mass (amount)**
3:1	0.59 mL (2.0 mmol)	6.15 g (24.0 mmol)	2.25 g (6.0 mmol)
1:1	1.18 mL (4.0 mmol)	6.15 g (24.0 mmol)	1.50 g (4.0 mmol)
1:3	1.78 mL (6.0 mmol)	6.15 g (24.0 mmol)	0.75 g (2.0 mmol)

Table 7.3 Quantities of $Ti(O^iPr)_4$, $Mg(NO_3)_2 \cdot 6H_2O$ and $Al(NO_3)_3 \cdot 9H_2O$ for different Al:Ti metal ratios, for the urea hydrothermal method.

Al:Ti ratio	**$Ti(O^iPr)_4$ volume (amount)**	**$Mg(NO_3)_2 \cdot 6H_2O$ mass (amount)**	**$Al(NO_3)_3 \cdot 9H_2O$ mass (amount)**
3:1	0.47 mL (1.6 mmol)	4.92 g (19.2 mmol)	1.80 g (4.8 mmol)
1:1	0.95 mL (3.2 mmol)	4.92 g (19.2 mmol)	1.20 g (3.2 mmol)
1:3	1.42 mL (4.8 mmol)	4.92 g (19.2 mmol)	0.6 g (1.6 mmol)

7.3.5 Ti-LDH product workup

After ageing, all Ti-LDH products, with the exception of the organic co-precipitation products, were washed with about 1 litre of DI water until the filtrate reached a pH of 7, followed by drying overnight in a vacuum oven at room temperature.

The organic co-precipitation products were first washed with about 1 litre of DI water until the filtrate reached a pH of 7, followed by washing with about 1 litre of ethanol. Finally, the products were dried overnight in a vacuum oven at room temperature.

Table 7.4 The PXRD peak positions, FWHM data, d-spacings, lattice parameters and mean crystallite domain lengths (CDLs) of NiTi-LDHs prepared with different Ni:Ti ratios and different synthetic methods.

Ni:Ti ratio	Synthetic method	PXRD peak positions (° 2θ)		$FWHM_{003}$ (° 2θ)[a]	d-spacing (Å)[b]		Lattice parameters (Å)		CDL (Å)[e]	
		(003)	(110)		d_{003}	d_{110}	*c* [c]	*a* [d]	*c*-axis	*ab*-plane
2:1	Variable pH aq. co-precip.	12.870	60.127	3.212	6.88	1.54	20.64	3.08	24.63	123.70
	Organic co-precipitation	/	60.850	/	/	1.52	/	3.04	/	69.84
	Aqueous urea reflux	11.965	59.263	0.167	7.40	1.56	22.2	3.12	472.53	184.75
3:1	Variable pH aq. co-precip.	11.393	60.074	0.335	7.77	1.54	23.31	3.08	236.14	193.90
	Organic co-precipitation	/	60.054	/	/	1.54	/	3.08	/	34.78
	Aqueous urea reflux	12.119	59.332	0.151	7.30	1.53	21.9	3.06	525.00	245.88
4:1	Variable pH aq. co-precip.	11.329	59.961	0.301	7.81	1.52	23.43	3.04	262.40	339.20
	Organic co-precipitation	/	60.436	/	/	1.53	/	3.06	/	23.23
	Aqueous urea reflux	12.181	59.423	0.368	7.27	1.53	21.81	3.06	214.86	270.55
5:1	Variable pH aq. co-precip.	11.270	59.971	0.268	7.85	1.54	23.55	3.08	295.24	387.59
	Organic co-precipitation	/	60.227	/	/	1.54	/	3.08	/	30.94
	Aqueous urea reflux	12.138	59.403	0.602	7.29	1.56	21.87	3.12	131.30	300.62
6:1	Variable pH aq. co-precip.	11.193	59.979	0.937	7.91	1.54	23.73	3.08	84.33	169.58
	Organic co-precipitation	/	59.802	/	/	1.55	/	3.1	/	92.62
	Aqueous urea reflux	12.188	59.373	0.218	7.26	1.56	21.78	3.12	363.54	386.43

[a] Full width at half maximum of the (003) PXRD reflection.
[b] Where d-spacing is defined by the Bragg equation as $n\lambda = 2d\sin\theta$, with n = 1 and λ = 1.541847 Å.
[c] Where lattice parameter $c = 3d_{003}$.
[d] Where lattice parameter $a = b = 2d_{110}$.
[e] Where the crystallite domain length was determined using the Scherrer equation: $CDL = 0.89\lambda/\beta\cos\theta$, λ = 1.541847 Å, β = FWHM in radians.

Table 7.5 The yield, colour of the powder product, specific surface area and positions of FTIR bands of NiTi-LDHs prepared with different Ni:Ti ratios and different synthetic methods.

Ni:Ti ratio	Synthetic method	Yield (%)[a]	Colour	N_2 BET specific surface area (m^2g^{-1})	FTIR bands (cm^{-1})[b]
2:1	Variable pH aq. co-precip.	82	Light green	152	3,682 – 2,941 (b), 1,641 (m), 1,345 (m), 678 (s)
	Organic co-precipitation	90	Light yellow-green	274	3,678 – 2,918 (b), 1,636 (m), 1373 (m), 1048 (w), 674 (s)
	Aqueous urea reflux	66	Light green	201	3,636 (sh), 3,691 – 2,932 (b), 2,191 (m), 1,636 (m), 1,488 (m), 1,363 (m), 1,289 (w), 678 (s)
3:1	Variable pH aq. co-precip.	92	Light green	97	3,682 – 2,941 (b), 1,641 (m), 1,345 (m), 678 (s)
	Organic co-precipitation	85	Light yellow-green	220	3,678 – 2,918 (b), 1,610 (m), 1,373 (m), 1,048 (w,) 674 (s)
	Aqueous urea reflux	68	Light green	167	3,640 (sh), 3,691 – 2,929 (b), 2,224 (m), 2,191 (m), 1,636 (m), 1,488 (m), 1,363 (m), 1,289 (w), 674 (s)
4:1	Variable pH aq. co-precip.	93	Light green	65	3,682 – 2,941 (b), 1,641 (m), 1,345 (m), 678 (s)
	Organic co-precipitation	81	Light yellow-green	326	3,678 – 2,918 (b), 1,632 (m), 1,373 (m), 674 (s)
	Aqueous urea reflux	67	Light green	153	3,640 (sh), 3,682 – 3,057 (b), 2,220 (m), 2,191 (m), 1,636 (m), 1,488 (w), 1,363 (m), 1,289 (w), 664 (s)
5:1	Variable pH aq. co-precip.	98	Light green	42	3,682 – 2,941 (b), 1,641 (m), 1,345 (m), 678 (s)
	Organic co-precipitation	89	Light yellow-green	289	3,678 – 2,918 (b), 1,636 (m), 1,363 (m), 1,048 (w) 674 (s)
	Aqueous urea reflux	70	Light green	124	3,640 (sh), 3,682 – 3,071 (b), 2,224 (m), 2,191 (m), 1,636 (m), 1,488 (m), 1,363 (m), 1,289 (w), 674 (s)
6:1	Variable pH aq. co-precip.	87	Light green	41	3,682 – 2,941 (b), 1,641 (m), 1,345 (m), 678 (s)
	Organic co-precipitation	77	Light yellow-green	230	3,678 – 2,918 (b), 1,627 (m), 1,363 (m), 1,048 (w), 674 (s)
	Aqueous urea reflux	70	Light green	124	3,636 (sh), 3,682 – 3,067 (b), 2,224 (m), 2,191 (m), 1,636 (m), 1,488 (m), 1,363 (m), 1,289 (w), 669 (s)

[a] Yields were calculated based on the LDH chemical formulae determined by ICP-MS and TGA, tabulated in Table A.3 in Appendix A.
[b] Where (b) = broad, (m) = medium, (s) = strong, (w) = weak and (sh) = sharp. The absorption bands in the 1,800 – 2,300 cm^{-1} range are due to the instrument setup and were omitted.

Table 7.6 The PXRD peak positions, FWHM data, d-spacings, lattice parameters and mean crystallite domain lengths (CDLs) of MgAlTi-LDHs prepared with different Al:Ti ratios and different synthetic methods.

Al:Ti ratio	Synthetic method	PXRD peak positions (° 2θ)		$FWHM_{003}$ (° 2θ)[a]	d-spacing (Å)[b]		Lattice parameters (Å)		CDL (Å)[e]	
		(003)	(110)		d_{003}	d_{110}	*c*-axis	*a* [d]	*c*-axis	*ab*-plane
3:1	Constant pH aq. co-precip.	11.207	60.296	0.368	7.90	1.53	23.7	3.06	214.68	453.03
	Variable pH aq. co-precip.	11.463	60.680	0.201	7.72	1.53	23.16	3.06	393.72	136.15
	Organic co-precipitation	11.132	60.263	0.602	7.95	1.54	23.85	3.08	131.18	135.87
	Aqueous urea reflux	11.781	60.965	0.218	7.51	1.52	22.53	3.04	363.41	272.67
	Aqueous urea hydrothermal	11.710	60.901	0.251	7.56	1.52	22.68	3.04	315.01	545.15
1:1	Constant pH aq. co-precip.	11.149	60.296	0.268	7.94	1.53	23.82	3.06	295.21	169.85
	Variable pH aq. co-precip.	11.378	60.459	0.736	7.78	1.53	23.34	3.06	107.35	136.00
	Organic co-precipitation	11.135	60.160	1.360	7.95	1.54	23.85	3.08	58.07	117.66
	Aqueous urea reflux	11.771	61.018	0.100	7.52	1.52	22.56	3.04	787.25	247.99
	Aqueous urea hydrothermal	11.669	60.945	0.246	7.58	1.52	22.74	3.04	321.14	238.87
1:3	Constant pH aq. co-precip.	11.350	60.036	0.335	7.80	1.54	23.4	3.08	236.14	169.63
	Variable pH aq. co-precip.	11.402	60.323	1.382	7.76	1.53	23.28	3.06	57.18	106.96
	Organic co-precipitation	11.135	59.107	1.366	7.95	1.56	23.85	3.12	57.83	131.68
	Aqueous urea reflux	11.671	60.918	0.234	7.58	1.52	22.74	3.04	337.46	340.85
	Aqueous urea hydrothermal	11.669	61.375	0.277	7.58	1.51	22.74	3.02	284.91	249.39

[a] Full width at half maximum of the (003) PXRD reflection.
[b] Where d-spacing is defined by the Bragg equation as $n\lambda = 2d\sin\theta$, with n = 1 and λ = 1.541847 Å.
[c] Where lattice parameter $c = 3d_{003}$.
[d] Where lattice parameter $a = b = 2d_{110}$.
[e] Where the crystallite domain length was determined using the Scherrer equation: $CDL = 0.89\lambda/\beta\cos\theta$, λ = 1.541847 Å, β = FWHM in radians.

Table 7.7 The yield, colour of the powder product, specific surface area and positions of FTIR bands of MgAlTi-LDHs prepared with different Al:Ti ratios and different synthetic methods.

Al:Ti ratio	Synthetic method	Yield (%)[a]	Colour	N_2BET specific surface area (m^2g^{-1})	FTIR bands (cm^{-1})[b]
3:1	Constant pH aq. co-precip.	97	White	44	3,743 - 2,928 (b), 1,641 (m), 669 (s)
	Variable pH aq. co-precip.	106	White	0.5	3,733 – 2,766 (b), 1,641 (m), 1,363 (s), 734 (m), 669 (s)
	Organic co-precipitation	101	Very pale orange	107	3,691 (sh), 3,737 – 2,932 (b), 1,636 (m), 1,396 (s), 762 (m), 674 (s)
	Aqueous urea reflux	83	White	128	3,655 – 2,863 (b), 1,627 (m), 1,354 (s), 942 (m), 766 (s), 678 (s)
	Aqueous urea hydrothermal	84	White	64	3,636 – 3,076 (b), 1,590 (w), 1,359 (s), 947 (w), 776 (s), 683 (s)
1:1	Constant pH aq. co-precip.	102	White	0.6	3,747 – 2,924 (b), 1,641 (m), 669 (s)
	Variable pH aq. co-precip.	97	White	0.3	3,737 – 2,686 (b), 1,641 (m), 1,373 (s), 674 (s)
	Organic co-precipitation	73	Very pale orange	79	3,691 (sh), 3,745 – 2,691 (b), 1,646 (m), 1,377 (s), 840 (m), 669 (s)
	Aqueous urea reflux	73	White	169	3,710 – 2,641 (b), 1,636 (m), 1,354 (s), 942 (m), 766 (s), 678 (s)
	Aqueous urea hydrothermal	74	White	63	3,659 – 2,946 (b), 1,646 (w), 1,354 (s), 877 (sh), 785 (m), 744 (s), 678 (s)
1:3	Constant pH aq. co-precip.	83	White	5	3,733 – 2,678 (b), 1,641 (m), 674 (s)
	Variable pH aq. co-precip.	84	White	0.7	3,733 – 2,664 (b), 1,641 (m), 1,381 (s), 678 (s)
	Organic co-precipitation	73	Very pale orange	185	3,691 (sh), 3,737 – 2,670 (b), 1,646 (m), 1,354 (s), 854 (m), 674 (s)
	Aqueous urea reflux	55	White	256	3,724 – 2,636 (b), 1,641 (m), 1,359 (s), 933 (m), 752 (s), 674 (s)
	Aqueous urea hydrothermal	79	White	76	3,686 – 2,845 (b), 1,650 (w), 1,428 (s), 882 (sh), 743 (sh), 683 (s)

[a] Yields were calculated based on the LDH chemical formulae determined by ICP-MS and TGA, tabulated in Table A.4 in Appendix A. Yields above 100% indicate impurity formation.
[b] Where (b) = broad, (m) = medium, (s) = strong, (w) = weak and (sh) = sharp. The absorption bands in the 1,800 – 2,300 cm^{-1} range are due to the instrument setup and were omitted.

7.4 Experimental details for Chapter 3

7.4.1 Materials

Potassium ferrioxalate trihydrate ($K_3Fe(C_2O_4)_3 \cdot 3H_2O$), sulfuric acid ($H_2SO_4$), 1,10-phenanthroline monohydrate ($C_{12}H_8N_2 \cdot H_2O$), sodium acetate (CH_3COONa), diphenylmethanol (benzhydrol, $(C_6H_5)_2CHOH$), titanium dioxide (TiO_2, anatase powder), acetonitrile (CH_3CN, anhydrous, 99.8%) and deuterated chloroform ($CDCl_3$) were purchased from Sigma Aldrich and used without further purification.

7.4.2 Photo-reactor setup

The photo-reactor setup was purchased from Photochemical Reactors Ltd, and comprises an immersion well photo-reactor with a 125 W medium pressure mercury lamp, which emits radiation primarily in the UV region of the electromagnetic spectrum, with the most intense emission peak at 365 nm. The immersion well photo-reactor consists of a three-necked 100 mL borosilicate reaction flask, as well as a quartz and a borosilicate jacketed immersion well that allows the circulation of cooling water, set to a constant temperature of 15 ºC. The UV lamp is positioned in the centre of this setup for maximum irradiation.

A magnetic stirring bar allowed the photochemical reaction mixture to be stirred at 1,000 rpm throughout the reaction. Pure oxygen gas was bubbled through the reaction mixture at a constant gas flow rate of 70 cm^3min^{-1}, controlled with a gas flow reader. The reaction flask was wrapped with a layer of 'heavy-duty' aluminium foil and contained within a black two-part enclosure cabinet to minimise the possibility of exposure to UV radiation.

7.4.3 Actinometry

$K_3Fe(C_2O_4)_3 \cdot 3H_2O$ (1.47 g, 3.0 mmol) was dissolved in a mixture of 400 mL DI water and 50 mL of 0.1 M H_2SO_4 solution, and then diluted to 500 mL with DI water (Solution A). 1,10-phenanthroline (0.05 g, 0.025 mmol) was dissolved in 50 mL of DI water (Solution B). 300 mL of 1 M sodium acetate solution was mixed with 180 mL of 1 M H_2SO_4 solution, and then diluted to 500 mL with DI water (Solution C).

100 mL (V_1) of Solution A was irradiated in the photo-reactor setup for 10 – 15 minutes, then an aliquot volume of 5 mL was removed (V_2) and pipetted into a 25 mL volumetric flask. 4 mL of Solution B were added, followed by 2 mL of Solution C. The resulting solution was diluted to 25 mL with DI water (V_3). This was allowed to stand for 30 minutes in the dark. The blank/reference sample was prepared by an equivalent procedure without the initial irradiation step.

The two samples were analysed by UV-vis spectroscopy, measuring the absorption at 510 nm in a 1 cm quartz cuvette (with the blank sample as the reference). Then, the following equations were used to determine the total number of photons emitted by the UV lamp per second:

$$\sum n_{Fe2+} = \frac{6.023\times10^{20}\times V_1 V_3\times Abs}{V_2\times l\times\varepsilon} = 2.713\times10^{19}\times Abs$$

$$\sum n_{abs} = \frac{\sum n_{Fe2+}}{\phi_\lambda} = 2.380\times10^{19}\times Abs$$

$$n_{abs} = \frac{\sum n_{abs}}{t[s]}$$

Where $\sum n_{Fe2+}$ is the sum of all the Fe^{3+} reduced to Fe^{2+} during the irradiation, V_1 = 100 mL, V_2 = 5 mL, V_3 = 25 mL, l is the width of the cuvette (1 cm), ε is the

extinction coefficient, *Abs* is the absorbance measured at 510 nm, $\sum n_{abs}$ is the sum of all the photons absorbed, ϕ_λ is the quantum yield for the Fe^{2+} formation, n_{abs} is the rate of photon absorption and t[s] is the time of irradiation in seconds.

These calculations assume that every photon absorbed results in the reduction of one Fe^{3+} centre into Fe^{2+}, such that the number of absorbed photos and Fe^{2+} cations is equal.

7.4.4 Control reactions

No catalyst

Diphenylmethanol (1.84 g, 10.0 mmol, 100 mM) was dissolved in 100 mL acetonitrile, with stirring at 300 rpm. The solution was irradiated for 1 hour with oxygen gas bubbling through the reaction mixture at a gas flow rate of 70 cm^3min^{-1}, in the photo-reactor setup with a quartz or a borosilicate immersion well.

No light

Diphenylmethanol (1.84 g, 10.0 mmol, 100 mM) was dissolved in 100 mL acetonitrile, with stirring at 300 rpm. TiO_2 (5 mg) or MgAlTi-LDH (5 mg) was added into the solution, which was then sonicated for 15 minutes. The reaction mixture was kept in the dark for 1 hour with stirring at 1,000 rpm and oxygen gas bubbling through it at a gas flow rate of 70 cm^3min^{-1}.

No oxygen, under an inert nitrogen atmosphere

Diphenylmethanol (1.84 g, 10.0 mmol, 100 mM) was dissolved in 100 mL acetonitrile, with stirring at 300 rpm. TiO_2 (5 mg) or MgAlTi-LDH (5 mg) was added into the solution, which was then sonicated for 15 minutes. The reaction mixture was irradiated for 1 hour

with stirring at 1,000 rpm and nitrogen gas bubbling through it, in the photo-reactor setup with a quartz or a borosilicate immersion well.

7.4.5 Product mixture workup

After each photocatalytic reaction, the solid catalyst (if present) was removed from the product mixture using a syringe filter. The acetonitrile was then removed from the product mixture using rotary evaporation.

7.4.6 TiO_2 baseline reactions

Variation of TiO_2 loading

Diphenylmethanol (1.84 g, 10.0 mmol, 100 mM) was dissolved in 100 mL acetonitrile, with stirring at 300 rpm. TiO_2 was added into the solution, which was then sonicated for 15 minutes. The reaction mixture was irradiated for 1 hour with stirring at 1,000 rpm and oxygen gas bubbling through it at a gas flow rate of 70 cm^3min^{-1}, in the photo-reactor setup with a borosilicate immersion well. The TiO_2 amount was varied between 5, 10, 25 and 50 mg.

Variation of diphenylmethanol concentration

Diphenylmethanol was dissolved in 100 mL acetonitrile, with stirring at 300 rpm. TiO_2 (5 mg) was added into the solution, which was then sonicated for 15 minutes. The reaction mixture was irradiated for 1 hour with stirring at 1,000 rpm and oxygen gas bubbling through it at a gas flow rate of 70 cm^3min^{-1}, in the photo-reactor setup with a borosilicate immersion well. The diphenylmethanol amount was varied between 92.0 mg (0.5 mmol, 5 mM), 0.18 g (1.0, 10 mM), 0.46 g (2.5 mmol, 25 mM), 0.92 g (5.0 mmol, 50 mM) and 1.84 g (10.0 mmol, 100 mM).

Variation of irradiation time (kinetics)

Diphenylmethanol (1.84 g, 10.0 mmol, 100 mM) was dissolved in 100 mL acetonitrile, with stirring at 300 rpm. TiO_2 (5 mg) was added into the solution, which was then sonicated for 15 minutes. The reaction mixture was irradiated with stirring at 1,000 rpm and oxygen gas bubbling through it at a gas flow rate of 70 cm^3min^{-1}, in the photo-reactor setup with a borosilicate immersion well. The irradiation time was varied between 15 or 30 minutes and 1, 2, 4 or 6 hours.

7.4.7 Variation of the Ti-LDH photocatalysts

Diphenylmethanol (1.84 g, 10.0 mmol, 100 mM) was dissolved in 100 mL acetonitrile, with stirring at 300 rpm. A series of NiTi- and MgAlTi-LDHs (5 mg, with different synthetic methods and metal ratios, their synthesis is outlined in Section 7.3) were added into the solution, which was then sonicated for 15 minutes. Each reaction mixture was irradiated for 1 hour with stirring at 1,000 rpm and oxygen gas bubbling through it at a gas flow rate of 70 cm^3min^{-1}, in the photo-reactor setup with a borosilicate immersion well.

7.4.8 Variation of catalyst loading

Diphenylmethanol (1.84 g, 10.0 mmol, 100 mM) was dissolved in 100 mL acetonitrile, with stirring at 300 rpm. Urea reflux Ni_2Ti-LDH or urea hydrothermal $Mg_{12}AlTi_3$-LDH was added into the solution, which was then sonicated for 15 minutes. The reaction mixture was irradiated for 1 hour with stirring at 1,000 rpm and oxygen gas bubbling through it at a gas flow rate of 70 cm^3min^{-1}, in the photo-reactor setup with a borosilicate immersion well. The Ti-LDH amount was varied between 5, 10, 25 and 50 mg.

7.4.9 Variation of reactant concentration

Diphenylmethanol was dissolved in 100 mL acetonitrile, with stirring at 300 rpm. Urea hydrothermal $Mg_{12}AlTi_3$-LDH (25 mg) was added into the solution, which was then sonicated for 15 minutes. The reaction mixture was irradiated for 1 hour with stirring at 1,000 rpm and oxygen gas bubbling through it at a gas flow rate of 70 cm^3min^{-1}, in the photo-reactor setup with a borosilicate immersion well. The diphenylmethanol amount was varied between 92.0 mg (0.5 mmol, 5 mM), 0.18 g (1.0, 10 mM), 0.46 g (2.5 mmol, 25 mM), 0.92 g (5.0 mmol, 50 mM) and 1.84 g (10.0 mmol, 100 mM).

7.4.10 Kinetic studies

Diphenylmethanol (1.84 g, 10.0 mmol, 100 mM) was dissolved in 100 mL acetonitrile, with stirring at 300 rpm. Urea hydrothermal $Mg_{12}AlTi_3$-LDH (25 mg) was added into the solution, which was then sonicated for 15 minutes. The reaction mixture was irradiated with stirring at 1,000 rpm and oxygen gas bubbling through it at a gas flow rate of 70 cm^3min^{-1}, in the photo-reactor setup with a borosilicate immersion well. The irradiation time was varied between 15 or 30 minutes and 1, 2, 4 or 6 hours.

7.4.11 Catalyst re-cycling

Diphenylmethanol (1.84 g, 10.0 mmol, 100 mM) was dissolved in 100 mL acetonitrile, with stirring at 300 rpm. Urea hydrothermal $Mg_{12}AlTi_3$-LDH (25 mg) was added into the solution, which was then sonicated for 15 minutes. The reaction mixture was irradiated for 2 hours with stirring at 1,000 rpm and oxygen gas bubbling through it at a gas flow rate of 70 cm^3min^{-1}, in the photo-reactor setup with a borosilicate immersion well.

After the first irradiation/photocatalytic reaction, the solvent was removed by rotary evaporation to give a dispersion of the solid catalyst in the product mixture. A <0.1 mL aliquot was removed to be analysed by ^{1}H NMR spectroscopy. Then, 100 mL of 100 mM solution of diphenylmethanol in acetonitrile was added to the catalyst dispersion in the product mixture and irradiated for 2 hours. This process was repeated three times to give a total of four cycles.

7.5 Experimental details for Chapter 4

7.5.1 Materials

Benzyl alcohol ($C_6H_5CH_2OH$, anhydrous, 99.8%), benzylamine ($C_6H_5CH_2NH_2$, 99%), cyclooctanol ($C_8H_{16}O$, ≥95%), titanium dioxide (TiO_2, anatase powder), acetonitrile (CH_3CN, anhydrous, 99.8%) and deuterated chloroform ($CDCl_3$) were purchased from Sigma Aldrich and used without further purification.

7.5.2 Photo-reactor setup

The photo-reactor setup was the same as that outlined in Section 7.4.2.

7.5.3 No catalyst control reactions

The reactant was dissolved in 100 mL acetonitrile, with stirring at 300 rpm. The solution was irradiated for 1 hour with oxygen gas bubbling through the reaction mixture at a gas flow rate of 70 cm^3min^{-1}, in the photo-reactor setup with a borosilicate immersion well. The reactants used were benzyl alcohol (1.0 mL, 10.0 mmol, 100 mM), cyclooctanol (1.3 mL, 10.0 mmol, 100 mM) and benzylamine (1.1 mL, 10.0 mmol, 100 mM).

7.5.4 Benzyl alcohol photo-oxidation

Variation of the catalyst

Benzyl alcohol (1.0 mL, 10.0 mmol, 100 mM) was dissolved in 100 mL acetonitrile, with stirring at 300 rpm. The catalyst was added into the solution, which was then sonicated for 15 minutes. Each reaction mixture was irradiated for 1 hour with stirring at 1,000 rpm and oxygen gas bubbling through it at a gas flow rate of 70 cm^3min^{-1}, in the photo-reactor

setup with a borosilicate immersion well. The catalysts considered were TiO_2 (5 mg), urea reflux Ni_2Ti-LDH (5 mg) and urea hydrothermal $Mg_{12}AlTi_3$-LDH (5 and 25 mg).

Variation of the irradiation time (kinetics)

Benzyl alcohol (1.0 mL, 10.0 mmol, 100 mM) was dissolved in 100 mL acetonitrile, with stirring at 300 rpm. Urea hydrothermal $Mg_{12}AlTi_3$-LDH (25 mg) was added into the solution, which was then sonicated for 15 minutes. The reaction mixture was irradiated with stirring at 1,000 rpm and oxygen gas bubbling through it at a gas flow rate of 70 cm^3min^{-1}, in the photo-reactor setup with a borosilicate immersion well. The irradiation time was varied between 15 or 30 minutes and 1, 2, 4 or 6 hours.

7.5.5 Cyclooctanol photo-oxidation

Variation of the catalyst

Cyclooctanol (1.3 mL, 10.0 mmol, 100 mM) was dissolved in 100 mL acetonitrile, with stirring at 300 rpm. The catalyst was added into the solution, which was then sonicated for 15 minutes. Each reaction mixture was irradiated for 1 hour with stirring at 1,000 rpm and oxygen gas bubbling through it at a gas flow rate of 70 cm^3min^{-1}, in the photo-reactor setup with a borosilicate immersion well. The catalysts considered were TiO_2 (5 mg), urea reflux Ni_2Ti-LDH (5 mg) and urea hydrothermal $Mg_{12}AlTi_3$-LDH (5 and 25 mg).

Variation of the irradiation time (kinetics)

Cyclooctanol (1.3 mL, 10.0 mmol, 100 mM) was dissolved in 100 mL acetonitrile, with stirring at 300 rpm. Urea hydrothermal $Mg_{12}AlTi_3$-LDH (25 mg) was added into the solution, which was then sonicated for 15 minutes. The reaction mixture was irradiated with stirring at 1,000 rpm and oxygen gas bubbling through it at a gas flow rate of

70 cm^3min^{-1}, in the photo-reactor setup with a borosilicate immersion well. The irradiation time was varied between 1, 2, 4 or 6 hours.

7.5.6 Benzylamine photo-oxidation

Variation of the catalyst

Benzylamine (1.1 mL, 10.0 mmol, 100 mM) was dissolved in 100 mL acetonitrile, with stirring at 300 rpm. The catalyst was added into the solution, which was then sonicated for 15 minutes. Each reaction mixture was irradiated for 1 hour with stirring at 1,000 rpm and oxygen gas bubbling through it at a gas flow rate of 70 cm^3min^{-1}, in the photo-reactor setup with a borosilicate immersion well. The catalysts considered were TiO_2 (5 mg), urea reflux Ni_2Ti-LDH (5 mg) and urea hydrothermal $Mg_{12}AlTi_3$-LDH (5 and 25 mg).

Variation of the irradiation time (kinetics)

Benzylamine (1.1 mL, 10.0 mmol, 100 mM) was dissolved in 100 mL acetonitrile, with stirring at 300 rpm. Urea hydrothermal $Mg_{12}AlTi_3$-LDH (25 mg) was added into the solution, which was then sonicated for 15 minutes. The reaction mixture was irradiated with stirring at 1,000 rpm and oxygen gas bubbling through it at a gas flow rate of 70 cm^3min^{-1}, in the photo-reactor setup with a borosilicate immersion well. The irradiation time was varied between 15 or 30 minutes and 1, 2, 4 or 6 hours.

7.6 Experimental details for Chapter 5

7.6.1 Materials

Titanium dioxide (TiO_2, anatase powder), titanium isopropoxide ($Ti(O^iPr)_4$), nickel nitrate hexahydrate ($Ni(NO_3)_2 \cdot 6H_2O$), magnesium nitrate hexahydrate ($Mg(NO_3)_2 \cdot 6H_2O$), aluminium nitrate nonahydrate ($Al(NO_3)_3 \cdot 9H_2O$), concentrated hydrochloric acid (HCl, 37%), sodium hydroxide (NaOH), sodium carbonate (Na_2CO_3), sodium ethoxide (NaOEt, 21 wt% solution in ethanol), urea ($CO(NH_2)_2$), ethanol (EtOH, ≥99.8%), diphenylmethanol (benzhydrol, $(C_6H_5)_2CHOH$), acetonitrile (CH_3CN, anhydrous 99.8%) and deuterated chloroform ($CDCl_3$) were purchased from Sigma Aldrich and used without further purification.

7.6.2 Synthesis of TiO_2@NiTi-LDHs

TiO_2@Ni_4Ti-LDH: aqueous co-precipitation at constant pH

TiO_2@Ni_4Ti-LDH was synthesised by the constant pH aqueous co-precipitation method adapted from the one used to synthesise pure Ni_4Ti-LDH (Section 7.3.2). TiO_2 (1.25 g, 15.7 mmol) was dispersed in 30 mL DI water, followed by 15 minutes of sonication. $Ti(O^iPr)_4$ (0.74 mL, 2.5 mmol) was added dropwise to 0.30 mL concentrated HCl under an inert nitrogen atmosphere, with stirring at 400 rpm. $Ni(NO_3)_2 \cdot 6H_2O$ (2.91 g, 10.0 mmol) was dissolved in 50 mL DI water and added dropwise to the $Ti(O^iPr)_4$/HCl solution with stirring at 300 rpm.

Na_2CO_3 (0.80 g, 7.5 mmol) was dissolved in 20 mL DI water, added to the TiO_2 dispersion and the pH of the resulting mixture was adjusted to 10 by the dropwise addition of 4 M NaOH. The Ni^{2+}/Ti^{4+} solution was added dropwise to the TiO_2/Na_2CO_3 mixture

over the period of 1 hour with stirring at 500 rpm, and the pH of the precipitation was maintained at ~10 using 4 M NaOH solution. The resulting reaction mixture was aged in an oil bath at 60 °C for 18 hours with stirring at 650 rpm.

TiO_2@Ni_4Ti-LDH: aqueous co-precipitation at variable pH

TiO_2@Ni_4Ti-LDH was synthesised by the variable pH aqueous co-precipitation method adapted from the one used to synthesise pure Ni_4Ti-LDH (Section 7.3.2). TiO_2 (1.25 g, 15.7 mmol) was dispersed in 30 mL DI water, followed by 15 minutes of sonication. $Ti(O^iPr)_4$ (0.74 mL, 2.5 mmol) was added dropwise to 0.30 mL concentrated HCl under an inert nitrogen atmosphere, with stirring at 400 rpm. $Ni(NO_3)_2 \bullet 6H_2O$ (2.91 g, 10.0 mmol) was dissolved in 30 mL DI water and added dropwise to the $Ti(O^iPr)_4$/HCl solution with stirring at 300 rpm. The resulting Ni^{2+}/Ti^{4+} solution was added to the TiO_2 dispersion.

Na_2CO_3 (0.80 g, 7.5 mmol) and NaOH (0.66 g, 16.5 mmol) were dissolved in 40 mL DI water and the resulting solution was added dropwise to the $TiO_2/Ni^{2+}/Ti^{4+}$ mixture over the period of 1 hour with stirring at 500 rpm, up to a final pH of ~10. The resulting reaction mixture was aged in an oil bath at 60 °C for 18 hours with stirring at 650 rpm.

TiO_2@Ni_4Ti-LDH: organic co-precipitation

TiO_2@Ni_4Ti-LDH was synthesised by the organic co-precipitation method adapted from the one used to synthesise pure Ni_4Ti-LDH (Section 7.3.2). TiO_2 (1.25 g, 15.7 mmol) was dispersed in 30 mL ethanol, followed by 15 minutes of sonication. $Ti(O^iPr)_4$ (0.74 mL, 2.5 mmol) was added dropwise to 0.30 mL concentrated HCl under an inert nitrogen atmosphere, with stirring at 400 rpm. $Ni(NO_3)_2 \bullet 6H_2O$ (2.91 g, 10.0 mmol) was dissolved

in 30 mL ethanol and added dropwise to the $Ti(O^iPr)_4$/HCl solution with stirring at 300 rpm. The resulting Ni^{2+}/Ti^{4+} solution was added to the TiO_2 dispersion.

NaOEt (9.5 mL of 21 wt% solution in ethanol, 25.0 mmol) was dissolved in a mixture of 2.5 mL DI water and 40 mL ethanol, and the resulting solution was added dropwise to the $TiO_2/Ni^{2+}/Ti^{4+}$ mixture over the period of 1 hour with stirring at 500 rpm. The resulting reaction mixture was aged in an oil bath at 80 °C for 18 hours with stirring at 650 rpm.

TiO_2@Ni_4Ti-LDH: aqueous urea reflux

TiO_2@Ni_4Ti-LDH was synthesised by the aqueous urea reflux method adapted from the one used to synthesise pure Ni_4Ti-LDH (Section 7.3.2). TiO_2 (1.25 g, 15.7 mmol) was dispersed in 30 mL DI water, followed by 15 minutes of sonication. $Ti(O^iPr)_4$ (0.74 mL, 2.5 mmol) was added dropwise to 0.30 mL concentrated HCl under an inert nitrogen atmosphere, with stirring at 400 rpm. $Ni(NO_3)_2 \bullet 6H_2O$ (2.91 g, 10.0 mmol) was dissolved in 30 mL DI water and added dropwise to the $Ti(O^iPr)_4$/HCl solution with stirring at 300 rpm. The resulting Ni^{2+}/Ti^{4+} solution was added to the TiO_2 dispersion.

Urea (2.25 g, 37.5 mmol, [urea]:[metal salts] = 3:1) was dissolved in 50 mL DI water and added to the $TiO_2/Ni^{2+}/Ti^{4+}$ mixture. The resulting reaction mixture was aged under reflux conditions in an oil bath at 100 °C for 18 hours with stirring at 650 rpm.

7.6.3 Synthesis of TiO_2@MgAlTi-LDHs

TiO_2@$Mg_{12}Al_3$Ti-LDH: aqueous co-precipitation at constant pH

TiO_2@$Mg_{12}Al_3$Ti-LDH was synthesised by the constant pH aqueous co-precipitation method adapted from the one used to synthesise pure $Mg_{12}Al_3$Ti-LDH (Section 7.3.3). TiO_2 (1.25 g, 15.7 mmol) was dispersed in 30 mL DI water, followed by 15 minutes of sonication. $Ti(O^iPr)_4$ (0.30 mL, 1.0 mmol) was added dropwise to 0.15 mL concentrated HCl under an inert nitrogen atmosphere, with stirring at 400 rpm. $Mg(NO_3)_2 \cdot 6H_2O$ (3.08 g, 12.0 mmol) and $Al(NO_3)_3 \cdot 9H_2O$ (1.13 g, 3.0 mmol) were dissolved in 50 mL DI water and added dropwise to the $Ti(O^iPr)_4$/HCl solution with stirring at 300 rpm.

Na_2CO_3 (1.06 g, 10.0 mmol) was dissolved in 20 mL DI water, added to the TiO_2 dispersion and the pH of the resulting mixture was adjusted to 10 by the dropwise addition of 4 M NaOH. The $Mg^{2+}/Al^{3+}/Ti^{4+}$ solution was added dropwise to the TiO_2/Na_2CO_3 mixture over the period of 1 hour with stirring at 500 rpm, and the pH of the precipitation was maintained at ~10 using 4 M NaOH solution. The resulting reaction mixture was aged at room temperature for 18 hours with stirring at 650 rpm. For the experiments where the ageing time was varied, the reaction mixture was also aged at room temperature for 1 and 4 hours.

For the experiments where the TiO_2:LDH ratio was changed to 2:1, the quantities of the reagents used are as follows: TiO_2 (1.25 g, 15.7 mmol), $Ti(O^iPr)_4$ (0.15 mL, 0.5 mmol), 0.1 mL HCl, $Mg(NO_3)_2 \cdot 6H_2O$ (1.54 g, 6.0 mmol), $Al(NO_3)_3 \cdot 9H_2O$ (0.57 g, 1.5 mmol) and Na_2CO_3 (0.53 g, 5.0 mmol).

TiO_2@$Mg_{12}Al_3$Ti-LDH: aqueous co-precipitation at variable pH

TiO_2@$Mg_{12}Al_3$Ti-LDH was synthesised by the variable pH aqueous co-precipitation method adapted from the one used to synthesise pure $Mg_{12}Al_3$Ti-LDH (Section 7.3.3). TiO_2 (1.25 g, 15.7 mmol) was dispersed in 30 mL DI water, followed by 15 minutes of sonication. $Ti(O^iPr)_4$ (0.30 mL, 1.0 mmol) was added dropwise to 0.15 mL concentrated HCl under an inert nitrogen atmosphere, with stirring at 400 rpm. $Mg(NO_3)_2 \cdot 6H_2O$ (3.08 g, 12.0 mmol) and $Al(NO_3)_3 \cdot 9H_2O$ (1.13 g, 3.0 mmol) were dissolved in 30 mL DI water and added dropwise to the $Ti(O^iPr)_4$/HCl solution with stirring at 300 rpm. The resulting $Mg^{2+}/Al^{3+}/Ti^{4+}$ solution was added to the TiO_2 dispersion.

Na_2CO_3 (1.06 g, 10.0 mmol) and NaOH (0.60 g, 15.0 mmol) were dissolved in 40 mL DI water and the resulting solution was added dropwise to the $TiO_2/Mg^{2+}/Al^{3+}/Ti^{4+}$ mixture over the period of 1 hour with stirring at 500 rpm, up to a final pH of ~10. The resulting reaction mixture was aged at room temperature for 18 hours with stirring at 650 rpm.

TiO_2@$Mg_{12}Al_3$Ti-LDH: organic co-precipitation

TiO_2@$Mg_{12}Al_3$Ti-LDH was synthesised by the organic co-precipitation method adapted from the one used to synthesise pure $Mg_{12}Al_3$Ti-LDH (Section 7.3.3). TiO_2 (1.25 g, 15.7 mmol) was dispersed in 30 mL ethanol, followed by 15 minutes of sonication. $Ti(O^iPr)_4$ (0.30 mL, 1.0 mmol) was added dropwise to 0.15 mL concentrated HCl under an inert nitrogen atmosphere, with stirring at 400 rpm. $Mg(NO_3)_2 \cdot 6H_2O$ (3.08 g, 12.0 mmol) and $Al(NO_3)_3 \cdot 9H_2O$ (1.13 g, 3.0 mmol) were dissolved in 30 mL ethanol and added dropwise to the $Ti(O^iPr)_4$/HCl solution with stirring at 300 rpm. The resulting $Mg^{2+}/Al^{3+}/Ti^{4+}$ solution was added to the TiO_2 dispersion.

NaOEt (12.0 mL of 21 wt% solution in ethanol, 32.0 mmol) was dissolved in a mixture of 2.5 mL DI water and 40 mL ethanol, and the resulting solution was added dropwise to the $TiO_2/Mg^{2+}/Al^{3+}/Ti^{4+}$ mixture over the period of 1 hour with stirring at 500 rpm. The resulting reaction mixture was aged at room temperature for 18 hours with stirring at 650 rpm.

TiO_2@$Mg_{12}Al_3$Ti-LDH: aqueous urea reflux

TiO_2@$Mg_{12}Al_3$Ti-LDH was synthesised by the aqueous urea reflux method adapted from the one used to synthesise pure $Mg_{12}Al_3$Ti-LDH (Section 7.3.3). TiO_2 (1.25 g, 15.7 mmol) was dispersed in 30 mL DI water, followed by 15 minutes of sonication. $Ti(O^iPr)_4$ (0.30 mL, 1.0 mmol) was added dropwise to 0.15 mL concentrated HCl under an inert nitrogen atmosphere, with stirring at 400 rpm. $Mg(NO_3)_2 \cdot 6H_2O$ (3.08 g, 12.0 mmol) and $Al(NO_3)_3 \cdot 9H_2O$ (1.13 g, 3.0 mmol) were dissolved in 30 mL DI water and added dropwise to the $Ti(O^iPr)_4$/HCl solution with stirring at 300 rpm. The resulting $Mg^{2+}/Al^{3+}/Ti^{4+}$ solution was added to the TiO_2 dispersion.

Urea (5.77 g, 96.0 mmol, [urea]:[metal salts] = 6:1) was dissolved in 40 mL DI water and added to the $TiO_2/Mg^{2+}/Al^{3+}/Ti^{4+}$ mixture. The resulting reaction mixture was aged under reflux conditions in an oil bath at 100 °C for 18 hours with stirring at 650 rpm.

TiO_2@$Mg_{12}Al_3$Ti-LDH: aqueous urea hydrothermal

TiO_2@$Mg_{12}Al_3$Ti-LDH was synthesised by the aqueous urea hydrothermal method adapted from the one used to synthesise pure $Mg_{12}Al_3$Ti-LDH (Section 7.3.3). TiO_2 (0.70 g, 8.8 mmol) was dispersed in 25 mL DI water, followed by 15 minutes of sonication. $Ti(O^iPr)_4$ (0.24 mL, 0.8 mmol) was added dropwise to 0.10 mL concentrated HCl under an inert nitrogen atmosphere, with stirring at 400 rpm. $Mg(NO_3)_2 \cdot 6H_2O$

(2.46 g, 9.6 mmol) and $Al(NO_3)_3 \bullet 9H_2O$ (0.90 g, 2.4 mmol) were dissolved in 25 mL DI water and added dropwise to the $Ti(O^iPr)_4$/HCl solution with stirring at 300 rpm. The resulting $Mg^{2+}/Al^{3+}/Ti^{4+}$ solution was added to the TiO_2 dispersion.

Urea (3.08 g, 51.2 mmol, [urea]:[metal salts] = 4:1) was dissolved in 30 mL DI water and added to the $TiO_2/Mg^{2+}/Al^{3+}/Ti^{4+}$ mixture. The resulting reaction mixture was divided between two 50 mL Teflon inner vessel within a stainless steel outer vessel (40 mL of reaction mixture in each), followed by ageing in an oven at 100 °C for 18 hours.

7.6.4 TiO_2@Ti-LDH product workup

After ageing, all TiO_2@Ti-LDH products, with the exception of the organic co-precipitation products, were washed with about 1 litre of DI water until the filtrate reached a pH of 7, followed by drying overnight in a vacuum oven at room temperature.

The organic co-precipitation products were first washed with about 1 litre of DI water until the filtrate reached a pH of 7, followed by washing with about 1 litre of ethanol. Finally, the products were dried overnight in a vacuum oven at room temperature.

Table 7.8 The PXRD peak positions, FWHM data, d-spacing and lattice parameters of the Ti-LDH shell components of TiO_2@Ti-LDH core-shell hybrid materials prepared with different Ti-LDH metal compositions and different synthetic methods.

Core-shell	Synthetic method	LDH PXRD peak positions (° 2θ)		$FWHM_{003}$[a] (° 2θ)	LDH d-spacing (Å)[b]		LDH lattice parameters (Å)	
		(003)	(110)		d_{003}	d_{110}	*c*-axis[c]	*a*-axis[d]
TiO_2@Ni_4Ti-LDH	Constant pH aq. co-precip.	11.157	59.883	0.916	7.93	1.54	23.79	3.08
	Variable pH aq. co-precip.	11.332	59.964	1.173	7.81	1.54	23.43	3.08
	Organic co-precipitation	/	/	/	/	/	/	/
	Aqueous urea reflux	12.167	59.290	0.405	7.27	1.56	21.81	3.12
TiO_2@$Mg_{12}Al_3$Ti-LDH	Constant pH aq. co-precip. (1:1 TiO_2:LDH ratio, 18 hours ageing)	11.237	60.206	0.783	7.87	1.54	23.61	3.08
	Variable pH aq. co-precip.	11.332	60.624	1.099	7.81	1.53	23.43	3.06
	Organic co-precipitation	11.157	60.799	1.205	7.93	1.52	23.79	3.04
	Aqueous urea reflux	11.655	60.799	0.301	7.59	1.52	22.77	3.04
	Aqueous urea hydrothermal	11.749	61.042	0.269	7.53	1.52	22.59	3.04
TiO_2@$Mg_{12}Al_3$Ti-LDH	Constant pH aq. co-precip. (2:1 TiO_2:LDH ratio, 18 hours ageing)	11.237	60.381	0.827	7.87	1.53	23.61	3.06
	Constant pH aq. co-precip. (1:1 TiO_2:LDH ratio, 1 hour ageing)	11.237	60.301	0.905	7.87	1.53	23.61	3.06
	Constant pH aq. co-precip. (1:1 TiO_2:LDH ratio, 4 hours ageing)	11.237	60.206	0.902	7.87	1.54	23.61	3.08

[a] Full width at half maximum of the LDH (003) PXRD reflection.
[b] Where d-spacing is defined by the Bragg equation as $n\lambda = 2d\sin\theta$, with $n = 1$ and $\lambda = 1.541857$ Å.
[c] Where LDH lattice parameter $c = 3d_{003}$.
[d] Where LDH lattice parameter $a = b = 2d_{110}$.

7.6.5 Diphenylmethanol photo-oxidation

Diphenylmethanol (1.84 g, 10.0 mmol, 100 mM) was dissolved in 100 mL acetonitrile, with stirring at 300 rpm. The catalyst was added into the solution, which was then sonicated for 15 minutes. The reaction mixture was irradiated for 1 hour with stirring at 1,000 rpm and oxygen gas bubbling through it at a gas flow rate of 70 cm^3min^{-1}, in the photo-reactor setup with a borosilicate immersion well. The catalysts used were the TiO_2@$Mg_{12}Al_3Ti$-LDH core-shell hybrid material (25 mg, prepared by aqueous constant pH co-precipitation or urea reflux), or a 1:1 mixture of TiO_2 (12.5 mg) and $Mg_{12}Al_3Ti$-LDH (12.5 mg, prepared by aqueous constant pH co-precipitation or urea reflux).

7.7 References

1 D. G. Cory and W. M. Ritchey, *J. Magn. Reson.*, 1988, **80**, 128–132.
2 C. Chen, A. Wangriya, J.-C. Buffet and D. O'Hare, *Dalton Trans.*, 2015, **44**, 16392–16398.
3 C. Chen, M. Yang, Q. Wang, J.-C. Buffet and D. O'Hare, *J. Mater. Chem. A*, 2014, **2**, 15102–15110.
4 Y. Zhao, B. Li, Q. Wang, W. Gao, C. J. Wang, M. Wei, D. G. Evans, X. Duan and D. O'Hare, *Chem. Sci.*, 2014, **5**, 951–958.
5 U. Costantino, F. Marmottini, M. Nocchetti and R. Vivani, *Eur. J. Inorg. Chem.*, 1998, **1998**, 1439–1446.
6 M. Ogawa and H. Kaiho, *Langmuir*, 2002, **18**, 4240–4242.

Appendix A: Appendix for Chapter 2

A.1 TEM of constant pH aqueous co-precipitation NiTi-LDH

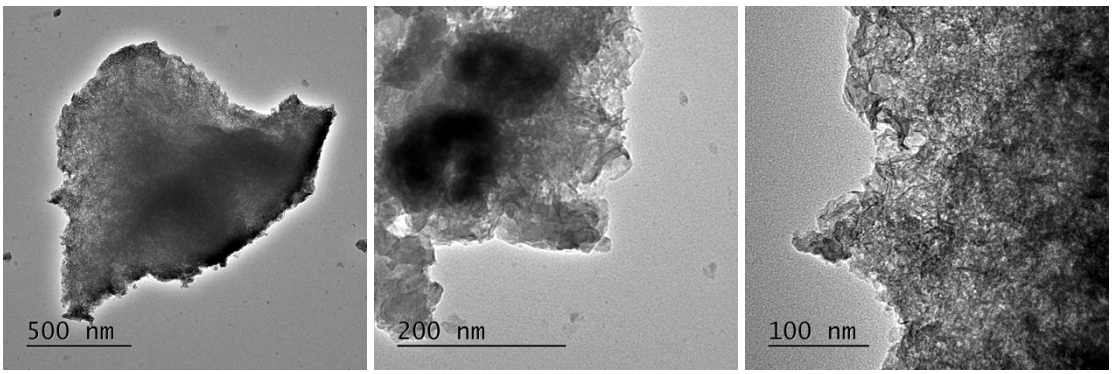


Figure A.1 TEM images of Ni_4Ti-LDH prepared by the constant pH aqueous co-precipitation method.

A.2 PXRD patterns of NiTi- and MgAlTi-LDHs

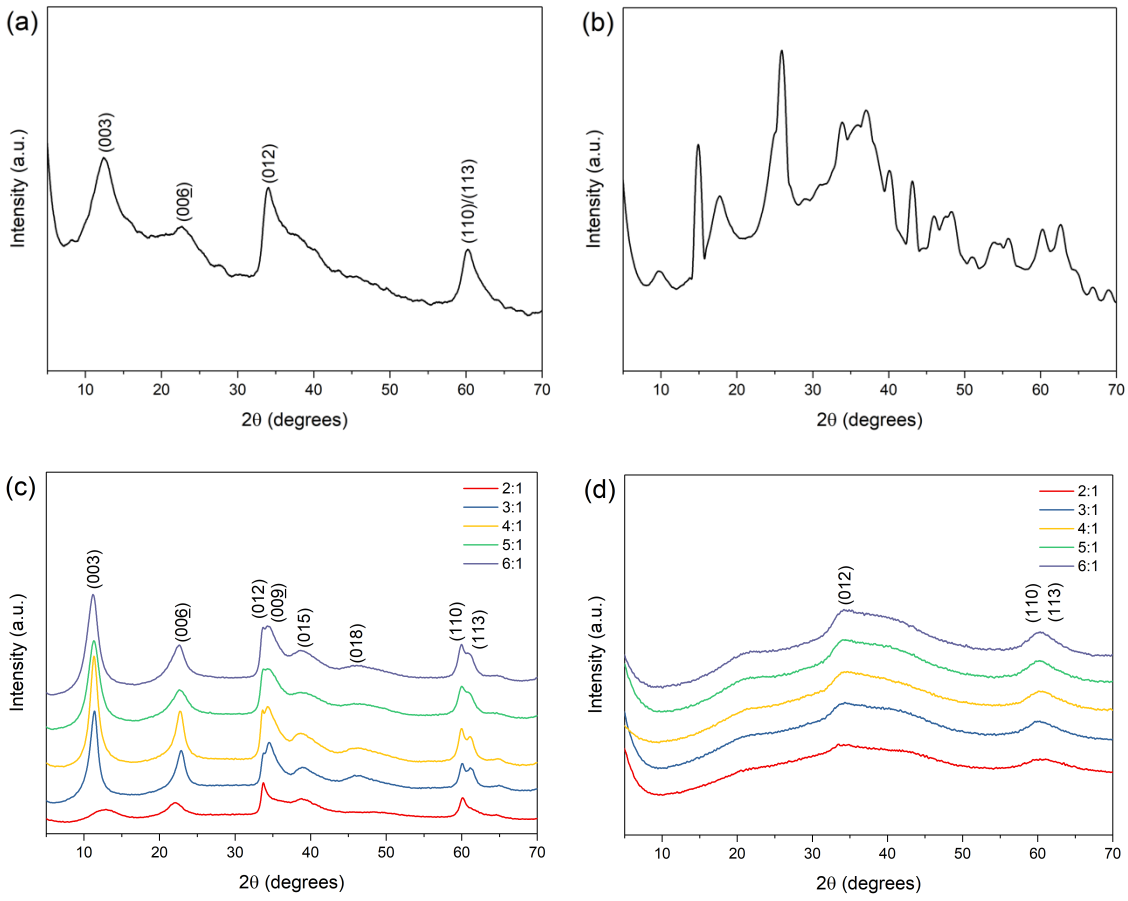


Figure A.2 PXRD patterns of NiTi-LDHs: (a) constant pH aqueous co-precipitation Ni_4Ti-LDH, (b) urea hydrothermal Ni_4Ti-LDH, (c) variable pH aqueous co-precipitation NiTi-LDHs with different Ni:Ti ratios, and (d) organic co-precipitation NiTi-LDHs with different Ni:Ti ratios.

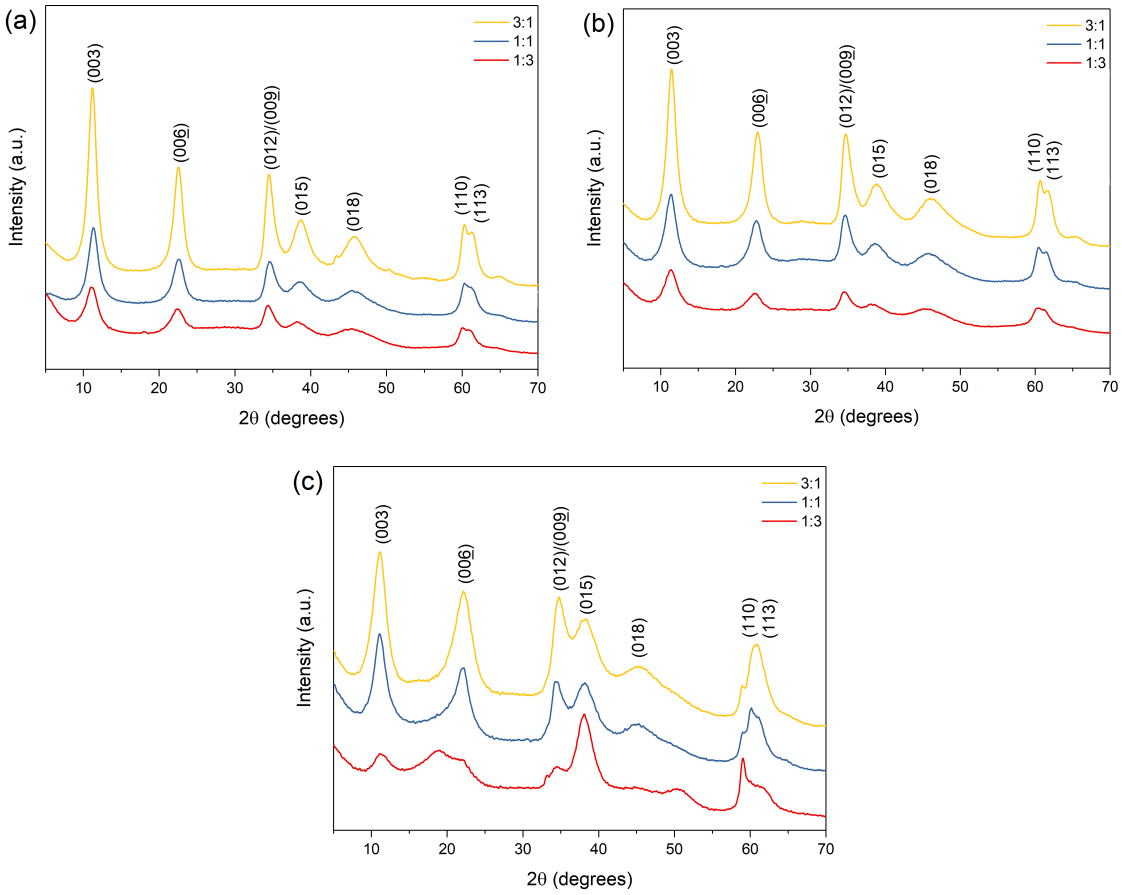


Figure A.3 PXRD patterns of MgAlTi-LDHs with different Al:Ti ratios, prepared by (a) constant pH aqueous co-precipitation, (b) variable pH aqueous co-precipitation and (c) organic co-precipitation.

A.3 FTIR spectra of NiTi- and MgAlTi-LDHs

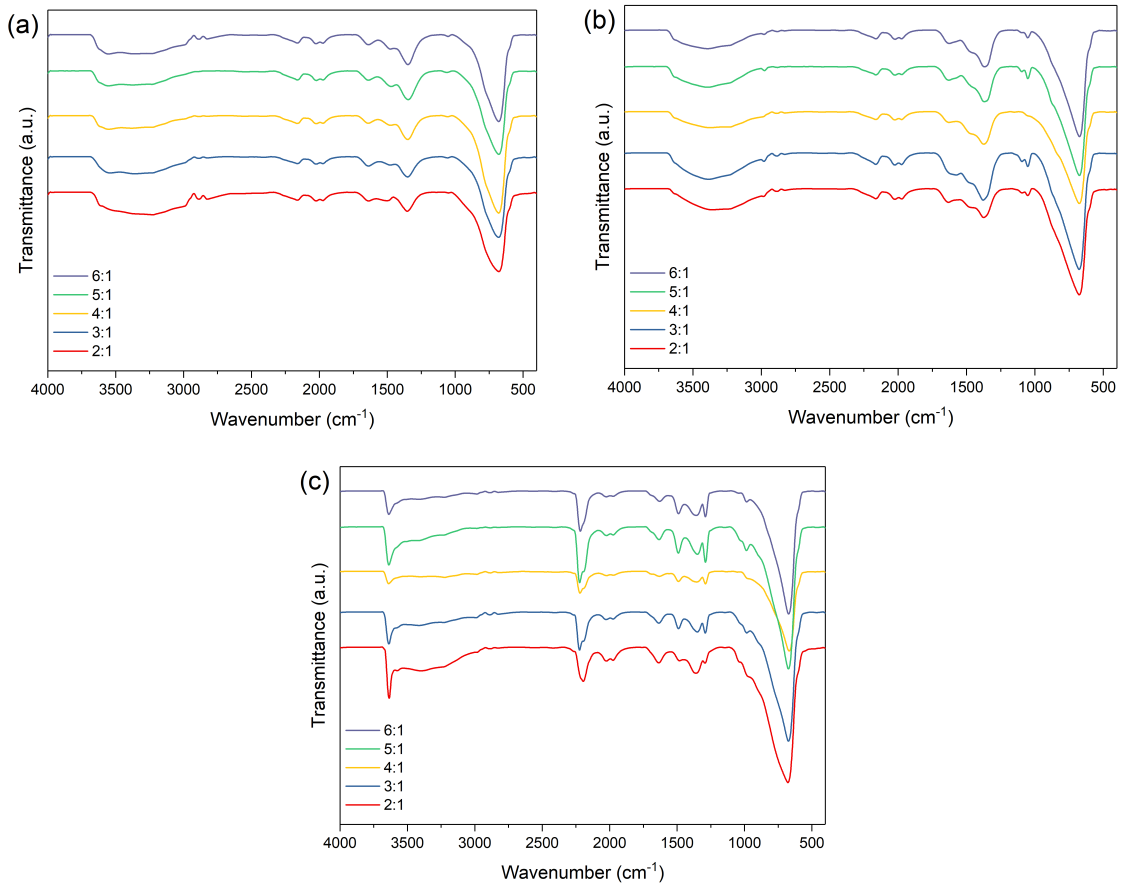


Figure A.4 FTIR spectra of NiTi-LDHs with different Ni:Ti ratios prepared by (a) variable pH aqueous co-precipitation, (b) organic co-precipitation and (c) aqueous urea reflux.

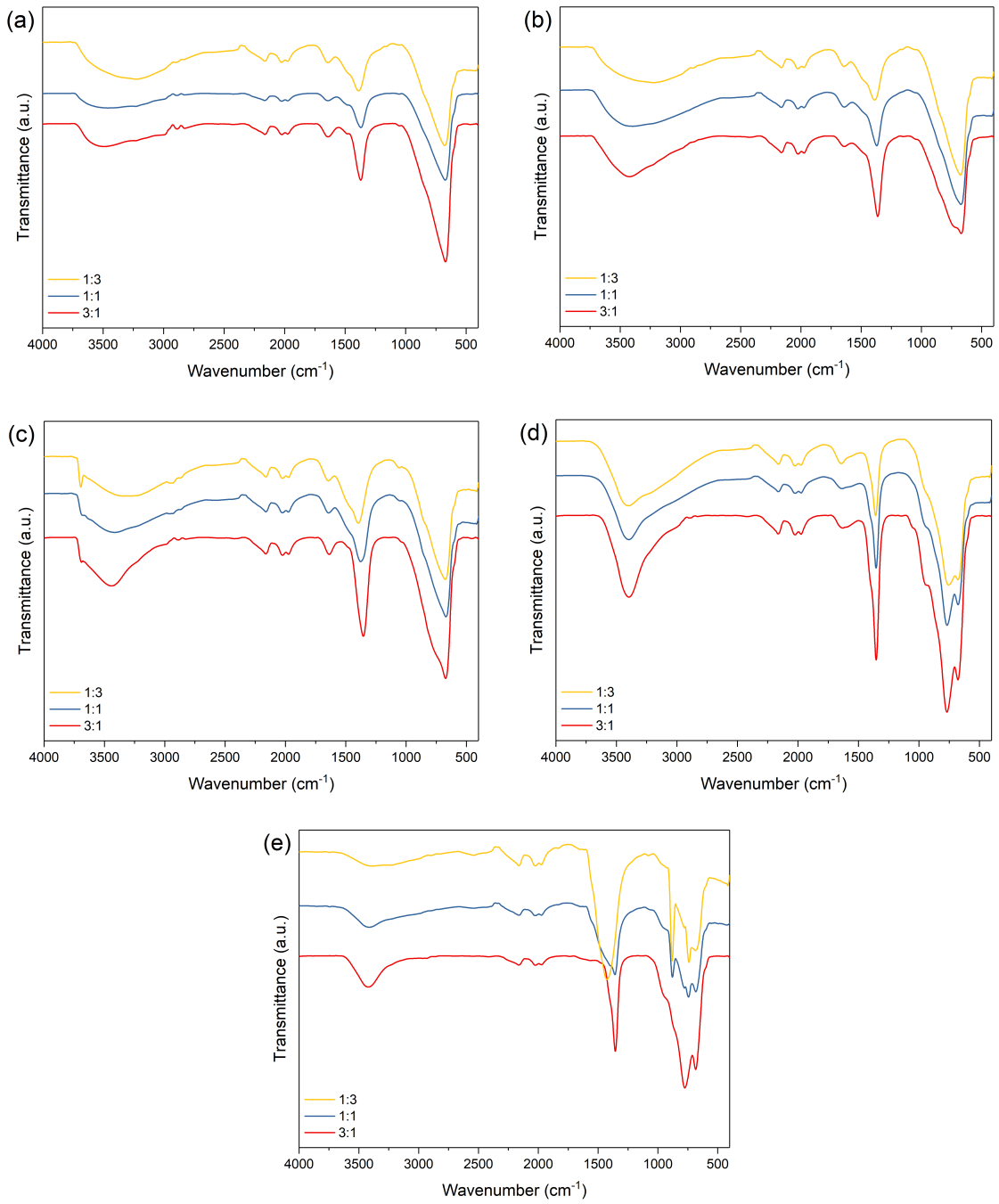


Figure A.5 FTIR spectra of MgAlTi-LDHs with different Al:Ti ratios prepared by (a) constant pH aqueous co-precipitation, (b) variable pH aqueous co-precipitation, (c) organic co-precipitation, (d) aqueous urea reflux and (e) aqueous urea hydrothermal.

A.4 BET specific surface areas of NiTi- and MgAlTi-LDHs

Table A.1 The BET specific surface areas (in m^2g^{-1}) of NiTi-LDHs prepared by different synthetic methods and with different Ni:Ti ratios.

Synthetic method/Ni:Ti ratio	**2:1**	**3:1**	**4:1**	**5:1**	**6:1**
Organic co-precipitation	274	220	326	289	230
Aqueous co-precip. at variable pH	152	97	65	42	41
Aqueous urea reflux	201	167	153	124	124

Table A.2 The BET specific surface areas (in m^2g^{-1}) of MgAlTi-LDHs prepared by different synthetic methods and with different Al:Ti ratios.

Synthetic method/Al:Ti ratio	**1:3**	**1:1**	**3:1**
Organic co-precipitation	185	79	107
Aqueous co-precip. at constant pH	5	0.6	44
Aqueous co-precip. at variable pH	0.7	0.3	0.5
Aqueous urea reflux	256	169	128
Aqueous urea hydrothermal	76	63	64

A.5 TEM images of NiTi-LDHs with different Ti content

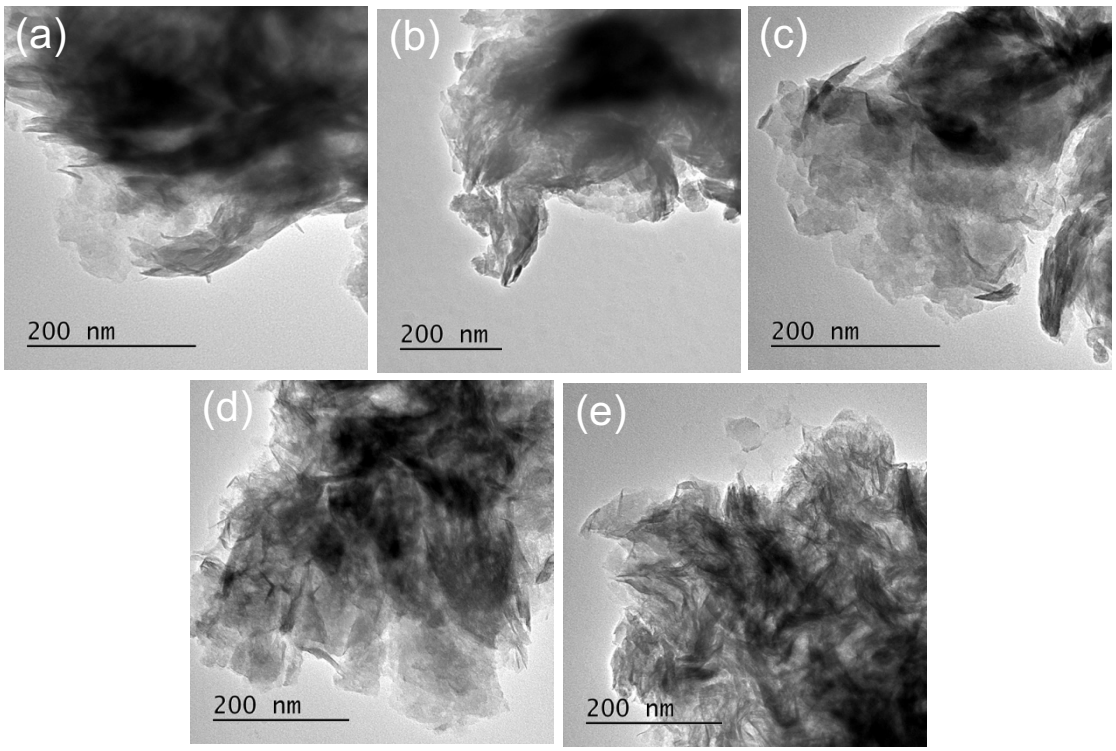


Figure A.6 TEM images of variable pH aqueous co-precipitation NiTi-LDHs with Ni:Ti ratios of (a) 2:1, (b) 3:1, (c) 4:1, (d) 5:1 and (e) 6:1.

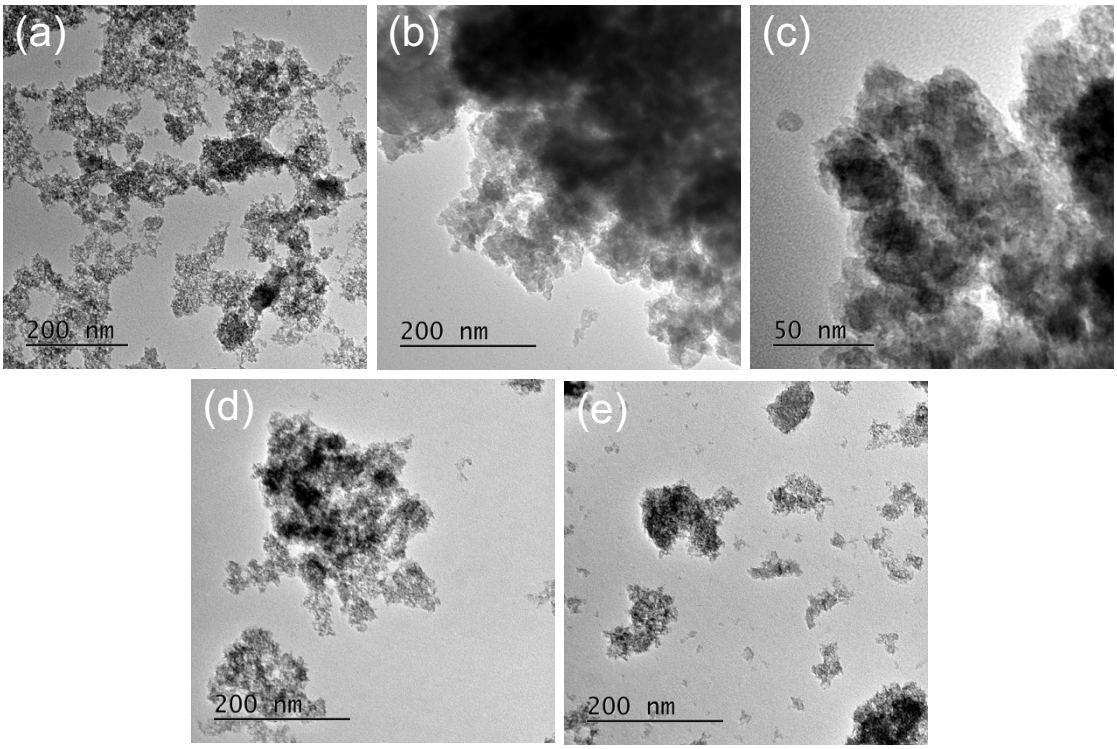


Figure A.7 TEM images of organic co-precipitation NiTi-LDHs with Ni:Ti ratios of (a) 2:1, (b) 3:1, (c) 4:1, (d) 5:1 and (e) 6:1.

A.6 TEM images of MgAlTi-LDHs with different Ti content

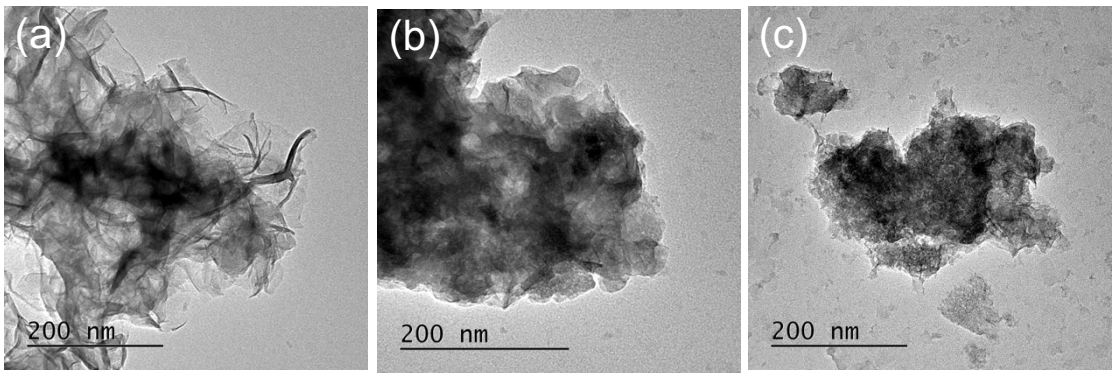


Figure A.8 TEM images of constant pH aqueous co-precipitation MgAlTi-LDHs with Al:Ti ratios of (a) 3:1, (b) 1:1 and (c) 1:3.

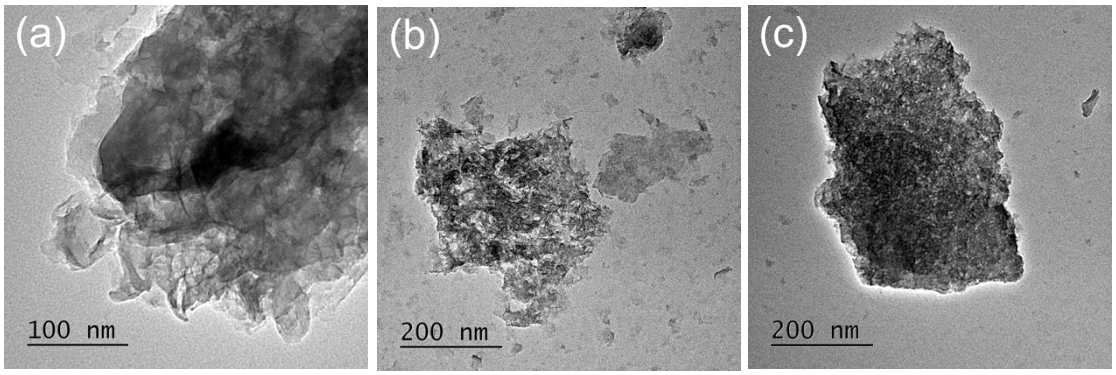


Figure A.9 TEM images of variable pH aqueous co-precipitation MgAlTi-LDHs with Al:Ti ratios of (a) 3:1, (b) 1:1 and (c) 1:3.

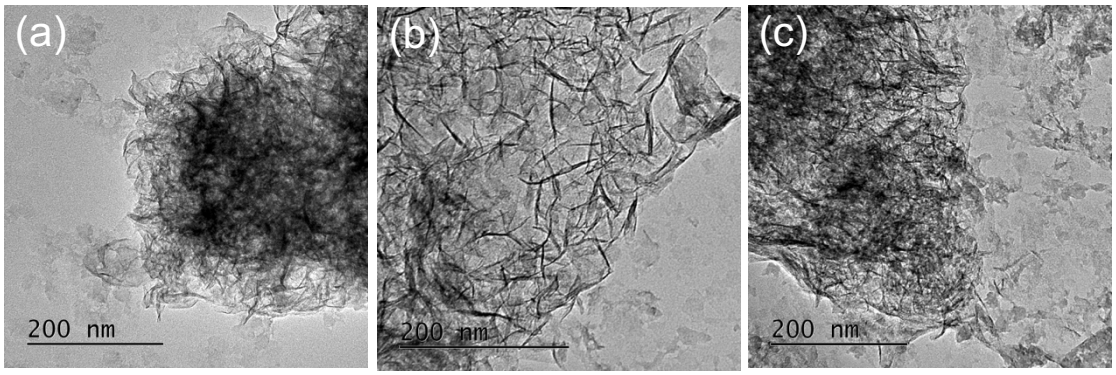


Figure A.10 TEM images of variable pH organic co-precipitation MgAlTi-LDHs with Al:Ti ratios of (a) 3:1, (b) 1:1 and (c) 1:3.

A.7 TGA plots of NiTi-LDHs

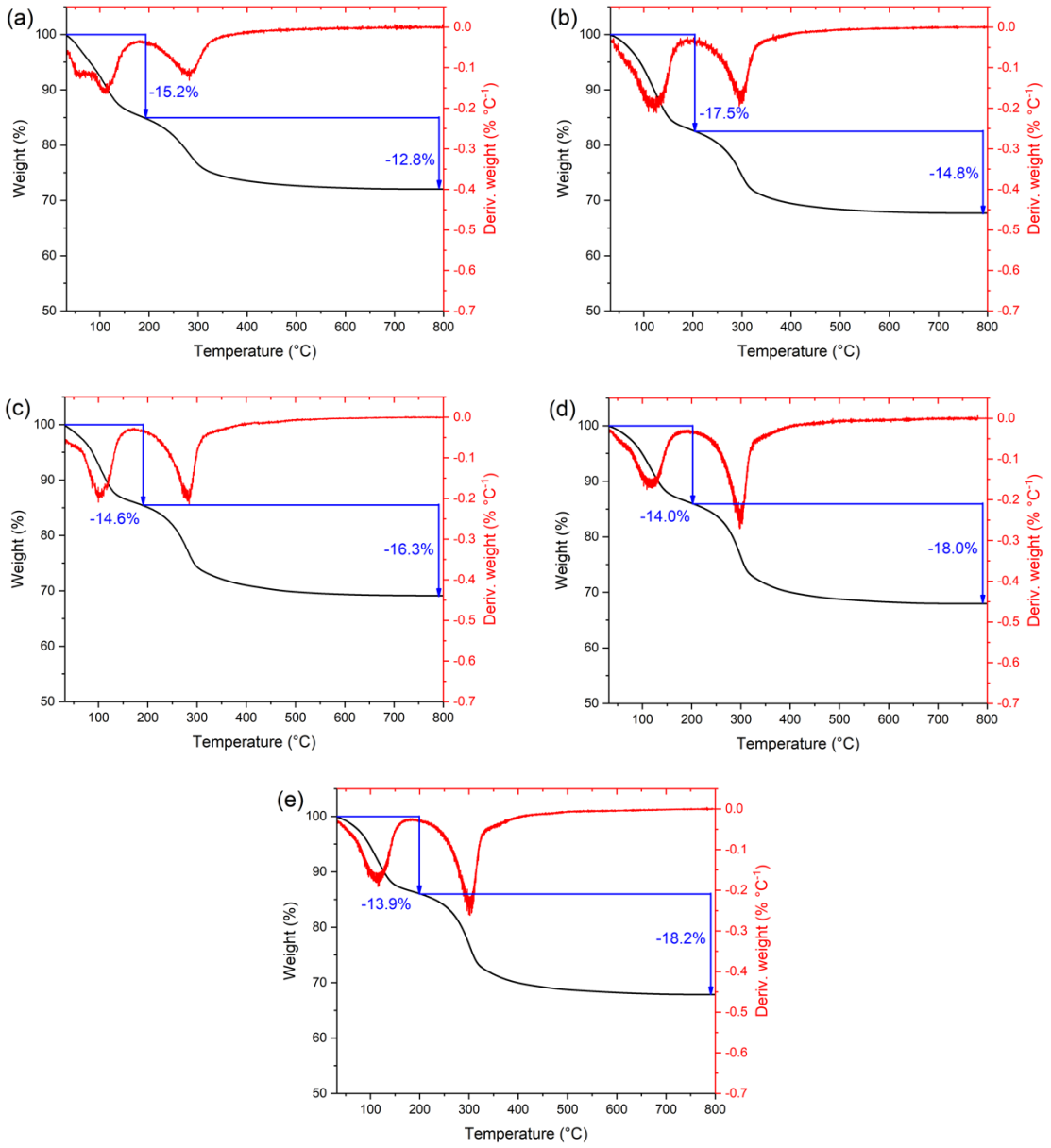


Figure A.11 TGA (black) and dTGA (red) curves for variable pH aqueous co-precipitation NiTi-LDHs with Ni:Ti ratios of (a) 2:1, (b) 3:1, (c) 4:1, (d) 5:1 and (e) 6:1.

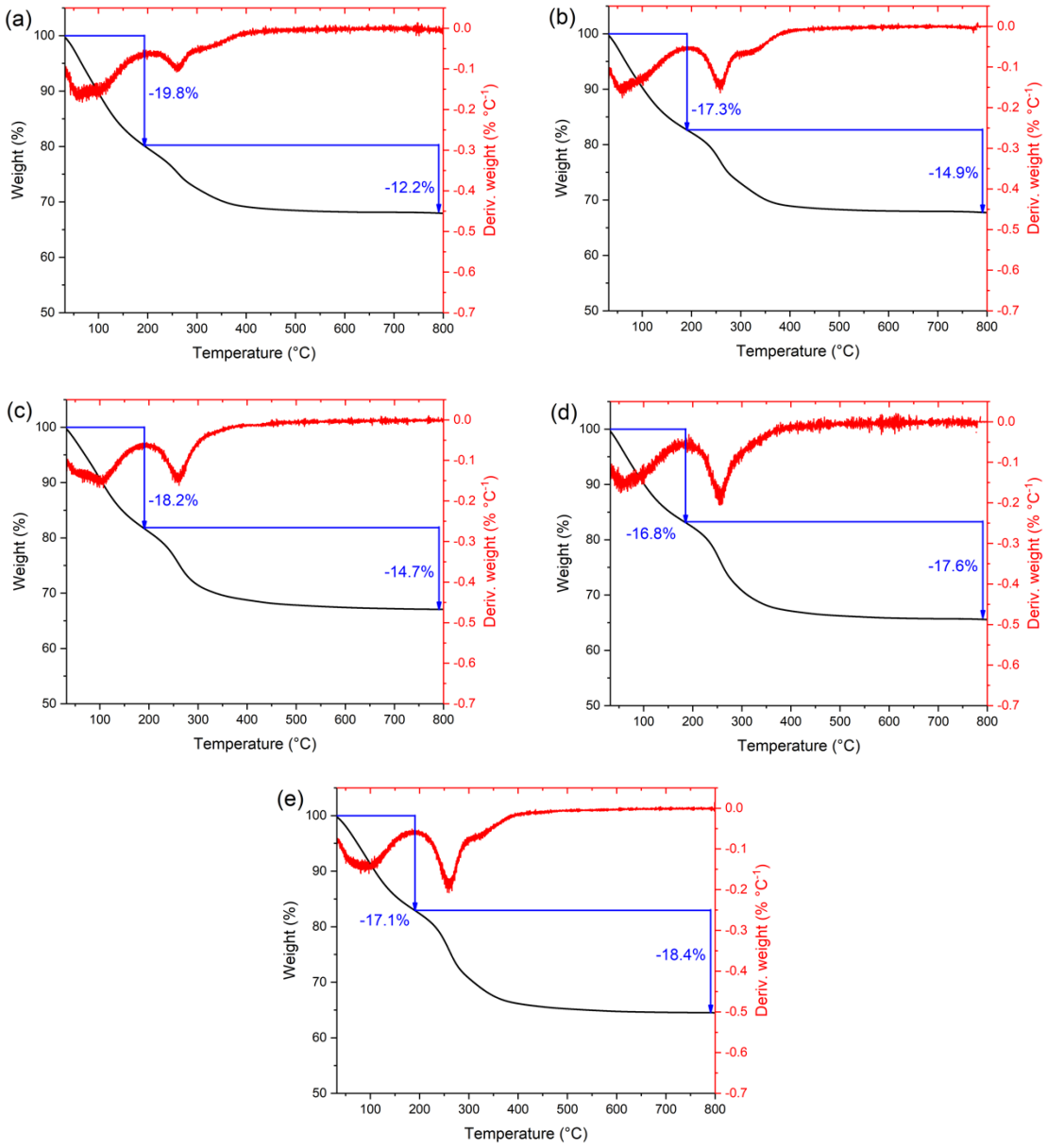


Figure A.12 TGA (black) and dTGA (red) curves for organic co-precipitation NiTi-LDHs with Ni:Ti ratios of (a) 2:1, (b) 3:1, (c) 4:1, (d) 5:1 and (e) 6:1.

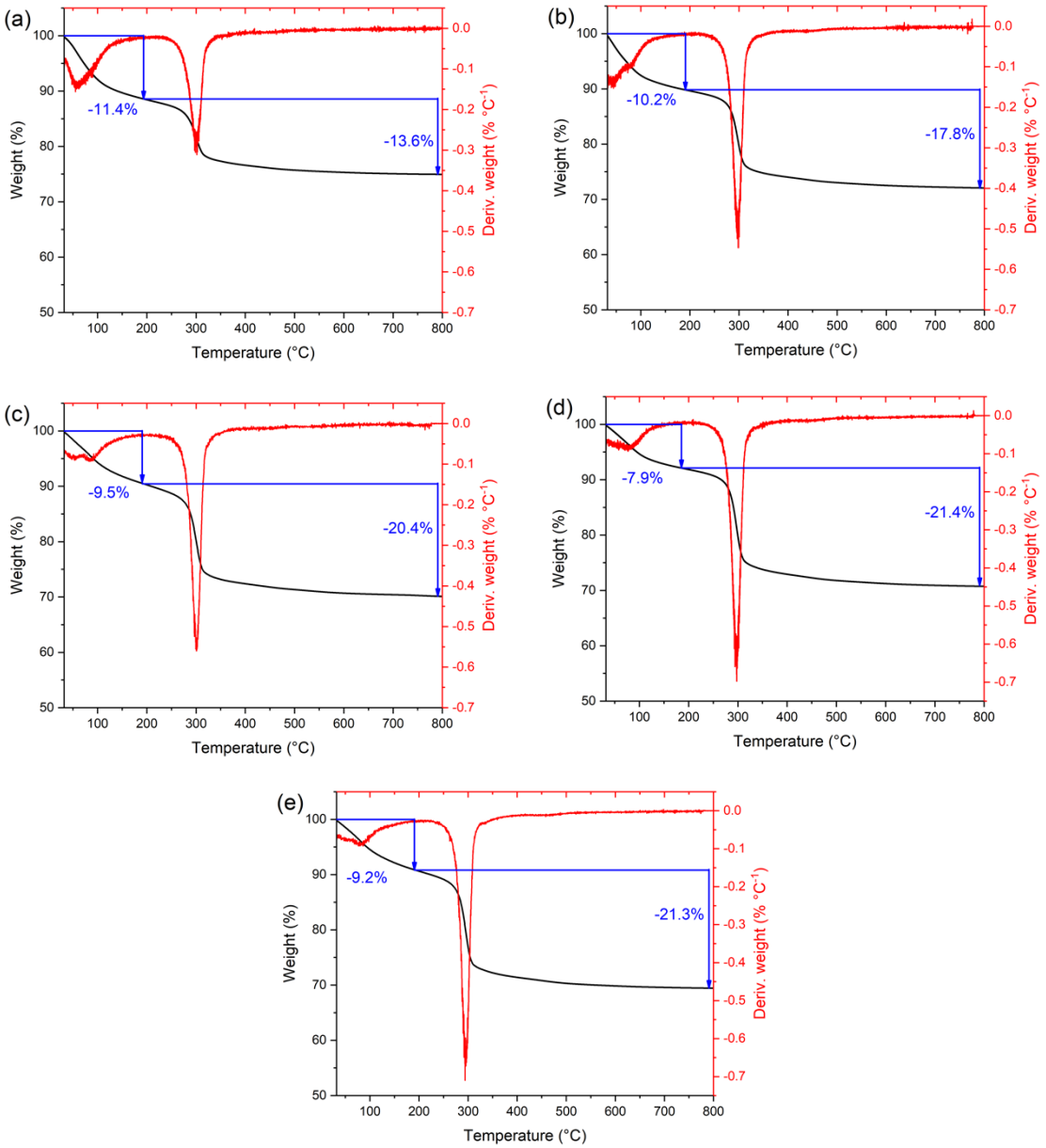


Figure A.13 TGA (black) and dTGA (red) curves for aqueous urea reflux NiTi-LDHs with Ni:Ti ratios of (a) 2:1, (b) 3:1, (c) 4:1, (d) 5:1 and (e) 6:1.

A.8 TGA plots of MgAlTi-LDHs

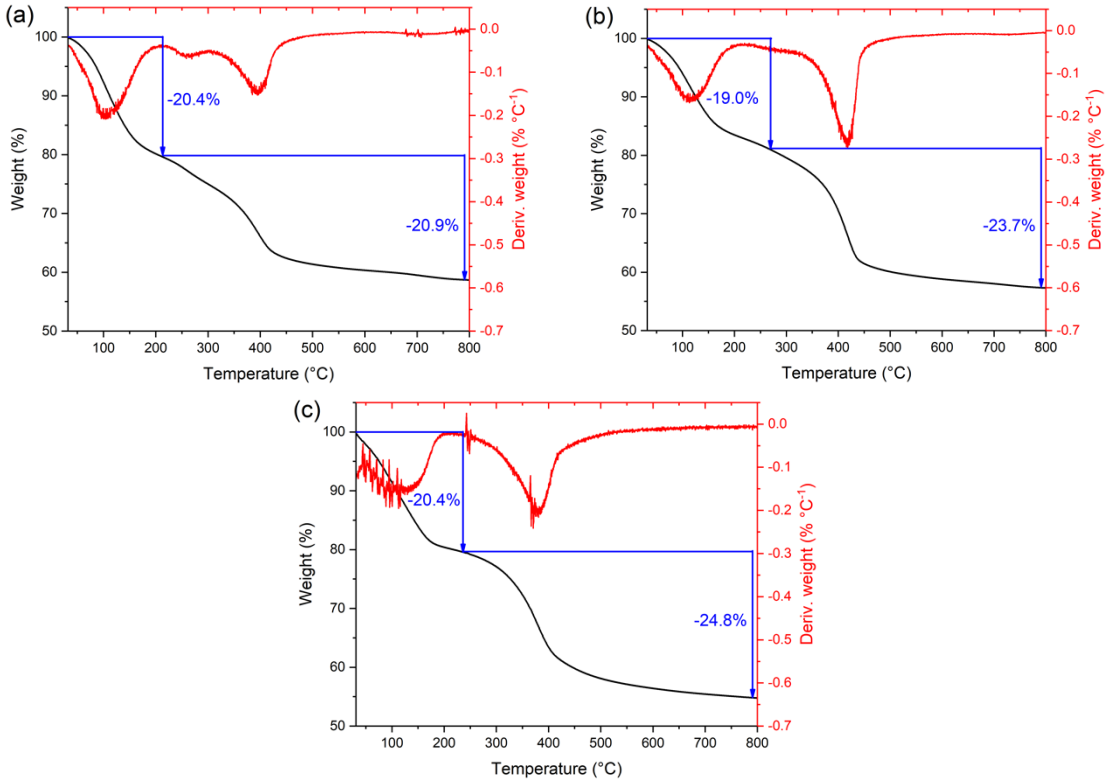


Figure A.14 TGA (black) and dTGA (red) curves for constant pH aqueous co-precipitation MgAlTi-LDHs with Al:Ti ratios of (a) 1:3, (b) 1:1 and (c) 3:1.

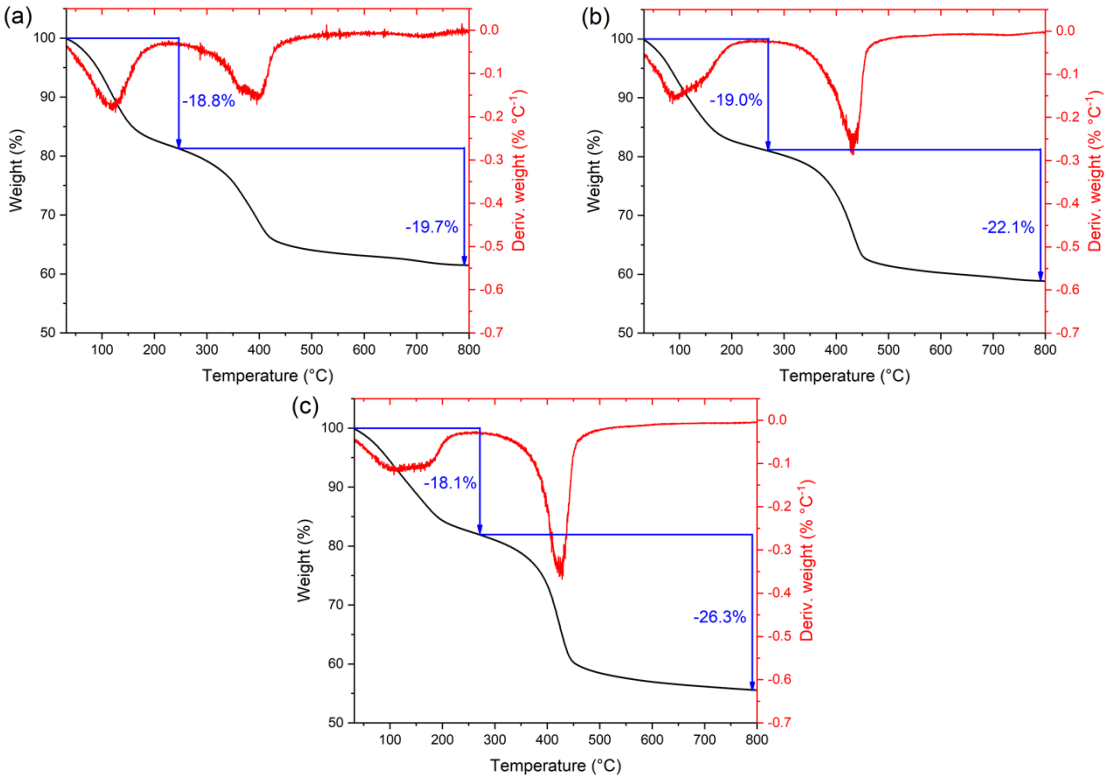


Figure A.15 TGA (black) and dTGA (red) curves for variable pH aqueous co-precipitation MgAlTi-LDHs with Al:Ti ratios of (a) 1:3, (b) 1:1 and (c) 3:1.

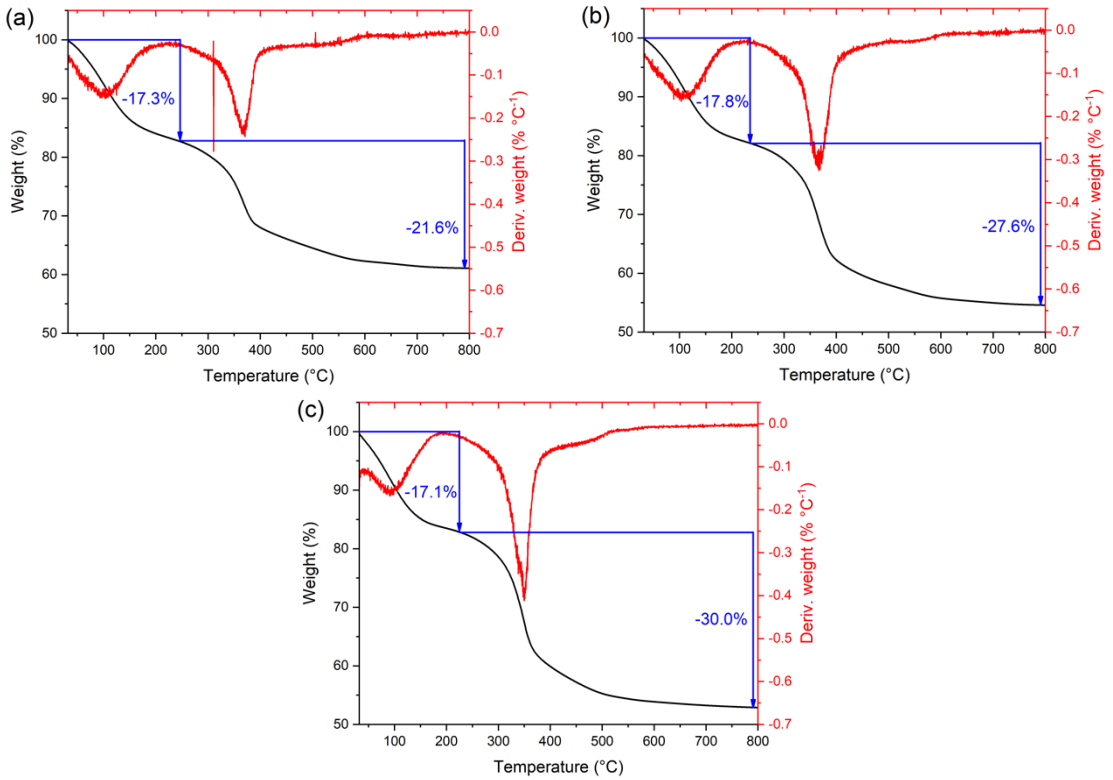


Figure A.16 TGA (black) and dTGA (red) curves for organic co-precipitation MgAlTi-LDHs with Al:Ti ratios of (a) 1:3, (b) 1:1 and (c) 3:1.

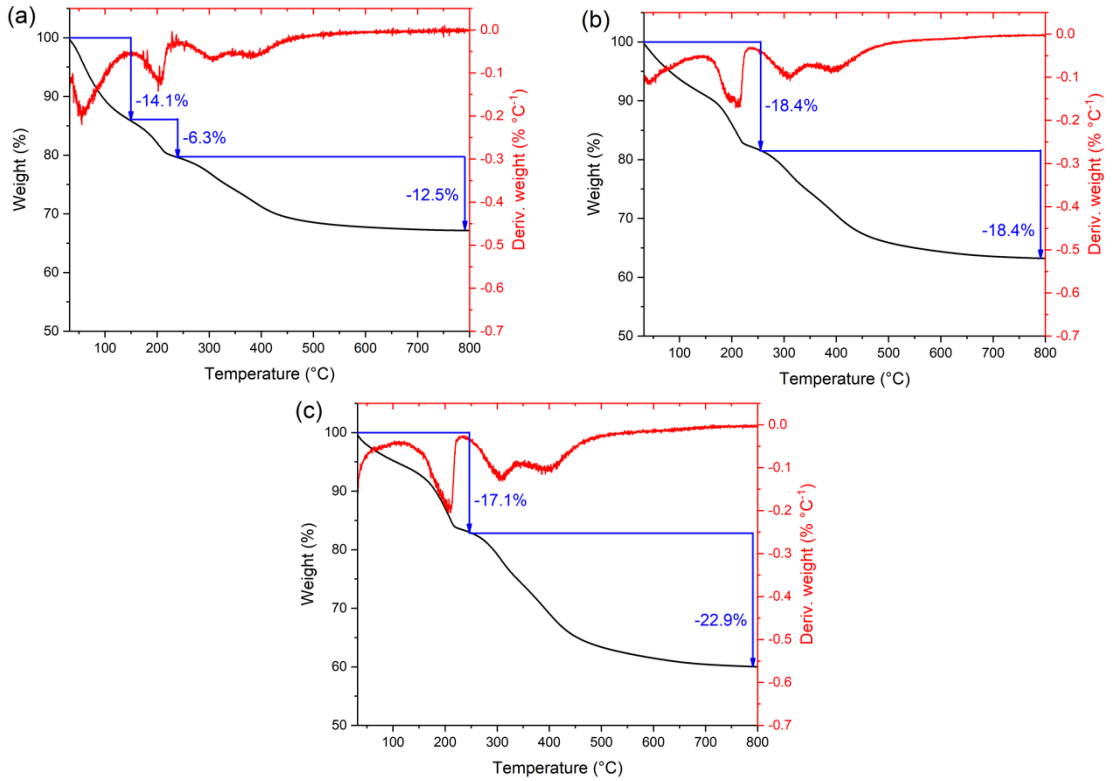


Figure A.17 TGA (black) and dTGA (red) curves for aqueous urea reflux MgAlTi-LDHs with Al:Ti ratios of (a) 1:3, (b) 1:1 and (c) 3:1.

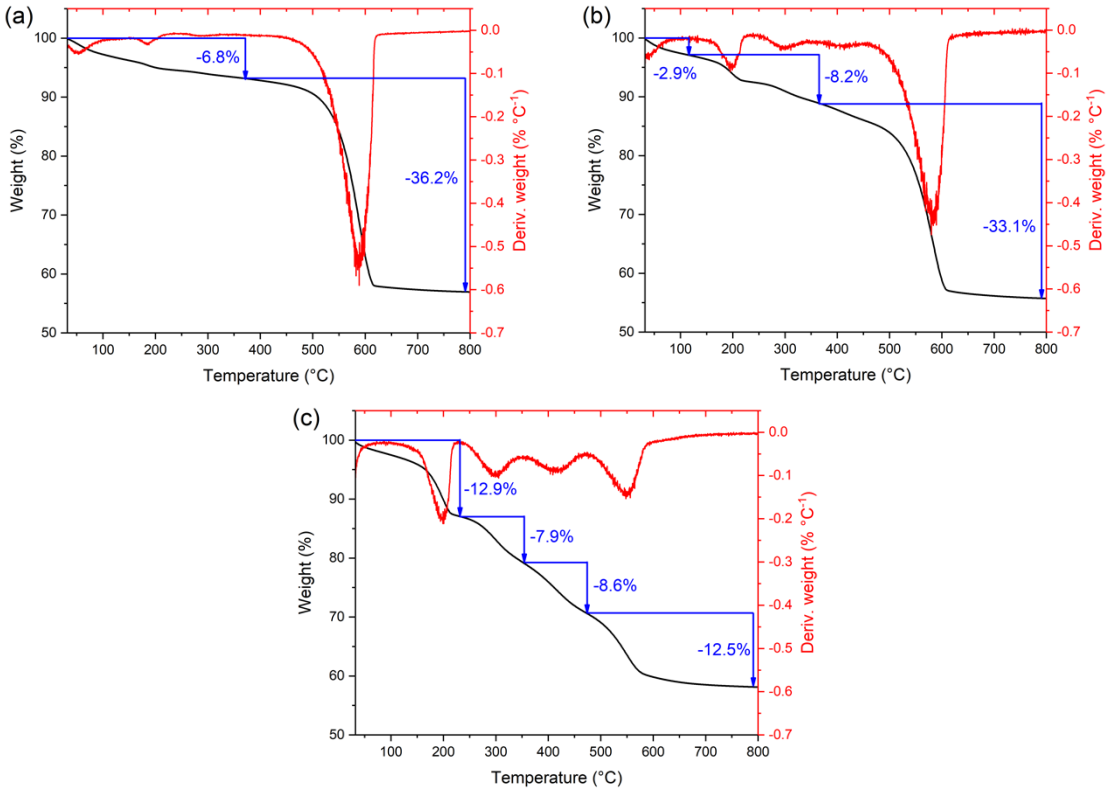


Figure A.18 TGA (black) and dTGA (red) curves for aqueous urea hydrothermal MgAlTi-LDHs with Al:Ti ratios of (a) 1:3, (b) 1:1 and (c) 3:1.

A.9 Chemical formulae of NiTi- and MgAlTi-LDHs

Table A.3 Estimated chemical formulae of NiTi-LDHs prepared with different synthetic methods and with different theoretical Ni:Ti ratios.

Synthetic method	Theoretical Ni:Ti ratio	Estimated chemical formula
Variable pH aqueous co-precipitation	2:1	$[Ni_{0.66}Ti_{0.34}(OH)_2](CO_3)_{0.34} \cdot 1.1H_2O$
	3:1	$[Ni_{0.74}Ti_{0.26}(OH)_2](CO_3)_{0.26} \cdot 1.2H_2O$
	4:1	$[Ni_{0.78}Ti_{0.22}(OH)_2](CO_3)_{0.22} \cdot 1.0H_2O$
	5:1	$[Ni_{0.82}Ti_{0.18}(OH)_2](CO_3)_{0.18} \cdot 0.9H_2O$
	6:1	$[Ni_{0.86}Ti_{0.14}(OH)_2](CO_3)_{0.14} \cdot 0.9H_2O$
Organic co-precipitation	2:1	$[Ni_{0.64}Ti_{0.36}(OH)_2](CO_3)_{0.36} \cdot 1.5H_2O$
	3:1	$[Ni_{0.76}Ti_{0.24}(OH)_2](CO_3)_{0.24} \cdot 1.2H_2O$
	4:1	$[Ni_{0.80}Ti_{0.20}(OH)_2](CO_3)_{0.20} \cdot 1.3H_2O$
	5:1	$[Ni_{0.82}Ti_{0.18}(OH)_2](CO_3)_{0.18} \cdot 1.1H_2O$
	6:1	$[Ni_{0.86}Ti_{0.14}(OH)_2](CO_3)_{0.14} \cdot 1.1H_2O$
Aqueous urea reflux	2:1	$[Ni_{0.72}Ti_{0.28}(OH)_2](CO_3)_{0.28} \cdot 0.8H_2O$
	3:1	$[Ni_{0.79}Ti_{0.21}(OH)_2](CO_3)_{0.21} \cdot 0.7H_2O$
	4:1	$[Ni_{0.83}Ti_{0.17}(OH)_2](CO_3)_{0.17} \cdot 0.6H_2O$
	5:1	$[Ni_{0.87}Ti_{0.13}(OH)_2](CO_3)_{0.13} \cdot 0.5H_2O$
	6:1	$[Ni_{0.86}Ti_{0.14}(OH)_2](CO_3)_{0.14} \cdot 0.6H_2O$

Table A.4 Estimated chemical formulae of MgAlTi-LDHs prepared with different synthetic methods and with different theoretical Al:Ti ratios.

Synthetic method	Theoretical Al:Ti ratio	Estimated chemical formula
Constant pH aqueous co-precipitation	3:1	$[Mg_{0.58}Al_{0.30}Ti_{0.12}(OH)_2](CO_3)_{0.27} \cdot 1.1H_2O$
	1:1	$[Mg_{0.55}Al_{0.20}Ti_{0.25}(OH)_2](CO_3)_{0.35} \cdot 1.1H_2O$
	1:3	$[Mg_{0.53}Al_{0.11}Ti_{0.36}(OH)_2](CO_3)_{0.42} \cdot 1.3H_2O$
Variable pH aqueous co-precipitation	3:1	$[Mg_{0.54}Al_{0.33}Ti_{0.13}(OH)_2](CO_3)_{0.31} \cdot 1.0H_2O$
	1:1	$[Mg_{0.52}Al_{0.22}Ti_{0.25}(OH)_2](CO_3)_{0.37} \cdot 1.1H_2O$
	1:3	$[Mg_{0.51}Al_{0.10}Ti_{0.39}(OH)_2](CO_3)_{0.44} \cdot 1.2H_2O$
Organic co-precipitation	3:1	$[Mg_{0.58}Al_{0.29}Ti_{0.13}(OH)_2](CO_3)_{0.28} \cdot 0.9H_2O$
	1:1	$[Mg_{0.58}Al_{0.18}Ti_{0.24}(OH)_2](CO_3)_{0.33} \cdot 1.0H_2O$
	1:3	$[Mg_{0.59}Al_{0.09}Ti_{0.32}(OH)_2](CO_3)_{0.37} \cdot 1.0H_2O$
Aqueous urea reflux	3:1	$[Mg_{0.46}Al_{0.41}Ti_{0.14}(OH)_2](CO_3)_{0.34} \cdot 0.9H_2O$
	1:1	$[Mg_{0.47}Al_{0.30}Ti_{0.23}(OH)_2](CO_3)_{0.40} \cdot 1.1H_2O$
	1:3	$[Mg_{0.37}Al_{0.12}Ti_{0.51}(OH)_2](CO_3)_{0.57} \cdot 1.5H_2O$
Aqueous urea hydrothermal	3:1	$[Mg_{0.65}Al_{0.27}Ti_{0.08}(OH)_2](CO_3)_{0.22} \cdot 0.6H_2O$
	1:1	$[Mg_{0.77}Al_{0.13}Ti_{0.10}(OH)_2](CO_3)_{0.17} \cdot 0.5H_2O$
	1:3	$[Mg_{0.80}Al_{0.06}Ti_{0.14}(OH)_2](CO_3)_{0.17} \cdot 0.3H_2O$

A.10 Detailed compositional analysis of Ti-LDHs

Table A.5 Detailed compositional analysis of NiTi-LDHs.

Synthetic method	Theoretical Ni:Ti ratio	Metal content from chemical formula		Metal content from ICP-MS		Water content from chemical formula (wt%)	Water content from TGA (wt%)
		Ni (wt%)	Ti (wt%)	Ni (wt%)[a]	Ti (wt%)[b]		
Constant pH aq. co-precipitation	2:1	30.0	12.6	34.5	15.0	15.3	15.2
	3:1	34.2	9.8	36.9	10.6	17.0	17.5
	4:1	37.7	8.7	41.3	9.4	14.8	14.6
	5:1	40.9	7.3	44.0	8.0	13.8	14.0
	6:1	43.6	5.8	45.6	6.2	14.0	13.9
Organic co-precipitation	2:1	27.3	12.5	31.2	14.6	19.7	19.8
	3:1	35.4	9.1	36.8	9.8	17.1	17.3
	4:1	37.3	7.6	38.9	8.0	18.6	18.2
	5:1	39.7	7.1	41.5	7.3	16.3	16.8
	6:1	42.3	5.6	43.7	5.8	16.6	17.1
Aqueous urea reflux	2:1	35.0	11.1	35.7	11.1	11.9	11.4
	3:1	40.1	8.7	40.5	8.7	10.9	10.2
	4:1	43.6	7.3	42.3	7.2	9.7	9.5
	5:1	47.2	5.8	46.9	5.9	8.3	7.9
	6:1	45.7	6.1	47.1	6.3	9.8	9.2

[a] Each sample was analysed three times by ICP-MS and the mean values of Ni content are reported. All standard deviations are below 0.8 wt%.
[b] Each sample was analysed three times by ICP-MS and the mean values of Ti content are reported. All standard deviations are below 0.4 wt%.

Table A.6 Detailed compositional analysis of MgAlTi-LDHs.

Synthetic method	Theoretical Al:Ti ratio	Metal content from chemical formula			Metal content from ICP-MS			Water content from chemical formula (wt%)	Water content from TGA (wt%)
		Mg (wt%)	Al (wt%)	Ti (wt%)	Mg (wt%)[a]	Al (wt%)[b]	Ti (wt%)[c]		
Constant pH aq. co-precipitation	3:1	14.4	8.3	5.9	18.6	6.1	4.4	20.2	20.4
	1:1	12.7	5.1	11.3	14.3	4.3	10.0	18.8	19.0
	1:3	11.1	2.6	14.9	10.9	2.5	15.5	20.2	20.4
Variable pH aq. co-precipitation	3:1	13.3	9.0	6.3	17.9	7.1	5.1	18.2	18.1
	1:1	12.1	5.6	11.2	16.3	4.8	10.0	18.5	19.0
	1:3	10.7	2.3	16.1	11.4	2.7	17.2	18.7	18.8
Organic co-precipitation	3:1	14.8	8.2	6.5	10.2	6.4	5.1	17	17.1
	1:1	13.8	4.7	11.2	9.6	3.4	9.8	17.6	17.8
	1:3	13.5	2.3	14.4	10.4	1.8	11.5	16.9	17.3
Aqueous urea reflux	3:1	11.0	11.1	6.7	11.6	11.1	6.2	16.3	17.1
	1:1	10.5	7.5	10.2	13.0	7.3	10.9	18.3	18.4
	1:3	6.8	2.5	18.5	8.4	3.0	20.7	20.5	20.4
Aqueous urea hydrothermal	3:1	18.6	8.6	4.5	16.7	7.7	4.3	12.7	12.9
	1:1	23.3	4.4	6.0	18.7	3.7	4.9	11.2	11.1
	1:3	25.1	2.1	8.7	19.9	1.6	7.1	7.0	6.8

[a] Each sample was analysed three times by ICP-MS and the mean values of Mg content are reported. All standard deviations are below 0.2 wt%.
[b] Each sample was analysed three times by ICP-MS and the mean values of Al content are reported. All standard deviations are below 0.1 wt%.
[c] Each sample was analysed three times by ICP-MS and the mean values of Ti content are reported. All standard deviations are below 0.4 wt%.

A.11 UV-vis spectra of NiTi- and MgAlTi-LDHs

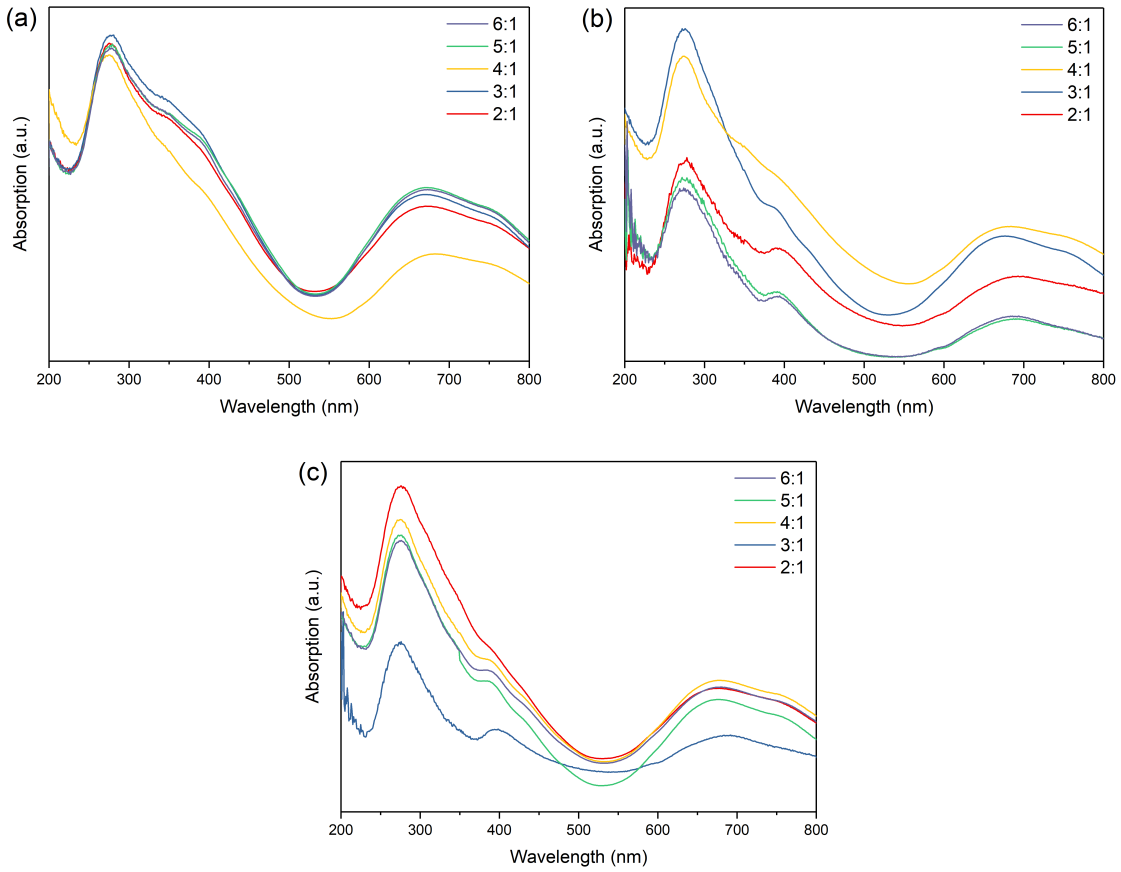


Figure A.19 UV-vis spectra of NiTi-LDHs with different Ni:Ti ratios prepared by (a) variable pH aqueous co-precipitation, (b) organic co-precipitation and (c) aqueous urea reflux.

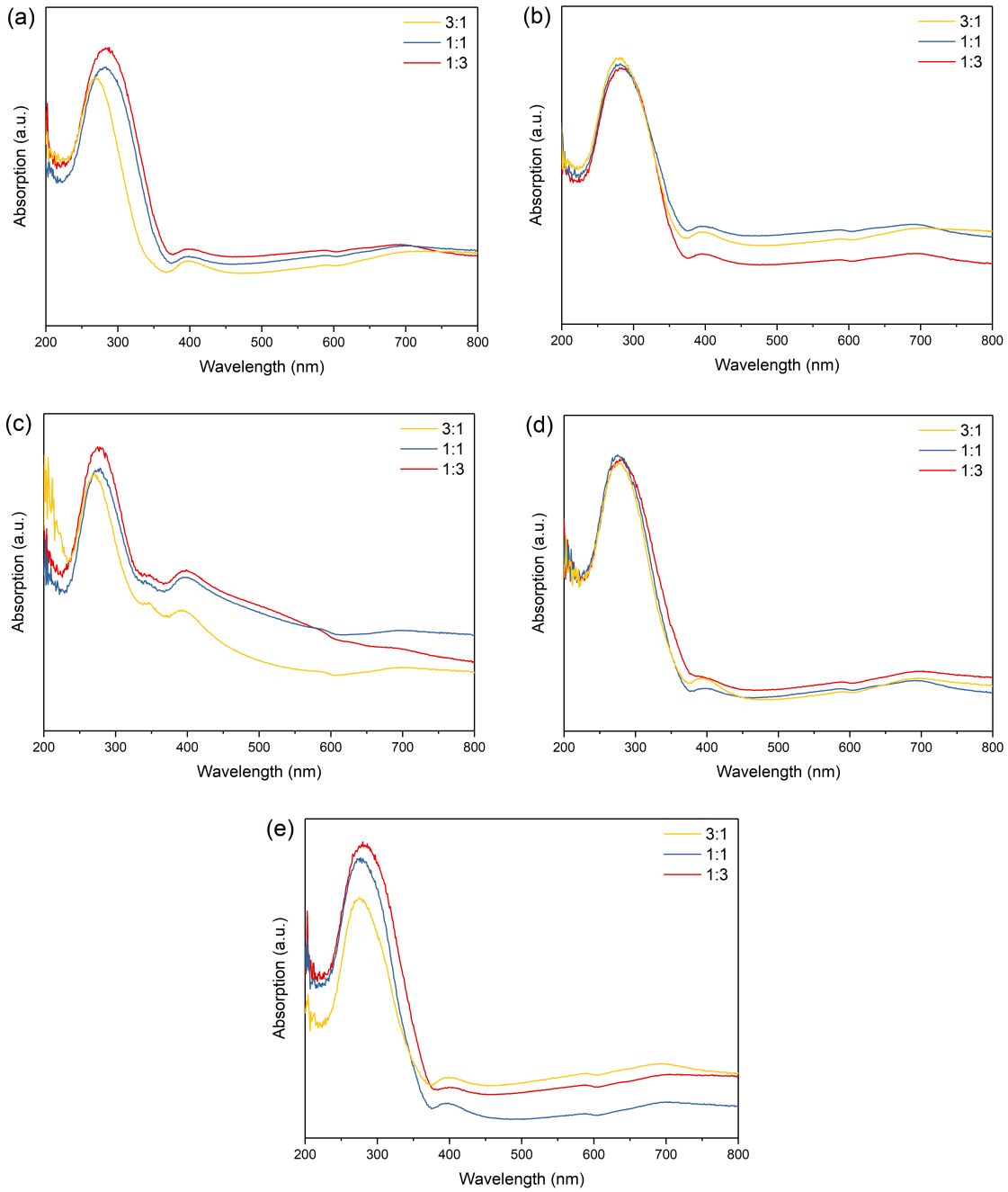


Figure A.20 UV-vis spectra of MgAlTi-LDHs with different Al:Ti ratios prepared by (a) constant pH aqueous co-precipitation, (b) variable pH aqueous co-precipitation, (c) organic co-precipitation, (d) aqueous urea reflux and (e) aqueous urea hydrothermal.

Appendix B: Appendix for Chapter 3

B.1 An overview of reactant concentrations and catalyst loadings in diphenylmethanol photo-oxidation reactions

Table B.1 An overview of the reactant concentrations and catalyst loadings, in terms of weight (mg) and concentration (wt%), used in diphenylmethanol photo-oxidation reactions.

Experimental series	Reactant concentration (mM)	Reactant weight (mg)	Catalyst loading (mg)	Catalyst loading (wt%)[a]
Variation of catalyst loading	100	1,840	5	0.3
	100	1,840	10	0.5
	100	1,840	25	1.4
	100	1,840	50	2.7
Variation of reactant concentration with 5 mg catalyst loading	5	92	5	5.4
	10	184	5	2.7
	25	460	5	1.1
	50	920	5	0.5
	100	1,840	5	0.3
Variation of reactant concentration with 25 mg catalyst loading	5	92	25	27.2
	10	184	25	13.6
	25	460	25	5.4
	50	920	25	2.7
	100	1,840	25	1.4

[a] Where catalyst loading (wt%) = m(catalyst)/m(reactant) x 100%.

Appendix C: Appendix for Chapter 4

C.1 An overview of reactant concentrations and catalyst loadings in benzyl alcohol, cyclooctanol and benzylamine photo-oxidation reactions

Table C.1 An overview of the reactant concentrations and catalyst loadings, in terms of weight (mg) and concentration (wt%), used in benzyl alcohol, cyclooctanol and benzylamine photo-oxidation reactions.

Reactant	Reactant concentration (mM)	Reactant weight (mg)	Catalyst loading (mg)	Catalyst loading (wt%)[a]
Benzyl alcohol	100	1,081	5	0.5
	100	1,081	25	2.3
Cyclooctanol	100	1,282	5	0.4
	100	1,282	25	1.9
Benzylamine	100	1,071	5	0.5
	100	1,071	25	2.3

[a] Where catalyst loading (wt%) = m(catalyst)/m(reactant) x 100%.

Appendix D: Appendix for Chapter 5

D.1 PXRD patterns of TiO_2@MgAlTi-LDHs

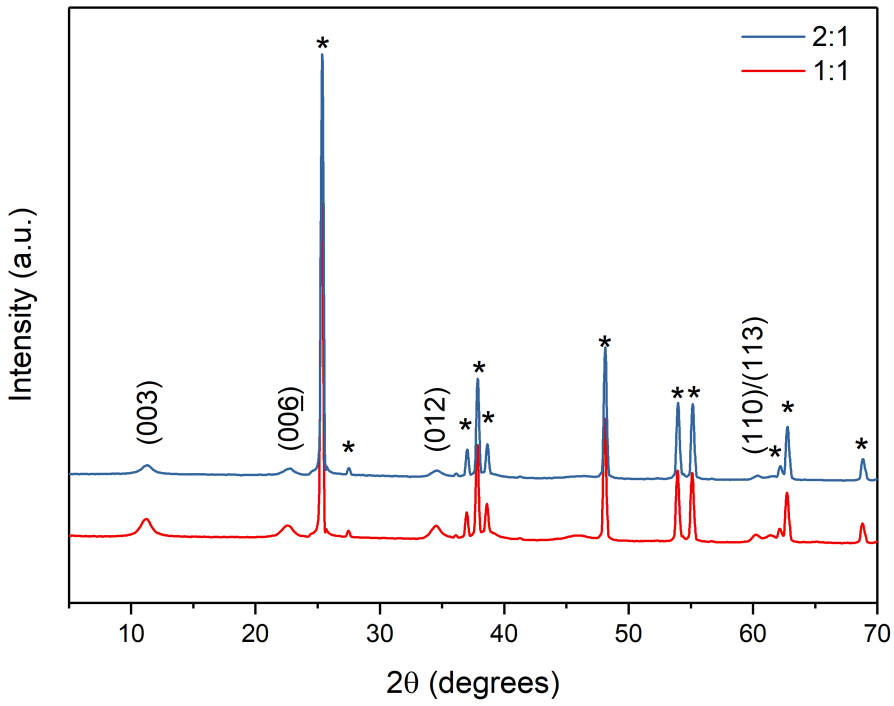


Figure D.1 PXRD patterns of TiO_2@$Mg_{12}Al_3$Ti-LDHs synthesised by the constant pH aqueous co-precipitation method with a TiO_2:LDH ratio of 2:1 and 1:1. * denotes the TiO_2 anatase phase.

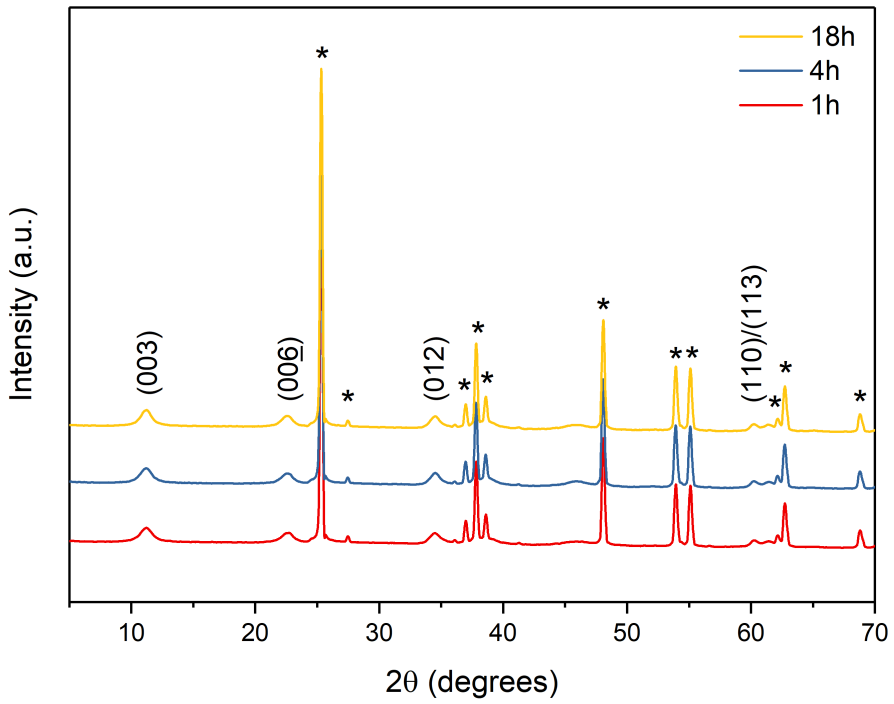


Figure D.2 PXRD patterns of TiO_2@$Mg_{12}Al_3$Ti-LDHs synthesised by the constant pH aqueous co-precipitation method with an ageing time of 1, 4 and 18 hours. * denotes the TiO_2 anatase phase.